

THE BIOPHYSICAL ROLE OF THE CELLULAR GLYCOCALYX:
ENGINEERING GLYCOPROTEINS TO CONTROL CELL-SURFACE
PROPERTIES

A Dissertation

Presented to the Faculty of the Graduate School
of Cornell University

In Partial Fulfillment of the Requirements for the Degree of
Doctor of Philosophy

by

Carolyn Renee Shurer

August 2019

© 2019 Carolyn Renee Shurer

THE BIOPHYSICAL ROLE OF THE CELLULAR GLYCOCALYX:
ENGINEERING GLYCOPROTEINS TO CONTROL CELL-SURFACE
PROPERTIES

Carolyn Renee Shurer, Ph. D.

Cornell University 2019

The glycocalyx is the sugary coating on the surface of essentially all mammalian cells. Despite being a major class of biomolecules, research into carbohydrates has lagged behind other classes of biomolecules such as nucleic acids and proteins. The constituent parts of the glycocalyx are not encoded in our genome, but rather dynamically regulated by protein expression rates, post-translational modification rates, and metabolic flux. Therefore, we can view the glycocalyx as a complex and dynamic biomaterial on the surface of cells; however, research into the impact of the glycocalyx as a biomaterial is lacking. Coating the cellular surface, the glycocalyx is uniquely positioned to impact many different cell-surface properties including regulation of cell-cell and cell-extracellular matrix interactions, cell-surface features, and cellular migration.

Throughout this work, we approach the glycocalyx as a biomaterial coating on the surface of cells with the goal of appreciating the physical properties and implications of the material. We first use an engineering approach to develop a new set of genetically encoded mucin biopolymers to facilitate in studying the cancer glycocalyx. We then apply our expertise in synthetic biology approaches and mucin biopolymer expression to produce some of the first ever recombinant mucins for therapeutic applications. Taking

advantage of the anti-adhesive properties of mucin, we apply mucin expression as an innovative technology for reduced aggregation of cells grown in suspension in bioreactors. With our unique viewpoint of the glycocalyx from a physical perspective, we apply polymer brush theory to develop a model for membrane bending driven by glyco-biopolymers. Finally, we investigate what role the anti-adhesive glycocalyx may play in regulating cellular migration both *in vitro* and *in vivo*. Together, these projects utilize engineered glycoproteins to elucidate new functions for the mammalian glycocalyx in various avenues of cellular behavior and inform future research into the physical role of the glycocalyx at the cell surface.

BIOGRAPHICAL SKETCH

Carolyn grew up in Clearfield, Pennsylvania and graduated from Clearfield Area High School in 2008. She attended Virginia Polytechnic Institute and State University where she conducted research in the Goldstein Lab in Chemical Engineering. She graduated *summa cum laude*, earning a Bachelor of Science degree in Chemical Engineering and a Bachelor of Arts certificate in Chemistry in May 2013. She entered Cornell University's Chemical and Biomolecular Engineering Ph. D. program in Fall 2013, eventually joining Professor Matthew Paszek's lab.

To my parents, Kenneth and Pamela Shurer,
who have supported me every step of the way and made me into who I am.

ACKNOWLEDGMENTS

Professor Matthew Paszek – Thank you for your belief in me throughout this process and your continued support for me and my career.

To the Paszek lab – Thank you all for your contributions to my research over the past several years. Every single lab member has contributed to my success in some way. My co-authors are many.

Professor Abraham Stroock and Professor Jan Lammerding – Thank you for serving on my thesis committee and for providing me with valuable advice, both research and career related.

To my other collaborators and co-authors – Research is no longer a matter for the lone wolf, if it ever was. Many others have contributed to this work, and every single contribution has been essential to the quality of the finished product.

To my friends and colleagues at Cornell – You brought joy to even the darkest days of graduate school. I am glad to have met each of you.

To the Friedl lab – The final year of my Ph.D. spent in Houston has been an invaluable experience which could not have happened without your friendship and guidance, especially related to the animal procedures.

Yaset Acevedo – Thank you for your love and support. I know that it is for discrete and immutable reasons. You are an essential component to everything

that I do.

This work has been funded by the National Institute of General Medical Sciences Ruth L. Kirschstein National Research Service Award 2T32GM008267, the Knight Family Foundation Graduate Research Fellowship in Nanoscience and Technology, and the Samuel C. Fleming Family Graduate Fellowship. I genuinely appreciate the funding support which has afforded me flexibility and independence during my Ph.D. research.

TABLE OF CONTENTS

Biographical Sketch	iii
Dedication	v
Acknowledgements	vii
Table of Contents	ix
List of Figures	xi
List of Tables	xiv
Chapter 1 – Introduction and Summary	1
1.1 Introduction	1
1.2 Summary	5
Chapter 2 – Genetically encoded toolbox for glycoalyx engineering: tunable control of cell adhesion, survival, and cancer cell behaviors	10
2.1 Summary	10
2.2 Introduction	11
2.3 Results and discussion	13
2.4 Conclusions	29
2.5 Materials and methods	31
2.6 Acknowledgements	38
2.7 Supporting figures	39
2.8 Supporting text	40
Chapter 3 – Stable recombinant production of codon-scrambled lubricin and mucin in human cells	44
3.1 Abstract	44
3.2 Introduction	45
3.3 Results and discussion	49
3.4 Conclusion	65
3.5 Materials and methods	65
3.6 Acknowledgements	71
3.7 Supplemental figures and table	72
Chapter 4 – Mucin technologies for protection and reduced aggregation of cellular production systems	76
4.1 Abstract	76
4.2 Introduction	77
4.3 Materials and methods	80
4.4 Results	86
4.5 Discussion	100

4.6 Acknowledgements	102
4.7 Supporting figure	103
Chapter 5 – Physical principles of membrane shape regulation by the glycocalyx	104
5.1 Summary	104
5.2 Introduction	104
5.3 Results	108
5.4 Discussion	129
5.5 Acknowledgements	131
5.6 Key resource table	134
5.7 STAR methods	143
5.8 Supporting figures	161
5.9 Supplemental note: theoretical considerations	170
Chapter 6 – The cancer glycocalyx dynamically tunes cellular migration	181
6.1 Abstract	181
6.2 Introduction	182
6.3 Results and discussion	187
6.4 Conclusion and future work	197
6.5 Methods	198
6.6 Acknowledgements	203
Chapter 7 – Conclusion and Perspective	205
Appendix A – Solid surface stresses direct cellular behaviors through integrin-based mechanotransduction	208
References	233

LIST OF FIGURES

Figure 1.1 – Ubiquitous glycosylation changes in cancer.	3
Figure 1.2 – Human Mucin-1 features.	5
Figure 2.1 – Vector for stable expression.	15
Figure 2.2 – Genetically encoded glycoproteins for glycocalyx editing.	18
Figure 2.3 – Glycoproteins of tunable length.	19
Figure 2.4 – Engineering the chemical and physical properties of the glycocalyx.	21
Figure 2.5 – Expression of a bulky glycocalyx inhibits cellular adhesion.	23
Figure 2.6 – Expression of a bulky glycocalyx enhances cell survival in suspension.	25
Figure 2.7 – Cellular division is associated with adhesion.	28
Figure 2.S1 – Immunoblot.	39
Figure 2.S2 – RTK screen.	40
Figure 3.1 – Design and synthesis of synonymous lubricin (SynLubricin).	53
Figure 3.2 – Sorting strategy to isolate stable polyclonal cell populations that produce high levels of SynLubricin.	57
Figure 3.3 – Integrated SynLubricin cDNA is stable in the cellular genome.	58
Figure 3.4 – Optimization of SynLubricin production.	61
Figure 3.5 – Purification of SynLubricin by anionic exchange chromatography.	64
Figure 3.6 – Lubrication of cartilage explants shows functionality of SynLubricin.	64
Figure 3.S1 – Transient expression of SynLubricin altered adherent cell morphology.	72
Figure 3.S2 – Validation of new transposon-based gene delivery vector.	73
Figure 3.S3 – Application of the codon-scrambling strategy for Mucl.	73
Figure 3.S4 – SynLubricin has low affinity for immobilized-metal-affinity-chromatography (IMAC) resin.	74
Figure 4.1 – Engineering biopolymer-coated cell lines.	89
Figure 4.2 – Validation of biopolymer coatings.	91
Figure 4.3 – Biopolymer coatings reduced cell aggregation.	94

Figure 4.4 – Mucin-270 reduced aggregation in high calcium culture media.	96
Figure 4.5 – Biopolymer coating enhanced resistance to shear stresses.	97
Figure 4.6 – Biopolymer coated cells can be transfected.	99
Figure 4.7 – Mucin-270 cells produced comparable levels of recombinant protein expression.	99
Figure 4.S1 – Additional data to accompany Figure 4.3 acquired 24 h prior.	103
Figure 5.1 – Flexible glycocalyx polymers induce membrane projections.	112
Figure 5.2 – Mucin polymer expression levels predict tumor cell morphologies.	115
Figure 5.3 – Membrane morphology of tissue synoviocytes is regulated by the glycocalyx.	117
Figure 5.4 – Polymer brush model of the glycocalyx and generation of preferred membrane shapes.	120
Figure 5.5 – Preferred membrane shape depends on cell-surface biopolymer concentrations.	124
Figure 5.6 – Glycocalyx-mediated membrane instabilities and microvesicle biogenesis.	125
Figure 5.S1 – Related to Figure 5.1; Validation of genetically encoded mucins.	161
Figure 5.S2 – Related to Figure 5.4; Supporting information for physical characterization of individual mucins and mucin ensembles.	163
Figure 5.S3 – Related to Figure 5.4; Additional polymer brush theory predictions for curvature generation by intermolecular interactions in the glycocalyx.	165
Figure 5.S4 – Related to Figure 5.5; Fluorescence-activated sorting and quantification of Muc1 surface densities.	167
Figure 5.S5 – Related to Figure 5.6; Tubular membrane shapes contain filamentous actin cores and resemble microvilli.	169
Figure 6.1 – Characterization of 4T1 Muc1 Δ CT cell line.	189
Figure 6.2 – Muc1 Δ CT expression blocks integrin and cadherin interactions.	190
Figure 6.3 – Muc1 Δ CT cells migrate as single-cells in 3D.	192
Figure 6.4 – Muc1 Δ CT cells exhibit a distinct 3D migration phenotype.	193

Figure 6.5 – Tracking cell migration <i>in vivo</i> using a mammary imaging window.	194
Figure 6.6 – Evolution by selective pressure of an isogenic Muc1 Δ CT-expressing cell population which is highly adhesive.	195
Figure 6.7 – Hypoxia induces changes to the glycocalyx.	196
Figure A.1 – Relationships among cell morphology, substrate elastic modulus, and ECM substrate surface energy.	213
Figure A.2 – Surface stresses in compliant ECM substrates.	216
Figure A.3 – Substrate surface tension activates stress fiber formation, focal adhesion assembly and signaling.	219
Figure A.4 – Substrate surface tension directs YAP/TAZ-mediated gene expression.	221
Figure A.5 – Substrate surface tension promotes cell proliferation and survival.	222
Figure A.S1 – Mechanical characterization of PA and silicone substrates.	231
Figure A.S2 – Fibronectin coating on PA and silicone substrates.	232
Figure A.S3 – Contact angles of water droplets on PA and silicone substrates.	232

LIST OF TABLES

Table 3.S1: Amino acid compositions in the tandem repeats of human PRG4 isoform A and SynLubricin.	75
Table 5.1 – Key Resource Table.	134
Table 6.1 – Collagen gel preparation calculations.	201

CHAPTER 1

INTRODUCTION AND SUMMARY

1.1 INTRODUCTION

1.1.1 The mammalian glycocalyx

The mammalian glycocalyx is made up of the complex sugar chains known as glycans attached to proteins and lipids and the glycosyl amino glycans assembled on the surface of eukaryotic cells (Varki and Sharon, 2009). The glycocalyx is known to play a role in most biological processes including embryonic development (Haltiwanger and Lowe, 2004), cell migration (Janik et al., 2010; Radhakrishnan et al., 2014), the immune response (Hudak and Bertozzi, 2014; Marth and Grewal, 2008; Xiao et al., 2016), and human disease (Freeze, 2013; Ohtsubo and Marth, 2006). The composition of the glycocalyx is incredibly complex in terms of the possible combinations of individual sugars and linkages between those sugar structures (Schachter, 1986; Varki et al., 2009a). The composition is also dynamically regulated by the expression level of glycan scaffolds (i.e., glycoproteins) (Reitsma et al., 2007; Varki, 1998), glycan-modifying enzymes such as glycotransferases (Nairn et al., 2008; Schachter, 1986), and cellular metabolism, especially the hexosamine biosynthetic pathway (Chatham et al., 2008; Metallo and Heiden, 2010). Due to this dynamic regulation, significant changes to the glycocalyx are observed with cell fate transitions including differentiation into different cellular lineages (Satomaa et al., 2009) and transformation (Buck et al., 1971; Hakomori, 2001).

The glycocalyx is an important structural material on the cell surface, having roles in controlling the flow of biomolecules to the cell surface, the organization and signaling of cell-surface receptors, and protecting cells from external forces (Cruz-Chu et al., 2014; Dennis et al., 2009; Kesimer et al., 2013;

Lajoie et al., 2007; Thi et al., 2004). Previous studies which have focused on the specific chemical interactions of glycans with proteins may have overlooked the important structural role of the glycocalyx. Physically separating the cell membrane from the microenvironment, the cellular glycocalyx is perfectly situated to physically mediate cell-cell and cell-extracellular matrix (ECM) interactions (Paszek et al., 2014; Soler et al., 1998; Wesseling et al., 1996). More research is needed to gain an appreciation of the physical role of the glycocalyx in essential cell surface interactions. Also, given the dynamic nature of glycocalyx remodeling in both normal physiological process and disease states, the physical properties of the glycocalyx are expected to have a broad impact on cellular behaviors.

1.1.2 Ubiquitous glycosylation changes occur in cancer

Aberrant glycosylation is a universal feature of cancer (Varki et al., 2009b). Despite the inherent complexity and heterogeneity of protein glycosylation discussed earlier, consistent and distinct changes are observed in the cellular glycocalyx upon oncogenesis with little or no tissue-specificity due to cancer-associated changes in glycoprotein levels, glycotransferase levels, and metabolic flux (Fig. 1.1A) (Charras et al., 2005; Chatterjee et al., 1979; Daye and Wellen, 2012; Guillaumond et al., 2013; Kudo et al., 1998; Kufe, 2009; LaMont and Isselbacher, 1975; Wellen et al., 2010). The cancer glycocalyx presents specific glycan motifs which are not typically observed on healthy cells and change global features of the glycocalyx by increasing the net charge (Kim and Varki; Pinho and Reis, 2015).

The majority of cancer-associated changes in glycosylation are carried on mucin-type *O*-linked glycans (Hang and Bertozzi, 2005; Ju et al., 2013; Pinho

and Reis, 2015; Varki et al., 2009b). Cancer-associated alterations in O-glycan complexity result in truncated O-glycans such as the Tn antigen (GalNAc- α -Ser/Thr) and the sialyl Tn antigen (STn, Neu5Ac2,6GalNAc1- α -Ser/Thr) (Fig. 1.1B) (Bennett et al., 2012; Ju et al., 2013; Pinho and Reis, 2015; Rahn et al., 2001; Varki et al., 2009b). Despite the pervasive glycosylation changes in cancer, researchers have still barely scratched the surface of understanding the molecular roles played by glycans.

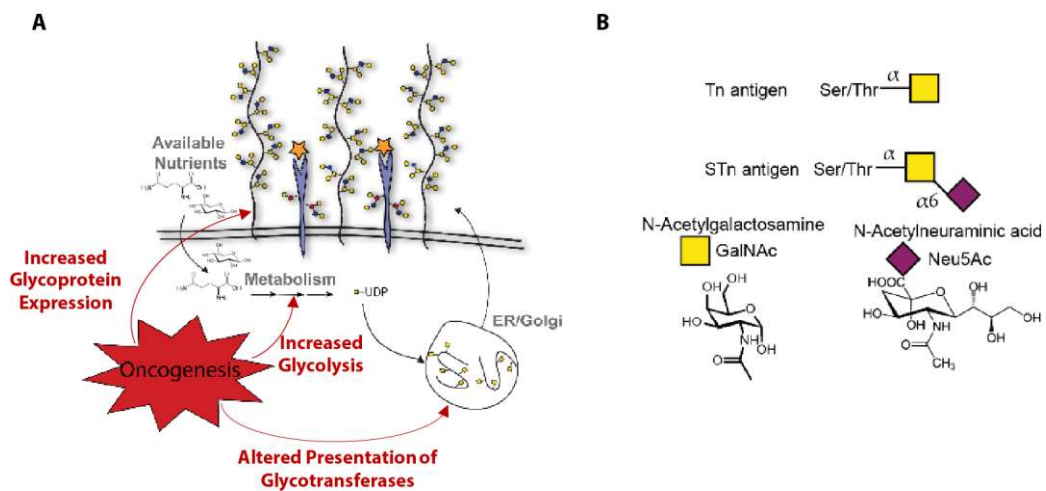


Figure 1.1 – Ubiquitous glycosylation changes in cancer. **A**, Cartoon of the cell-surface glycocalyx showing the general process of metabolism creating sugar-nucleotide substrates for glycotransferases in the ER and Golgi. Oncogenesis alters many of these normal steps in glycosylation by increasing the expression of glycoproteins, increasing the expression of glycotransferases or glycan modifying enzymes, and ramping up glycolysis which increases metabolic flux through the hexosamine biosynthesis pathway which provides precursor sugars for glycosylation. **B**, Two examples of ‘mucin-type’ O-linked glycans which specifically appear on cancer cells.

1.1.3 Bulky glycoproteins such as Mucin-1 are upregulated in cancer

In addition to specific glycosylation changes, bulky glycoproteins such as Mucin-1 (Muc1) have also been reported to be upregulated in cancer

(Paszek et al., 2014). Muc1 is over-expressed in more than 70% of human carcinomas (Gendler, 2001; Kufe, 2009) with expression level correlating with cancer aggressiveness, poor therapeutic response, and decreased patient survival in many types of cancer (Guddo et al., 1998; Hinoda et al., 2003; Hollingsworth and Swanson, 2004; Horm and Schroeder, 2013; Joshi et al., 2009).

Muc1 is a type I transmembrane protein consisting of a large ectodomain of tandem repeating units of the amino acid sequence PDTRPAPGSTAPPAHGVTS_A. The ectodomain extends about ten times farther from the cell surface than a typical transmembrane receptor (Fig. 1.2A) (Hattrup and Gendler, 2008; Nath and Mukherjee, 2014). More than half of the molecular weight of Muc1 comes from the pendant glycans (Gendler, 2001).

Not only is Muc1 over-expressed, but there is loss of the organization of Muc1 on oncogenesis. In healthy cells, Muc1 is expressed on the luminal surface of the polarized epithelium (Kufe et al., 1984). However, on oncogenesis, there is a loss of cell polarity (Vermeer et al., 2003), and Muc1 coats the entire cell surface (Rahn et al., 2001). This means that in cancer, Muc1 is found in between cells and in between cells and their microenvironment, essentially in spaces where it normally should not be (Fig. 1.2B).

1.1.4 Existing tools and methods of studying the glycocalyx are limited

Despite the prevalent and well-established role of the glycocalyx in human cancer, tools to study the impact of the cancer glycocalyx on the cellular and molecular level on various cellular process are limited. There are few chemical tools to inhibit glycan-modifying enzymes such as glycotransferases are available (Hang and Bertozzi, 2005). Studies involving genetic disruption of

glycotransferases have not produced changes in the phenotype of the glycocalyx, most likely due to redundancy of glycotransferases (Haltiwanger and Lowe, 2004; Hooper and Gordon, 2001). Even if these tools existed, these types of tools would be most useful for studies aimed at depleting a dense glycocalyx. Rather, to appreciate the impact of a bulky, mucinous glycocalyx, such as the one found on cancer cells, on the physiology of cells, we should look for tools that inflate the glycocalyx of a normal cells and test to see if or how cancer behaviors are recapitulated.

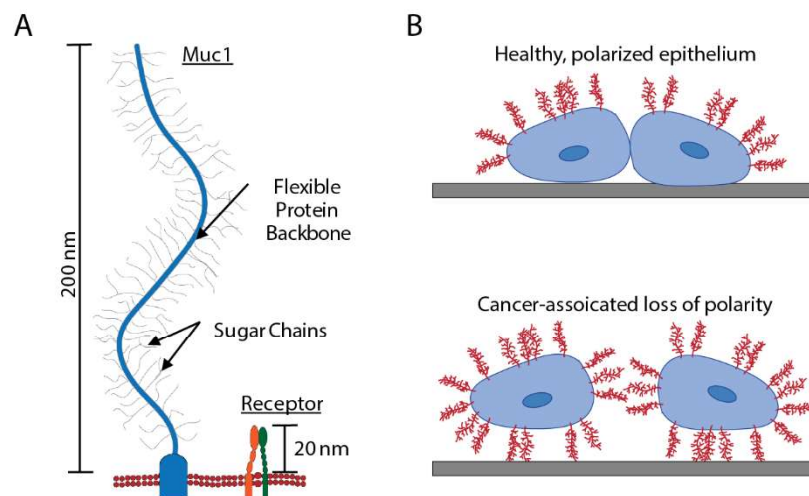


Figure 1.2 – Human Mucin-1 features. **A**, Human Mucin-1 (Muc1) is a large, type I transmembrane protein consisting of a flexible protein ectodomain decorated with many pendant *O*-linked glycans which extends approximately ten time farther from the membrane than typical transmembrane receptors. **B**, On a healthy polarized epithelium, Muc1 is excluded from cell-cell and cell-extracellular matrix junctions (top). However, on oncogenesis, there is a loss of cell polarity, and Muc1 distributes over the entire cell surface.

1.2 SUMMARY

1.2.1 Engineering and understanding the role of a bulky, mucinous glycocalyx

Throughout this work, we aim to develop an appreciation for the glycocalyx as a polymeric biomaterial coating the surface of cells.

1.2.2 Chapter 2: Genetically encoded toolbox for glycocalyx engineering: tunable control of cell adhesion, survival, and cancer cell behaviors

Limited tools exist to increase the density of the cell surface glycocalyx. The Bertozzi lab has developed a system of synthetic polymers which structurally mimic glycoproteins and can be inserted into the membrane of living cells (Godula et al., 2009a, 2009b). However, little work has been done to develop a genetically encoded toolbox which would empower long term *in vitro* and *in vivo* experiments while using native, relevant glycoprotein structures. We develop a toolkit of genetically encoded biopolymers which create a cancer-like glycocalyx. Using this toolkit, we observe decrease cellular adhesion and cancer-like behaviors of noncancerous cell lines including enhanced survival in suspension.

1.2.3 Chapter 3: Stable recombinant production of codon-scrambled lubricin and mucin in human cells

Changes in the expression of various mucinous glycoproteins are also associated with disease states other than cancer such as ocular disease and arthritis (Dhanisha et al., 2018; Elsaid et al., 2008; Kosinska et al., 2015). As such, there is commercial interest in the application of recombinant mucins as treatments for several human diseases (Le Graverand-Gastineau, 2010). While small mucin peptides have been recombinantly produced, no one has been able to produce full-length recombinant Muc1 (Backstrom et al., 2003). Using the insights gained from working with and developing our genetically-incorporated toolkit for glycocalyx manipulation, we develop strategies for

producing and purifying recombinant mucins which could be used for therapeutic purposes.

1.2.4 Chapter 4: Mucin technologies for protection and reduced aggregation of cellular production systems

Protein therapeutics are a rapidly growing fraction of the pharmaceutical market with most new protein therapeutics being produced recombinantly in mammalian cell culture (Dumont et al., 2016; Wurm, 2004). One factor limiting the production and yield of these valuable protein therapeutics is the propensity for mammalian cells to aggregate when grown in suspension (Wurm and Bernard, 1999), despite ongoing efforts to reduce aggregation by optimizing medium formulations and the development of cell culture additives (Han et al., 2006; Liu and Goudar, 2013; Peshwa et al., 1993; Tolbert et al., 1980; Zanghi et al., 2000). Given the highly anti-adhesive nature of Muc1-expression, and our observations that Muc1-expression increases survival in suspension and causes suspension cells to exist as singlets, we applied mucin-coating strategies to cell lines used in biomanufacturing.

1.2.5 Chapter 5: Physical principles of membrane shape regulation by the glycocalyx

Dramatic tubular and spherical protrusions exist on the plasma membrane comprising a large variety of different cellular structures such as cytonemes (Bischoff et al., 2013; Kornberg and Roy, 2014), microvesicles and blebs (Paluch and Raz, 2013; Tricarico et al., 2017), microvilli (D'Aloia et al., 2018; Jung et al., 2016), and cilia (Sanderson and Sleight, 1981). Cancer cells have also been shown to exhibit similar highly curved cell surface structures

(Antonyak et al., 2011; Becker et al., 2016; Bergert et al., 2015; Friedl and Wolf, 2010). There is a correlation between these types of plasma membrane structures and a mucinous glycocalyx (Bennett Jr. et al., 2001; Button et al., 2012; Hattrup and Gendler, 2008; Kesavan et al., 2009; Kesimer et al., 2013). Yet canonical models of membrane shape generation do not consider any contribution by the glycocalyx. By thinking of the glycocalyx as a polymer meshwork at the cell surface and mucin itself as bottle brush polymer, we applied existing polymer brush theory to the cell surface glycocalyx.

1.2.6 Chapter 6: The cancer glycocalyx dynamically tunes cellular migration

Cells migrate *in vivo* using a variety of mechanisms which depend on features of the ECM as well as features of the cells themselves (Friedl and Wolf, 2003, 2010; Ilina et al., 2018; Liu et al., 2015). One important determinant of cellular migratory mode is adhesion strength (Friedl and Wolf, 2010; Liu et al., 2015). Given the anti-adhesive properties of Muc1, we studied the impact of the bulky, mucinous glycocalyx on cellular migration mode. We also examined how changes to glycan presentation may influence Muc1-mediated migration switching.

1.2.7 Chapter 7: Conclusions and perspectives

In this work, we reimagined the glycocalyx as a dynamic biomaterial physically regulating cellular process at the cell surface. A greater appreciation for role of the bulky, mucinous glycocalyx frequently present on cancer cells could result in new therapeutic avenues for future cancer treatments. Insights gained from studying the physical role of a thick glycocalyx in cancer could also lead to new insights into the significance of the glycocalyx in development and

other disease states. Future research should continue to apply both this appreciation of the glycocalyx and the tools and insights learned in these studies.

CHAPTER 2

GENETICALLY ENCODED TOOLBOX FOR GLYCOCALYX ENGINEERING: TUNABLE CONTROL OF CELL ADHESION, SURVIVAL, AND CANCER CELL BEHAVIORS^{1,2}

2.1 SUMMARY

The glycocalyx is a coating of protein and sugar on the surface of all living cells. Dramatic perturbations to the composition and structure of the glycocalyx are frequently observed in aggressive cancers. However, tools to experimentally mimic and model the cancer-specific-glycocalyx remain limited. Here we develop a genetically encoded toolkit to engineer the chemical and physical structure of the cellular glycocalyx. By manipulating the glycocalyx structure, we are able to switch the adhesive state of cells from strongly adherent to fully detached. Surprisingly, we find that a thick and dense glycocalyx with high *O*-glycan content promotes cell survival even in a suspended state, characteristic of circulating tumor cells during metastatic dissemination. Our data suggest that glycocalyx-mediated survival is largely independent of receptor tyrosine kinase and mitogen activated kinase signaling. While anchorage is still required for proliferation, we find that cells with a thick glycocalyx can dynamically attach to a matrix scaffold, undergo cellular division, and quickly disassociate again into a suspended state. Together, our technology provides a needed toolkit for engineering the glycocalyx in glycobiology and cancer research.

¹Reproduced with permission from C. R. Shurer *et al.*, Genetically Encoded Toolbox for Glycocalyx Engineering: Tunable Control of Cell Adhesion, Survival, and Cancer Cell Behaviors. *ACS Biomater. Sci. Eng.* (2017), doi:10.1021/acsbomaterials.7b00037. Copyright 2017 American Chemical Society.

²C.R.S. prepared the cDNA vectors and stable cell lines and performed Western and lectin blot, flow cytometry, live-cell microscopy, RTK screen, and EdU analysis. See sections 2.6.1 and 2.6.2 for a complete author list and specific author contributions.

2.2 INTRODUCTION

The glycocalyx is a polymer meshwork comprised of proteins and complex sugar chains called glycans that assemble on the surface of the eukaryotic cell (Hudak and Bertozzi, 2014). By mediating receptor-ligand interactions (Kaszuba et al., 2015), cell-to-cell communication (Wesseling et al., 1996), and cell-matrix adhesion (Wesseling et al., 1995), glycans within the glycocalyx are now known to play an essential role in most biological processes, including development (Haltiwanger and Lowe, 2004), migration (Janik et al., 2010; Radhakrishnan et al., 2014), adhesion (Paszek et al., 2014), immune response (Hudak et al., 2014; Marth and Grewal, 2008; Xiao et al., 2016), and disease progression (Freeze, 2013; Ohtsubo and Marth, 2006). A unique feature of the glycocalyx is its dynamic nature. The composition, density, and structural organization of the glycocalyx changes profoundly with cell fate transitions, including differentiation (Satomaa et al., 2009) and transformation (Buck et al., 1971; Hakomori, 2001). A key challenge that remains is to understand on a mechanistic level how changes to the glycocalyx regulate and refine complex cellular and multicellular programs.

While much attention has focused on the biochemical properties of glycans and their chemical interactions, the glycocalyx also functions as an important structural material on the cell surface (Cruz-Chu et al., 2014; Kesimer et al., 2013; Thi et al., 2004). Separating the cell membrane and membrane proteins from the local microenvironment, the glycocalyx is uniquely positioned to biophysically regulate cell-extracellular matrix (ECM) and cell-cell interactions (Soler et al., 1998). For example, the physical properties of the glycocalyx are now known to dictate the kinetics and thermodynamics of integrin ligation with the ECM, thus controlling the spatial organization of

integrin bonds and downstream signaling processes (Paszek et al., 2014). Moreover, all cell-surface receptors are at least partially embedded within the glycocalyx, and the structural properties of the glycocalyx impact receptor diffusion, activation, and signaling (Dennis et al., 2009; Lajoie et al., 2007). Consequently, glycocalyx remodeling in normal physiological processes and disease states is expected to have broad biophysical consequences on cellular signaling and associated behaviors.

Aberrant glycosylation is a universal feature of cancer, but in most cases, the implications of a cancer specific glycocalyx are poorly understood (Ju et al., 2013; Pinho and Reis, 2015). For example, circulating tumor cells (CTCs) express an abundance of large, heavily glycosylated proteins, such as the mucin Muc1, which serves as a biomarker for isolation and detection of CTCs in clinical practice (Cheng et al., 2011; Horm and Schroeder, 2013; Paszek et al., 2014). Aberrant glycosylation and associated biochemical interactions are now recognized to contribute to nearly every step in cancer progression, including proliferation (Lau et al., 2007), survival (Paszek et al., 2014; Radhakrishnan et al., 2014; Raina et al., 2004), angiogenesis (Crocì et al., 2014), and metastatic dissemination (Häuselmann and Borsig, 2014; Snyder et al., 2015). Whether biophysical changes in the glycocalyx also contribute to some of the unique features of aggressive cancer cells and CTCs, including detachment from the ECM and survival in circulation, must still be determined.

A major roadblock to advancing cancer glycobiology has been the relative lack of tools for precision editing of the glycocalyx. One of the most successful approaches to date is based on membrane incorporation of fully synthetic polymers that mimic key features of glycoproteins (Godula et al., 2009a, 2009b). Glycopolymers enable tunable control over the types and

frequencies of glycoconjugates, membrane densities, and cell surface retention times (Woods et al., 2015; Xiao et al., 2016). The library of glycopolymers, referred to here as the synthetic toolkit, has been applied successfully to investigate cell adhesion processes (Paszek et al., 2014), immune cell activation (Hudak et al., 2014), and host-pathogen interactions (Huang et al., 2015).

Relatively little work has been done in developing a genetic toolbox specifically designed for glycocalyx engineering. A genetically encoded toolbox could provide several unique capabilities that would enable new research in biophysical glycoscience and cancer glycobiology. First, genetic encoding would support prolonged surface expression of glycocalyx elements for long-term *in vitro* and *in vivo* experiments (Gossen et al., 1995). Second, a genetic approach would afford the use of native glycoproteins that are relevant to the particular biological system or disease model of interest. Third, DNA technology provides the flexibility to quickly generate a diverse library of glycoprotein mutants through modern synthetic biology approaches (Hughes et al., 2011; Ma et al., 2012).

Here, we address this unmet need in glycobiology and develop a toolkit of genetically encoded glycoproteins and expression systems to engineer the structure and composition of the cellular glycocalyx. We apply our system to model the CTC glycocalyx and find that the glycocalyx itself could contribute to the unique adhesive properties and survival characteristics of CTCs.

2.3 RESULTS AND DISCUSSION

2.3.1 System for stable incorporation of engineered glycoproteins

Our first goal was to develop and validate a strategy for stable expression of glycoproteins in mammalian cells for glycocalyx engineering. We

envisioned that incorporation of our constructs and promoters in the cellular genome could (1) provide consistent and reliable levels of glycoprotein expression and glycan presentation, (2) support sorting and selection methods for high expression levels, and (3) enable temporal control over expression through the use of inducible promoters. Our choice for the promoter was the reverse tetracycline-controlled transactivator (rtTA) system, which can provide temporal control as well as tunable expression levels through titration of doxycycline, the chemical inducer of expression (Gossen et al., 1995). As a test glycoprotein, we chose the mucin Muc1, a key structural element in the glycocalyx of many cancer cell types (Hatstrup and Gendler, 2008; Kufe, 2009). For stable integration of the inducible promoter, transgene, and selectable marker, we first tested the utility of standard lentiviral systems (Fig. 2.1A). We found that Muc1 expression levels in epithelial cells were low, and the glycoprotein product was often of lower molecular weight than expected (Fig. 2.1B). We suspected that the highly repetitive sequences in the Muc1 tandem repeats were recombined at some stage of viral packaging or cellular transduction, and we discontinued further use of lentiviral systems.

We next tested the viability of a transposon-based system (Li et al., 2013; Wilson et al., 2007; Woodard and Wilson, 2015) for stable expression of large, repetitive glycoproteins like mucins (Fig. 2.1A) (Wilson et al., 2007). We found that Muc1 expression levels were dramatically improved with the transposon system compared to lentiviral transduction (Fig. 2.1B, C). The mucins expressed in transposon-edited cells were heavily glycosylated and had a high molecular weight (Fig. 2.1B). Finally, we confirmed that the mucin expression levels could be tuned through doxycycline induction (Fig. 2.1D, E). Based on this

performance, the inducible transposon system was applied for all subsequent editing of the glycoalyx.

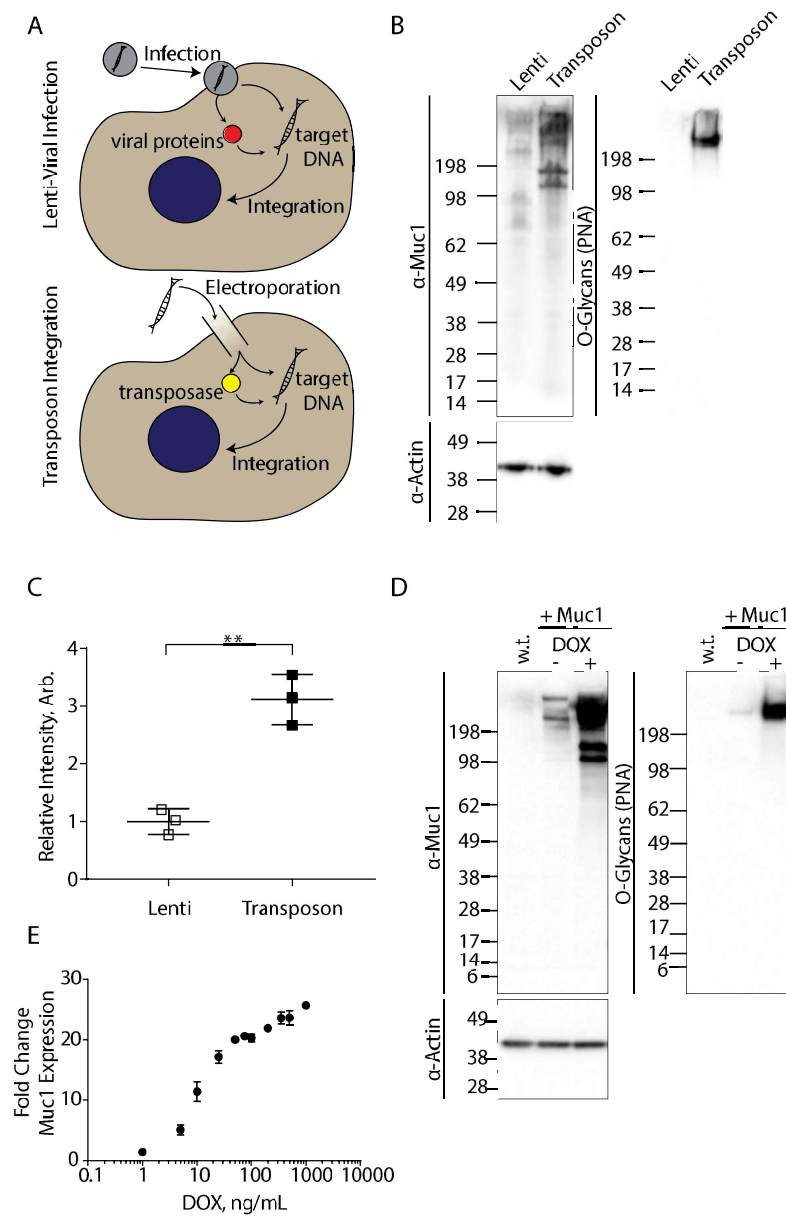


Figure 2.1 – Vector for stable expression. **A**, Graphic illustration of the lentiviral and transposon stable incorporation systems. **B**, Representative immunoblot (left) and lectin blot (right) comparison of stable Muc1 expression and PNA binding in lentiviral infection versus transposon integration, n=3. **C**, Mean integrated signal density from α -Muc1 immunoblots in B normalized to

lenti-viral samples, error bars represent the s.d., n=3. **D**, Immunoblot (left) and lectin blot (right) of Muc1 Δ CT expression in w.t. MCF10A cells compared to stable expression lines uninduced and after 24 hours induction with $0.2 \mu\text{g mL}^{-1}$ doxycycline, n=1. Cell lines were prepared with the transposon incorporation system. **E**, Fold change in Muc1 Δ CT GFP signal analyzed by flow cytometry upon induction with various doxycycline concentrations, n=3. * $p < 0.05$; ** $p < 0.01$ (two-tailed *t* test).

2.3.2 A genetically encoded toolkit for editing the O-linked glycocalyx

Our next goal was to design and fabricate a series of constructs for engineering the structure and O-glycan composition of the glycocalyx. Mucin glycoproteins are defined by their densely-clustered O-glycans, which help to extend and rigidify the mucin polypeptide backbone (Hattrup and Gendler, 2008; Kramer et al., 2015). As a consequence, mucins extend above most other glycoproteins on the cell surface and are ideal candidates for glycocalyx engineering. Our strategy was to create a library of mutant and semi-synthetic mucins that would serve as structural elements and glycan scaffolds on the cell surface. Starting with two relevant mucins in the cancer cell glycocalyx, Muc1 and Podocalyxin (Podxl, a structurally analogous glycoprotein) (Nielsen and McNagny, 2009), we removed their cytoplasmic signaling domains (Δ CT; Fig. 2.2A, B). Our goal was to minimize the biochemical activity of the mucins so that the mutants would function primarily as structural elements in the glycocalyx. In order to track phenotypic and morphological changes as a function of glycocalyx thickening, we also inserted a fluorescent protein between the O-glycan rich membrane proximal domains of Muc1 (Δ CT moxGFP; Fig. 2.2A). To effectively eliminate signaling motifs that could be present in native mucins, we next created a series of semi-synthetic constructs. We fused the O-glycan rich domains from Muc1 and Podxl to a fully synthetic

membrane proximal region, cytoplasmic domain, and transmembrane domain (Mercanti et al., 2010) (SynMuc1 and SynPodxl; Fig. 2.2A, B). We designated these semi-synthetic glycoproteins as SynMucins. All constructs were expressed efficiently through our transposon-based system and modified the *O*-glycan content of the cell surface accordingly (Fig. 2.2C, D).

We also developed a modular strategy for generating SynMucins of varying length. We introduced Bsu36I restriction sites that would serve as handles for removal or addition of *O*-glycan rich blocks in our SynPodxl construct. We validated this approach by generating synthetic mucins with *O*-linked glycosylation domains of 4/3 and 2/3 the length of native Podxl (Fig. 2.3A). In principle, this approach could be adopted to generate constructs of increasingly large size. Lectin blots confirmed the expression of *O*-rich glycoproteins of varying size by our 2/3, 1/1, and 4/3 length SynPodxl constructs (Fig. 2.3B). Notably, lectin binding to the 2/3 mutant is decreased compared to 1/1 and 4/3 lengths indicating an expected decrease in *O*-glycosylation due to the decrease in glycosylation sites on the protein. Immunoblot analysis with an anti-Podxl antibody verified expression of the higher molecular weight 4/3 SynPodxl while the 2/3 length glycoprotein was not detected by immunoblot, likely due to the inadvertent deletion of the antibody recognition motif in this construct (Fig. 2.S1). Together, our library of constructs and expression systems provide a toolkit for expression of structural glycoproteins of varying size and density on the cell surface.

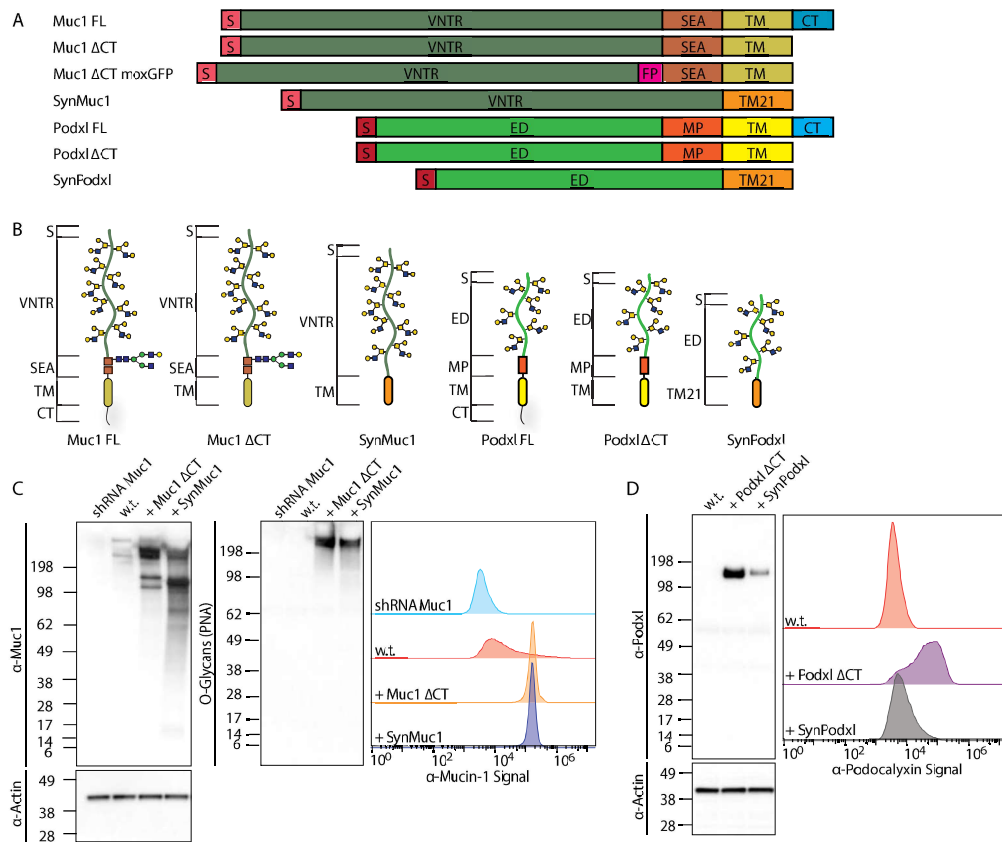


Figure 2.2 – Genetically encoded glycoproteins for glycocalyx editing. **A**, Schematic representation of the components and features of the native and engineered glycoproteins used in this study. S – signal sequence; VNTR – variable number tandem repeat; SEA – sea-urchin sperm protein, enterokinase and agrin domain; TM – transmembrane; CT – cytoplasmic tail; FP – fluorescent protein; TM21 – synthetic transmembrane domain, 21 amino acids; ED – O-glycosylation rich ecto-domain region. **B**, Cartoon illustration of the approximate relative size and features of various engineered glycoproteins. **C**, Immunoblot (left) and lectin blot (center) showing the molecular weights and expression levels of Muc1 mutants in mammary epithelial cells (MECs) stably expressing the indicated gene, n=3. Flow cytometry histograms (right) of the α -Muc1 antibody binding in cells expressing each of the engineered mutants compared to knockdown (shRNA) and w.t. cells, >50,000 cells measured per condition. **D**, Immunoblot (left) showing the relative size and expression level of Podxl mutants in stable MEC cell lines, n=3. Flow cytometry histograms (right) of α -Podxl antibody binding in the same cell lines, >50,000 cells measured per condition.

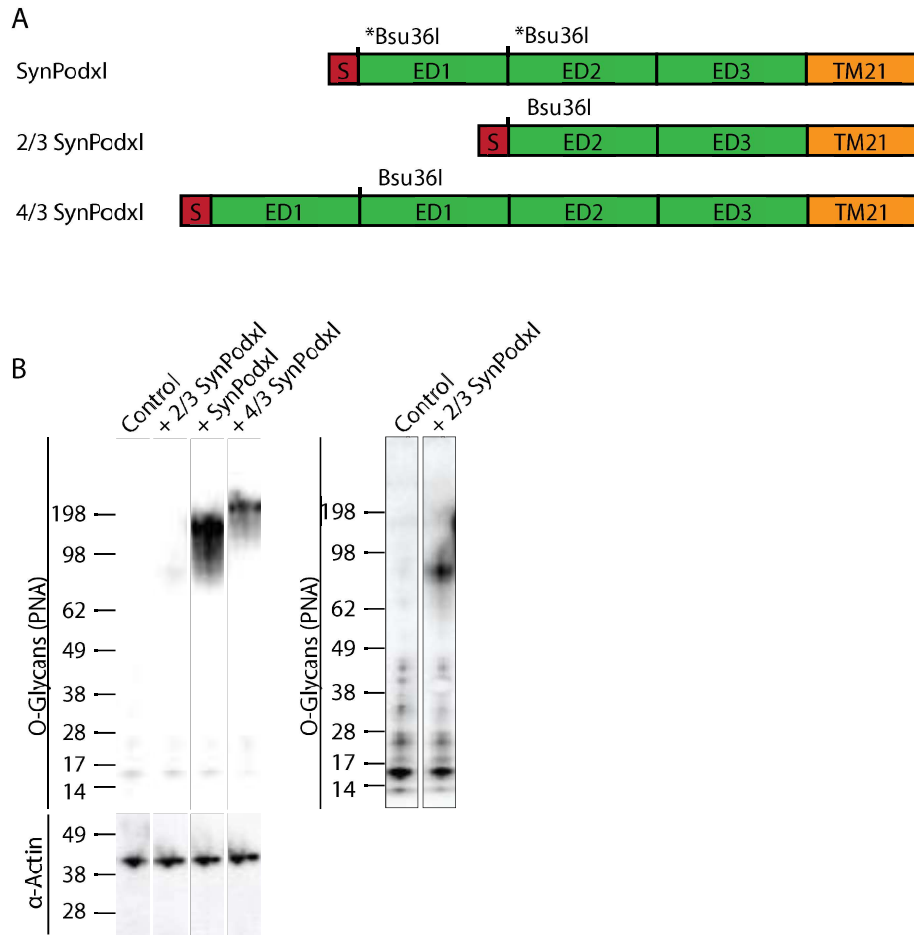


Figure 2.3 – Glycoproteins of tunable length. **A**, Schematic illustration of the restriction sites introduced via mutation (*), reassembly fragments, and relative lengths of the engineered SynPodxl variants. **B**, Lectin blot (left) of the relative O-glycosylation level of each mutant transiently expressed in HEK293T cells and an increased exposure time of same lectin blot (right), n=2.

2.3.3 Altering the chemical and physical environment at the cell surface

We next tested the ability of our toolkit to modify the chemical composition and physical structure of the cell surface. Our model cell line was the nontransformed mammary epithelial cell (MEC) line, MCF10A, which has low endogenous Muc1 and undetectable Podxl expression. We found that the MCF10A cell line has low overall levels of cell-surface O-glycans, making it an

ideal system for rational and directed assembly of an *O*-glycan rich glycocalyx (Fig. 2.4A, B). We first demonstrated an ability of our mutant and semi-synthetic mucins to alter the chemical environment of the cell surface (Fig. 2.4A, B). We observed significantly increased levels of *O*-glycans on the surface of cells expressing our mutant and semi-synthetic mucins compared to control MCF10A and Muc1-knockdown cells (Muc1 shRNA). We did not detect changes in N-glycosylation or sialic acids by our mucin constructs as detected by lectins (Fig. 2.4B).

We also tested the performance of our genetic tools in modifying the physical structure of the cellular glycocalyx. We used Scanning Angle Interference Microscopy (SAIM) (Paszek et al., 2012), a fluorescence localization technique with 5 – 10 nm axial precision, to map changes in the plasma membrane topography and glycocalyx thickness following expression of our mutant and synthetic constructs (Fig. 2.4C, D). We made all measurements on cells that were adhered to silicon substrates absorbed with fibronectin. Muc1 knockdown MECs had an average ventral membrane height of 30.3 nm (s.d. 7.83), while Muc1 Δ CT expression increased the separation between the ventral plasma membrane and the substrate by an average of 120 nm (150.3 nm, s.d. 15.9) in comparison. The shorter Podxl Δ CT generated a more modest average change of 87 nm (117.3 nm, s.d. 13.1) compared to the knockdown cells, as expected based on the lower molecular weight of Podxl versus Muc1. Notably, the SynMuc1 and SynPodxl constructs significantly expanded the glycocalyx and performed comparably to the Δ CT mutants of the same glycoproteins (156.6, s.d. 6.12 and 119.6, s.d. 13.9 nm, respectively). Together, these results confirm the utility of our toolkit in editing both the chemical composition and physical structure of the glycocalyx.

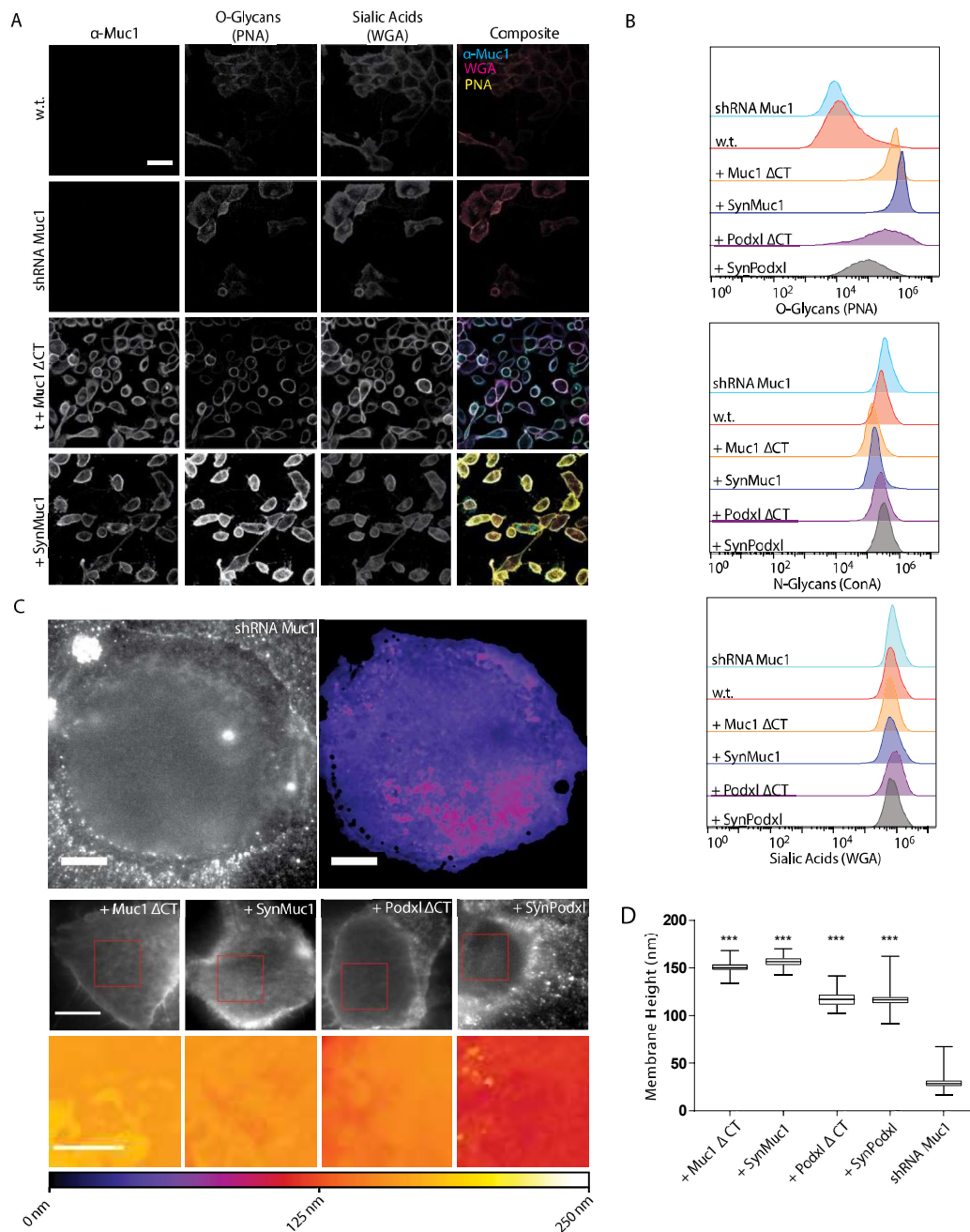


Figure 2.4 – Engineering the chemical and physical properties of the glycocalyx. **A**, Confocal images of Muc1 (left), O-glycan (center left) and sialic acid (center right) showing cell surface localization in control and stably expressing MECs for each of the engineered Muc1 cell lines used (scale bar 25 μ m), n=3. **B**, Representative flow cytometry histograms showing cell surface O

and N-glycan and sialic acid levels of Muc1 and Podxl Δ CT and SynMucin mutants, >20,000 cells measured per condition, n=3. **C**, Representative fluorescence maximum intensity projections of SAIM image sequences (top left, second row, scale bar 10 μ m) and membrane height reconstructions (top right, scale bar 10 μ m, bottom row, scale bar 5 μ m) of the ROIs boxed in red. **D**, Average membrane height from 2k pixels in each of 5 cells per condition. Boxes correspond to s.d. and whiskers to extrema. Asterisks indicate statistical comparison of each mutant-expressing cell line to shRNA Muc1 expressing cells. * p<0.05; ** p<0.01, *** p<0.001 (one-way ANOVA).

2.3.4 A thick and dense glycocalyx can trigger cellular detachment from the matrix

Using our toolkit, we generated cellular models to investigate the consequence of a thick, O-glycan rich glycocalyx on cellular behaviors. This glycocalyx is typical of many cancer cells, including highly aggressive cancers presenting with circulating tumor cells (Paszek et al., 2014). We first tested the implications of dense and thick glycocalyx on cellular adhesion to an ECM. Our analysis focused on our Muc1 mutant construct, which is the largest of our engineered glycoproteins. Notably, we found that a thick and dense glycocalyx could trigger complete cellular detachment from the ECM (Fig. 2.5A, B). In live-cell time-course experiments that tracked morphological changes dynamically following doxycycline induction, we observed a transition from a classical cuboidal cell phenotype to a more rounded morphology, and finally to a completely detached state, where cells float as spheres above the ECM substrate (Fig. 2.5B).

The fraction of detached cells correlated with Muc1 surface expression, strongly suggesting that detachment was a consequence of high mucin surface densities (Fig. 2.5C). Indeed, the kinetics of cellular detachment during the first 24 hours after doxycycline addition roughly matched the temporal increase in

mucin protein expression levels (Fig. 2.5D). We continued to see an increase in the detached cell fraction after 24 hours, the time at which maximal protein expression was obtained (Fig. 2.5D). Unexpectedly, we discovered that the majority of the detached cells were viable 24 and 48 hours after induction (Fig. 2.5E). Based on these observations, we hypothesized that the thick, *O*-glycan rich glycocalyx enhanced cell survival in poorly adhesive conditions.

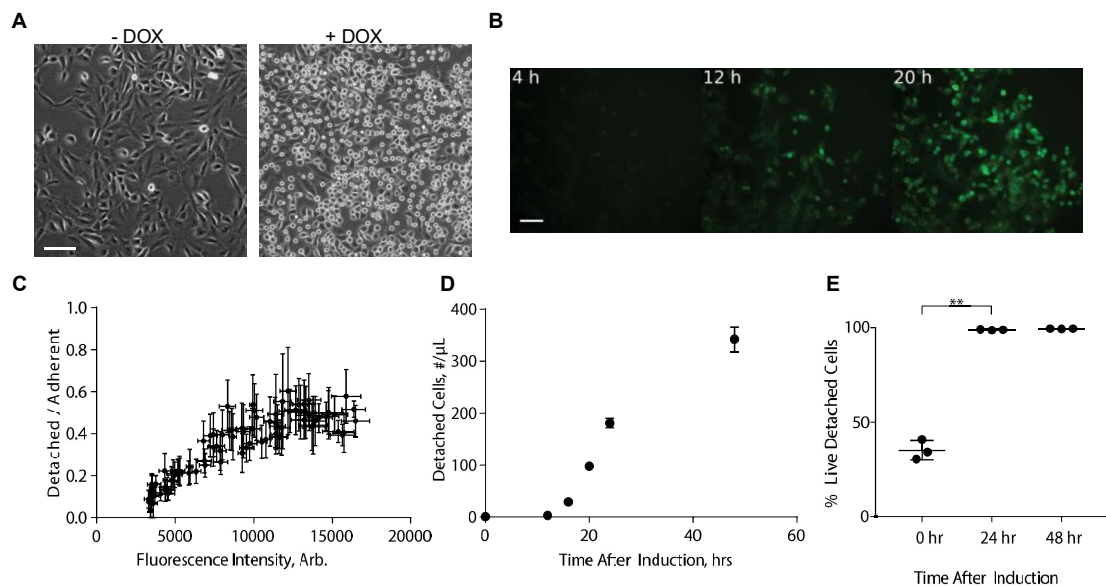


Figure 2.5 – Expression of a bulky glycocalyx inhibits cellular adhesion. **A**, Representative phase-contrast images of MECs expressing Muc1 Δ CT, uninduced and induced for 24 hours (scale bar 100 μ m). **B**, Representative epifluorescence images of MECs expressing Muc1 Δ CT moxGFP 4, 12, and 20 hours post-induction (scale bar 100 μ m), n=2. **C**, Ratio of detached MECs to adherent as a function of relative Muc1 expression measured by Muc1 Δ CT moxGFP fluorescence intensity, n=2. **D**, Concentration of live, detached MECs expressing Muc1 Δ CT as a function of time post-induction, quantified by flow cytometry with live/dead cell stain, n=3. **E**, Percentage of live cells in total detached population at various time points after induction quantified by flow cytometry with live/dead cell stain, n=3. All error bars are s.d.

2.3.5 The glycocalyx prolongs cellular survival in suspension

Given the surprising ability of cells with a prominent glycocalyx to survive in anchorage-free conditions, we investigated the survival and proliferation of these cells in suspension culture over longer timeframes. We envisioned these studies would provide a basic model of circulating tumor cells, which frequently have a thick *O*-glycan rich glycocalyx and survive, suspended in circulation during dissemination (Paszek et al., 2014). We observed that MECs engineered to have a thick and dense glycocalyx live approximately four times longer in suspension than control cells (Fig. 2.6A). The viability of control and engineered cells in suspension was well modeled by an exponential decay with a single decay constant, the half-life. We found that the half-life for MECs with an engineered glycocalyx is 3.12 days (1.96 to 6.51, 95% CI) compared to control MECs, which have a half-life of 0.797 days (0.623 to 1.03, 95% CI). We next tested whether this survival phenotype could be attributed to increased receptor tyrosine kinase (RTK) signaling. In a screen of 28 RTKs and 11 signaling nodes, no apparent differences in phosphorylation were observed when comparing engineered and control MECs grown in suspension for 24 hours (Fig. 2.2 and 2.6B). Furthermore, inhibition of MAPK signaling with the inhibitor U-0126 did not significantly change the decay constant for survival in engineered MECs, suggesting the promotion of survival by the glycocalyx was independent of MAPK (Fig. 2.6C).

We next assayed whether cells in suspension were actively proliferating. We confirmed that our engineered cells still required anchorage to a solid substrate for proliferation (Fig. 2.6D). Using time-lapse imaging and single cell tracking, we determined that the engineered cells proliferate while in an anchored state, but frequently detach from the matrix following division (Fig. 2.6E). Prior to division, cells expressing Muc1 Δ CT adopted a nearly spherical

morphology but did not fully detach from the substrate. At the moment of division, however, one or both daughter cells would often lose attachment. Taken together these results indicate that high levels of cell-surface mucins can trigger a switch from an adhesion-dependent phenotype to an adhesion-free phenotype with enhanced viability.

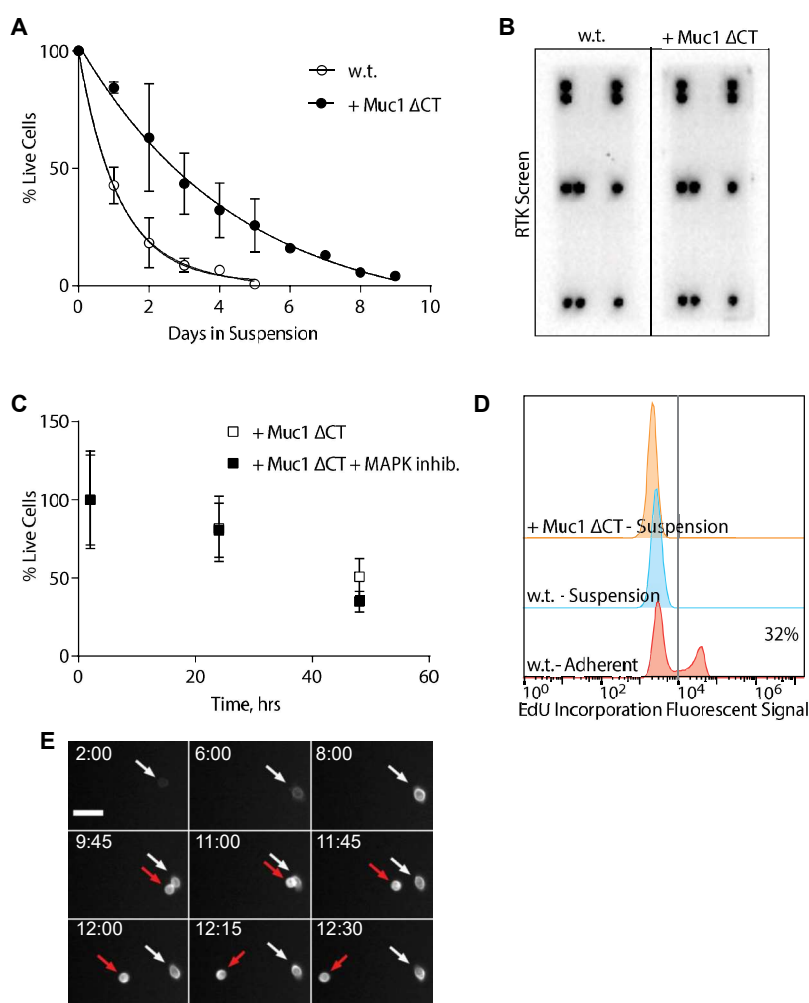


Figure 2.6 – Expression of a bulky glycocalyx enhances cell survival in suspension. **A**, Percentage live cells as a function of time for MECs growing in suspension culture, $n=3$. The solid curves represent a single exponential decay fit, $t_{w.t.}^{1/2} = 0.797 d$, $t_{Muc1}^{1/2} = 3.12 d$. **B**, Receptor tyrosine kinase signaling screen for MECs grown in suspension in full serum for 24 hours, $n=2$. Visible signal

from positive controls. See Supplementary Fig. 2.1 for full details. **C**, Percent live MECs expressing Muc1 Δ CT grown in suspension with 10 μ M MAPK inhibitor U-0126 or DMSO control, n=2. **D**, Representative flow cytometry histogram showing incorporation of EdU into MECs under adherent or in suspension culture conditions, >100,000 cells measured per condition, n=2. Percentage indicates the fraction of cells with signal > 10^4 (gray line) after background subtraction. **E**, Epifluorescence images of an MEC undergoing division with increasing expressing of Muc1 Δ CT moxGFP. Following separation, one of the new cells retains attachment to the substrate (white arrow) while the other detaches and drifts out of frame (red arrow) (scale bar 50 μ m). All error bars are s.d.

2.3.6 Cells with a thick glycocalyx dynamically attach to the aatrix for proliferation

We next considered two possible mechanisms for how cells with a thick glycocalyx might proliferate: (1) that upon division, the majority of glycocalyx was transferred to a single daughter cell, leading to a split population of adherent and detached cells, or (2) that previously detached cells could regain attachment to divide. We reasoned that if the detached cells were in fact receiving the majority of the glycocalyx bulk such that they were unable to retain substrate adhesion they would also be unable to re-establish substrate anchorage, and the initially detached population would remain in the detached state, whereas the initially adherent population would continue to produce detached cells. On the other hand, if cells were able to reattach, both the initially attached and initially detached populations would proceed toward an equilibrium point. To prevent artifacts due to matrix modification over the course of the experiment or cell-cell interactions that may be involved in attachment/detachment kinetics, we generated two populations of Muc1 Δ CT expressing MECs, one with constitutive cytoplasmic EGFP and a second with

cytoplasmic mCherry. Twenty-four hours following the induction of Muc1 Δ CT expression, the supernatant of each culture containing detached cells was exchanged, giving mixed cultures of mCherry and EGFP cells, allowing us to track the progress of both starting conditions in a single experiment.

In these experiments a variety of behaviors were observed, including temporary reattachment of floating cells or reattachment then division leading to detachment of a single daughter cell (Fig. 2.7A, rows 1 and 2). Another frequent occurrence was the temporary detachment of one or both daughter cells following division (Fig. 2.7A, row 3). Most interestingly, however, floating cells were also observed to temporarily attach to the substrate, divide, then detach again (Fig. 2.7A, row 4). In the case of the initially attached condition we observed a monotonically increasing ratio of floating to adherent cell populations over the 28 hours following exchange, suggesting that the dynamically adherent subpopulation continuously generated suspended daughter cells (Fig. 2.7B). On the other hand, the initially detached population reached an equilibrium within 10 hours of exchange as demonstrated by the constant population ratio (Fig. 2.7C). Similar results were observed for both starting conditions in the mCherry and EGFP cell lines leading to mixed populations in both states, indicating that the transfer was bidirectional for either starting condition (Fig. 2.7D). These results show that cells cycle between the substrate attached and free-floating states with individual cells occupying both as a function of cell cycle.

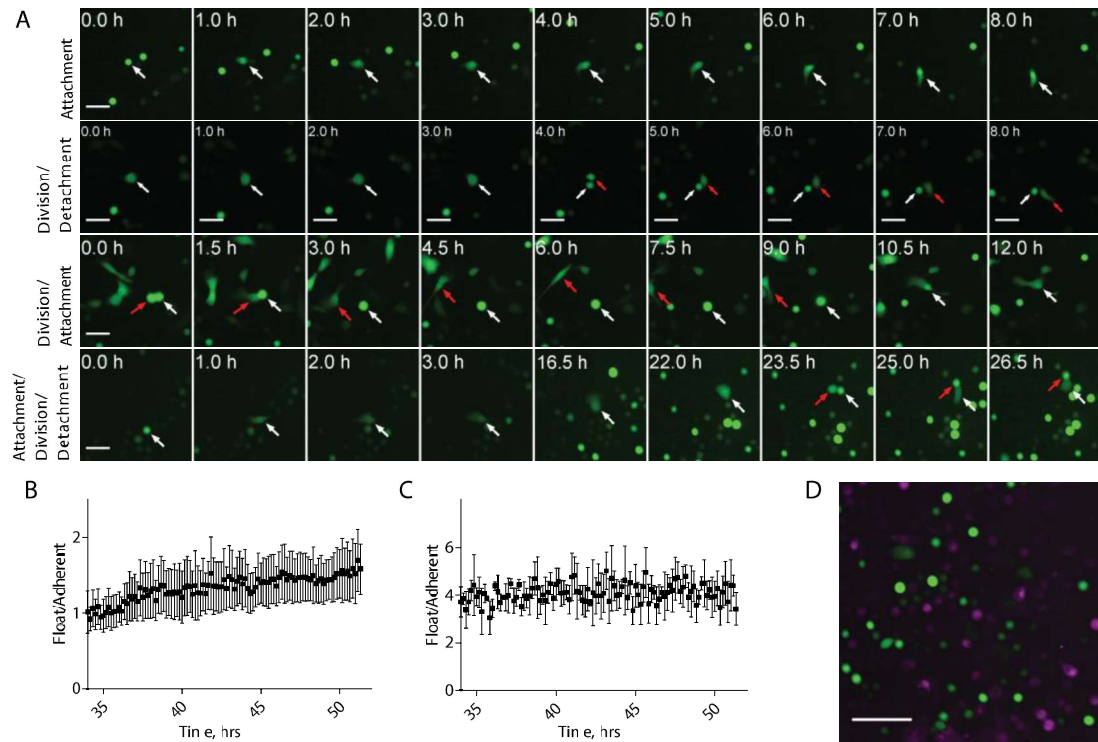


Figure 2.7 – Cellular division is associated with adhesion. **A**, Live cell time-course images of a detached cell reattaching to the substrate (top), a division event wherein one of the new cells detaches from the substrate (top center, white arrow), a division event wherein a new cell briefly detaches then reattaches to the substrate (bottom center, white arrow) and a detached cell attaches to the substrate, divides, then one of the new cells detaches (bottom, white arrow) (scale bars 50 μm). **B**, Ratio of detached, floating cells to adherent as a function of time in an initially attached population expressing Muc1 ΔCT . **C**, Same measurement as B for an initially detached population. Error bars in B and C represent one s.d., $n=3$ for both conditions. **D**, Epifluorescence image of a mixed population of MECs expressing Muc1 ΔCT and either cytoplasmic EGFP (green, initially detached) or mCherry (magenta, initially attached) demonstrating the exchange of states occurs in both directions (scale bar 100 μm).

2.4 CONCLUSION

We developed a library of mutant and semi-synthetic constructs for expressing heavily *O*-glycosylated proteins of varying size. Combined with a system for temporal control over expression levels, our systems constitute a genetically encoded toolbox for engineering the cellular glycocalyx. We anticipate that our technology for glycocalyx editing will open new avenues of research previously inaccessible, including more precise modeling of the cancer-specific glycocalyx for *in vitro* and *in vivo* studies. Indeed, the temporal control and stable expression that our systems afford enable dynamic tuning of the glycocalyx in organoids, as well as syngeneic and xenogeneic mouse models. Furthermore, our system provides “knobs” for tuning key features of the glycocalyx, including glycan content, glycoprotein size distribution, and glycoprotein surface density.

An important contribution by this work is the design and validation of a series of semi-synthetic mucins. While cell-surface mucins have a dominant structural function in the cancer cell glycocalyx, they also have strong biochemical activities mediated by their cytoplasmic and membrane proximal domains (Carraway et al., 2003). Our semi-synthetic mucins, SynMuc1 and SynPodxl, fuse the *O*-glycan rich structural elements of mucins to fully synthetic membrane proximal, transmembrane, and cytoplasmic domains. These constructs should enable more reliable physical editing of the glycocalyx while minimizing the direct biochemical activity of the expressed glycoproteins. We show that our approach for manufacturing synthetic glycoproteins is effective in modulating the thickness and biochemical properties of the glycocalyx. Future studies could further refine the flexural rigidity of individual structural elements. For example, the degree of

glycosylation can control the persistence length of mucin biomimetic polymers (Kramer et al., 2015) and an analogous strategy to engineer the number of serine and threonine glycosylation sites in genetically encoded mucins could be conducted. As another example, membrane-proximal regions of native Muc1 have been shown to play a role in Muc1 trafficking and glycosylation including extent of glycosylation and sialylation (Engelmann et al., 2005; Litvinov and Hilkens, 1993; Parry et al., 2001). The dependence of glycosylation on trafficking may explain the increased under-glycosylated mucin band observed when probing the SynMuc1 stable line which lacks native membrane proximal and transmembrane domains (Fig. 2.2C). This may also explain the surprising result that, while we increase the *O*-glycan content of the glycocalyx upon expression of our various constructs, we do not observe a significant change in sialic acid content of the glycocalyx (Fig. 2.4B). Additional rounds of protein engineering could also optimize the hinge point between the *O*-rich glycodomains and our synthetic membrane proximal region to control the extent of glycosylation and sialylation and to prevent collapse of individual glycoproteins under compressive forces. Thus, we envision that future efforts would expand our library to provide even more precise control over the physical structure and deformability of the glycocalyx.

Our toolkit overcomes some of the key technical hurdles that have historically limited the generation of cell lines with a cancer-specific glycocalyx. Foremost, we provide a strategy for generating cells with a thick and dense glycocalyx, similar to those of aggressive cancer cells. Based on our observation that cells with a thick and dense glycocalyx frequently detach from the extracellular matrix substrate, we envision a strong negative pressure would quickly select against cells with a prominent glycocalyx in culture. Indeed,

many of the existing cancer cell lines have been generated through repeated sub-culturing, which would likely select against a thick and less compliant glycocalyx that causes cells to detach from the culture vessel. Our inducible system solves this problem by enabling temporal control over glycocalyx biosynthesis in real-time at the start of experimentation.

An unexpected observation in our work is the strong induction of survival by the glycocalyx for cells in a suspended state. Previous work has shown that a thick glycocalyx can support cell survival of anchored cells by promoting integrin assembly, signaling, and crosstalk with growth factor receptor pathways. Now we show that the glycocalyx can also support survival of suspended cells. Importantly, our RTK screen and MAPK inhibitor data suggest that this survival mechanism is independent of growth factor receptor signaling. The precise mechanism of action for the glycocalyx in this adhesion-independent survival pathway must be resolved in future studies.

In summary, our work describes a set of genetic tools for glycocalyx engineering and rational construction of a cancer-specific glycocalyx on cell lines of interest. Our toolkit provides critical infrastructure for addressing unresolved questions in cancer glycobiology, including why CTCs and tumor cells from highly aggressive cancers so frequently express large glycoproteins at high surface densities.

2.5 MATERIALS AND METHODS

2.5.1 Antibodies and reagents

The following antibodies were used: FITC-Human CD227 (Muc1) (559774, BD Biosciences), Human CD227 (555925, BD Biosciences) (Muc1), Alexa-488-Human Podocalyxin (222328, R&D Systems), Actin (sc1615, Santa

Cruz), Goat anti-Mouse IgG-HRP (sc-2005, Santa Cruz), Mouse anti-Goat IgG-HRP (sc-2354, Santa Cruz). Lectins used were: Biotinylated Peanut Agglutinin (PNA; B-1075, Vector Laboratories), CF568 *Arachis hypogaea* Lectin PNA (29061, Biotium), CF640R *Arachis hypogaea* Lectin PNA (29063, Biotium), CF633 Wheat Germ Agglutinin (WGA; 29024, Biotium), and FITC Concanavalin A (ConA; FL-1001, Vector Laboratories). Biotinylated lectins were detected using ExtrAvidin-Peroxidase (E2886, Sigma). MAPK inhibitor was U-0126 (70970, Cayman Chemical). To induce transactivator cell lines, doxycycline was used (sc-204734, Santa Cruz).

2.5.2 Cloning and constructs

Full details on cloning and assembly of lentiviral, piggybac, and transient expression vectors with SynMucins is given in the Supporting Text.

2.5.3 Cell lines and culture

MCF10A and HEK293T cells were obtained from ATCC. MCF10A cells were cultured in DMEM/F12 media supplemented with 5% horse serum, 20 ng/mL EGF, 10 μ g/ml insulin, 500 ng/mL hydrocortisone, and 100 ng/mL cholera toxin. HEK293T cells were cultured in DMEM high glucose supplemented with 10% fetal bovine serum. Cells were maintained at 37°C, 5% CO₂, and 90% RH. MCF10A shRNA Muc1 cells were prepared by lentiviral transformation using Muc1 shRNA pLKO.1. MCF10A rtTA stable line was prepared by lentiviral transformation using pLV rtTA-NeoR plasmid as previously described (Paszek et al., 2012, 2014). Cells were further modified with the transposon system to create stable lines expressing Muc1 Δ CT; SynMuc1; Muc1 Δ CT moxGFP; Podxl Δ CT; and 2/3, 1/1, and 4/3 SynPodxl. These stable lines were generated using Nucleofection Kit V (Lonza) and HypBase, an expression plasmid for a hyperactive version of the PiggyBac

transposase (Yusa et al., 2011) (kindly provided by Dr. Alan Bradley, Wellcome Trust Sanger Institute, UK). MCF10A rtTA Muc1 Δ CT and MCF10A rtTA SynMuc1 were sorted for expression using the FITC-Human CD227 antibody. MCF10A rtTA Muc1 Δ CT EGFP and MCF10A rtTA Muc1 Δ CT mCherry cells were generated by further lentiviral modification of MCF10A rtTA Muc1 Δ CT cells with pLenti EGFP (Addgene plasmid #17446(Campeau et al., 2009)) and pCDH mCherry, respectively. Additionally, a Muc1 Δ CT stable line was created by lentiviral transformation of the MCF10A rtTA cell line using a pLV tetOn Muc1 Δ CT plasmid. HEK293T cells were transiently transfected using a calcium phosphate transfection protocol with pMAX GFP, pcDNA3.1(+) 2/3 SynPodxl, pcDNA3.1(+) 1/1 SynPodxl, and pcDNA3.1(+) 4/3 SynPodxl plasmids.

2.5.4 Immunoblot analysis

Cells were plated at 20,000 cells/cm² and grown for 24 hours. Cells were then induced with 0.2 μ g/mL Doxycycline for 24 hours before lysis with Tris-Triton lysis buffer (Abcam). Any detached cells were included in lysates. Lysates were separated on Nupage 4-12% Bis-Tris gels and transferred to PVDF membranes. Membranes were blocked with 3% BSA TBST solutions for 2 hours at room temperature or overnight at 4°C. Primary antibodies were diluted 1:1000 and lectins were diluted to 1 μ g/mL in 3% BSA TBST and incubated 4 hours at room temperature or overnight at 4°C. Secondary antibodies or ExtrAvidin were diluted 1:2000 in 3% BSA TBST and incubated for 2 hours at room temperature. Blots were developed in Clarity ECL (BioRad) substrate, imaged on a ChemiDoc (BioRad) documentation system, and quantified in Fiji (Schindelin et al., 2012).

2.5.5 Flow cytometry

Cells were plated at 20,000 cells/cm² and grown for 24 hours. Cells were

then induced with 0.2 µg/mL doxycycline for 24 hours. Adherent cells were nonenzymatically detached by incubating with 1 mM EGTA in PBS at 37°C for 20 min and added to the population of floating cells, if present. Antibodies were diluted 1:200 and lectins were diluted to 1 µg/mL in 0.5% BSA PBS and incubated with cells at 4°C for 30 min. The BD Accuri C6 flow cytometer was used for analysis. For doxycycline-titration flow cytometry, Muc1 ΔCT GFP expressing cells were plated and induced similarly with varying concentrations of doxycycline (0, 1, 5, 10, 25, 50, 75, 100, 200, 350, 500, 1000 ng/mL). Cells were nonenzymatically detached as described above, fixed with 4% paraformaldehyde, and GFP signal was analyzed on the BD Accuri C6 flow cytometer. Median GFP signal is reported.

2.5.6 Confocal microscopy

Cells were plated at 5,000 cells/cm² and grown for 24 hours and subsequently induced with 0.2 µg/mL of doxycycline for 24 hours before being fixed with 4% paraformaldehyde. Samples were blocked with 5% normal goat serum PBS for 1 hour at room temperature. Antibodies were diluted 1:200 in 5% normal goat serum PBS and incubated overnight at 4°C. Lectins were diluted to 1 µg/mL in 5% normal goat serum PBS and incubated for 2 hours at room temperature. Samples were imaged on a Zeiss LSM inverted 880 confocal microscope using a 40x water immersion objective.

2.5.7 Cell detachment time-course

Cells were plated at 20,000 cells/cm² and grown for 24 hours. All media was changed to remove any detached cells at this time. Cells were induced by spiking 0.2 µg/mL doxycycline into the media at the designated timepoints. Detached cells were collected, stained with Sytox-Green (Thermo), and analyzed with a BD Accuri C6 flow cytometer.

2.5.8 Suspension cultures

Cells were grown and induced with 0.2 µg/mL doxycycline for 24 hours using adherent cell culture technique. Cells were then detached with 0.05% trypsin EDTA (Thermo) and resuspended at 375,000 cells/mL. Cells were grown in suspension using a cell-culture magnetic stirrer at 100 rpm, 37°C, 5% CO₂, 90% RH. Every 24 hours, a small sample was drawn and cells were counted with a hemocytometer using Trypan Blue (Thermo) to differentiate live and dead cells. For inhibitor studies, 10 µM MAPK inhibitor or DMSO (control) was added when cells were transferred to suspension.

2.5.9 RTK screen

Cells were grown in suspension or adherent populations and induced for 24 hours. Cells were then lysed per previous discussion with the addition of sodium fluoride and sodium orthovanadate to the lysis buffer. The PathScan RTK Signaling Antibody Array Kit (7982, Cell Signaling) protocol was used to complete the assay using 0.5 mg/mL of each lysate.

2.5.10 EdU proliferation assay

Click-iT Plus EdU Alexa Fluor 594 Flow Cytometry Assay Kit (Thermo) was used. Cells were grown in suspension for 22 hours as described above before adding 10 µM EdU to the culture for 2 hours. Adherent cells were plated at 20,000 cells/cm² and grown for 46 hours before adding 10 µM EdU to the culture. The procedure was completed per the assay kit manual, and samples were analyzed on a BD Accuri C6 flow cytometer.

2.5.10 Scanning angle interference microscopy

Silicon wafers with 1900 nm thermal oxide were purchased from Addison Engineering and diced into 1 cm² chips, cleaned in 5 M NaOH, rinsed extensively with deionized water then oxygen plasma cleaned for 60 s before

coating with 50 ug/mL human plasma fibronectin (Millipore) for 2 hours at 37°C. Cells were seeded onto the prepared substrates at 5,000 cells/cm² and cultured for 24 hours before the addition of doxycycline, cultured for an additional 24 hours then fixed in 4% paraformaldehyde at 37° C for 15 min. Following fixation samples were rinsed extensively in PBS, then stained with 1 µg/mL DiI-DS (ThermoFisher) for 1 hour at RT. Samples were imaged with a custom SAIM microscope based on a Nikon Ti-E body with ultra-stage and focus lock (FocalPoint) with a 560 nm excitation laser (MFB). Experiments were automated with a home-made microscope controller and galvanometer scanning mirror (Cambridge Technology), and images were acquired over a series of 62 angles from 0 to 36.7° with a 60x NA 1.2 water immersion objective (Nikon) on a sCMOS camera (Zyla 4.2, Andor) controlled with µManager software (Open Imaging)(Edelstein et al., 2014). Image sequences were fit pixel-wise in a least-squares sense according to the SAIM optical model (Paszek et al., 2012) with a custom software application (source code available upon request) and the resulting reconstructions were post-processed using Fiji. For each condition 2-4 independent samples were imaged. Due to variability in label density and the effects of dye aggregates in many cells only a small portion of the membrane provided an adequate reconstruction. Cells with globally low residuals and continuous 40x50 (2k total) pixel regions in the reconstructions were selected from the pooled samples after reconstruction. A rectangular box of 40x50 pixels was drawn directly under the cell body, as the region on the periphery is prone to artifacts in reconstruction owing to the membrane being oriented roughly orthogonal to the optical axis or close proximity between the ventral and apical membranes. The pixels heights within these boxes were used for quantification of membrane height.

2.5.11 In-incubator microscope

Live cell time-course imaging was carried out on a custom-built microscope designed to operate in a standard cell culture incubator. The microscope consists of a mechanical XY stage, with separate focus drive and filter wheel controlled by a central hub (ASI Tiger) and operated through μ Manager control software (Edelstein et al., 2014). Excitation by LED sources (ThorLabs) was controlled by an Arduino board through μ Manager. A Nikon 10x NA 0.50 CFI S Fluor objective was used to image onto a CMOS camera (PointGrey). Full details on microscope design are available upon request.

2.5.12 Live-cell time course imaging

Glass bottom cell culture plates (Cellvis) were oxygen plasma cleaned for 60 s then coated with 50 μ g/mL human plasma fibronectin for 2 hours at 37° C. Cells were seeded at 5,000 cells/cm² and cultured for 24 hours prior to the addition of doxycycline. Following induction, the sample was placed on the in-incubator microscope and allowed to equilibrate for 4 hours. Images were then acquired for 20 hours at multiple positions in 2 different wells for induction time-course series. For adhesion/detachment studies cells were initially imaged for 24 hours following induction, then the plate removed and supernatant swapped between each of 3 wells of EGFP and mCherry cell lines. The plate was then replaced and imaging continued for an additional 33 hours. Images were analyzed with custom analysis software written by the authors and available upon request. Briefly, in each frame circular cells and all cells are identified, then a mean intensity calculated for all cells in the frame. The number of adherent cells is then inferred as the difference between circular and total cells.

2.5.13 Statistics

Statistical significance was determined by Student's *t* test, two-tailed, or ordinary one-way ANOVA as appropriate. Statistical analysis was performed using Prism (GraphPad).

2.6 ACKNOWLEDGEMENTS

We thank V. Weaver for the lentiviral and transposon plasmids, as well as helpful discussions. This investigation was supported by the National Institute of General Medical Sciences Ruth L. Kirschstein National Research Service Award 2T32GM008267 (C.R.S, M.J.C.), Knight Family Foundation Graduate Research Fellowship in Nanoscience and Technology (C.R.S), Samuel C. Fleming Family Graduate Fellowship (C.R.S), National Science Foundation Graduate Research Fellowship DGE-1650441 (M.J.C.), Canadian Institutes of Health Research (F.K.), National Institute of Health New Innovator DP2 GM229133 (M.J.P), and National Cancer Institute U54 CA210184 (M.J.P) and R33-CA193043 (M.J.P). Confocal imaging was supported through the Cornell University Biotechnology Resource Center (BRC) Imaging Facility (NIH S10OD018516).

2.6.1 Complete author list

Carolyn R. Shurer[†], Marshall J. Colville[†], Vivek K. Gupta, Shelby E. Head, FuiBoon Kai, Jonathon N. Lakins, and Matthew J. Paszek

[†]These authors contributed equally to this work.

2.6.2 Author contributions

All authors contributed to the design of the studies and the preparation of the manuscript. C.R.S., M.J.C., S.E.H., F.K., and J.N.L. prepared the cDNA vectors. C.R.S. prepared stable cell lines and performed Western and lectin blot, flow cytometry, live-cell microscopy, RTK screen, and EdU analysis. M.J.C.

performed SAIM experiments and time-course microscopy image analysis.
S.E.H. performed suspension cell culture experiments.

2.6.3 Competing interests

Authors declare no competing interests.

2.7 SUPPORTING FIGURES

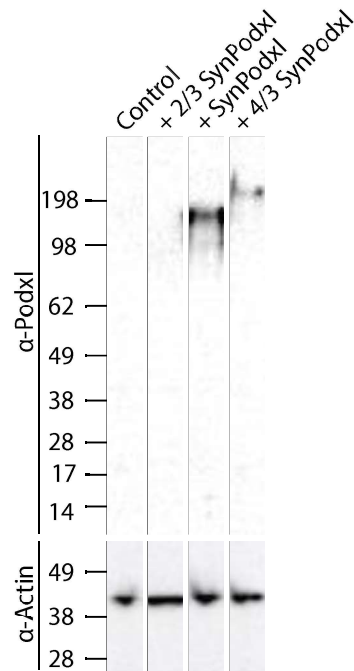


Figure 2.S1 – Immunoblot. Immunoblot showing the relative molecular weight of each of the Podxl mutants expressed transiently in HEK293T cells, n=2. Not that the 2/3 length Podxl is not detected by the anti-Podxl antibody due to deletion of the recognition domain during cloning.

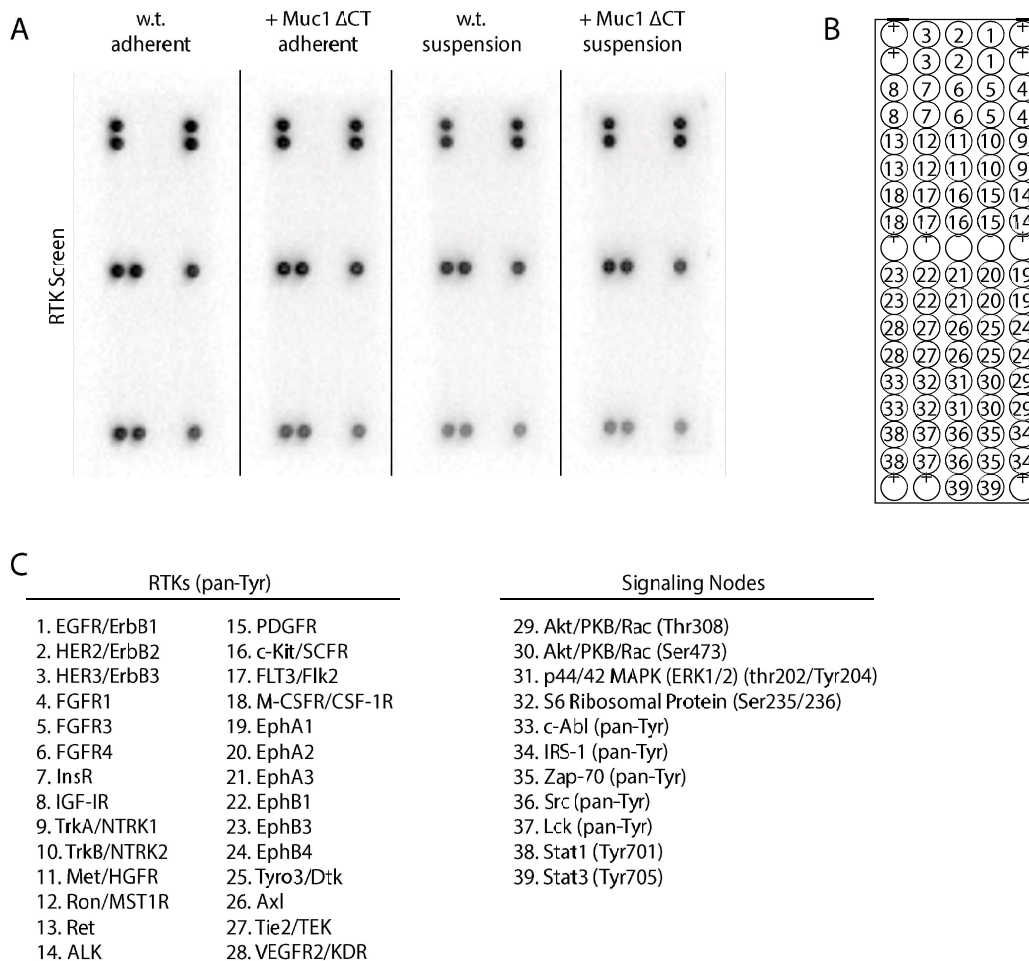


Figure 2.S2 – RTK screen. **A**, Full array image of PathScan RTK antibody slide. Induced cells were grown for 24 hours in either adherent or suspension conditions before being lysed and analyzed per the kit protocol. **B**, Schematic of RTK array slide. **C**, Key for schematic of RTK array slide.

2.8 SUPPORTING TEXT

2.10.1 Cloning and constructs

Muc1 Δ CT was inserted into a second-generation lentiviral vector with a doxycycline inducible promoter and puromycin resistance cassette as previously described (Paszek et al., 2014). A lentiviral vector for stable, shRNA-mediated knockdown of Muc1 was constructed by inserting the shRNA sequence 5'- CCG GGA CAC AGT TCA ATC AGT ATA ACT CGA GTT ATA

CTG ATT GAA CTG TGT CTT TTT G -3' into the pLKO.1 lentiviral backbone. The inducible PiggyBac transposon vector pPB tetOn was created first by PCR amplification and insertion of 5' and 3' PiggyBac ITRs from pPB 5'PTK3' (kindly provided by Dr. Alan Bradley, Wellcome Trust Sanger Institute, UK) into a minimal backbone for bacterial propagation and selection consisting of ampicillin resistance gene and ColE1 origin of replication PCR amplified from pBluescriptII KS+ (Stratagene). Between ITRs a puromycin resistance expression cassette consisting of SV40 promoter puromycin acetyltransferase gene and SV40 polyadenylation sequence was then inserted back to back with a Tet regulatable expression cassette consisting of hybrid heptamerized Tet operator minimal CMV promoter, chimeric synthetic intron between human β -globulin, and immunoglobulin heavy chain introns, multiple cloning site (MCS) and polyadenylation sequence from bovine growth hormone. To clone Muc1 Δ CT into transposon vector, Muc1 N-terminus (fragment A) was amplified with PCR using a forward primer 5'- ACT ACT ACT AGT ACC ATG ACA CCG GGC ACC CAG T -3' and a reverse primer 5'- ACT ACT AGA TCT GGT CGT CGT CAT CCT TGT AAT CAG CA -3' using MMTV-Muc1 construct as the template (kindly provided by Sandra Gendler). The central sequence of Muc1 harboring tandem repeats (fragment B) was excised from the same construct using BglII and ApaLI. The C-terminus of the Muc1 Δ CT (fragment C) was amplified using a forward primer 5'- ACT ACT GTG CAC AAC GGC ACC TCT GCC AGG GCT -3' and a reverse primer that introduced a stop codon immediately following the Muc1 transmembrane domain 5'- ACT ACT GAA TTC CTA GCA CTG ACA GAC AGC CAA GGC AAT -3'. The fragments A, B, and C were digested with SpeI/BglII, BglII/ApaLI, and ApaLI/EcoRI, respectively. These three fragments were subsequently cloned into SpeI/EcoRI-

digested transposon vector. pPB tetOn SynMuc1 was prepared by inserting the DNA sequence 5'- TCA GGC ATA CTT TAT TGG CGA AAC CCA ACG GAA AGT GAT AGC ATC GTT TTG GCA ATT ATC GTC CCC AGT CTG CTC CTC TTG CTC TGC CTG GCT TTG TTG TGG TAC ATG CGC CGA CGA AGT ATG TAG GG -3' into the Bsu36I and EcoRI sites of pPB tetOn Muc1 Δ CT. pPB tetOn Muc1 Δ CT moxGFP was prepared by PCR of the moxGFP gene, Addgene plasmid #68070 (Costantini et al., 2015), using the forward primer 5'- GGC ACC ATG GCA TGG TGT CCA AGG GCG AGG AGC TGT -3' and the reverse primer 5'- GGC ACC ATG GGC CTT GTA CAG CTC GTC CAT GCC GTG A -3' and non-directional insertion into the NcoI site of pPB tetOn Muc1 Δ CT.

For creation of pPB tetOn Podxl, the human Podxl cDNA (clone ID 9051823, Dharmacon) was amplified via PCR with forward and reverse primers 5'- GGC AGG ATC CAC GAC ACG ATG CGC TGC GCG CT -3' and 5'- GGC AGA ATT CCT AGA GGT GTG TGT CTT CCT CCT C -3'. The PCR product was subsequently inserted into the BamHI and EcoRI sites of pPB tetOn. pPB tetOn Podxl Δ CT was generated through amplification of the Podxl cDNA with 5'- GGC AGG ATC CAT GCG CTG CGC GCT GGC GCT CTC G -3' and 5'- CCG TCC TGA GGT TAG AGG CGC TGG TGG CAG CAG CCA TAG AGG -3' and insertion into the pPB tetOn vector as before. SynPodxl was created by amplification of the *O*-glycosylation rich ecto-domain from full-length human Podxl via PCR amplification with 5'- GGC AGG ATC CAT GCG CTG CGC GCT GGC GCT CTC G -3' and 5'- CCG TCC TGA GGT TAG CAT GCT GAA GCG GTC CTC GGC C -3' forward and reverse primers to add 5' BamHI and 3' Bsu36I restriction sites. Following restriction digest, the ectodomain was ligated with the synthetic membrane proximal domain and 21-amino acid transmembrane domain into the pPB tetOn vector. Podxl Δ CT and SynPodxl

were subcloned into the BamHI and EcoRI sites of pcDNA3.1(+) vector for transient expression and further cloning.

Modular SynPodxl constructs were generated by introducing Bsu36I restriction sites between residues T40D41 and A179E180 (relative locations at the end of the signal peptide and 1/3 through the *O*-glycosylation rich region) by site-directed mutagenesis with the following primers: T40D41 forward 5'- CCT AAG GAC TCA TCT AAC AAA ACA GC -3', reverse 5'- CGT AGT AGT CTG GGT TGC -3'; A179E180 forward 5'- CCT AAG GAA CAT CTG ACG ACC CCT -3', reverse 5'- TGC CTT AGT GGA TGT GAG -3'. One mutant was generated for each new restriction site, and the resulting plasmids as well as pcDNA3.1(+) SynPodxl were digested with Bsu36I and BamHI to yield 2 fragments from each mutant and the vector with transmembrane sequence from SynPodxl. 2/3 SynPodxl was constructed by ligation of the 129 bp fragment from T40D41 and 865 bp fragment from A179E180 into the vector. 4/3 SynPodxl was constructed in the same manner from the 537 bp fragment from A179E180 and 1.3 kbp fragment from T40D41.

CHAPTER 3

STABLE RECOMBINANT PRODUCTION OF CODON-SCRAMBLED LUBRICIN AND MUCIN IN HUMAN CELLS^{1,2}

3.1 ABSTRACT

Widespread therapeutic and commercial interest in recombinant mucin technology has emerged due to the unique ability of mucin glycoproteins to hydrate, protect, and lubricate biological surfaces. However, recombinant production of the large, highly repetitive domains that are characteristic of mucins remains a challenge in bio-manufacturing likely due, at least in part, to the inherent instability of DNA repeats in the cellular genome. To overcome this challenge, we exploit codon redundancy to encode desired mucin polypeptides with minimal nucleotide repetition. The codon-scrambling strategy was applied to generate synonymous genes, or “synDNAs,” for two mucins of commercial interest: lubricin and Muc1. Stable, long-term recombinant production in suspension-adapted human 293-F cells was demonstrated for the synonymous lubricin cDNA, which we refer to as SynLubricin. Under optimal conditions, a 293-F sub-population produced recombinant SynLubricin at more than 200 mg/L of media and was stable throughout two months of continuous culture. Functionality tests confirmed that the recombinant lubricin could effectively inhibit cell adhesion and lubricate cartilage explants. Together, our work provides a viable workflow for cDNA design and stable mucin

¹This work was originally published in *Biotechnology and Bioengineering* and has been reproduced here under the author use and publication permission policy of Wiley. Shurer, C.R., Wang, Y., Feeney, E., Head, S.E., Zhang, V.X., Su, J., Cheng, Z., Stark, M.A., Bonassar, L.J., Reesink, H.L., and Paszek, M.J. (2019) Stable recombinant production of codon-scrambled lubricin and mucin in human cells. *Biotechnology and Bioengineering*. <https://doi.org/10.1002/bit.26940>

²C.R.S. produced and analyzed recombinant SynMuc1, analyzed protein expression time-course and effects of VPA, and optimized purification of recombinant proteins. See sections 3.6.1 and 3.6.2 for a complete author list and specific author contributions.

production in mammalian host production systems.

3.2 INTRODUCTION

Mucins are membrane-bound or secreted glycoproteins containing a variable number of tandem repeats that are defined by their densely clustered sites for O-glycosylation (Hang and Bertozzi, 2005). This extensive glycosylation gives rise to a bottlebrush molecular structure that confers mucins with remarkable physical properties (Kuo et al., 2018). Mucins at biological interfaces can coordinate with water molecules to form hydrated layers that protect delicate cellular or tissue structures, deter biofouling, and resist pathological cellular deposition (Hattrup and Gendler, 2008). For instance, transmembrane mucins such as Muc1 and Muc16 are densely grafted on the ocular surface, where they maintain hydration, resist abrasion, and provide a selective barrier to macromolecules (Gipson et al., 2014; Mauris and Argüeso, 2012). Similarly, the secreted mucin-like glycoprotein called proteoglycan 4 (PRG4), or lubricin, can bind to cells and tissue interfaces, including the articular cartilage and ocular surfaces, enabling low friction lubrication and protection from pathological cellular deposition and biofouling (Rhee et al., 2005; Schmidt et al., 2013).

Alterations in mucin expression and glycosylation are observed in various pathological conditions, ranging from cancer and inflammatory bowel disease to ocular disease (Dhanisha et al., 2018). Patients with genetic mutations that preclude functional lubricin synthesis demonstrate symptoms of Campodactyly-Arthropathy-Coxa Vara-Pericarditis (CACP) syndrome, including early-onset polyarthropathy as a result of pannus formation and impaired joint lubrication (Bahabri et al., 1998; Marcelino et al., 1999). Decreased

synovial fluid lubricin concentrations have also been observed in patients with anterior cruciate ligament injury, osteoarthritis, and rheumatoid arthritis (Elsaid et al., 2008; Kosinska et al., 2015). As such, there has been significant interest in the development of recombinant lubricin and other mucins as injectable therapeutics for osteoarthritis and rheumatic diseases (Le Graverand-Gastineau, 2010) and as topical treatments for chronic dry eye and other conditions that require application of exogenous lubricants (Schmidt et al., 2013).

Despite this commercial interest, recombinant production has proven challenging for Muc1, lubricin, and other mucins that contain a high number of tandem repeats. Although highly productive clones of Chinese Hamster Ovary (CHO) cells have been isolated for a truncated Muc1 with approximately 1/3 of its native tandem repeats, similar attempts to isolate clones for full-length recombinant Muc1 have failed (Backstrom et al., 2003). Likewise, stable clones for recombinant lubricin with the complete 76-78 native tandem repeats produced the glycoprotein at low levels (Jones et al., 2007), but a modified recombinant lubricin protein construct (LUB:1), which contained only 1/3 of the tandem repeats, was more amenable to large scale production (Flannery et al., 2009). More recently, the production of full-length recombinant human lubricin expressed in suspension-adapted CHO cells has been reported and has demonstrated potential as an ocular lubricant for treating dry eye disease or hydrating contact lenses (Samsom et al., 2014). The precise details of how recombinant production was achieved for the full-length lubricin remain proprietary, and at the current time, no published strategy for large-scale lubricin production is available.

The exact biology that underlies the difficulty of producing mucins at

high levels remains unclear. However, long, repetitive DNA sequences, such as those common in the cDNAs of mucin tandem repeats, are relatively unstable in the cellular genome (Pearson et al., 2005). The fidelity of nearly all DNA processing steps can be compromised by slippage and other errors linked to repetitive sequences (López Castel et al., 2010). Consequently, repeats can mutate by addition or loss of their unit nucleotide sequence up to 100,000 times more frequently than point mutations in non-repetitive regions (Oren et al., 2016). The variation in tandem repeat numbers for Muc1 and other mucins in humans and mammals provides an evolutionary argument that these genomic cDNAs are mutational hotspots (Gemayel et al., 2010). Recombination and truncation of exogenous Muc1 cDNAs in bacteria have also been reported, suggesting a high level of instability for these repetitive sequences in host microbial cells, as well (Backstrom et al., 2003).

Now that advances in custom gene synthesis (CGS) enable fast and cost-effective synthesis of long cDNAs (Kosuri and Church, 2014), a new possibility for improved genomic stability of mucins would be to exploit codon redundancy to find synonymous gene sequences that are less repetitive but encode the same desired polypeptide. Such codon optimization algorithms have now been developed and successfully applied for elastin-like proteins and some other repetitive protein domains (Tang and Chilkoti, 2016). However, optimized synthetic cDNAs have yet to be designed, synthesized and tested for bio-manufacturing of large mucins of commercial interest.

To date, most biologics, including mucins, have been produced in CHO cells due to their fast growth, adaptability to suspension culture, and capacity for glycosylation and other important post-translational modifications. However, CHO cells can generate glycan epitopes that are now suspected to

elicit adverse immunological responses in humans (Butler and Spearman, 2014). Namely, the α 1,3-galactosyltransferases of CHO and other non-primate cells produce glycans with Gal α 1,3-Gal residues that can be immunogenic to humans, apes, and other old-world monkeys that have lost α 1,3-galactosyltransferase activity (Bosques et al., 2010; Brooks, 2004). CHO cells also can generate Neu5Gc, a terminal sialic acid that is common in most mammalian cells but has been lost in humans and primates (Ghaderi et al., 2012). These glycans are of particular concern for recombinant mucins, which can consist of 75% or more carbohydrate by mass and are often highly sialylated (Estrella et al., 2010). Recombinant production of the glycoproteins in human cells would avoid the risk of Gal α 1,3-Gal and Neu5Gc residues; but, to our knowledge, no successful attempts at large-scale mucin production in a human cell host production system has been reported.

Thus, our objective was to determine whether cDNA optimization through codon scrambling could be an effective strategy to achieve stable recombinant production of mucins and mucin-like glycoproteins and whether this strategy would be viable in suspension-adapted human 293-F cells. Notably, the United States Food and Drug Administration (FDA) has recently approved several biologics produced in 293-F cells, establishing the cell platform as a viable alternative to CHO and other non-human systems for manufacturing specialized therapeutics (Dumont et al., 2016). Here, the codon-scrambling approach is demonstrated for Muc1 and lubricin, and the production strategy is further developed to achieve stable production of a functional, full-length recombinant lubricin.

3.3 RESULTS AND DISCUSSION

3.3.1 Design and synthesis of cDNA for synonymous lubricin

As an approach for recombinant mucin production, we applied a codon-scrambling and optimization strategy to design synthetic mucin cDNAs within minimal codon repetition (Fig. 3.1A). A global codon optimization algorithm was applied to find the least repetitive gene sequence that encoded the desired mucin tandem repeats (Tang and Chilkoti, 2016). To tailor the sequences for production in a human host system, such as 293-F, a subsequent optimization was conducted to replace any codons with less than 10% usage frequency in humans (Fig. 3.1A). Based on previous findings with elastin-like proteins, we envisioned that the optimized mucin cDNAs could be synthesized through rapid and low-cost services for CGS (Kosuri and Church, 2014; Tang and Chilkoti, 2016).

We first tested the strategy for human lubricin, which has approximately 59 tandem repeats with a consensus sequence of KXPXPTTX, with KEPAPTTTP being the most frequent repeat. For our synthetic lubricin, we optimized the codons for 59 perfect repeats of the KEPAPTTTP consensus sequence (Fig. 3.1B). The protein sequence for the perfect repeats had approximately 88% similarity to the native human PRG4 repeats (Fig. 3.1C). The synthetic tandem repeats were flanked by additional sequences encoding the native N- and C- termini of human PRG4. These sequences included the native somatomedin and hemopexin domains of lubricin. We also included an IgK leader sequence, 6x histidine tag, and N-terminal SumoStar tag to aid in protein secretion and purification (Fig. 3.1B). We named the new semi-synthetic gene encoded by the codon-optimized cDNA “synonymous lubricin” or “SynLubricin.”

The nucleotides encoding SynLubricin were significantly less repetitive

than native PRG4. We analyzed the nucleotide sequences with an alignment algorithm that detects tandem repeats and scores their degree of repetitiveness based on how frequently they repeat and how closely the identified consensus matches the nucleotides of the queried sequence (Benson, 1999). The detected repeats were aligned with the queried sequence through a Smith-Waterman style local alignment, and the overall repetitiveness was scored by assigning +2 for each nucleotide match and -7 for each mismatch or indel (Benson, 1999). Thus, a higher score was indicative of more nucleotide repetition. The tandem repeats of SynLubricin had a modest score of 168, whereas the native PRG4 repeats had a much higher repetition score of 1001.

We also aligned the amino acids of the SynLubricin tandem repeats to the 59 tandem repeats of human PRG4 isoform A (Fig. 3.1D). We noted that the perfect repeats of SynLubricin and the native repeats of human PRG4-A have similar compositions of alanine, glutamic acid, lysine, and threonine, while proline content is slightly higher in the SynLubricin repeats (37% vs 30.5%; Table 3.S1). We also noted that the native repeats contain small amounts of asparagine (0.2%), aspartic acid (0.4%), glycine (0.8%), isoleucine (0.2%), leucine (1.4%) and serine (2.6%), which are not contained in SynLubricin (Table 3.S1).

The low-repetition of nucleotides in the SynLubricin gene enabled synthesis of the desired cDNA through standard CGS services. We also commissioned the generation of a cDNA for the native human lubricin/PRG4 sequence through a specialized service for highly repetitive genes. However, our attempts to subsequently clone the native PRG4 cDNA sequence into a mammalian expression vector and recombinantly express the product in mammalian cells failed. Consequently, we discontinued further efforts at recombinant production of lubricin with the full-length, native cDNA.

Efforts to produce SynLubricin in transiently transfected mammalian cells were successful. The SynLubricin cDNA was fused to a bicistronic copGFP reporter and transiently transfected into adherent human embryonic kidney 293-T cells. The protein product of the SynLubricin gene was highly glycosylated, as desired, and exhibited the anti-adhesive properties that we expected. Transfected cells maintained large gaps between cells in the monolayer, particularly at locations where visible copGFP fluorescence reported high expression levels of the bicistronic mRNA (Fig. 3.S1A). We noted that these observations were consistent with the known anti-adhesive functionality of native lubricin (Rhee et al., 2005). In contrast, mock transfected cells grew to a highly confluent monolayer in culture (Fig. 3.S1A). A western blot of the media supernatant from the SynLubricin-transfected cultures revealed a high molecular weight protein of approximately 460 kDa, which was similar in size to the native lubricin that we detected in equine synovial fluid (Fig. 3.S1B). The expected molecular weight of the peptide backbone of SynLubricin was 145 kDa, indicating that SynLubricin was extensively glycosylated.

We next considered strategies for stable production of the synthetic mucins in 293-F suspension cultures. Based on our previous findings that mucin cDNAs could be efficiently integrated into host cell genomes through transposition, we created a non-viral transposon vector for “all-in-one” inducible expression of mucins (Shurer et al., 2018). The vector contained a tetracycline-responsive promoter for inducible expression of the desired gene and a bicistronic copGFP reporter. The vector also contained a second cassette under control of an EF1alpha promoter for expression of the rtTA-M2 tetracycline transactivator and a bicistronic neomycin resistance gene for

selection (Fig. 3.1E). To test the performance of the expression system, we cloned mCherry2 into the vector and transfected 293-F cells with cationic polyethylenimine (PEI) condensates following standard protocols (Boussif et al., 1995; de los Milagros Bassani Molinas et al., 2014; Sonawane et al., 2003). Stable cell populations were isolated after two weeks of selection, and mCherry2 production was validated by flow cytometry. Based on the flow cytometric analysis, we found that stable cells produced high levels of mCherry2, and that the fluorescence readout of the copGFP reporter was generally a good indicator of recombinant protein production (Fig. 3.S2).

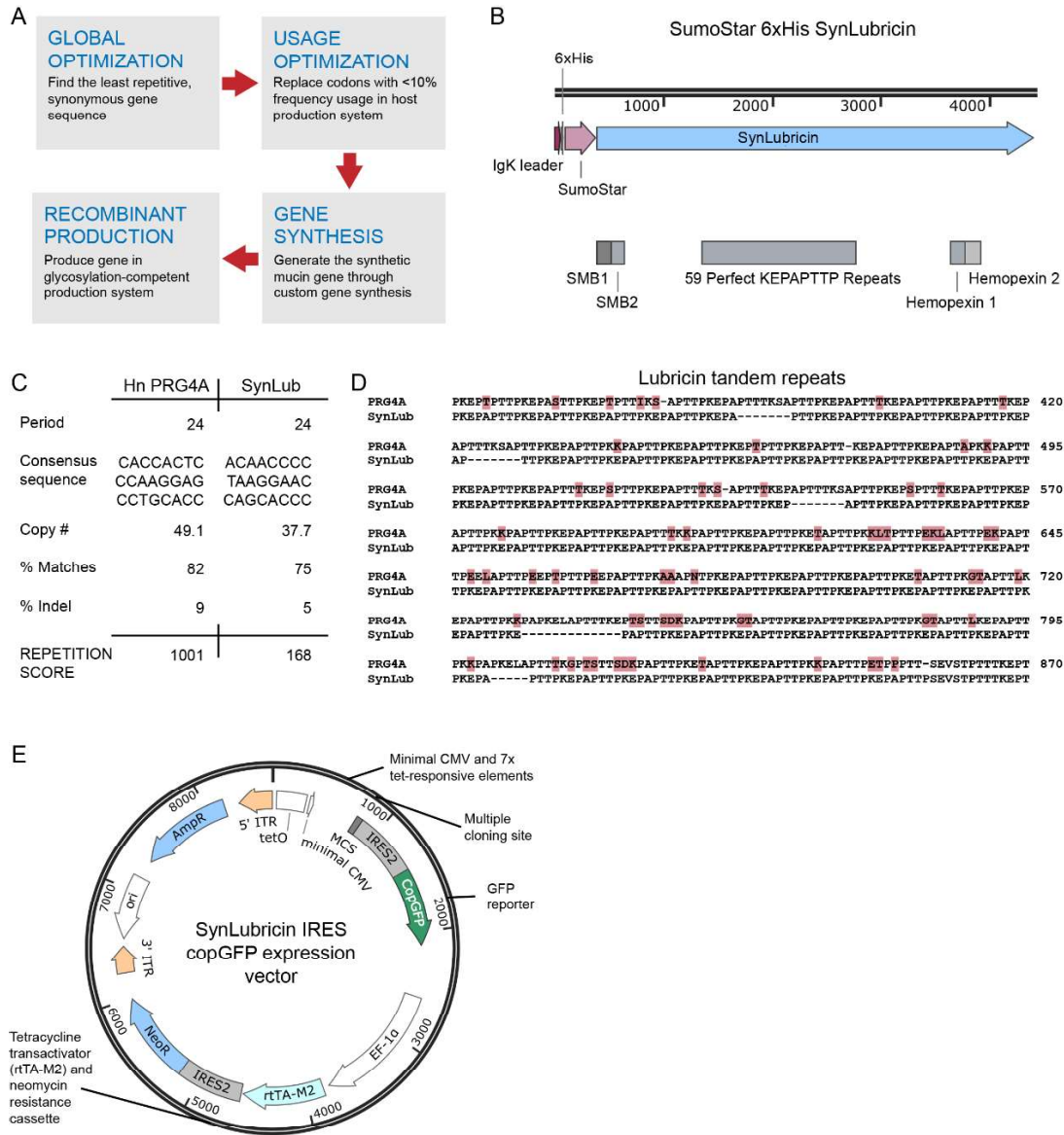


Figure 3.1 – Design and synthesis of synonymous lubricin (SynLubricin). **A**, Overview of the design and production strategy for synthetic, codon-scrambled mucins. DNA sequences for the desired protein product were optimized through a global optimization to minimize repetitive DNA sequences by codon scrambling, followed by a second optimization that reassigned codons with infrequent usage in the host cell system. **B**, SynLubricin was constructed of 59 perfect repeats of KEPAPTTTP flanked by the native human N- and C-termini of PRG4. An IgK signal sequence and SumoStar tag was fused to SynLubricin for secretion and purification. SynLubricin also retains the two somatomedin B domains (SMB 1 and 2) and the two Hemopexin domains of the native protein. **C**, Calculated repetition score for the nucleotides encoding the tandem

repeats of human PRG4 isoform A (PRG4A) and SynLubricin. **D**, Alignment of amino acid sequence of human PRG4 and SynLubricin. **E**, Vector map illustrating the tetracycline-inducible promoter, multiple cloning site (MCS) for cDNA of interest, bicistronic GFP reporter (IRES2 CopGFP), and second expression cassette for the rtTA-M2 tetracycline transactivator and neomycin-resistance gene.

3.3.2 Design and synthesis of cDNA for synonymous Muc1

We tested whether our strategy for mucin-type cDNAs was generalizable and could be applied to other mucins. We chose the mucin Muc1, which is important in the hydration and protection of the cornea and other epithelial surfaces (Mantelli and Argüeso, 2008). We noted that the native tandem repeats of Muc1 are polymorphic, with 42 perfect repeats being most frequent in humans (Nath and Mukherjee, 2014). We applied the codon optimization strategy to design a cDNA for 42-perfect Muc1 repeats, PDTRPAPGSTAPPAHGV TSA. The optimized sequence was fused to the codons for the native N-terminus of human Muc1. We also added the IgK leader sequence, 6x histidine tag, and SumoStar tag, similarly to SynLubricin (Fig. 3.S3A). We calculated a very high repetition score of 4997 for the nucleotide coding sequence of the native human Muc1 tandem repeats. The repetition score was reduced to 220 in our synthetic cDNA, which we referred to as SynMuc1 (Fig. 3.S3B).

The optimized coding sequence for SynMuc1 was synthesized through standard CGS services, whereas our request to synthesize the extremely repetitious sequence of the native Muc1 cDNA was rejected by multiple commercial service providers. The custom synthesized SynMuc1 cDNA was transfected into 293-F cells. The recombinant protein was purified from the media supernatant via immobilized metal affinity chromatography (IMAC) and

detected by Western blot with an antibody against the native human tandem repeats (Fig. 3.S3C). The recombinant mucin was extensively *O*-glycosylated, as indicated by the strong signal when probed with peanut agglutinin (PNA), a lectin that is specific for a core-1, mucin-type disaccharide (Fig. 3.S3D).

During purification, we noticed that a significant percentage of the mucin failed to bind to the IMAC resin and was detected in the flow through (Fig. 3.S3C, D). Western blotting confirmed the presence of the 6x-histidine SumoStar purification tag on the recombinant protein in the flow through and eluted fractions, suggesting that the N-terminus and purification tag were present but inaccessible to the immobilized IMAC cations as would be the case, for example, if the tag was buried in the random coil of the mucin biopolymer (Fig. 3.S3E). Since our goal was to demonstrate the production of the recombinant SynMuc1 and not optimize its purification, alternative chromatography approaches were not explored.

3.3.3 Stable host production of recombinant SynLubricin

Using our chosen transposon system, we tested its application for SynLubricin production (Fig. 3.2A). Unexpectedly, we found that after selection with G418, comparatively few cells exhibited high copGFP reporter levels following doxycycline induction (Fig. 3.2B). To overcome the issue, we applied a two-round sorting strategy using the copGFP reporter to isolate a sub-population of cells that expressed SynLubricin at high levels. Stable cells were expanded and sorted for the top 5% copGFP expressers, which were then expanded and sorted a second time for the top 10% expressers. We found that the sorting strategy improved SynLubricin production 15-fold and did not impact the molecular weight of the glycosylated protein product (Fig. 3.2B, C).

The sorted cell populations displayed noticeably higher levels of the copGFP reporter after induction with doxycycline, indicating successful isolation of a polyclonal population with higher gene expression levels.

To confirm the cDNA stability of the integrated SynLubricin gene in our stable 293-F cells, genomic DNA was extracted from modified 293-F cells after two months of continuous culture. The SynLubricin cDNA was then amplified by polymerase chain reaction (PCR) using primers that were specific to SynLubricin (Fig. 3.3). The amplified gene was approximately 4 kb in length, as expected for full-length lubricin, and indistinguishable in size from similarly amplified genes obtained using the original SynLubricin plasmid as the template or DNA extracted from transiently transfected cells (Fig. 3.3). Even after culture for 2 months, the polyclonal cell population exhibited no indications of SynLubricin gene application or deletion, indicating a high level of genomic stability (Fig. 3.3).

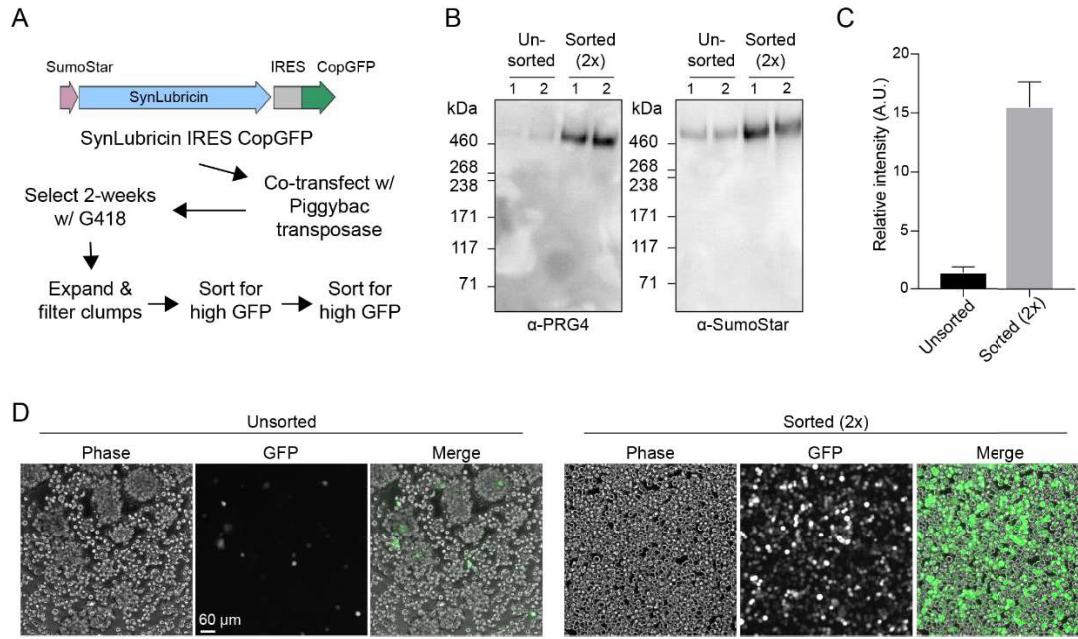


Figure 3.2 – Sorting strategy to isolate stable polyclonal cell populations that produce high levels of SynLubricin. **A**, Strategy for isolation of stable cell populations expressing high levels of SynLubricin. **B**, Western blots of 293-F media supernatant showing relative SynLubricin production in unsorted and twice-sorted (2x) cell populations; 1 and 2 indicate samples from two independent experiments; probed with anti-PRG4 (MABT401) and SUMO antibodies. **C**, Quantification of the relative intensity of signal from anti-PRG4 Western blots in **B**. **D**, Phase-contrast and fluorescence micrographs of unsorted and twice-sorted 293-F cells expressing SynLubricin.

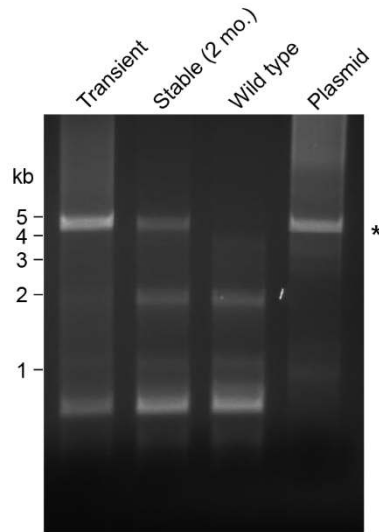


Figure 3.3 – Integrated SynLubricin cDNA is stable in the cellular genome. PCR amplification of SynLubricin coding region in genomic DNA extracts of wild-type and stably integrated 293-F cells cultured continuously for 2 months. As positive controls, PCR amplifications of SynLubricin plasmid and DNA extract from SynLubricin transiently transfected 293-F cells (Transient) are shown. The expected size of full-length SynLubricin is indicated by the star.

3.3.4 Optimization of SynLubricin production

We considered whether SynLubricin productivity could be improved through addition of the histone deacetylase inhibitor, valproic acid (VPA), which has previously been shown to drastically increase production of some recombinant proteins in 293-F cells (Backliwal et al., 2008). Our sorted cell population was induced with doxycycline in the presence or absence of 3.5 mM VPA, and media supernatants were sampled each subsequent day from batch cultures. The molecular weights of the protein products were similar, suggesting that VPA did not appreciably affect the total extent of glycosylation of the protein product (Fig. 3.4A). Interestingly, the recombinant protein levels peaked at approximately 2-3 days post-induction in cultures without VPA and declined rapidly thereafter (Fig. 3.4B). In VPA treated cultures, SynLubricin

levels in the media did not decline as significantly over time. We ruled out protein degradation as a likely explanation for the decline of recombinant protein in cultures without VPA, since we saw no prominent degradation products for lubricin on Western blots (Fig. 3.4A). We instead considered the possibility that the 293-F culture might consume the recombinant protein in conditions of reduced nutrient availability. Consistent with this possibility, we observed that the decline in recombinant protein levels coincided with the depletion of glucose in the cultures without VPA (Fig. 3.4C). Metabolic activity largely ceased in VPA treated cultures after 3 days, as indicated by a sharp decline in glucose consumption (Fig. 3.4C). Thus, VPA may prevent the loss of recombinant protein in batch cultures through slowing 293-F cellular metabolism.

We next scaled up production to 1-liter bioreactors operated in batch mode and conducted two independent production runs with VPA added. Each production run yielded plentiful recombinant protein that was comparable in molecular weight to both recombinant protein isolated from transiently transfected cultures and native lubricin detected in equine synovial fluid (Fig. 3.4D). An ELISA using purified bovine lubricin as a standard reported approximately 200 mg/L of SynLubricin in the batch runs with our stable 293-F lines. Less than 50% of the stable cell population showed strong expression of the copGFP reporter in the batch bioreactors, suggesting that increases in productivity could likely be achieved with clonal expansion of the production cell line (Fig. 3.2D). We noted that an important limitation of our ELISA-based quantification is the use of a bovine standard, which may over- or underestimate SynLubricin levels.

Finally, we tested whether stable protein production could be achieved

with periodic media changes to avoid nutrient depletion. Conditioned media was harvested from doxycycline-induced cultures that were maintained for 10 consecutive days in the absence of VPA. Media in the batch cultures was exchanged every 48 hrs to replenish nutrients and remove metabolic waste products. Viable cell concentration was also reduced to 1×10^6 cells/mL every 48 hrs. SynLubricin production levels were stable over the 10 days of culture, and the SynLubricin molecular weight was constant, indicating that glycosylation was also stable (Fig. 3.4E). While there appears to potentially be a slight decrease in SynLubricin production with time, there is no significant difference in protein yield (Fig. 3.4F).

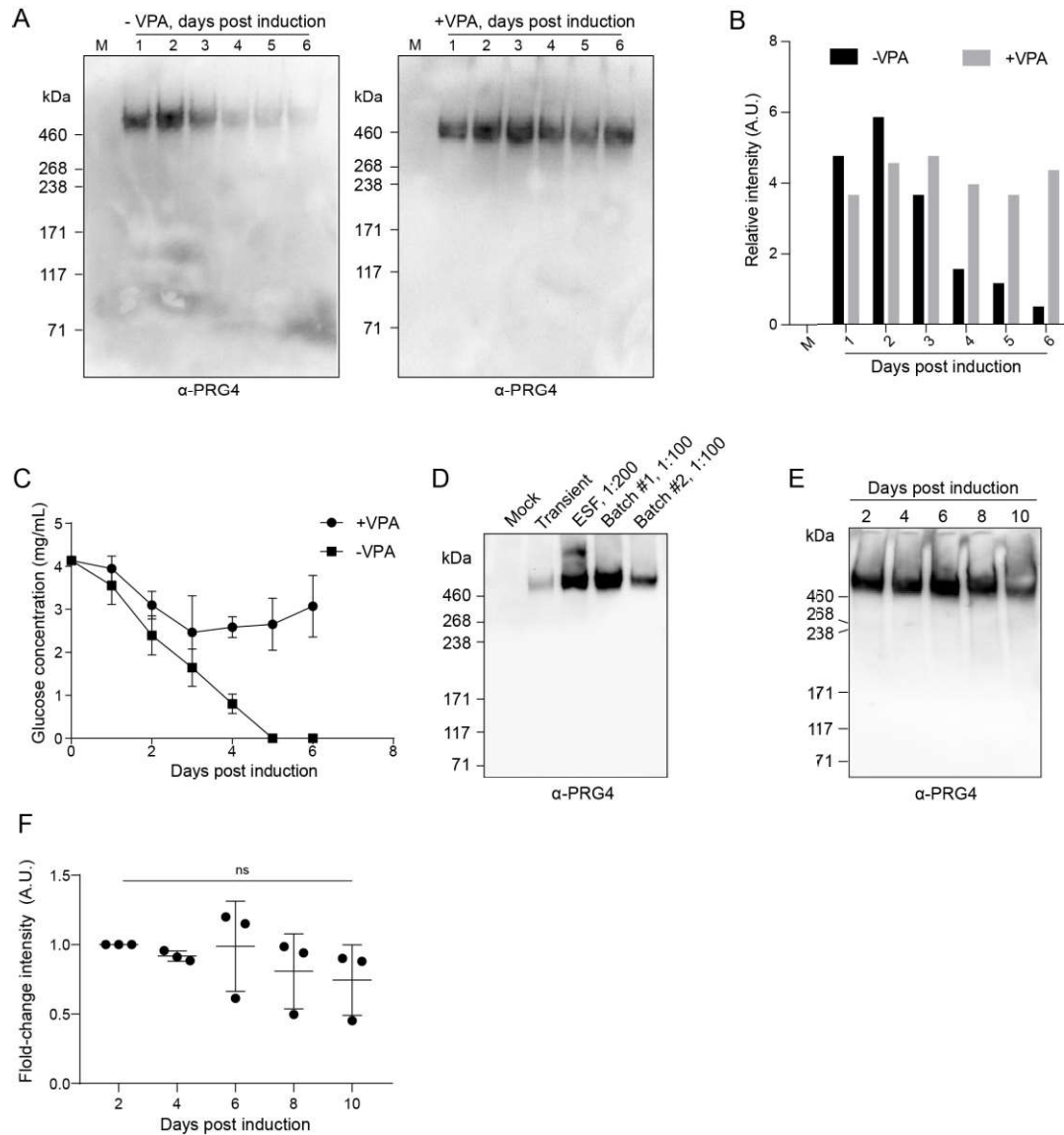


Figure 3.4 – Optimization of SynLubricin production. **A**, Western blots showing relative production of SynLubricin over time in media of control cells and sorted 293-F cells induced with 1 μ g/mL doxycycline for the indicated number of days in the absence or presence of the histone deacetylase inhibitor valproic acid (VPA; 3.5 mM). **B**, Quantification of the relative intensity of signal for the blots shown in A. **C**, Time course for glucose consumption in sorted 293-F cells induced at day 0 with 1 μ g /mL doxycycline with or without 3.5 mM VPA. Mean and S.D. shown, n = 3. **D**, Western blot showing lubricin in the media harvested from non-producing control cells (Mock), cells transiently transfected with SynLubricin cDNA (Transient), and two successive 1-L batch cultures of sorted 293-F cells induced for three days with 1 μ g /mL doxycycline

and 3.5 mM VPA (Batch #1 and Batch #2); equine synovial fluid (ESF) was loaded as a control. **E**, Representative Western blot of SynLubricin produced from stably expressing 293-F cells collected at indicated time points after 1 $\mu\text{g}/\text{mL}$ doxycycline induction on day 0. **F**, Quantification of Western blot replicates represented in B, $n = 3$, ns – not significant.

3.3.5 SynLubricin is a functional biolubricant

Recombinant SynLubricin was effectively purified with anion-exchange chromatography following our previously reported strategy for isolation of native lubricin from equine synovial fluid, with slight modification from using DEAE-Sepharose® to using Q Sepharose (Reesink et al., 2016). We also attempted IMAC to purify the native lubricin, but the recombinant SynLubricin had poor affinity to IMAC resins (Fig. 3.S4). As for SynMuc1, we reasoned that the N-terminal histidine-tag could be buried in the large, random coil of the SynLubricin tandem repeats and abandoned the IMAC approach. In contrast, SynLubricin bound to the anion-exchange resin strongly and eluted continuously over high salt concentrations ranging from approximately 350 mM to 1.5 M (Fig. 3.5A, B). The continuous elution of SynLubricin was likely explained by a varying frequency of anionic sialic acids in the *O*-glycans of the recombinant SynLubricin (Estrella et al., 2010). We found that a stringent wash step of approximately 500 mM NaCl could remove most protein contaminants detectable by silver stain, although some SynLubricin was inevitably lost to this high-salt wash (Fig. 3.5C, D).

To ensure functionality of our recombinant SynLubricin, we tested its ability to lubricate cartilage and reduce friction. Recombinant SynLubricin was purified via anion exchange chromatography using the stringent 500 mM NaCl wash step to eliminate most protein contaminants (Fig. 3.5D). Following purification, SynLubricin was dialyzed in saline and diluted to physiological

concentrations. Lubrication was tested on bovine articular cartilage explants where the native lubricin boundary layer had been extracted using a custom linear reciprocating tribometer (Jones et al., 2007). Compared to a saline control, we found that SynLubricin-containing solutions, as well as control synovial fluid, significantly reduced the boundary friction of cartilage explants (Fig. 3.6; $p < 0.001$ and 0.0001 , respectively).

We also tested a small quantity of a second SynLubricin sample that was purified without the stringent wash of the anion exchange column with 500 mM NaCl. Notably, cartilage friction coefficients were markedly lower for this SynLubricin preparation than any of the measured friction coefficients for the more stringently washed SynLubricin preparations (Fig. 3.6). It should be noted that a low sample volume for the unwashed SynLubricin preparation precluded obtaining enough independent measurements for meaningful statistical comparisons (Fig. 3.6). However, further optimization of purification conditions may yield recombinant lubricin fractions with improved performance in biolubrication. For instance, future studies should investigate whether less negatively charged lubricin fractions that elute at lower salt concentrations (350-500 mM NaCl) are important for cartilage biolubrication either by acting independently or in synergy with more negatively charged lubricin fractions. Alternatively, studies should consider whether any 'contaminants' that are eliminated with the 500 mM NaCl wash might act synergistically with lubricin in cartilage lubrication.

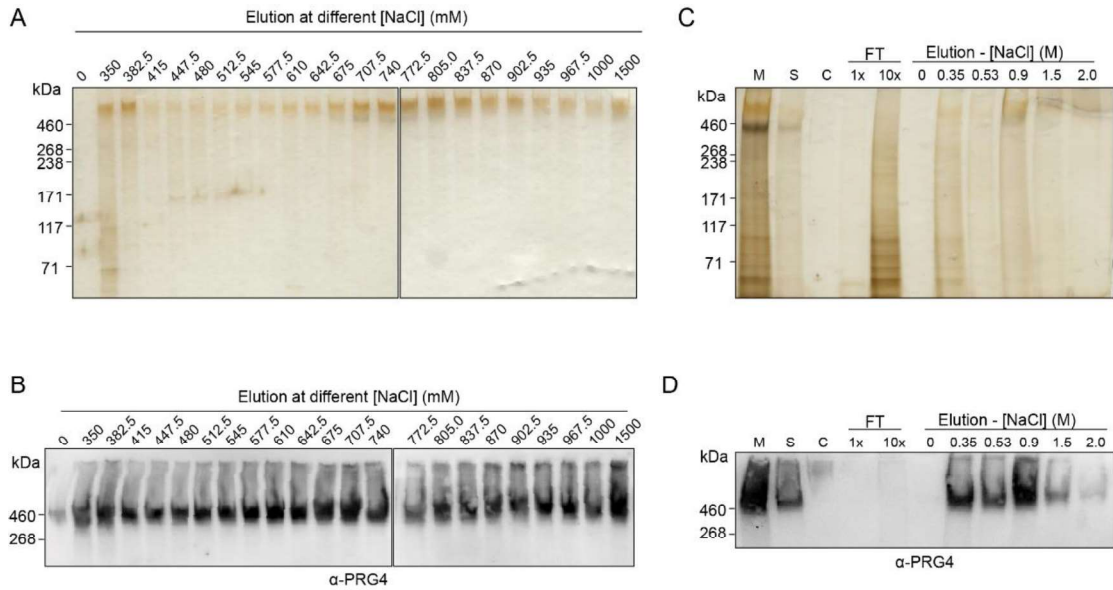


Figure 3.5: Purification of SynLubricin by anionic exchange chromatography. **A**, Silver stain and **B**, Western blot showed SynLubricin eluted continuously from Q Sepharose® resin over a broad range of NaCl concentrations (concentrations indicated above lanes in mM). **C**, Silver stain and **D**, Western blot showing harvested SynLubricin media supernatant (M), 10-fold diluted SynLubricin media supernatant (S), wild-type 293-F conditioned media (C), flow through (FT-1x), 10-fold concentrated flow through (FT-10x), and eluted fractions at indicated salt concentration (shown above lanes in mM).

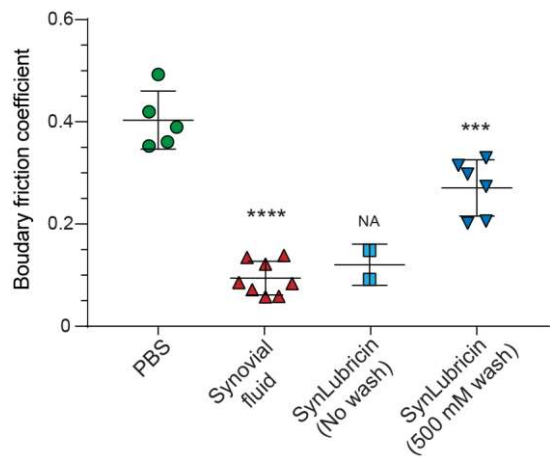


Figure 3.6: Lubrication of cartilage explants shows functionality of SynLubricin. Friction coefficients of NaCl-extracted cartilage explants bathed in saline (PBS), bovine synovial fluid, or SynLubricin eluted either without

washing or with a stringent 500 mM NaCl wash. Mean and S.D. are shown with independent measurements indicated. *** $p < 0.001$, **** $p < 0.0001$; NA: statistical testing is not applicable due to sample size.

3.4 CONCLUSIONS

Taken together, our studies provide a potential roadmap to larger-scale, mucin bio-manufacturing. Success in the design and synthesis of new semi-synthetic genes for both Muc1 and lubricin, combined with our success in isolating highly stable, lubricin-expressing cell populations, suggests that this approach may be broadly applicable for recombinant mucins with long, repetitive domains. Also of note is the successful demonstration of recombinant production in a human cell system that avoids the risk of immunogenic Gal α 1,3-Gal and Neu5Gc epitopes. We find that the recombinant product of our SynLubricin gene is functional in its ability to resist cellular adhesion (Fig. 3.S1A) and lubricate biological surfaces, such as cartilage (Fig. 3.6). Thus, SynLubricin may have potential for diverse applications ranging from injectables for osteoarthritis to topical treatments for chronic dry eye. Moreover, given the speed and low cost of CGS, the approach presented in this work could, in principle, be applied to rapidly prototype designer mucins with new or modified functional domains.

3.5 MATERIALS AND METHODS

3.5.1 Antibodies and reagents

The following antibodies were used: mouse anti-human CD227 (555925, BD Biosciences) (Muc1), mouse anti-human lubricin (MABT401, EMD Millipore), goat anti-mouse IgG-HRP (sc-2005, Santa Cruz), mouse anti-SUMO (4G11E9, GenScript). Lectins used were biotinylated Peanut Agglutinin (PNA;

B-1075, Vector Laboratories). Biotinylated lectins were detected using ExtrAvidin-Peroxidase (E2886, Sigma). To induce transactivator cell lines, doxycycline was used (sc-204734, Santa Cruz). For neomycin selection, G418 was used (10131035, Thermo Fisher). Valproic acid (VPA) was used as a histone deacetylase inhibitor (Sigma P4543-100G).

3.5.2 Constructs

A tetracycline-inducible, transposon based Piggybac expression vector with an integrated, co-expressed reverse tetracycline transactivator gene (pPB tet rtTA NeoR) was used for stable line generation (kindly provided by Dr. Valerie Weaver, University of California San Francisco, USA). The pPB tet rtTA NeoR plasmid was modified by the insertion of the internal ribosome entry site (IRES) of the encephalomyocarditis virus followed by the fluorescent protein copGFP into the NotI and XbaI sites of the plasmid (pPB tet IRES copGFP rtTA NeoR). Synthetic cDNA for a lubricin analog with 78 perfect repeats of KEPAPPTTP, native N-and C-terminal domains, and an N-terminal SumoStar tag (lifesensors) were generated through custom gene synthesis (General Biosystems) and cloned into the multiple cloning site of pPB tet IRES copGFP rtTA NeoR using BamHI and EcoRI restriction sites. Similarly, cDNA for a soluble, codon-scrambled Muc1 having 42 perfect repeats of PDTRPAPGSTAPPAHGVTS A and a native human Muc1 N-terminus with SumoStar tag was generated by custom gene synthesis in the pcDNA3 plasmid. For construction of an mCherry2 IRES2 copGFP expression plasmid, an mCherry2 cDNA was isolated by EcoRI and NotI digestion of pmCherry2 N1 and cloned into the EcoRI and NotI digested pPB tet IRES copGFP rtTA NeoR vector to create pPB tet mCherry2 IRES copGFP rtTA NeoR.

3.5.3 Cell lines and culture

FreeStyle 293-F (293-F) cells were obtained from Thermo Fisher Scientific. Cells were cultured and maintained according to the manufacturer's guidelines in 100-ml Wheaton Celstir glass spinner flasks. Cells were maintained between 0.5×10^6 and 3×10^6 cells/mL at 120 rpm, 37°C, and 8% CO₂ in FreeStyle 293 Expression Medium (Thermo). 293-F transfections were performed using polyethyleneimine (PEI) as previously reported (Durocher et al., 2002). Stable cell lines were created by co-transfection of the pPB tet IRES copGFP rtTA NeoR plasmids described above with a hyperactive transposase plasmid (Shurer et al., 2018) and subsequently selected with 750 µg/mL of G418 for two weeks. Human embryonic kidney cells transformed with the SV40 large T antigen (293-T; ATCC) were maintained in high-glucose DMEM supplemented with 10% fetal bovine serum and penicillin/streptomycin. 293-T cells were transfected through a standard calcium phosphate transfection protocol. Cell proliferation was quantified by cell counting on a hemocytometer with trypan blue exclusion.

3.5.4 Cell sorting and SynLubricin production

293-F cells with stable incorporation of PRG4 IRES copGFP were expanded and induced at 1×10^6 cells/mL with 1 µg/mL doxycycline for 24 hours. The top 5% of copGFP-expressing cells were collected through Fluorescence Activated Cell Sorting (FACS) on a FACSAria Fusion (BD Biosciences). Cells were subsequently expanded in the absence of doxycycline to 1×10^6 cells/mL. Cells were induced with 1 µg/mL doxycycline for 24 hours and sorted a second time, collecting the top 10% of copGFP-expressing cells. For PRG4 production, cells were transferred to a 1 L ProCulture glass spinner flask (Corning) and induced at 2×10^6 cells/mL with 1 µg/mL doxycycline and 3.5 mM VPA. Smaller scale production of lubricin was also conducted in 100-ml

Wheaton Celstir glass spinner flasks for measurement of lubricin production rates and glucose consumption rates in the presence or absence of VPA. Glucose levels were recorded with a GlucCell glucose monitoring system (CESCO BioProducts).

3.5.5 Immuno- and lectin blot analysis

Protein in culture supernatants or purified samples were separated on NuPAGE 3-8% Tris-Acetate gels (Invitrogen) and transferred to PVDF membranes. Membranes were blocked with 3% BSA TBST for 2 hours. Primary antibodies were diluted 1:1000 and lectins were diluted to 1 µg/mL in 3% BSA TBST and incubated on membranes overnight at 4°C. Secondary antibodies or ExtrAvidin were diluted 1:2000 in 3% BSA TBST and incubated for 2 hours at room temperature. Blots were developed in Clarity ECL (BioRad) substrate and imaged on a ChemiDoc (BioRad) documentation system. Fiji was used for image processing (Schindelin et al., 2012).

3.5.6 Enzyme-linked immunosorbent assay (ELISA)

A custom sandwich ELISA was used to assess the concentration of SynLubricin, similarly to previous descriptions. A 96-well plate (Costar) was incubated overnight at 4°C with 10 µg/mL peanut agglutinin (Sigma) in 50mM sodium bicarbonate buffer, pH 9.5. Plates were blocked with 3% BSA PBS for 1 hour at room temperature. Serial dilutions of FPLC-purified bovine synovial fluid lubricin were used as standards. Samples were loaded at 1:200 dilution in DPBS for 1 hour at room temperature, followed by three washes in PBS + 0.1% Tween20. The primary antibody used (Millipore MABT401) binds to the native PRG4 tandem repeats of human and bovine lubricin, which have approximately 90% sequence similarity to the repeats of SynLubricin. Primary antibody and secondary antibody (Millipore AP126P) were diluted 1:5000 and 1:2000,

respectively, and each incubated for 1 hour at room temperature, with three washes with PBS-T in between antibody incubations and following the secondary antibody incubation. The ELISA was developed at room temperature with 1-Step Ultra TMB (ThermoFisher) for 9-12 minutes or until a royal blue color appeared, at which point the reaction was stopped with 2N H₂SO₄. Absorbance was measured at 450 nm with 540 nm background subtraction on a Tecan Spark® 3M microplate reader, and concentrations were calculated using Magellan software with a four parameter Marquardt fit.

3.5.7 Purification of recombinant SynMuc1

293-F cells were transiently transfected using the PEI protocol previously described. After 24 hours, the media supernatant was collected. The media supernatant was diluted 1:4 in 20 mM sodium phosphate, 0.5 M NaCl, pH 7.4 and incubated with 100 µL Ni Sepharose excel resin (17371201, GE) overnight at 4°C. Sample flow through was collected using a gravity column (29922, Thermo). The resin was washed with 5 mL 20 mM sodium phosphate, 0.5 M NaCl, 5 mM imidazole, pH 7.4. SynMuc1 was eluted with 5 mL of 20 mM sodium phosphate, 0.5 M NaCl, 500 mM imidazole, pH 7.4. SynMuc1 was desalted into PBS using a Zeba Spin Desalting Column (87766, Thermo).

3.5.8 Purification of recombinant SynLubricin

SynLubricin was purified from PRG4 IRES copGFP positive 293-F cell culture supernatant by fast protein liquid chromatography (FPLC) with Q Sepharose® resin (GE). The supernatant was diluted 1:10 with 50mM Tris-HCl buffer, pH 7.5, and loaded onto the column. The column was washed with 50mM Tris-HCl, 525mM NaCl, pH7.5. Purified SynLubricin was collected by eluting with 50mM Tris-HCl, 1M NaCl, pH 7.5. The purified SynLubricin was dialyzed into PBS using a Tube-O-Dialyzer (G-Biosciences) overnight at 4°C.

The final purified product was obtained by concentrating with a SpeedVac on the low setting.

3.5.9 Tribology

The performance of SynLubricin as a boundary lubricant was assessed using a custom linear reciprocating tribometer as previously described (Gleghorn and Bonassar, 2008). Briefly, cylindrical cartilage explants (6mm diameter x 2mm thickness) were harvested from the femoral condyles of neonatal bovine stifles. Endogenous cartilage-bound lubricin was extracted using a 30 min incubation in 1.5M NaCl, followed by a 1-hour equilibration step in PBS. Explants were incubated in either PBS, SynLubricin, or bovine synovial fluid for 15-20 min prior to loading onto a tribometer in a 1 mL bath of the respective fluid. Explants were compressed to approximately 30% strain against a glass counter-face and permitted to depressurize over the course of one hour. After reaching an equilibrium normal load, the counter-face was linearly reciprocated at a speed of 0.3 mm/s for three cycles. Simultaneously, a biaxial load recorded the normal and shear loads. For both the forward and reverse directions and at each speed, the friction coefficient was calculated as the mean shear force while sliding divided by the equilibrium normal load.

3.5.10 Statistical analysis

Statistical significance was determined by one-way ANOVA or Student's *t* test (two-tailed) as appropriate using Prism (GraphPad). For the lubrication data, a one-way ANOVA with Tukey's post-hoc tests were performed to compare mean friction coefficients across all lubricants. All graphs were generated in Prism (GraphPad, La Jolla, CA).

3.6 ACKNOWLEDGEMENTS

We thank V. Weaver and J. Lakins for the original transposon plasmids that were further modified in this work. This investigation was supported by the National Institute of General Medicine Sciences Ruth L. Kirschstein National Research Service Award 2T32GM008267 (C.R.S.), Knight Family Foundation Graduate Research Fellowship in Nanoscience and Technology (C.R.S.), Samuel C. Fleming Family Graduate Fellowship (C.R.S. and Z.C.), National Science Foundation Graduate Research Fellowship (E.F., DGE-1650441), National Institute of Health T35 training grant OD010941 (M.A.S.), National Institute of Arthritis and Musculoskeletal and Skin Diseases/National Institute of Health K08AR068469 (H.L.R.), National Institute of Health New Innovator DP2 GM229133 (M.J.P.), National Cancer Institute U54 CA210184 (M.J.P.). Flow cytometry was carried out at the Cornell University Biotechnology Resource Center.

3.6.1 Complete author list

Carolyn R. Shurer, Yuyan Wang, Elizabeth Feeney, Shelby E. Head, Victoria X. Zhang, Jin Su, Zhu Cheng, Morgan A. Stark, Lawrence J. Bonassar, Heidi L. Reesink, and Matthew J. Paszek

3.6.2 Author contributions

M.J.P. and H.L.R. designed the codon-optimized cDNAs for the recombinant mucins and managed the project. J.S. prepared transposon-based vectors for expression of the codon-optimized cDNAs. M.J.P. and H.L.R. prepared and isolated stable cell populations for recombinant lubricin and conducted recombinant production in bioreactors. C.R.S. and S.E.H. produced and analyzed recombinant SynMuc1, analyzed protein expression time-course, and effects of VPA. C.R.S., S.E.H., and M.A.S. optimized recombinant lubricin

production. Y.W., C.R.S., V.Z., S.E.H. and M.A.S. optimized purification of recombinant proteins, and Y.W. purified recombinant lubricin for functional analysis. E.F. and L.B. oversaw and conducted tribological testing of cartilage explants. All authors contributed to the analysis of data and preparation of the manuscript.

3.6.3 Competing interests

The authors declare a potential financial interest due to a pending patent on the synthetic gene sequences reported.

3.7 SUPPLEMENTAL FIGURES AND TABLE

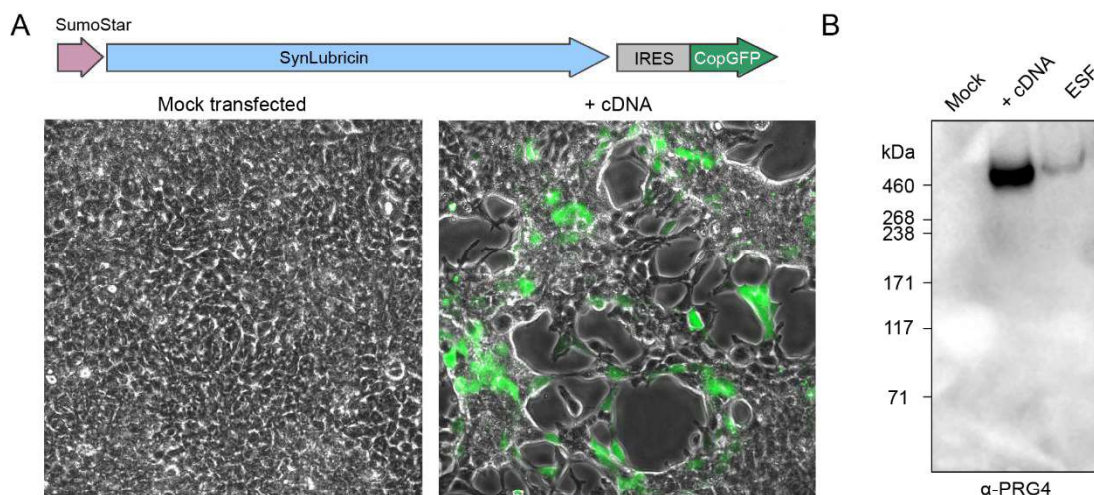


Figure 3.S1 – Transient expression of SynLubricin altered adherent cell morphology. **A**, Morphology of 293-T cells mock transfected or transfected with cDNA for bicistronic SynLubricin IRES copGFP. Images shown are a merged overlay of phase contrast and fluorescence micrographs. Note the inhibition of cell-cell adhesion near cells expressing high levels of the copGFP reporter. **B**, Western blot of equine synovial fluid (ESF) and media supernatant from mock-transfected and SynLubricin-transfected cells probed with MABT401 antibody against PRG4 tandem repeats.

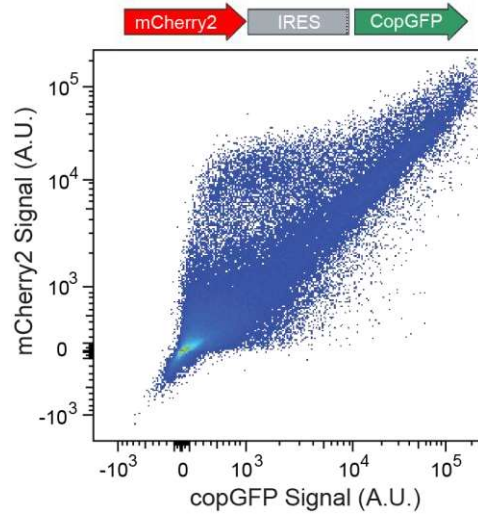


Figure 3.S2 – Validation of new transposon-based gene delivery vector. Flow cytometry results showing correlation of levels of mCherry2 and the copGFP reporter.

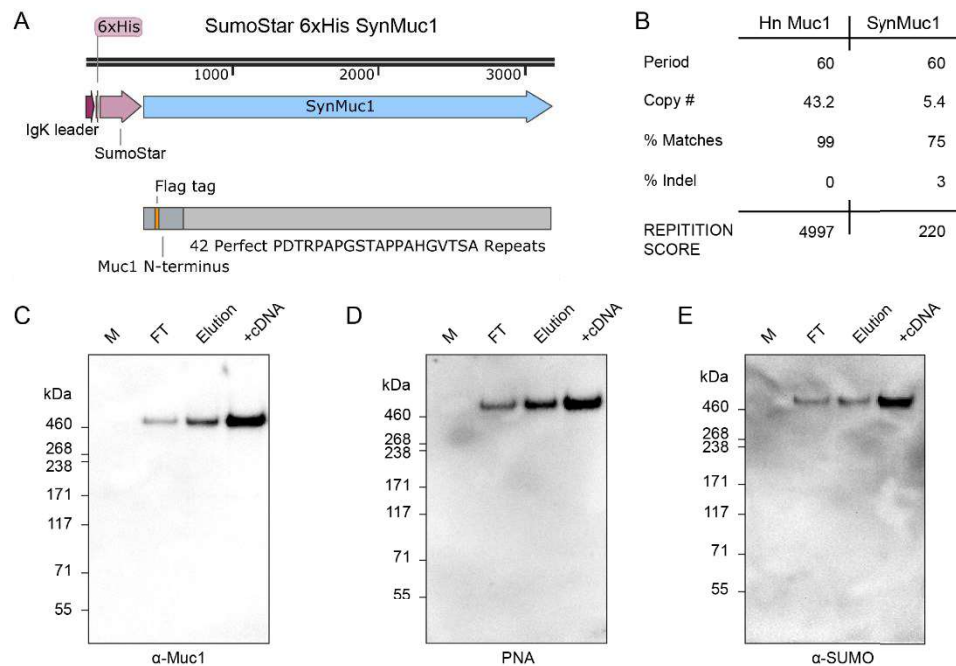


Figure 3.S3 – Application of the codon-scrambling strategy for Muc1. **A**, Schematic of SynMuc1 with codon-scrambled tandem repeats. **B**, Calculated repetition score for the nucleotides encoding the tandem repeats of human

Muc1 and SynMuc1. **C**, Western blot of media supernatant from 293-F cells transfected with SynMuc1 cDNA (+cDNA) or non-transfected cells (M), Ni-NTA resin flow through from His-affinity purification (FT), and eluted protein (Elution) probed with a Muc1 antibody. **D**, PNA-lectin blot of C. **E**, Western blot of C, probed with a SUMO antibody.

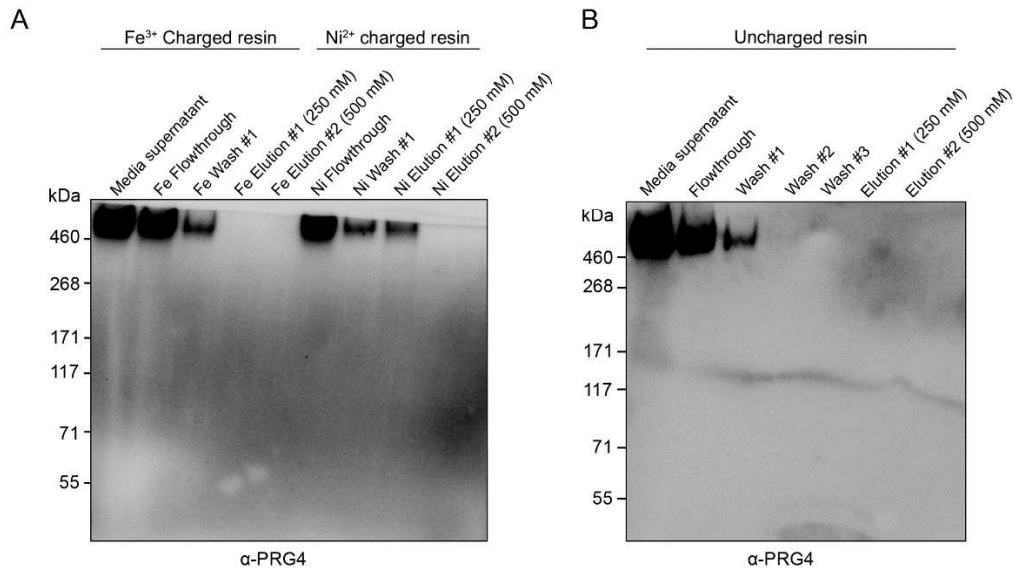


Figure 3.S4 – SynLubricin has low affinity for immobilized-metal-affinity-chromatography (IMAC) resin. **A**, Western blot of media supernatant and the IMAC purification flow throughs, washes, and eluted fractions from Fe³⁺ and Ni²⁺ loaded nitrotriactic acid (NTA) resins. Elutions were performed at the indicated NaCl concentration. No non-specific binding of sialic acids to multivalent Fe³⁺ was observed. **B**, Western blot of flow through, wash, and eluted fractions from uncharged NTA resin.

Human PRG4A RepeatsAmino acid composition

Ala (A)	58	11.4%
Arg (R)	0	0.0%
Asn (N)	1	0.2%
Asp (D)	2	0.4%
Cys (C)	0	0.0%
Gln (Q)	0	0.0%
Glu (E)	48	9.4%
Gly (G)	4	0.8%
His (H)	0	0.0%
Ile (I)	1	0.2%
Leu (L)	7	1.4%
Lys (K)	69	13.6%
Met (M)	0	0.0%
Phe (F)	0	0.0%
Pro (P)	155	30.5%
Ser (S)	13	2.6%
Thr (T)	150	29.5%
Trp (W)	0	0.0%
Tyr (Y)	0	0.0%
Val (V)	0	0.0%

SynLubricin RepeatsAmino acid composition

Ala (A)	59	12.5%
Arg (R)	0	0.0%
Asn (N)	0	0.0%
Asp (D)	0	0.0%
Cys (C)	0	0.0%
Gln (Q)	0	0.0%
Glu (E)	59	12.5%
Gly (G)	0	0.0%
His (H)	0	0.0%
Ile (I)	0	0.0%
Leu (L)	0	0.0%
Lys (K)	59	12.5%
Met (M)	0	0.0%
Phe (F)	0	0.0%
Pro (P)	177	37.5%
Ser (S)	0	0.0%
Thr (T)	118	25.0%
Trp (W)	0	0.0%
Tyr (Y)	0	0.0%
Val (V)	0	0.0%

Table 3.S1 – Amino acid compositions in the tandem repeats of human PRG4 isoform A and SynLubricin.

CHAPTER 4

MUCIN-COATING TECHNOLOGIES FOR PROTECTION AND REDUCED AGGREGATION OF CELLULAR PRODUCTION SYSTEMS^{1,2}

4.1 ABSTRACT

Optimization of host-cell production systems with improved yield and production reliability is desired in order to meet the increasing demand for biologics with complex post-translational modifications. Aggregation of suspension-adapted mammalian cells remains a significant problem that can limit the cellular density and per volume yield of bio-reactors. Here, we propose a genetically encoded technology that directs the synthesis of anti-adhesive and protective coatings on the cellular surface. Inspired by the natural ability of mucin glycoproteins to resist cellular adhesion and hydrate and protect cell and tissue surfaces, we genetically encode new cell-surface coatings through the fusion of engineered mucin domains to synthetic transmembrane anchors. Combined with appropriate expression systems, the mucin coating technology directs the assembly of thick, highly hydrated barriers to strongly mitigate cell aggregation and protect cells in suspension against fluid shear stresses. The coating technology is demonstrated on suspension adapted human 293-F cells, which resist clumping even in media formulations that otherwise would induce extreme cell aggregation and show improved performance over commercially available anti-clumping agent. The stable biopolymer coatings do not show deleterious effects on cell proliferation rate, efficiency of transient transfection

¹This work was originally published in *Biotechnology and Bioengineering* and has been reproduced here under the author use and publication permission policy of Wiley. Shurer, C.R., Head, S.E., Goudge, M.C., and Paszek, M.J. (2019). Mucin-Coating Technologies for Protection and Reduced Aggregation of Cellular Production Systems. *Biotechnology and Bioengineering*. <https://doi.org/10.1002/bit.26916>

²C.R.S. managed the project, prepared transposon-based vectors and stable cell lines, and conducted imaging, flow cytometry, shear, and cell clumping experiments. See sections 4.6.1 and 4.6.2 for a complete author list and specific author contributions.

with cDNAs, or recombinant protein expression. Overall, our mucin coating technology and engineered cell lines have the potential to improve the single-cell growth and viability of suspended cells in bioreactors.

4.2 INTRODUCTION

Protein therapeutic agents represent a large and rapidly growing portion of the pharmaceutical market (Dumont et al., 2016). Current biologics enable the treatment of a wide variety of human diseases, including cancer, autoimmune disorders, and infectious diseases (Carter, 2011; Leader et al., 2008). The commercial success of biologics has been a major impetus for the development of improved manufacturing technologies that reliably produce the biological agents on a large scale.

The majority of all recombinant protein pharmaceuticals are produced in mammalian cells at present (Wurm, 2004). Mammalian cells are preferred over prokaryotic organisms for production of protein therapeutics because eukaryote-specific post-translational modifications are often required for protein functionality and appropriate pharmacokinetics. As an example, monoclonal antibodies, a major class of protein therapeutics, must be post-translationally modified with sugar structures called glycans in a post-translational modification process called glycosylation (Shukla and Thömmes, 2010; Zhu, 2012). Without glycosylation, therapeutic antibodies typically have poor stability and pharmacokinetics *in vivo*.

Today, the majority of all recombinant protein pharmaceuticals are produced in the mammalian Chinese Hamster Ovary (CHO) cell line. However, a significant drawback CHO cells for bio-manufacturing is their capacity to generate glycans that are not native to humans (Ghaderi et al., 2012). These

glycans can produce deleterious immune responses and have been implicated in therapeutic resistance, which remains a significant concern for physicians and patients (Casademunt et al., 2012). The risk of patient immune responses from CHO-derived products has motivated a deeper consideration of the use of human cell lines for manufacturing recombinant protein therapies (Sandberg et al., 2012).

Suspension adapted human embryonic kidney 293 cells (293-F) have become the most popular host cell line for the production of biological therapeutics with human glycosylation patterns (Casademunt et al., 2012; Vink et al., 2014). The 293-F cell system has several desirable features for recombinant protein production, including a fast proliferation rate, a high level of protein production, and ease of transient transfection (Casademunt et al., 2012; Durocher et al., 2002; Swiech et al., 2011; Wurm and Bernard, 1999). Recently, the United States Food and Drug Administration (FDA) has approved several therapeutic agents produced in 293-F cells (Dumont et al., 2016). However, compared to CHO-cell systems, 293-F cells can exhibit a higher propensity to form large aggregates in suspension, limiting their yield and reliability for biomanufacturing (Wurm and Bernard, 1999). While special medium formulations have been developed to reduce cell clumping (Han et al., 2006; Peshwa et al., 1993; Tolbert et al., 1980; Zanghi et al., 2000), aggregation continues to be a challenge for mammalian suspension cell culture, especially at the high cell densities required for fast, high-yield protein production (Liu and Goudar, 2013). Exogenous addition of anti-clumping agents also introduces additional molecules that must be purified away from secreted protein products (Dee et al.; Tsao et al.; Li et al.; Park et al.). An alternative strategy would be to genetically engineer production cells to have reduced adhesion, but few

approaches have been developed at the current time.

A naturally occurring family of biopolymers called mucins are utilized in nature to reduce adhesion and fouling at biological interfaces. Mucins are characterized by amino acid sequences rich in serine and threonine residues, which are post-translationally modified with *O*-linked pendant glycan structures (Thornton et al., 2008). The bottlebrush molecular structure of mucins confers an anti-adhesive characteristic that is exploited in biological systems for diverse purposes, including antifouling coatings, lubrication, and modulation of cellular interactions (Jay and Waller, 2014; Kuo et al., 2018; Paszek et al., 2014). Of the mucin family members, Mucin-1 (Muc1) has long been recognized as an anti-adhesive protein that can interfere with integrin- and cadherin-mediated cell interactions (Klinken et al., 1995; Wesseling et al., 1995, 1996). The anti-adhesive properties of Muc1 are conferred by its large ectodomain, which is heavily *O*-glycosylated during trafficking to the cell surface. Neutral and anionic sugar residues of the glycans can coordinate with water to form a highly hydrated barrier on the cell surface (Gendler and Spicer, 1995).

In this work, we construct semi-synthetic mucin cDNAs to create a genetically-encoded technology for reduction of aggregation of human-cell host production systems. The work builds from and extends our previous work in developing a method for stable expression of native and engineered mucins on the cell surface (Shurer et al., 2018). Here, the mucin technology is further developed, tested, and refined specifically for use as an anti-adhesive coating on host-cell production systems. As a demonstration of concept, we develop new 293-F cell lines with stable anti-adhesive coatings and evaluate their performance in regards to proliferation rate, cell aggregation, resistance to shear stress, and efficiency of transfection with plasmid DNA.

4.3 MATERIALS AND METHODS

4.3.1 Antibodies and reagents

The following antibodies were used: Human CD227 (555925, BD Biosciences) (Muc1), β -Actin (sc-4778, Santa Cruz), Goat anti-Mouse IgG-HRP (sc-2005, Santa Cruz). Lectins used were: Biotinylated Peanut Agglutinin (PNA; B-1075, Vector Laboratories), CF568 PNA (29061, Biotium), CF640R PNA (29063, Biotium), CF633 Wheat Germ Agglutinin (WGA; 29024, Biotium). Biotinylated lectins were detected using ExtrAvidin-Peroxidase (E2886, Sigma). To induce transactivator cell lines, doxycycline was used (sc-204734, Santa Cruz). For gentamycin selection, G418 was used (10131035, Thermo Fisher).

4.3.2 Constructs

A tetracycline-inducible, transposon based Piggybac expression vector with an integrated, co-expressed reverse tetracycline transactivator gene (pPB tet rtTA NeoR) was used for stable line generation (kindly provided by Dr. Valerie Weaver, University of California San Francisco, USA). The pPB tet rtTA NeoR plasmid was modified by the insertion of the internal ribosome entry site (IRES) of the encephalomyocarditis virus followed by the fluorescent protein copGFP into the NotI and XbaI sites (pPB tet IRES GFP rtTA NeoR). Synthetic cDNAs containing either 21 or 42 tandem repeats (TR) of the amino acid sequence PDTRPAPGSTAPPAHGVTS A were codon optimized with codon scrambler (Tang and Chilkoti, 2016), generated through custom gene synthesis (General Biosystems), and cloned in place of the native tandem repeats in pcDNA3.1 Muc1 TM21 – previously described in (Paszek et al., 2014; Shurer et al., 2018) – using the BamHI and Bsu36I restriction sites. The Muc1 gene containing the engineered 21 or 42 tandem repeats was then cloned into the pPB tet IRES GFP rtTA NeoR plasmid using the BamHI and EcoRI sites to generate

Muc1 42TR TM21 pPB tet IRES GFP rtTA NeoR and Muc1 21TR TM21 pPB tet IRES GFP rtTA NeoR plasmids used to make the Mucin-270 and Mucin-135 biopolymer cell lines, respectively. To produce the Mucin-0 cell line, the native Muc1 tandem repeats were deleted from the pcDNA3.1 Muc1 TM21 through Q5 site directed mutagenesis with 5'-TGGAGGAGCCTCAGGCATACTTTATTG-3' (forward) and 5'-CCACCGCCGACCGAGGTGACATCCTG-3' (reverse) primers. The Muc1 gene with 0TR was then cut from the pcDNA3.1 Muc1 0TR TM21 and cloned into the pPB tet IRES GFP rtTA NeoR plasmid via the BamHI and EcoRI sites. The plasmid pLV puro mRuby2 was used for transient transfection experiments with cytoplasmic red fluorescent protein (RFP). For secreted RFP experiments, SS-mScarlet-I pPB tet IRES GFP rtTA NeoR plasmid was used. To construct this plasmid, the backbone was linearized using BamHI-HF and EcoRI-HF. A dsDNA oligo encoding the Muc1 signal sequence (MTPGTQSPFFLLLLLTVLTVVTGS) fused by a GGGGS linker to mScarlet-I was ordered from Integrated DNA Technologies. This fragment was inserted into the linearized backbone via NEB HiFi Assembly.

4.3.3 Cell lines and culture

FreeStyle 293-F Cells were obtained from Thermo Fisher Scientific. Cells were cultured and maintained according to the manufacturer's guidelines in an Eppendorf New Brunswick s41i incubator in Erlenmeyer flasks. Cells were maintained between 0.5×10^6 and 3×10^6 cells/mL at 120 rpm, 37°C, and 8% CO₂ in FreeStyle 293 Expression Medium (Thermo). Transfections were performed using polyethyleneimine (PEI) as previously reported (Durocher et al., 2002). Genetically-encoded stable cell lines were created by co-transfection of the pPB tet IRES GFP rtTA NeoR plasmids described above with a hyperactive

transposase plasmid (Shurer et al., 2018) and subsequently selected with 750 µg/mL of gentamycin for two weeks. Cell proliferation was quantified by cell counting on a hemocytometer with trypan blue exclusion.

4.3.4 Confocal microscopy

Samples were collected, pelleted at 200 rcf for 5 min, and fixed in 4% paraformaldehyde for 10 minutes at room temperature. Samples were washed three times with PBS. Cells were labeled with 1:1000 CF568 PNA for *O*-glycans and 1:1000 CF633 WGA for the cell membrane in PBS for 30 minutes at room temperature. Samples were washed three times with PBS and imaged on a Zeiss LSM800 with a 63x water immersion objective.

4.3.5 Flow cytometry analysis

All samples were measured using live cells, unless otherwise indicated. Cells were harvested from suspension culture, pelleted at 200 rcf for 5 min, and resuspended in 0.5% BSA PBS. Samples were filtered through a 0.22 µm filter cap and analyzed on a BD FACS Aria Fusion. For the doxycycline time-course, cells were induced with 1 µg/mL of doxycycline. Cellular samples from the cultures were taken at the indicated time points, pelleted at 200 rcf for 5 min, and fixed with 4% paraformaldehyde for 10 min at room temperature. Samples were rinsed three times with PBS and stored at 4°C until flow cytometry analysis. Analysis of all flow cytometry data was performed using FlowJo software.

4.3.6 Immuno- and lectin blot analysis

Cells are inoculated at 0.5×10^6 cells/mL and grown overnight, 16-18 hr. Biopolymer expression was then induced with 1 µg/mL doxycycline, and cells were grown with doxycycline for an additional 48 hr. After 48 hr, a sample was taken for each cell line, pelleted at 200 rcf for 5 min before the supernatant was

separated, and the cell pellet was lysed by resuspending in RIPA lysis buffer (Abcam), vortexing the sample for 30 seconds, and heating to 98°C for 10 min. Lysates were frozen on liquid nitrogen and stored at -80°C. Lysates were separated on Nupage 3-8% Tris-Acetate gels (Invitrogen) and transferred to PVDF membranes. Membranes were blocked with 3% BSA TBST for 2 hr. Primary antibodies were diluted 1:1000 and lectins were diluted to 1 µg/mL in 3% BSA TBST and incubated on membranes overnight at 4°C. Secondary antibodies or ExtrAvidin were diluted 1:2000 in 3% BSA TBST and incubated for 2 hr at room temperature. Blots were developed in Clarity ECL (BioRad) substrate and imaged on a ChemiDoc (BioRad) documentation system.

4.3.7 PCR amplification of Mucin-270 transgene in the transfected 293F cells

To test for amplification or deletion of stably integrated Mucin-270 cDNAs in 293F genomes, PCR amplification was performed with Q5 Hot start high-fidelity DNA polymerase (New England Biolabs Inc., Ipswich, MA) using extracted genomic DNA as the template. Genomic DNA was extracted with GeneJET genomic DNA purification kit (Thermo Scientific, Waltham, MA). A total of 60 ng of genomic DNA was used for PCR amplification. Primers: Mucin-270 FWD 5'-ATGACACCGGGCACCCAGTC-3' and Mucin-270 REV 5'-CTACATACTTCGTCGGCGCATGTAC-3'. Size of amplicon is 2994 bp.

4.3.8 Cell clumping analysis

Cells were inoculated at 0.75×10^6 cells/mL and induced with 1 µg/mL doxycycline after overnight growth (16-18 hr). Cells were then grown to a high cell density for an additional 48 or 72 hr in the presence of 1 µg/mL doxycycline. Cell density was quantified by collecting sample of the culture, mixing thoroughly to dissociate large clumps, and counting viable cells with a hemocytometer and trypan blue exclusion. For imaging, samples were drawn

with wide-bore pipette tips to reduce dissociation of large clumps and diluted in PBS to approximately 6.75×10^4 cells/cm² for imaging in 2D. Phase contrast images were acquired on an Olympus IX81 microscope with a 10x objective. Fiji was used for image processing (Schindelin et al., 2012). Two independent samples were collected and prepared as technical replicates for imaging with three regions of interest imaged per technical replicate. Three biological replicates were performed. Automated image analysis was performed using custom analysis software adapted from a previous publication (Shurer et al., 2018). Briefly, the analysis software located the center of each circular object. The coordinates of each cell's center were then used to calculate the Ripley's K function in MATLAB. The percent of single cells was calculated by counting the total number of cells which do not have any neighboring cells within 19 μ m and dividing by the total number of cells in the image. Similarly, the percent of cells in various cluster sizes was calculated by binning the cells into clusters based on the number of neighboring cells within 19 μ m.

To evaluate resistance to calcium induced cell aggregation, cultures were inoculated at 0.5×10^6 cells/mL and induced with 1 μ g/mL doxycycline after overnight growth (16-18 hr). After 48 hr, cells were resuspended at 4×10^6 cells/mL. The culture media was then supplemented with 2 mM CaCl₂, 1:300 anti-clumping agent (Thermo Fisher, 0010057AE), or both. Still images and videos of the cell suspension were acquired after 24 hr of treatment by transferring the culture to a glass test tube. The concentration of cells in suspension was determined by collecting duplicate samples from each culture after allowing the largest aggregates to settle out of suspension for 20 seconds. Cell concentration was measured using a hemocytometer and Trypan blue.

4.3.9 Shear stress experiments

Cells were inoculated at 0.5×10^6 cells/mL, grown overnight (16-18 hr), and induced with $1 \mu\text{g/mL}$ doxycycline for 48 hr. Using a 5 mL syringe with a 16-gauge needle connected to 6.5 in of 1.02 mm silicon tubing, cell suspensions were sheared by flowing through a $500 \mu\text{m}$ constriction (Teflon tubing) at a constant force generated by a 1 kg mass applied to a syringe with gravity. Samples were passed through the constriction five times. Cells were then stained with $1 \mu\text{g/mL}$ CF640R PNA for 15 min at 4°C . Cells were washed with 0.5% BSA PBS three times and then stained with Ethidium homodimer-1 (dead cell stain, Thermo Fisher, L3224). Three biological replicates were performed, with two technical replicates for each biological replicate. Percent dead cells was determined by measuring the fraction of cells that had taken up the dead cell stain on a BD FACS Aria Fusion. A control sample without shear was used to subtract background cell death for each cell line. For Mucin-135 and Mucin-270 cell lines, only PNA positive cells were considered for analysis. Data analysis was performed using FlowJo software.

4.3.10 Transfection experiments

Cells were inoculated at 0.5×10^6 cells/mL, grown overnight (16-18 hr), and induced with $1 \mu\text{g/mL}$ doxycycline for 48 hr. Cells were then diluted to 2×10^6 cells/mL in fresh medium containing $1 \mu\text{g/mL}$ doxycycline and transfected with $1 \mu\text{g}$ DNA per 10^6 cells. The next day (16-18 hr post-transfection), cells were diluted 1:1 with fresh medium containing $1 \mu\text{g/mL}$ doxycycline. To measure transfection efficiency, cells were transfected with the pLV puro mRuby2 plasmid and transfection efficiency was calculated by flow cytometry as the fraction of cells expressing RFP 72 hr post transfection. For production and secretion of recombinant RFP, cells were transfected with SS-mScarlet-I pPB tet IRES GFP rtTA NeoR. After 24 hr, secreted RFP fluorescence in the media

supernatant was quantified using a Tecan M1000 Pro plate reader.

4.3.11 Statistical analysis

Statistical significance was determined by ordinary one-way ANOVA or Student's *t* test (two-tailed) as appropriate using Prism (GraphPad). All graphs were generated in Prism (Graphpad) except for boxplot which were generated in R.

4.4 RESULTS

4.4.1 Genetically-encoded biopolymers expressed on the surface of 293-F cell lines

Drawing inspiration from the anti-adhesive properties of naturally occurring mucins, we created cDNAs that encoded Muc1-like biopolymers with transmembrane domains for anchorage to the cell surface. The biopolymer domains consisted of an unstructured protein backbone with 0 – 42 perfect repeats of PDTRPAPGSTAPPAHGVTSA, which is recognized by the *O*-glycosylation machinery of the endoplasmic reticulum and Golgi apparatus and heavily glycosylated while trafficked to the cell surface. Each biopolymer was targeted to the extracellular space by the native Muc1 signal sequence. The biopolymers were anchored to the cell membrane with a 21-amino acid transmembrane domain (Mercanti et al., 2010; Shurer et al., 2018). By replacing the native autocatalytic domain of Muc1 (Levitin et al., 2005) with the engineered 21-amino acid transmembrane domain, we mitigated the risk of ectodomain shedding from the cell surface. Our engineered constructs also lacked a cytoplasmic tail to avoid inadvertent transduction of biochemical or physical stimuli by the mucins.

The genetic modification of the 293-F cell line was performed non-virally

with an “all-in-one plasmid” that contained all necessary elements for selection and tetracycline-inducible expression (Fig. 4.1A). The vector included a tetracycline-responsive promoter for expression of the biopolymer coating and an additional cassette for constitutive expression of the reverse tetracycline transactivator (rtTA-M2) and neomycin-resistance gene (Gossen et al., 1995). A bicistronic green fluorescent protein (GFP) reporter was also included for visual confirmation of transcription of the mucin cDNA. The cDNA for the biopolymers was stably incorporated into the genome at random locations by transposon mediated integration (Li et al., 2013; Wilson et al., 2007; Woodard and Wilson, 2015). This approach avoided the use of any viral technology, which poses a serious safety concern in bio-manufacturing (Dumont et al., 2016). We hypothesized that the modified cells would be coated with a dense, inducible layer of mucin biopolymers on their surface (Fig. 4.1B).

We tested three different biopolymers size for their effects on 293-F cell aggregation. Mucin-like genes with 0, 21, and 42 tandem repeats were constructed. The contour lengths of the polymers with 21 and 42 repeats were predicted to be 135 nm and 270 nm, respectively. We therefore designated the biopolymers Mucin-0, Mucin-135, and Mucin-270 based on the relative length of the biopolymer (Fig. 4.1C). Because it lacks the large, glycosylated biopolymer domain, the Mucin-0 construct served as a control for any effects related to expression of the transmembrane anchor of the biopolymer.

We confirmed the expression and localization of the biopolymers to the cell surface. Fluorescent microscopy showed expression of the cDNA, reported by the bicistronic GFP signal, and the presence of *O*-glycans on the membrane of cells expressing the Mucin-135 and Mucin-270 semi-synthetic genes (Fig. 4.2A). We observed a large distribution of biopolymer expression levels, which

we attributed to the randomized transposition of the cDNAs into the genome (Fig. 4.2B). Despite the broad distribution, a large portion of the cell populations had stably integrated the cDNA, as shown by the GFP reporter (Fig. 4.2A-C). The expression and size of the biopolymers was further validated by Western blot (Fig. 4.2D). Both the Mucin-135 and Mucin-270 could be probed with antibodies against the native Muc1 tandem repeats (Fig. 4.2D, left). Wild-type (w.t.) cells had no detectable level of endogenous Muc1 expression and no significant *O*-linked mucin-like glycosylation (Fig. 4.2D). The Mucin-135 and Mucin-270 were heavily glycosylated when expressed. This is shown by the protein bands which are detected above the protein sequence molecular weight when probing with anti-Muc1 antibodies (Fig. 4.2D, left; predicted molecular weights 81 kDa and 120 kDa for Mucin-135 and Mucin-270, respectively). *O*-glycosylation is further demonstrated by the detection of the biopolymer with PNA which binds specifically to *O*-linked glycans such as those found on Muc1 (Fig. 4.2D, right).

No significant difference in cell proliferation rate was observed for any of our biopolymer-coated cell lines (Fig. 4.2E). We concluded that the additional protein load of our biopolymers did not adversely affect the rapid growth rate of parental 293-F cells. For our stable cell line, we used the well characterized reverse-tetracycline inducible promoter (Gossen et al., 1995) which initiates gene transcription upon addition of doxycycline and halts transcription on withdrawal of doxycycline. Our cell line responded as predicted to induction by doxycycline, demonstrating temporal control over expression of the mucin coating (Fig. 4.2F).

Highly repetitive cDNAs, such as mucins, are reported to have higher frequencies of amplification and deletion in the cellular genome (Gemayel et al.,

2010; Oren et al., 2016). The cDNAs for our Mucin-135 and Mucin-270 constructs were codon optimized to minimize their repetitiveness. We found that the optimized cDNAs were stable when integrated in the host cell genome. Notably, no noticeable amplification or deletion of stably integrated Mucin-270, the largest and most repetitive of our biopolymer cDNAs, was observed after 2 months of cell culture (Fig. 4.2G).

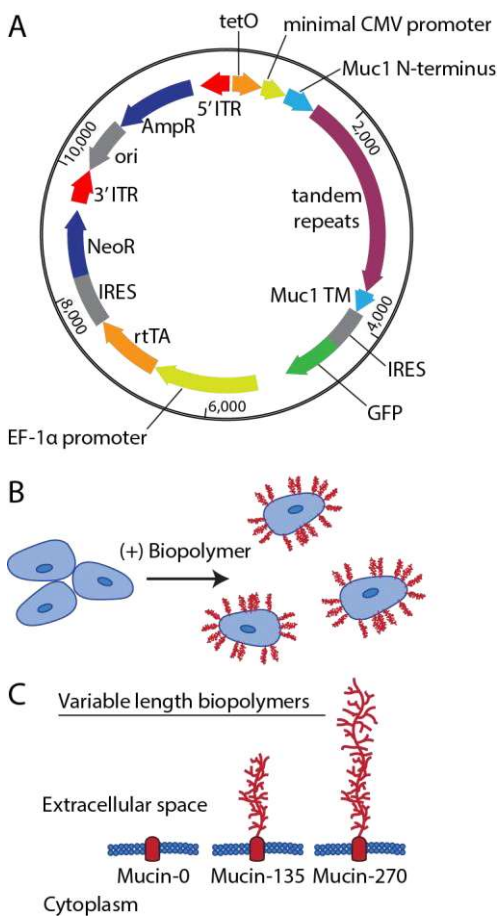


Figure 4.1 – Engineering biopolymer-coated cell lines. A transposon-based method was used to stably integrate the DNA encoding the engineered biopolymers under a doxycycline inducible promoter. **A**, Schematic representation of the all-in-one vector used for producing biopolymer-coated cell lines showing key elements. For incorporation into the cellular genome, the vector includes a tetracycline responsive element (tetO), a minimal CMV promoter, the Muc1 signal sequence (Muc1 N-terminus), the tandem repeats of

the biopolymer (0, 21, or 42 repeats of PDTRPAPGSTAPPAHGVTSA), the transmembrane domain of Muc1 (Muc1 TM), the bicistronic green fluorescent protein reporter (IRES GFP), a EF-1 α promoter, the reverse tetracycline transactivator (rtTA), and a second bicistronic neomycin resistance cassette (IRES NeoR). These elements were all flanked by 5' and 3' inverted terminal repeat sequences (ITRs) required for transposon-mediated incorporation into the genome. For vector replication and production in bacteria, there was also an ampicillin resistance cassette (AmpR) and an origin of replication (ori). **B**, Schematic representation of membrane bound biopolymers expressed by the cells and localized to the cells surface. **C**, Schematic of the relative size of the extracellular domain of the engineered biopolymers designated Mucin-0, Mucin-135, and Mucin-270 for their respective length in nm. The predicted molecular weight of these proteins was 42 kDa, 81 kDa, and 120 kDa, respectively.

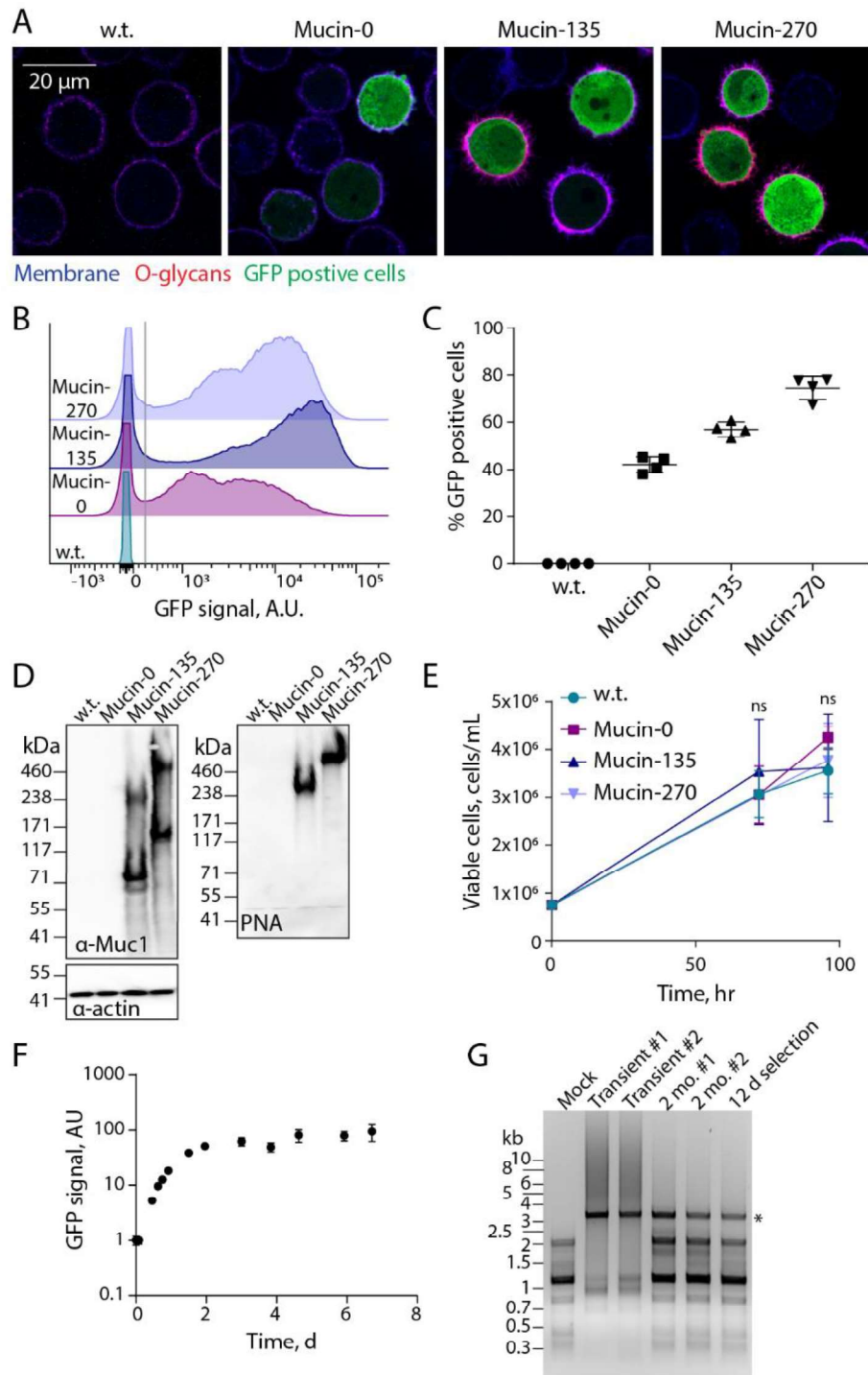


Figure 4.2 – Validation of biopolymer coatings. expression and cell-surface localization of biopolymer coatings was validated for the new, engineered 293-F cell lines. **A**, Representative confocal microscopy images of stable suspension adapted human embryonic kidney 293 (293-F) cell lines – wild type (w.t.), or

stably expressing the Mucin-0, Mucin-135, or Mucin-270 biopolymer. Images show the cell membrane (shown in blue, CF633 Wheat Germ Agglutinin, WGA), *O*-glycans covalently attached to the Mucin-135 and Mucin-270 biopolymers (shown in red, CF568 Peanut Agglutinin, PNA), and green-fluorescent protein (shown in green, GFP) which is co-expressed on the plasmid with the Mucin-0, Mucin-135 and Mucin-270 biopolymer. **B**, Representative flow cytometry histograms showing the polydisperse population of biopolymer expressing cell lines compared to w.t. cells, y-axis is scaled to show the population distribution of GFP positive cells. >50,000 cells per histogram. **C**, Quantification of the percent of cells which are GFP positive for each cell line. Cells with GFP signal above the gray line in Fig. 4.2B were considered GFP positive. Mean and S.D. are shown, >50,000 cells per sample, n = 4. **D**, Representative immunoblot (left) and lectin blot (right) of whole cell lysates for each generated stable cell line compared to w.t. cells, n = 3. **E**, Viable cell concentration determined by hemocytometer counting with trypan blue exclusion, n = 3. **F**, GFP signal of Mucin-270 cells after induction of expression at t = 0 hr, measured by flow cytometry, n = 3, >15,000 cells per sample. **G**, Agarose gel showing polymerase chain reaction (PCR) product of Mucin-270 gene from DNA extracted from non-transfected cells (Mock), w.t. cells transiently transfected (Transient), or cells with the Mucin-270 gene incorporated in the genome and cultured for 2 months (2 mo.) or 12 days (12 d) after gentamycin selection. Star indicates the predicted molecular weight of Mucin-270 PCR product. #1 and #2 are biological replicates. Mean and S.D. shown, ns – not significant.

4.4.2 Biopolymer coatings reduced cell aggregation

After establishing our stable populations, we set out to determine if the biopolymer coatings could reduce cell aggregation in suspension cell cultures. Phase contrast images of the cell lines qualitatively showed more cell aggregates in the w.t. and Mucin-0 cell lines than in the Mucin-135 and Mucin-270 lines (Fig. 4.3A). Quantification of the fraction of single cells in the sample showed an increase in the percent of single cells for the Mucin-135 and Mucin-270 coatings compared to the w.t. cells, while the Mucin-0 line showed no difference compared to w.t. cells (Fig. 4.3B and 4.S1A). Correspondingly, w.t. and Mucin-

0 coated cell lines were much more likely to form clusters of two or more cells than Mucin-135 or Mucin-270 cell lines (Fig. 4.3C and 4.S1B).

Inspection of phase contrast images of our 293-F lines engineered with Mucin-135 or Mucin-270 revealed that the majority of cells were singlets or doublets with few detectable higher order aggregates (Fig. 4.3B). Because of the absence of higher order aggregates, we reasoned that the doublets in the Mucin-135 and Mucin-270 samples may be actively dividing cells or cells that have yet to fully disassociate following cytokinesis. The appearance of doublets can also result from single cells randomly settling out of suspension too near each other to resolve in the 2D plane of the image formed on our microscope. To approximate the frequency of single cells which could randomly settle out of suspension in such a way, we created a simulated dataset of randomly placed centroids and conducted our clustering analysis. On average, the simulated centroids would be counted as singlets 66% of the time. By comparison, 57% of the Mucin-270 cells were singlets (Fig. 4.3B).

To quantify the extent of cell clustering, we analyzed the spatial distribution of cells in the image using the Ripley's K function, a spatial distribution statistic that counts the frequency at which neighboring particles are found within a given distance of any given particle. Using this statistical tool, we observed that the Mucin-135 and Mucin-270 biopolymers show decreased clustering compared to the w.t. and Mucin-0 cell lines (Fig. 4.3D and 4.S1C).

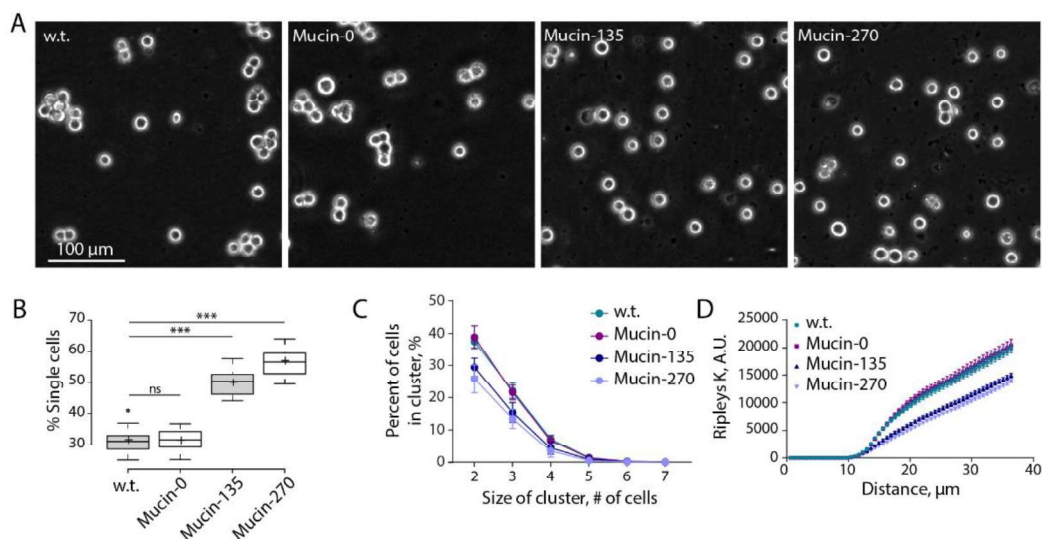


Figure 4.3 – Biopolymer coatings reduced cell aggregation. Genetically-encoded biopolymer coatings of Mucin-135 and Mucin-270 size reduce cell aggregation in suspension cell culture. **A**, Representative phase contrast images for w.t. and biopolymer cell lines. Images were for cells grown at a concentration of $3.8 \pm 0.7 \times 10^6$ cells/mL at 72 hr post-induction. **B**, Quantification of the fraction of cells in various cluster sizes from phase contrast images such as those shown in (A), 3 biological replicate samples, 2 technical replicate samples, 3 images analyzed per sample, samples (further discussion of replicates in Materials and Methods section). Center lines show the medians; box limits indicate the 25th and 75th percentiles as determined by R software; whiskers extend 1.5 times the interquartile range from the 25th and 75th percentiles, outliers are represented by dots; crosses represent sample means. **C**, Quantification of the fraction of cells which are in clusters of various sizes from phase contrast images such as those shown in (A). Mean and S.D. are shown. **D**, Ripley's K function versus distance calculated for the cell distribution acquired from phase contrast images such as those shown in (A). Mean and S.E.M. are shown, replicates described in (B). ns – not significant; * $p < 0.05$; ** $p < 0.01$; *** $p < 0.005$.

4.4.3 Mucin-270 coatings outperformed commercially available anti-clumping agent

We found that the Mucin-270 biopolymer coating could reduce cell aggregation even in extreme pro-clumping conditions. Suspension adapted cell

lines have previously been shown to significantly aggregate under specific media conditions, such as high calcium concentrations that are known to promote engagement of cadherins (Dee et al., 1997; Han et al., 2006; Kim et al., 2011; Meissner et al., 2001; Peshwa et al., 1993; Sjaastad and Nelson, 1997; Tolbert et al., 1980; Yamamoto et al., 2000; Zanghi et al., 2000). When cultured in high calcium conditions (2 mM CaCl₂), the Mucin-270 biopolymer coated cells showed qualitatively less aggregation than w.t. cells (Fig. 4.4A). Notably, cultures with Mucin-270 biopolymer coatings retained their turbidity in the pro-clumping conditions, whereas unmodified cells assembled into large clusters easily visible to the naked eye (Fig. 4.4A). Mucin-270-coated cells show a slight decrease in concentration of cells in suspension upon calcium treatment while w.t. cells have essentially no cells remaining in suspension (Fig. 4.4B).

Further, the Mucin-270 coating outperforms a commercially available anti-clumping agent in highly aggregating conditions. Under high calcium conditions, anti-clumping agent had no discernable efficacy in mitigating cell clumping (Fig. 4.4A). Addition of commercial anti-clumping agent to Mucin-270 coated cells did not further enhance their resistance to clumping in our assays (Fig. 4.4B). Together, these results demonstrated the ability of our genetically-encoded biopolymer coatings to reduce cell aggregation in suspension.

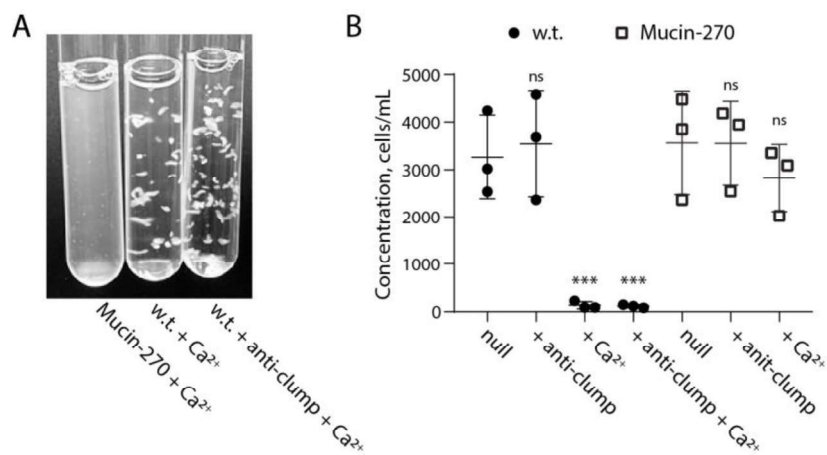


Figure 4.4 – Mucin-270 reduced aggregation in high calcium culture media. The Mucin-270 cell line out-performs commercial anti-clumping solution in highly aggregating conditions. **A**, Image of Mucin-270 and w.t. cultures grown in media with 2 mM CaCl₂ (+ Ca²⁺). Mucin-270 expression significantly decreases cell aggregation, even compared to commercially available anti-clumping reagent (+ anti-clump). **B**, Quantification of the concentration of w.t. or Mucin-270-expressing cells in suspension for control cultures with no treatment (null), with the addition of commercial anti-clumping reagent (+ anti-clump), with the addition of 2 mM CaCl₂ (+ Ca²⁺), or with both anti-clumping reagent and 2 mM CaCl₂ (+ anti-clump + Ca²⁺). Statistical comparison is to null condition for each cell line. Mean and S.D. are shown, n = 3. ns – not significant; * p < 0.05; ** p < 0.01; *** p < 0.005.

4.4.4 Biopolymer coatings provided resistance to shear stress

The sensitivity of suspension-adapted mammalian cells to shear stresses imposes a limit on the rate of mixing and mass transfer in typical bioreactors (Hu et al., 2011). Large volume bioreactors operated at high-cell densities require increased mixing to overcome mass transfer limitations (Hu et al., 2011). Thus, cellular sensitivity to shear places another limit on bioreactor productivity. Because protection of ductal epithelial cells to shear stress is a physiological function of mucins, we considered whether, as an added benefit, our biopolymer coatings might protect cells from shear stresses. To test this

possibility, suspended cells were sheared by passage through a narrow constriction and then analyzed for viability after reintroduction into culture (Fig. 4.5A). A 1 kg mass was applied to a vertically-oriented syringe to generate a constant and controlled pressure that drove the flow of suspended cells through a 7.6 cm length of 500 μm diameter Teflon tubing. Cell death was analyzed by flow cytometry using a live/dead cell stain. We found that the Mucin-135 and Mucin-270 biopolymer-coated cell lines had significantly greater viability after shearing compared to both w.t. and Mucin-0 cell lines (Fig. 4.5B), suggesting that the mucin coatings could allow for higher mixing rates in the bioreactor, although this possibility was not directly tested.

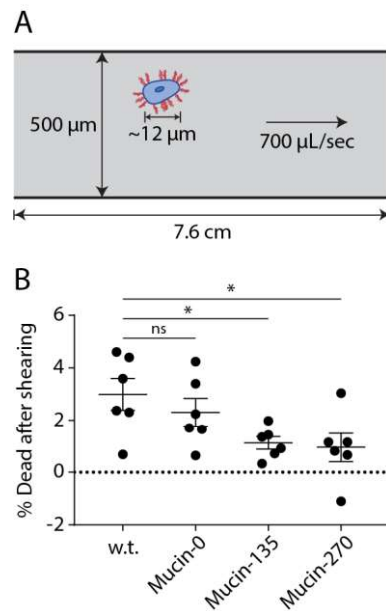


Figure 4.5 – Biopolymer coating enhanced resistance to shear stresses. Expression of the stably incorporated biopolymers protects cells from shear stresses. **A**, Schematic representation of the experimental setup for shearing cells. Briefly, cells were sheared by flowing through a 500 μm Teflon tube under a constant applied force of 1 kg in gravity before being analyzed by flow cytometry with a live/dead cell stain. **B**, Quantification of the fraction of dead cells after shearing the cells for the w.t. and biopolymer cell lines, Mean and

S.E.M. are shown, > 50,000 cells measured for each population, n = 6. ns – not significant; * p < 0.05; ** p < 0.01; *** p < 0.005.

4.4.5 Biopolymer coated cell lines can be transiently transfected and produced comparable levels of recombinant protein

We noted that the use of transient transfection of cells for recombinant protein production has recently become of interest to avoid the long development times associated with selection and isolation of stable cell lines for production of new pharmaceuticals (Derouazi et al., 2004; Durocher et al., 2002; Swiech et al., 2011). Given the potential barrier effect of a mucopolysaccharide coating on the cell surface, we tested whether expression of our biopolymers would affect transfection efficiency of the cell lines. To test, we transiently transfected our cell lines with a plasmid for expression of cytoplasmic red-fluorescent protein. We observed no statistically significant difference in the transfection efficiency of the Mucin-0, Mucin-135, or Mucin-270 cell lines compared to the w.t. cells (Fig. 4.6A). Single-cell analysis revealed similar distributions of recombinant protein production across the engineered and parental cell populations (Fig. 4.6B). Further, there is no significant difference in the RFP signal of transfected cells, indicating comparable expression of transiently transfected proteins in the different cell lines (Fig. 4.6C). We also tested the performance of our engineered cells for production of secreted recombinant proteins. As a test case, we fused a signal peptide to the fluorescent protein, mScarlet-I, and measured production of the secreted protein in medium supernatant from transiently transfected cultures. Mucin-270 coated cells produced the same quantities of secreted recombinant protein as w.t. cells (Fig. 4.7). We concluded that the biopolymer coatings did not adversely affect transfection efficiency and high protein production rate of the 293-F cell system.

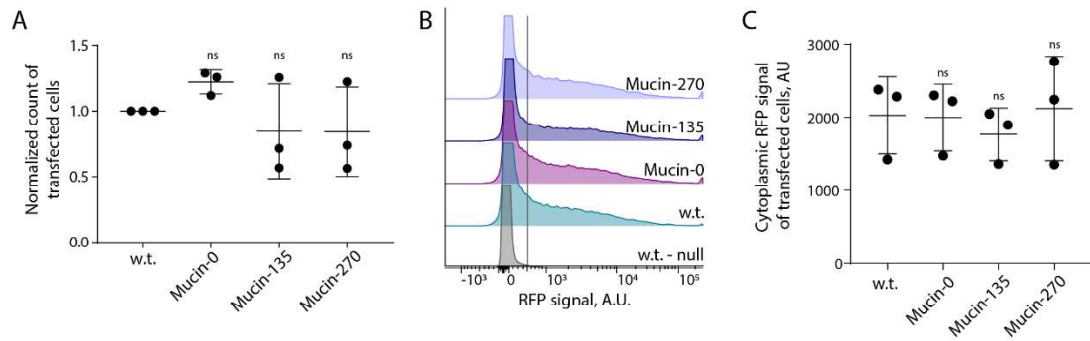


Figure 4.6 – Biopolymer coated cells can be transfected. Transfection was determined for the biopolymer coated cell lines by transfection with a cytoplasmic red-fluorescent protein (RFP). **A**, Quantification of the number of cells for w.t. and biopolymer coated cells transiently transfected with cytoplasmic RFP. The count of transfected cells was normalized to the count of w.t. cells transfected per experiment to account for variable transfection efficiency between replicate transfections. > 50,000 cells measured for each population, $n = 3$. **B**, Representative flow cytometry histogram showing the distribution of expression among transfected cell populations. The peak to the left of the gray line, centered around zero, represented the non-transfected population for each cell line which is further validated by the overlapping histogram of non-transfected w.t. cells (w.t.-null). **C**, Quantification of the geometric mean of RFP for positively transfected cells from B. Mean and S.D. shown, ns – not significant; * $p < 0.05$; ** $p < 0.01$; *** $p < 0.005$.

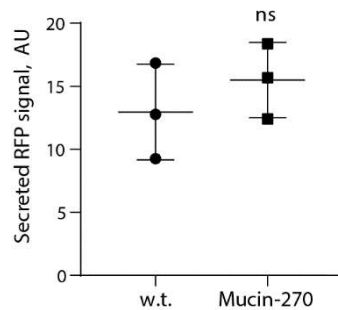


Figure 4.7 – Mucin-270 cells produced comparable levels of recombinant protein expression. Quantification of secreted, recombinant RFP from media supernatant of w.t. or Mucin-270-expressing cultures transiently transfected with secreted RFP, $n = 3$. Mean and S.D. shown, ns – not significant; * $p < 0.05$; ** $p < 0.01$; *** $p < 0.005$.

4.5 DISCUSSION

The expression of engineered biopolymer coatings shows promise as a technology for improved suspension cell culture for bio-manufacturing applications. In this work, we have shown that established cell lines can be genetically modified to express engineered mucin biopolymers for anti-adhesion. Expression of these biopolymers does not negatively impact the desirable characteristics of 293-F cells, including their fast proliferation rates (Fig. 4.1E) and high transfection efficiencies (Fig. 4.6A, B). Moreover, the expression of the biopolymers significantly reduces undesirable cell clumping (Fig. 4.3, 4.4, and 4.S1) and enhances resistance of the cells to shear forces (Fig. 4.5). Our Mucin-135 coating and thicker Mucin-270 coatings performed similarly in head-to-head tests and should be equally well-suited for the applications investigated in this work.

Our biopolymer coatings provide a significant reduction of cell aggregation in serum-free media formulations that are typically used for production in bioreactor formulations. Notably, our coatings could reduce aggregation further even in media formulations that were designed to minimize cell clumping (e.g. Invitrogen Freestyle 293-F media). Future studies could consider the effect of biopolymer expression on cell aggregation in media formulations that have historically been avoided due to issues of cell aggregation. For example, highly efficient transient transfections have long been performed with DNA-calcium phosphate precipitates (Jordan and Wurm, 2004). However, at the high calcium concentrations required, 293-F cells are known to form large cell aggregates (Meissner et al., 2001; Peshwa et al., 1993). Based on our results (Fig. 4.4), use of the Mucin-135 or Mucin-270 coatings significantly reduce cell aggregation in such conditions for improved protein

production from transiently transfected cultures.

Further refinement of the mucin coating technology may be achieved through additional optimization of the engineered mucins and their regulated expression. Notably, excessive over-production of highly glycosylated mucin-like proteins could possibly compete with recombinant glycoproteins for the cellular glycosylation machinery and the nucleotide sugar building blocks of glycans. Shedding of the engineered mucins from the cell surface is mitigated by our choice of membrane anchor, which lacks a proteolytic cleavage site. Nevertheless, mucin shedding from highly over-expressed surface coatings is a possibility that could present challenges during downstream product purification. Cellular clones for production should be isolated that provide the desired performance enhancements of the mucin coatings, while avoiding over-expression, which could affect downstream sample processing or compromise cellular growth, recombinant product quality, and overall productivity if too many cellular resources are dedicated to coating synthesis.

The mucin technology coating was originally conceived as a solution for suspension-adapted suspension systems that tend to aggregate in the bioreactor. However, the ability of our coatings to protect cells and strongly resist clumping could also benefit current bio-manufacturing platforms, like CHO cells, which can still aggregate under non-ideal reactor conditions or in non-optimal media formulations. As bio-manufacturing looks beyond CHO systems for next-generation production platforms that mitigate the risk of non-human glyco-conjugates and other antigenic epitopes, adaptation to growth in suspension remains a significant and time-consuming challenge for human, primate, and many other mammalian cell lines (Amaral et al., 2016; Rodrigues et al., 2013). By promoting cell viability and minimizing aggregation, our

coatings could help overcome some of the significant barriers to suspension adaptation.

Taken together, our work presents a mucin coating technology for improved single-cell growth of cells in suspension. Despite testing a relatively small number of mucin coatings, the system was largely successful in the primary goal of mitigating cell aggregation. Through future refinement and validation, the coating technology has potential as a viable solution for biomanufacturing with cellular production systems that have desirable features, but currently remain difficult to deploy in industrial practice due to poor single-cell growth behavior in suspension.

4.6 ACKNOWLEDGEMENTS

We thank V. Weaver and J. Lakins for transposon plasmids. We thank Jin Su for performing gene stability PCR experiments. This investigation was supported by the National Institute of General Medicine Sciences Ruth L. Kirschstein National Research Service Award 2T32GM008267 (C.R.S.), Knight Family Foundation Graduate Research Fellowship in Nanoscience and Technology (C.R.S.), Samuel C. Fleming Family Graduate Fellowship (C.R.S.), National Institute of Health New Innovator DP2 GM229133 (M.J.P.) and National Cancer Institute U54 CA210184 (M.J.P.) and R33-CA193043 (M.J.P.). Flow cytometry was carried out at the Cornell University Biotechnology Resource Center.

4.6.1 Complete author list

Carolyn R. Shurer[†], Shelby E. Head[†], Marc C. Goudge, and Matthew J. Paszek

[†]These authors contributed equally to this work.

4.6.2 Author contributions

M.J.P. and C.R.S. managed the project. C.R.S. and S.E.H. prepared transposon-based vectors and stable cell lines. C.R.S. and S.E.H. conducted imaging, flow cytometry, shear, and cell clumping experiments. M.C.G. conducted recombinant protein production analysis. All authors contributed to the analysis of data and preparation of the manuscript.

4.6.3 Competing interests

The authors declare a potential financial interest due to a pending patent on the biopolymer sequences.

4.7 SUPPORTING FIGURE

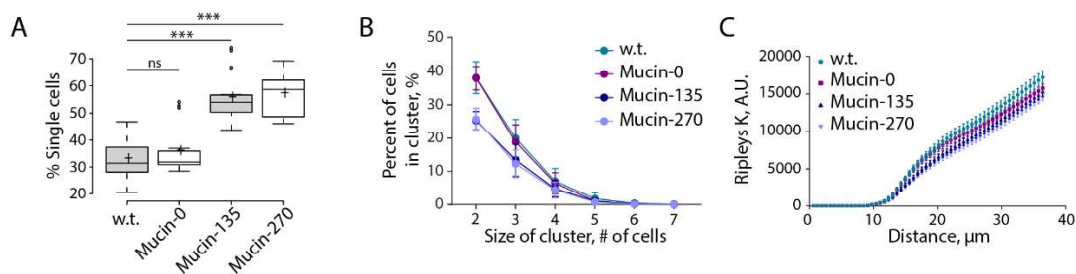


Figure 4.S1 – Additional data to accompany Figure 4.3 acquired 24 h prior. **A**, Quantification of the fraction of cells in various cluster sizes from phase contrast images such as those shown in Fig. 4.3A. Cells are grown at $3.2 \pm 0.7 \times 10^6$ cells/mL for 48 hr for all panels. Center lines show the medians; box limits indicate the 25th and 75th percentiles as determined by R software; whiskers extend 1.5 times the interquartile range from the 25th and 75th percentiles, outliers are represented by dots; crosses represent sample means. **B**, Quantification of the fraction of cells which are in clusters of various sizes from phase contrast images such as those shown in Fig. 4.3A. Mean and S.D. are shown. **C**, Ripley's K function versus distance calculated for the cell distribution acquired from phase contrast images such as those shown in Fig. 4.3A. Mean and S.E.M. are shown, replicates described in Fig. 4.3B, $n = 3$. ns – not significant; * $p < 0.05$; ** $p < 0.01$; *** $p < 0.005$.

CHAPTER 5

PHYSICAL PRINCIPLES OF MEMBRANE SHAPE REGULATION BY THE GLYCOCAYLX^{1,2}

5.1 SUMMARY

Cells bend their plasma membranes into highly curved forms to interact with the local environment, but how shape generation is regulated is not fully resolved. Here we report a synergy between shape-generating processes in the cell interior and the external organization and composition of the cell-surface glycocalyx. Mucin biopolymers and long-chain polysaccharides within the glycocalyx can generate entropic forces that favor or disfavor the projection of spherical and finger-like extensions from the cell surface. A polymer brush model of the glycocalyx successfully predicts the effects of polymer size and cell-surface density on membrane morphologies. Specific glycocalyx compositions can also induce plasma membrane instabilities to generate more exotic undulating and pearled membrane structures and drive secretion of extracellular vesicles. Together, our results suggest a fundamental role for the glycocalyx in regulating curved membrane features that serve in communication between cells and with the extracellular matrix.

5.2 INTRODUCTION

Tubular and spherical extensions of the plasma membrane play vital

¹This work was originally published in *Cell* and has been reproduced here under the author's rights policy of Cell Press. Shurer, C.R., Kuo J.C.H, Roberts, L.M., Gandhi, J., Colville, M.J., Enoki, T.A., Pan, H., Su, J., Noble, J.M., Hollander, M.J., O'Donnell, J.P., Yin, R., Pedram, K., Möckl, L., Kourkoutis, L.F., Moerner, W.E., Bertozzi, C.R., Feigenson, G.W., Reesink, H.L., and Paszek, M.J. (2019). Physical Principles of Membrane Shape Regulation by the Glycocalyx. *Cell*. <https://doi.org/10.1016/j.cell.2019.04.017>

²C.R.S. prepared the cDNA and guide RNA vectors, conducted fluorescence microscopy, flow cytometry analysis and cell sorting, and produced recombinant Muc1. See sections 5.5.1 and 5.5.2 for a complete author list and specific author contributions.

roles in human development and everyday cellular functions. While curved membrane protrusions have long been recognized to increase cell-surface area for secretion, absorption, and receptor-mediated communication, modern research has provided compelling examples of more diverse and sophisticated functionalities (Marshall, 2012). For instance, T-cells of the adaptive immune system generate a high density of tubular microvilli to engage antigen presenting cells, and such structures may be similarly important for the recognition of tumor cells by engineered immune cell therapies (D'Aloia et al., 2018; Jung et al., 2016). Membrane projections also enable cell-to-cell communication over long ranges and at precise three-dimensional locations in tissues. During development, long and thin membrane projections called cytonemes pinpoint delivery of morphogens from 'sender' cells to specific 'receiver' cells up to 40-microns away (Bischoff et al., 2013; Kornberg and Roy, 2014). Stem cells, immune cells, and many other cell types are also known to bend their plasma membranes into spherical microvesicles that can deliver macromolecular cargoes over long distances (Tricarico et al., 2017). Curved membrane features also enable physical communication and cell behaviors, such as migration. For example, spherical membrane expansions called blebs are generated by primordial germ cells, tumor cells, and other cell types for protrusion and frictional coupling with the tissue matrix during migration (Paluch and Raz, 2013).

Deregulation of membrane-shape generating processes can contribute directly to disease progression. As a notable example, tumor cells frequently extend thin, tubular structures, including microvilli for dynamic adhesion in the vasculature and tunneling nanotubes for long-rang intercellular communication with the stroma (Kramer and Nicolson, 1979; Liu et al., 2018;

Lou et al., 2012). Aggressive tumor cells also tend to generate microvesicles at high frequencies and project spherical blebs for migration (Antonyak et al., 2011; Becker et al., 2016; Bergert et al., 2015; Friedl and Wolf, 2010). Cargoes carried by tumor microvesicles are now recognized to have diverse modulatory roles, including reprogramming of other cell types in the stroma and the preparation of distant metastatic niches for colonization (Becker et al., 2016).

Forces originating from cytoskeletal dynamics are posited to generate membrane curvature for the diverse spherical and tubular structures on the cell surface. Polymerizing cytoskeletal filaments are envisioned to push out at discrete points along the plasma membrane for extension of microvilli, cilia, filapodia and other finger-like projections (Footer et al., 2007; Gupton and Gertler, 2007; Mogilner and Rubinstein, 2005; Peskin et al., 1993). Moreover, contraction of the cytoskeleton generates the hydrostatic pressure for spherical expansion of the membrane during bleb formation (Charras et al., 2005). The physical dynamics that bend sub-regions of the plasma membrane into microvesicles remain poorly understood; however, reports have implicated the actin cytoskeleton in their biogenesis (Tricarico et al., 2017).

While the cell-surface glycocalyx is not featured in canonical models of membrane shape regulation, correlations abound between glycocalyx composition and cell-surface morphology in both normal and disease states. In normal cell physiology, polypeptide and sugar co-polymers called mucins are frequently anchored at high densities on the surfaces of epithelial microvilli (Hattrup and Gendler, 2008; Kesavan et al., 2009; Kesimer et al., 2013), cilia (Button et al., 2012), and filapodia (Bennett Jr. et al., 2001); hyaluronan polymers densely coat the microvilli of oocytes and mesothelium (Evanko et al., 2007; Makabe, S. et al., 2006); and long chains of sialic acid and hyaluronan decorate

the highly curved surfaces of neuronal axons (Fowke et al., 2017; van den Pol and Kim, 1993; Zhang et al., 1992). T-cells and dendritic cells express cell-surface mucins upon activation or maturation, which coincides with often dramatic changes in membrane tubularization and microvilli generation (Agrawal et al., 1998; Cloosen et al., 2004; Jung et al., 2016; Pilon et al., 2009). Aggressive tumor cells frequently produce an abundance of mucins and hyaluronan on their cell surface (Kufe, 2009; Turley et al., 2016), and the expression of these polymers has been anecdotally linked to their unique membrane features, such as extensive microvilli (Polefka et al., 1984). Mucins and hyaluronan polymers are also densely arrayed on the surfaces of enterocytes, reactive astrocytes, dendritic cells, and tumor cells that are known to secrete high levels of microvesicles (Cloosen et al., 2004; Gangoda et al., 2015; McConnell et al., 2009; Paszek et al., 2014; Pelaseyed et al., 2014; Tricarico et al., 2017). While the ubiquity of these correlations suggests a possible causal relationship between glycocalyx polymer composition and plasma membrane morphologies, a specific mechanism of action has not been delineated.

Mucins and long-chain polysaccharides are anchored to the membrane in such a way that long polymer chains or loops are expected to extend from the cell surface (Hattrup and Gendler, 2008; Lee et al., 1993). The ensemble resembles a well-studied structure in polymer physics called a brush, where polymers are grafted on one end to a surface (Chen et al., 2017). Polymer brush theory has long recognized that steric interactions in a densely crowded brush restrict the number of molecular configurations each polymer can explore, thereby increasing the free energy of the system through reduced entropy (de Gennes, 1980). Similar to the thermodynamic basis of gas pressure, the entropic penalty associated with molecular crowding can generate pressure on the

anchoring surface (Hiergeist and Lipowsky, 1996; Lipowsky, 1995; Stachowiak et al., 2012). Experimental studies with synthetic polymers have confirmed that the pressures generated by these unstructured macromolecules is sufficient to deform flexible lipid membranes (Busch et al., 2015; Evans and Rawicz, 1997; Hansen et al., 2003; Kenworthy et al., 1995). However, whether biopolymers in the glycocalyx might regulate plasma membrane morphologies through a similar mechanism remains largely untested.

5.3 RESULTS

5.3.1 Glycocalyx polymers and membrane morphology

Guided by the framework of polymer brush theory, we hypothesized that glycocalyx polymers may generate an entropic bending force to favor the formation of specific membrane forms. As a corollary to this hypothesis, we envisioned that emergent membrane structures could be tuned through rational manipulation of the glycocalyx.

To test these hypotheses, we evaluated a genetically encoded library of native, semi-synthetic, and rationally designed mucin polymers of varying size, backbone sequence, and membrane anchorage (Fig. 5.1A). Polymers considered included the 42 native tandem repeats (TR) of Mucin-1 (Muc1-42TR), the serine and threonine-rich polymer domain of Podocalyxin (Podxl; S/T-Rich), and a new synthetic mucin that we rationally designed based on a consensus mucin O-glycosylation sequence, PASTSAPGA (Rational) (Fig. 5.1A).

Each polymer domain was fused to the native Muc1 transmembrane anchor with the cytoplasmic tail deleted (Δ CT) or the native mucin transmembrane anchor with a membrane proximal green fluorescent protein for imaging (GFP- Δ CT; Fig. 5.1A). The cytoplasmic tails of the native membrane

anchors were deleted to limit intracellular signal transduction by the mucins. We also created mucin chimeras with a synthetic 21-amino acid transmembrane domain (TM21) to rule out that any observed effects of mucin expression could be attributed to the native mucin transmembrane domain and membrane proximal sequences (Fig. 5.1A). Each mucin expressed well on the cell surface (Fig. 5.S1A-C). The mucin polymer backbones were heavily glycosylated with O-linked sugar side chains to form the bottlebrush molecular structures that define mucins (Fig. 5.S1B, C).

When expressed at high levels on the epithelial cell-surface, each of the long-chain mucins triggered a dramatic tubularization of the plasma membrane, as observed by scanning electron microscopy (SEM; Fig. 5.1B, C). The phenotype was observed whether the mucin polymers were tethered to the membrane by a native-mucin transmembrane domain or synthetic membrane anchor (Fig. 5.1B, C; Compare Δ CT, GFP- Δ CT, and TM21). All of the mucin polymer domains were expected to be unstructured due to their high proline content and densely clustered serine and threonine sites for O-glycosylation. To test whether a more rigid, folded protein construct of comparable size to the mucins could induce a similar phenotype, we created a chimeric glycoprotein through fusion of the native Muc1 transmembrane anchor with repeating units of highly stable, EGF-like motifs from the ectodomain of human Notch1 (Kovall et al., 2017; Weissshuhn et al., 2016). Although the expressed Notch1 chimera was similar in molecular weight to fully glycosylated Muc1, the glycoprotein was ineffective at inducing membrane tubularization (Fig. 5.1B, C, and S1B). We confirmed that our various mucin constructs and Notch1 chimera were all expressed at similar levels on the cell surface, ruling out that the differences could be explained by differential expression of the constructs (Fig. 5.S1C).

We tested whether enzymatic digestion of the mucin-rich glycocalyx would destabilize the curved membrane features and revert tubularization. Live Muc1-42TR Δ CT expressing cell cultures were treated for 2 h with a specific mucin backbone-digesting enzyme called secreted protease of C1 esterase inhibitor (StcE) from enterohemorrhagic *E. coli* (Malaker et al., 2018). Metabolic incorporation with N-azidoacetylgalactosamine (GalNAz) followed by Cu-click was used to fluorescently label O-glycans, and oxidation with mild periodate followed by hydroxylamine conjugation was used to label sialic acids of mucins and other glyco-conjugates. Cells were then fixed and subjected to single molecule localization microscopy, which enabled resolution of nanoscale-membrane morphologies (Möckl et al., 2018). Residual sialic acid derived fluorescent signal revealed that the tubulated morphology of Muc1-42TR Δ CT expressing cells was lost after mucin digestion (Fig. 5.1D). We concluded that the tubulated membrane morphologies were reversible, and mucin on the cell surface was required for maintenance of the highly curved membrane features.

The rapid reversibility of the membrane morphologies argued against excess membrane surface area as the underlying mechanism through which glycocalyx biopolymers exert control over cell-surface shapes. As an additional control, we conducted a standard transferrin-receptor internalization assay to evaluate the effects of mucin expression on endocytosis and recycling, which are key mechanisms of plasma membrane area regulation in cells. We found that Muc1 expression did not have a significant effect on transferrin endocytosis (Fig. 5.S1D, E). We also found that mucin glycocalyx biopolymers could induce spontaneous curvature in model membrane systems that lack the machinery for active regulation of surface area and surface tension. Notably, the S/T-rich

polymer domain of Podxl triggered spontaneous generation of spherical and tubular membrane structures when anchored to the surface of giant unilamellar vesicles (GUVs) (Fig. 5.1E and 5.S1F).

The tubularization phenomenon observed in cells was relatively insensitive to the length of the mucin polymer domain, provided that the polymers were expressed on the cell surface at moderate to high densities. We explored this through cDNAs for 0, 10, or 42 Muc1 tandem repeats that were fused with a GFP-tagged transmembrane anchor to encode cell-surface mucins with expected contour lengths of 0, 65, and 270 nm, respectively (Fig. 5.1F and 5.S1G). Cell lines expressing the constructs were sorted into populations with similar mucin surface densities using a nanobody that probed the GFP tag of cell surface mucins (Fig. 5.1F). The mucin polymer domain was required for efficient membrane tubularization. Both 10- and 42-TR mucins induced significantly more plasma membrane tubules than the construct with 0 TRs (Fig. 5.1G, H). We compared cells of similar spread area to rule out the possibility that changes in membrane surface tension and other effects associated with cell spreading could explain the morphological differences (Fig. 5.1G).

Similar to our observations with mucins, we found that a glycocalyx rich in large, linear polysaccharides could also trigger dramatic changes in plasma membrane morphology. Notably, hyaluronic acid synthase 3 (HAS3) expression increased the density of high molecular weight hyaluronic acid (HA) polymers on the cell surface and led to the protrusion of many finger-like membrane extensions (Fig. 5.S1H-K), consistent with prior observations (Koistinen et al., 2015). Together, these results suggested that diverse glycocalyx polymer types and sizes might influence cell morphological states.

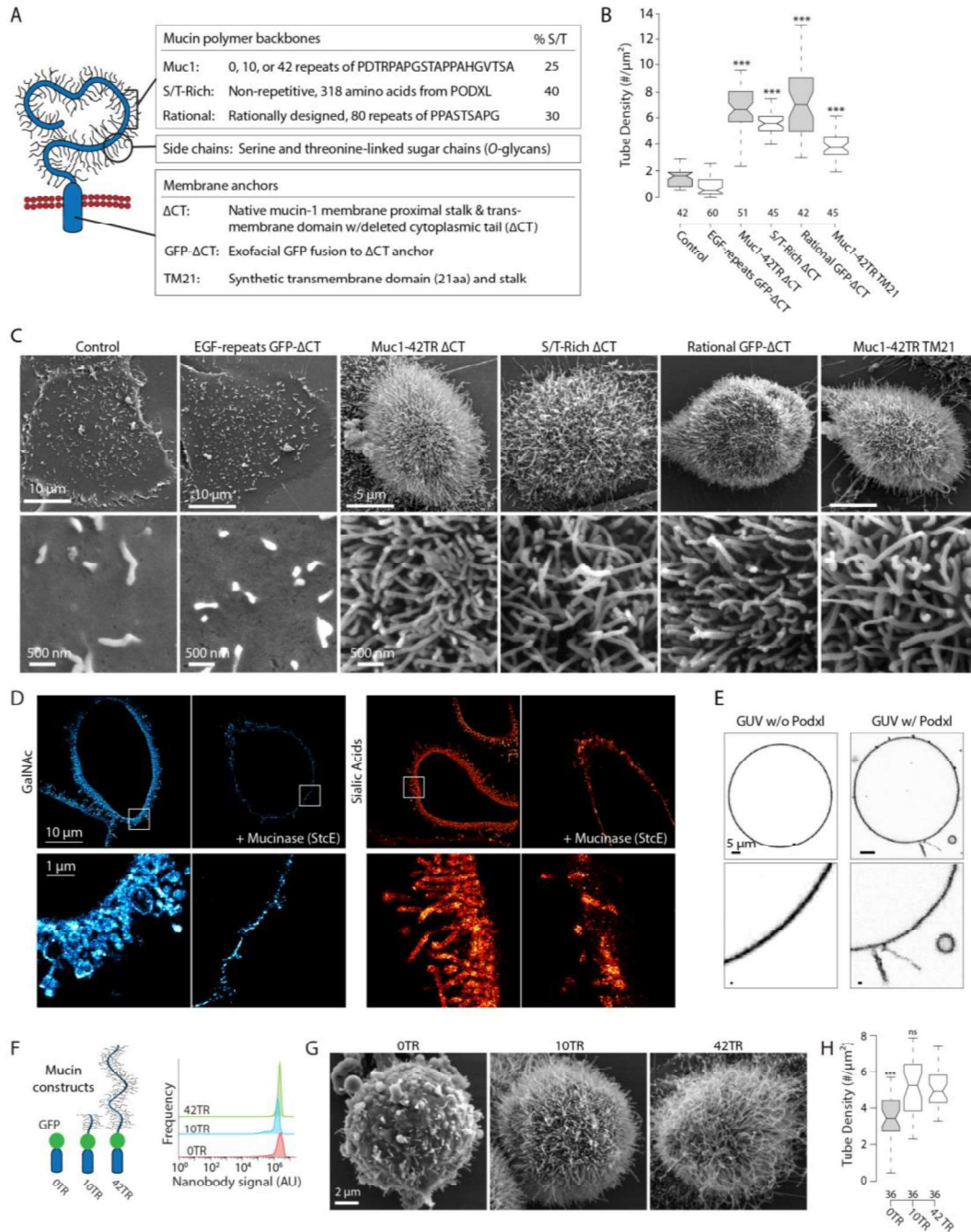


Figure 5.1 – Flexible glycocalyx polymers induce membrane projections. See also Figure 5.S1. **A**, Schematic and table illustrating the genetically encoded biopolymers that were constructed and used throughout this work. The gene library encoded native and synthetic mucins comprised of a central polypeptide core, sugar side chains linked to serine (S) and threonine (T) residues, and a transmembrane anchor. **B**, Quantification of membrane tube density in

epithelial cells. Mucin polymers induce dramatic tubularization compared to wild-type (Control) cells and compared to a similarly sized biopolymer composed of EGF-like repeats from Notch1 and the Muc1 transmembrane anchor with GFP reporter (EGF-repeats GFP- Δ CT) cells. Number of cells analyzed is shown on the x-axis for each condition. Box notches here and elsewhere indicate 95% confidence intervals. **C**, Scanning electron microscopy (SEM) images showing membrane morphologies of cells expressing the indicated biopolymer. **D**, Metabolically labelled glycans and membrane morphologies resolved with single molecule localization microscopy in Muc1-42TR Δ CT expressing cells before and after mucin backbone digestion with the StcE mucinase. Images are shown as 2D color-coded histograms of localizations with 32 nm bin width. **E**, Representative confocal images of GUVs with and without anchorage of recombinant Podocalyxin. **F**, (left) Cartoons of Muc1-GFP- Δ CT polymers of varying length, as indicated by the number of tandem repeats (TR). (right) Flow cytometry data showing similar cell-surface expression levels of indicated mucins using a GFP-binding nanobody, $n = 3, > 40,000$ cells per population. **G**, Representative SEM images of cells described with varying number of TR. **H**, Quantification membrane tube density for mucin with various TRs, significance compared to 42TR. *** $p < 0.001$, ns – not significant (*post-hoc* student's two-tailed t test).

5.3.2 Mucin expression predicts tumor cell morphologies

We considered whether specific mucin glycan structures were required for the generation or maintenance of the curved membrane morphologies. We abrogated extension of mucin *O*-glycan chains through CRISPR/Cas9 mediated knockout of the Core-1 β 3-T Specific Molecular Chaperone (COSMC), which is required for elongation of the primary *O*-linked, N-acetylgalactosamine monosaccharide into more complex Core *O*-glycans (Fig. 5.2A) (Stolfa et al., 2016; Wang et al., 2010). We also targeted mucin sialylation through knockout of solute carrier family 35 member A1 (SLC35A1), which shuttles activated nucleotide sugars from the cytoplasm into the Golgi for sialic acid addition to glycans (Fig. 5.2A) (Riemersma et al., 2015). The expected glycan perturbations

were confirmed with flow cytometry using the *Vicia villosa* lectin (VVA) to probe non-extended α R-N-acetylgalactosamine, peanut agglutinin (PNA) to probe Core-I glycans, and metabolic labelling with ManNAz to detect sialic acid incorporation (Fig. 5.2A).

Disruption of *O*-glycan extension or sialylation did not block the strong induction of cell-surface tubularization by the Muc1 polymer backbone, although the density of membrane tubes on the cell surface was somewhat reduced compared to wild-type cells expressing the mucin at similar levels (Fig. 5.2B, C). Thus, the mucin backbone and initial α R-N-acetylgalactosamine residues were sufficient for membrane tubularization. We noted that prior studies had found that the structural conformation of mucin biopolymers is largely determined by the initial α R-N-acetylgalactosamine residues of the mucin *O*-glycans (Coltart et al., 2002).

Together, our results suggested that plasma membrane morphologies might be predicted simply by profiling mucins or other biopolymers on the cell surface. We tested this possibility in carcinoma cell lines that are known to have abundant levels of Muc1 in their glycocalyx. In the three tumor cell lines that we tested – human breast cancer T47D, human breast cancer ZR-75-1, and human cervical HeLa – we observed widely varying Muc1 levels across sub-populations in each line (Fig. 5.2D). Notably, in each tumor cell line, sub-populations were present that expressed endogenous Muc1 at comparable or higher levels than in the epithelial cell lines in which we ectopically expressed Muc1 and observed significant changes in membrane morphology (Fig. 5.1B, C, and 5.2D). We sorted each tumor cell line into sub-populations that expressed low or high levels of Muc1 (Fig. 5.2E). Cells sorted for high Muc1 expression showed a significant increase in membrane tube density compared to cells

expressing lower native levels of the mucins (Fig. 5.2F, G). Taken together, the results provided evidence that the well-known prevalence of tubulated features on tumor cells may be linked to perturbation of their glycocalyx (Kolata, 1975).

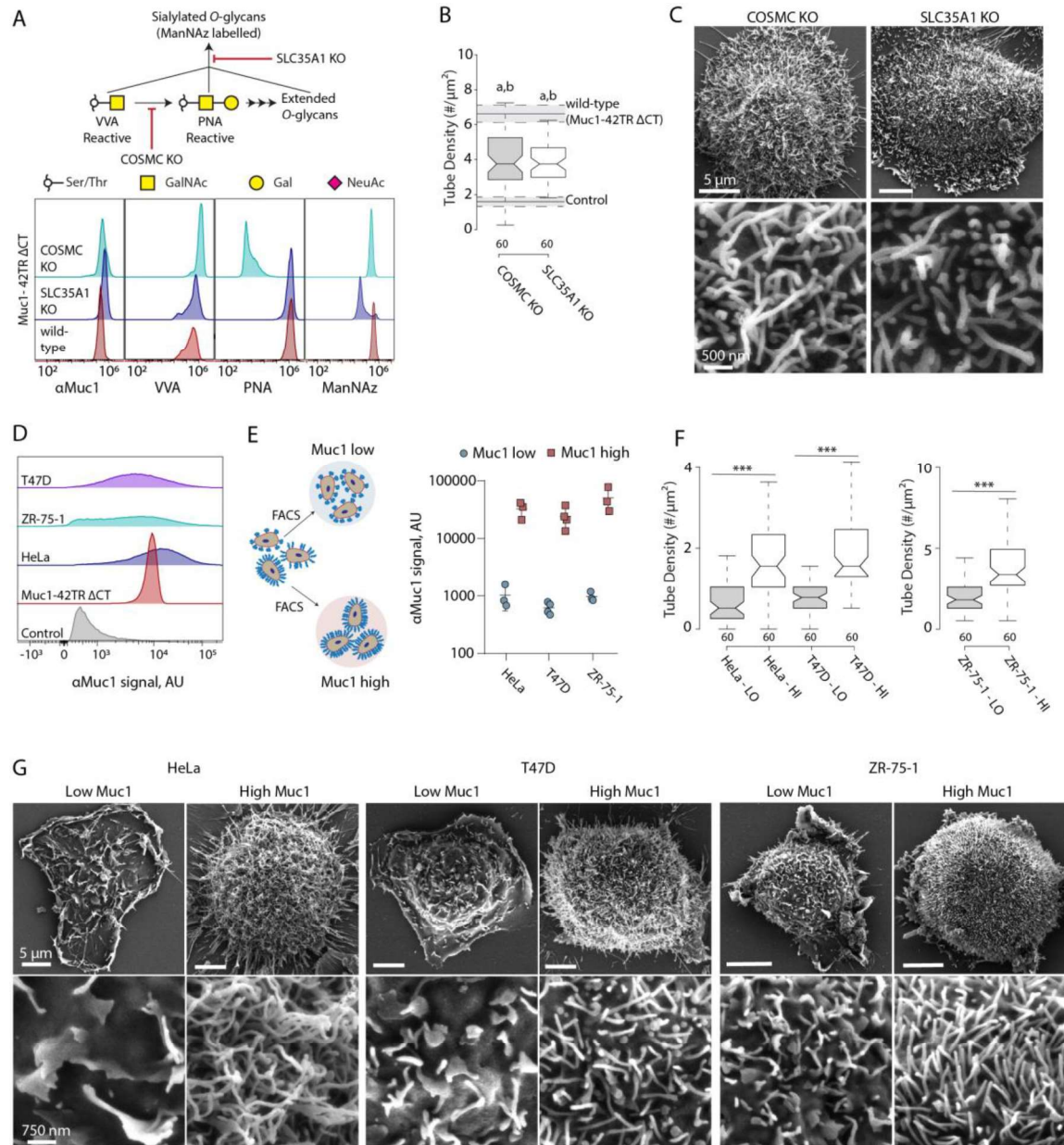


Figure 5.2 – Mucin polymer expression levels predict tumor cell morphologies. A, (top) Illustration of how COSMC and SLC35A1 knockout (KO) effects O-glycan extension, sialylation, and lectin reactivity. (bottom) Flow

cytometry data showing mucin levels, lectin reactivity, and sialylation (ManNAz labelling) of wild-type, COSMC KO and SLC35A1 KO cells expressing Muc1-42TR Δ CT. **B**, Quantification of membrane tube density on COSMC and SLC35A1 KO cells expressing Muc1-42TR Δ CT. For comparison, the mean tube density and 95% confidence intervals from Fig. 5.1B are shown for wild-type cells (Control) and wild-type cells expressing Muc1-42TR Δ CT, significance compared to wild-type cells (Control) ($a = p < 0.001$) and significance compared to wild-type Muc1-42TR Δ CT-expressing cells ($b = p < 0.001$). **C**, SEM images showing the tubulated membrane morphologies of COSMC and SLC35A1 KO cells expressing Muc1-42TR Δ CT. **D**, Representative flow cytometry histogram showing endogenous Muc1 levels on the surface of various cancer cell lines and ectopic Muc1 levels on the surface of Muc1-42TR Δ CT expressing cells, $n = 3$, $> 20,000$ cells per population. **E**, (left) Strategy for sorting tumor cell lines into sub-populations with low and high surface levels of Muc1. (right) Flow cytometry results confirming high and low surface levels on the sorted sub-populations; results presented as the geometric mean of the Muc1 signal across the indicated sub-population. **F**, Quantification of membrane tube density on the sorted sub-populations. **G**, SEM images showing typical membrane morphologies in each sorted sub-population. *** $p < 0.001$ (*post-hoc* student's two-tailed t test).

5.3.3 Specialized cells *in vivo*

Motivated by our observations *in vitro*, we considered whether glycocalyx polymers might play a role in shaping the morphology of specialized cell types *in vivo*. We elected to evaluate synoviocytes, since these secretory cells are known to produce large quantities of HA for joint lubrication and, thus, are expected to display a high density of HA polymers on their surface. We isolated synovial tissues from equine carpus (Fig. 5.3A) and found that primary synoviocytes expressing HAS3 were highly tubulated, but treatment with hyaluronidase (HyA) to degrade HA resulted in the rapid destabilization and disappearance of membrane tubules (Fig. 5.3B, C). We also evaluated synoviocyte morphology in tissues that were freshly extracted and

briefly cultured *ex vivo* (< 1 h). The synoviocytes in native synovial tissue displayed an HA-rich head that appeared highly tubulated and protruded from the tissue matrix (Fig. 5.3D, E). Brief treatment of the tissue with HyA *ex vivo* resulted in a dramatic retraction of synoviocyte tubules, suggesting a role for the glycocalyx in the maintenance of membrane projections *in vivo* (Fig. 5.3E).

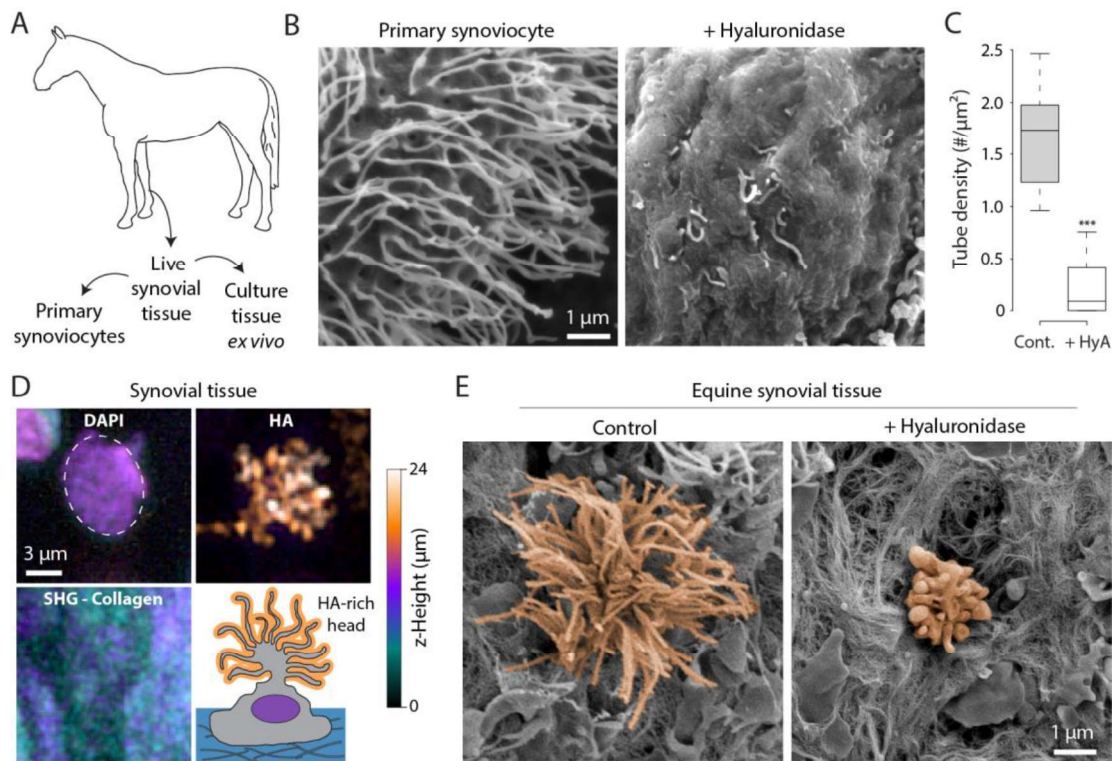


Figure 5.3 – Membrane morphology of tissue synoviocytes is regulated by the glycocalyx. **A**, Experimental workflow for resected equine synovial tissues. **B**, Representative SEM images of hyaluronic acid synthase 3 (HAS3) expressing primary synoviocytes showing retraction of membrane tubules following 30 minutes of hyaluronidase (HyA) treatment to digest hyaluronic acid (HA). **C**, Quantification showing tubule density was dependent on the presence of HA. **D**, Images of freshly resected synovial tissue showing the nucleus (DAPI), surface-anchored HA (hyaluronic acid binding protein, HABP) of a representative synoviocyte, and the tissue collagen (second harmonic generation, SHG). Depth along the z-axis is coded according to the color bar. Note the HA-enriched membrane extensions protruding from the synovial

tissue surface. Lower right panel shows a cartoon representation of the observed tissue synoviocyte. E, Membrane tubules are visible, by SEM, on synoviocytes in freshly excised equine synovial tissue. The synoviocyte head, pseudo-colored in orange, is protruding from the synovial tissue. HyA treatment to digest HA resulted in the rapid retraction of synoviocyte tubules (right). *** $p < 0.001$ (*post-hoc* student's two-tailed *t* test).

5.3.4 Polymer brush framework

To develop a more comprehensive understanding of membrane shape regulation by glycocalyx polymers, we considered whether the observed membrane shapes and their frequencies could be rationalized through the framework of polymer brush theory. We noted that two limiting regimes are classically described in polymer physics for end-grafted polymers: the “mushroom” regime, where polymers at low grafting densities have limited interactions with each other, and the “brush” regime, where crowded polymers can interact sterically and electrostatically with each other to exert larger pressures on the anchoring surface (Milner, 1991) (Fig. 5.4A). For mucins, we expected the transition from the mushroom to brush regime to occur at a surface density where the average distance between the polymers was approximately two times their radius of gyration in solution (Fig. 5.4A).

To measure the radius of gyration and flexibility of individual mucins, we produced recombinant Muc1-42TR with a terminal purification tag in place of its transmembrane anchor (Fig. 5.S2A, B). Size-exclusion chromatography coupled to multi-angle light scattering (SEC-MALS) reported $32 \text{ nm} \pm 0.4\%$ for the mucin radius of gyration in physiological buffer. Based on the estimated Muc1-42TR contour length of approximately 270 nm, we concluded that the mucin had a persistence length of approximately 7.5 nm and adopted the

extended random coil configuration expected for a semi-flexible polymer in solution.

We next asked whether polymer brush theory could capture the physical behavior of mucin ensembles on the cell surface. We tested whether mucins stretch and extend in a predictable manner as they become progressively more crowded, a characteristic physical behavior originally described by Alexander and de Gennes in their seminal theories on polymer brushes (Alexander, 1977; de Gennes, 1980; Milner, 1991). We chose to evaluate mucin extension on actin-containing tubules that resembled microvilli, since the curvature of these structures was highly uniform and essentially independent of the mucin surface density due to the rigid actin cores (Fig. 5.S2C). As such, we could approximate the tubule surface as a rigid cylinder of fixed radius for direct comparison to classical theory. A cDNA for Muc1-42TR with complimentary epitope tags flanking the mucin polymer domain was constructed. Following cellular expression, the encoded tags were labeled with fluorophore-conjugated probes and resolved on microvilli cross-sections using a super-resolution optical technique called expansion microscopy (ExM) (Fig. 5.4B and 5.S2D-F). We found that the mucin extension had an exponential dependence, or 'scaled,' with fluorescence intensity, and hence surface density, with an exponent of 0.48 ± 0.10 (Fig. 5.4B). This value compared well to the theoretically derived power law exponent of between 0.33 and 0.5 for polyelectrolytes grafted on a rigid cylindrical surface at physiological salt concentrations (Zhulina and Borisov, 1996).

Encouraged by these findings, we created a polymer brush model to describe the physical behavior of a mucin-rich glycocalyx assembled on the plasma membrane (see '5.9 Supplemental Note: theoretical considerations' for

full model details). In our model, the entropic pressure contributed by the mucin brush generated a spontaneous membrane curvature that strongly scaled with polymer density and weakly with polymer chain length (Hiergeist and Lipowsky, 1996) (Fig. 5.4C and 5.S3). The weak dependence on polymer length was consistent with our earlier findings that mucins with 10 and 42 repeats had comparable effects on cell-surface morphology despite their 4-fold difference in size (Fig. 5.1G, H and 5.S1G). For 10 and 42 TR mucins, our brush model predicted only a ~20% difference in spontaneous membrane curvature (Fig. 5.S3).

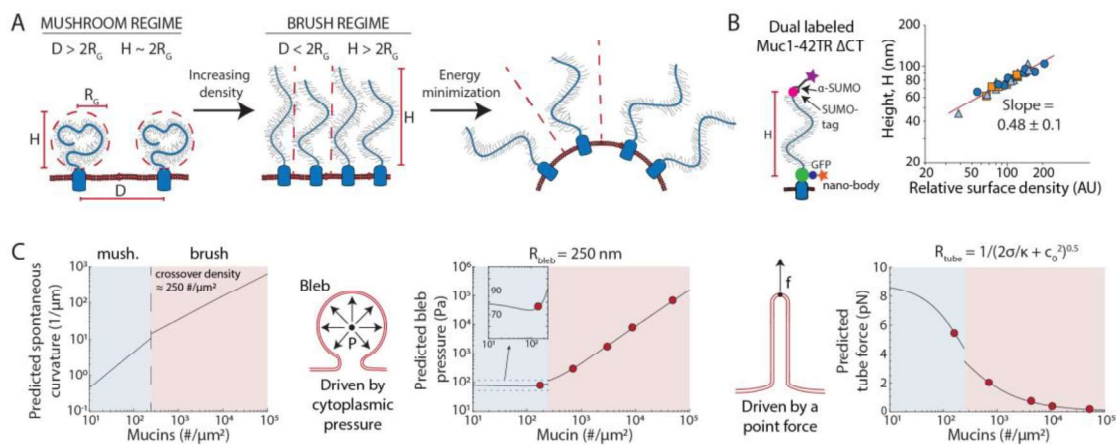


Figure 5.4 – Polymer brush model of the glycocalyx and generation of preferred membrane shapes. See also Figure 5.S2 and 5.S3. **A**, Polymer model of membrane bending illustrating proposed spontaneous membrane curvature induced by the cellular glycocalyx. Low density polymers are non-interacting and adopt a compact structure in the “mushroom” regime. In the “brush” regime, polymers overlap (the average distance between polymers, D , is less than the twice the radius of gyration, R_g) and extend to avoid each other, increasing the height of the polymer brush (H). Entropic pressures are the basis for membrane curvature generation by polymer mushrooms and brushes. **B**, Muc1 construct with SUMO and GFP tags flanking the polymer domain for visualization of polymer extension with expansion microscopy (ExM). Polymer extension versus polymer fluorescence intensity, a proportional measure of

surface density, showing the indicated scaling relation. Dots, squares, and triangles indicate measurements from three samples. The red line shows a linear regression through all data points. **C**, Theoretical prediction of spontaneous curvature generation by Muc1 polymer mushrooms and polymer brushes. Blue: estimated mushroom regime (mush.); pink: estimated brush regime (brush). The computational model here considers mucins of length 270 nm having monomeric segments of length 15 nm (Kuhn length). These parameters were based on experimental characterization of native Muc1-42TR and selected for comparison to experiments below. **D**, (left) Theoretical prediction of required pressure (Pa) as a function of mucin concentration for blebs of radii = 250 nm. The insert shows a pressure minimum near the mushroom-brush transition. (right) Theoretical prediction of the required point force (pN) as a function of mucin concentration for maintaining membrane tubules.

5.3.5 Preferred membrane shapes

We tested whether the polymer model could explain the frequency of finger-like and spherical protrusions from the cell surface. We reasoned that protrusion of a specific membrane feature would be disfavored when high intracellular forces were required to extend or maintain the protrusion and favored when these force requirements were minimal. Minimizing the standard Helfrich free energy function for membranes with induced spontaneous curvature, we calculated the equilibrium cytosolic pressure required to maintain a spherical membrane bleb and the point force required to maintain a membrane tubule (Derényi et al., 2002) (Fig. 5.4D; see '5.9 Supplemental note: theoretical considerations'). For experimental comparison, we evaluated the types, sizes, and frequencies of plasma membrane features as a function of mucin cell-surface density. Cells expressing Muc1-42TR-GFP- Δ ACT were labeled with an anti-GFP nanobody and sorted into populations of varying mucin surface levels (Fig. 5.5A, B). The average mucin surface density in each

population was estimated by SDS-PAGE through interpolation using a nanobody standard curve (Fig. 5.S4). Molecular surface densities in the sorted populations ranged from 180 to ~50,000 mucins per μm^2 . For reference, we expected the mushroom to brush transition to occur around 250 mucins per μm^2 based on the measured radius of gyration of recombinant Muc1-42TR in solution.

Initially, we evaluated membrane blebs. Using physical parameters measured for Muc1-42TR, we predicted that the pressure required for maintaining a bleb with a typical radius of 250 nm would be minimal at moderate mucin densities near the mushroom-brush transition (Fig. 5.5C, D). An important model prediction was that the required maintenance pressure would rise sharply at higher mucin densities, quickly reaching pressures that exceed the known limits of the cell's contractile machinery (Charras et al., 2008). Thus, theory suggested that blebbing would be supported by low mucin densities and suppressed by a highly dense glycocalyx (Fig. 5.5D). Our experimental observations showed good qualitative agreement with these predictions. Cells with a mucin density near the estimated mushroom-brush transition displayed a significant number of large, bleb-like forms with an average radius of 260 ± 100 nm (Fig. 5.5B-D; 180 mucins per μm^2). Upon crossover into the brush regime, the bleb frequency plummeted precipitously, consistent with the model's prediction of a quadratic rise in the necessary bleb maintenance pressure (Fig. 5.5B, D).

The glycocalyx polymer model predicted a much different dependence of tubule projection on mucin density. The predicted point force required for maintaining an extended tubule decreased progressively with high mucin densities and exhibited no sharp transitions (Fig. 5.4D). Accordingly, the

frequency of cell-surface tubules observed in our sorted cell populations increased steadily with mucin density throughout the mushroom and brush regimes until the cell was fully saturated with tubes at very high mucin densities (Fig. 5.5B-E). Notably, theory predicted that at these high densities, the required force for tubule extension is comparable to the polymerization force of a single cytoskeletal filament, ~ 1 pN (Footer et al., 2007). Based on the experimentally measured mucin densities, we estimated the theoretical point force, f , required to maintain tubules. Remarkably, the experimentally observed tube frequency on our sorted cell populations had a nearly perfect inverse correlation with the theoretical point force calculated the corresponding mucin density (Fig. 5.5F). The Pearson's correlation coefficient describing the relationship between tube density and $1/f$ was 0.97.

The polymer model also predicted that the spontaneous curvatures generated by high mucin surface densities exceeded the curvature of finger-like projections that we observed on the cell surface. We noted that the tubular membrane projections on our cells typically contained a filamentous actin (F-actin) core and did not contain microtubules (Fig. 5.6A, B and 5.S5A-D). Disruption of F-actin assembly with the drug Latrunculin A (LatA) led to a reduction in tubule diameter by approximately 30 nm (Fig. 5.6C, D and 5.S5E, F), indicating that the mucin-induced spontaneous curvature exceeded the curvature of the stable, actin-filled projections. It should be noted that our measurement of LatA-treated cells likely excluded very thin and delicate membrane tubules that were difficult to preserve throughout the SEM sample preparation. Nevertheless, our results clearly indicated that spontaneous curvatures generated by the glycocalyx can meet or exceed the curvature requirements for thin, finger-like projections, such as microtubules, cilia,

filopodia, axons, and cytonemes, which have characteristic diameters of approximately 100-200 nm.

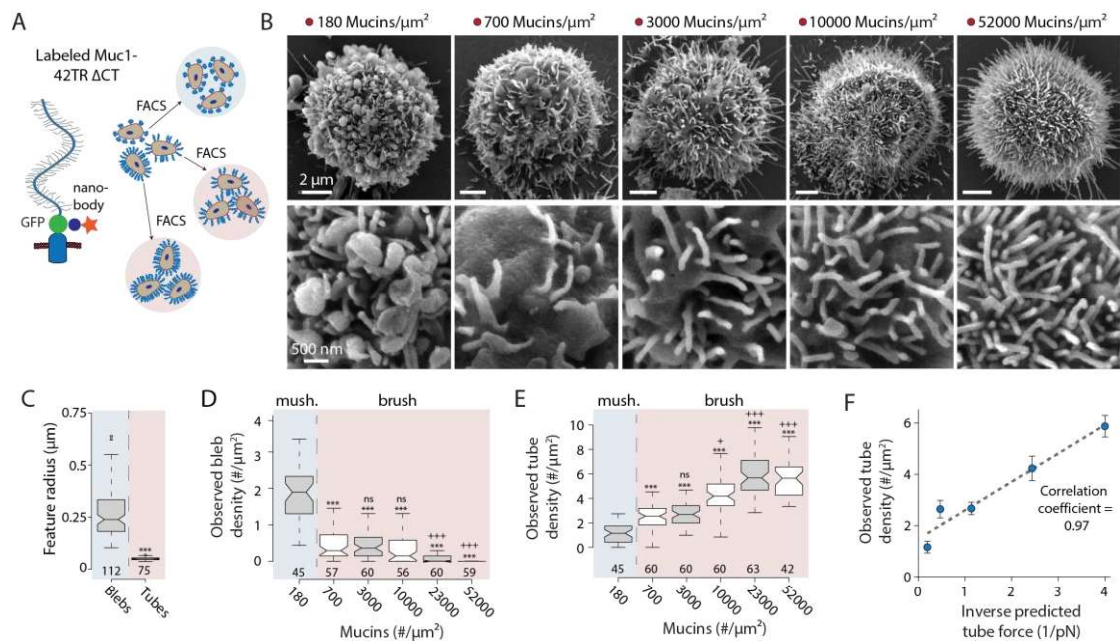


Figure 5.5 – Preferred membrane shape depends on cell-surface biopolymer concentrations. See also Figure 5.S4. **A**, Strategy for sorting cells into populations with varying levels of cell surface mucin (Muc1-42TR-GFP Δ CT) using fluorescence-activated cell sorting (FACS). **B**, Representative SEM images showing the transition of membrane morphological features of sorted cell populations with the indicated mucin surface density. Mucin densities were chosen to match the indicated points on the theoretical graphs (Fig. 5.3D). **C**, Average radius of bleb structures measured in the mushroom regime and tube structures measured in the brush regime. **D**, Observed density of membrane blebs on sorted cell populations having the indicated average mucin surface density. Significance was determined between mushroom regime and brush regime (*) or between the lowest brush regime density and all other brush mucin densities (+). **E**, Observed density of membrane tubes on sorted cell populations having the indicated average mucin surface density. Symbols defined in (D). **F**, Inverse predicted force from (Fig. 5.3D, right) versus the observed tube density from (E) exhibits a linear relationship and Pearson correlation coefficient of 0.97. Number of measurements shown on the x-axis of boxplots. Error bars indicate 95% confidence intervals. ns - not significant; */+ $p < 0.05$; **/+ $p < 0.01$; ***/+++ $p < 0.001$ (*post-hoc* student's two-tailed *t* test).

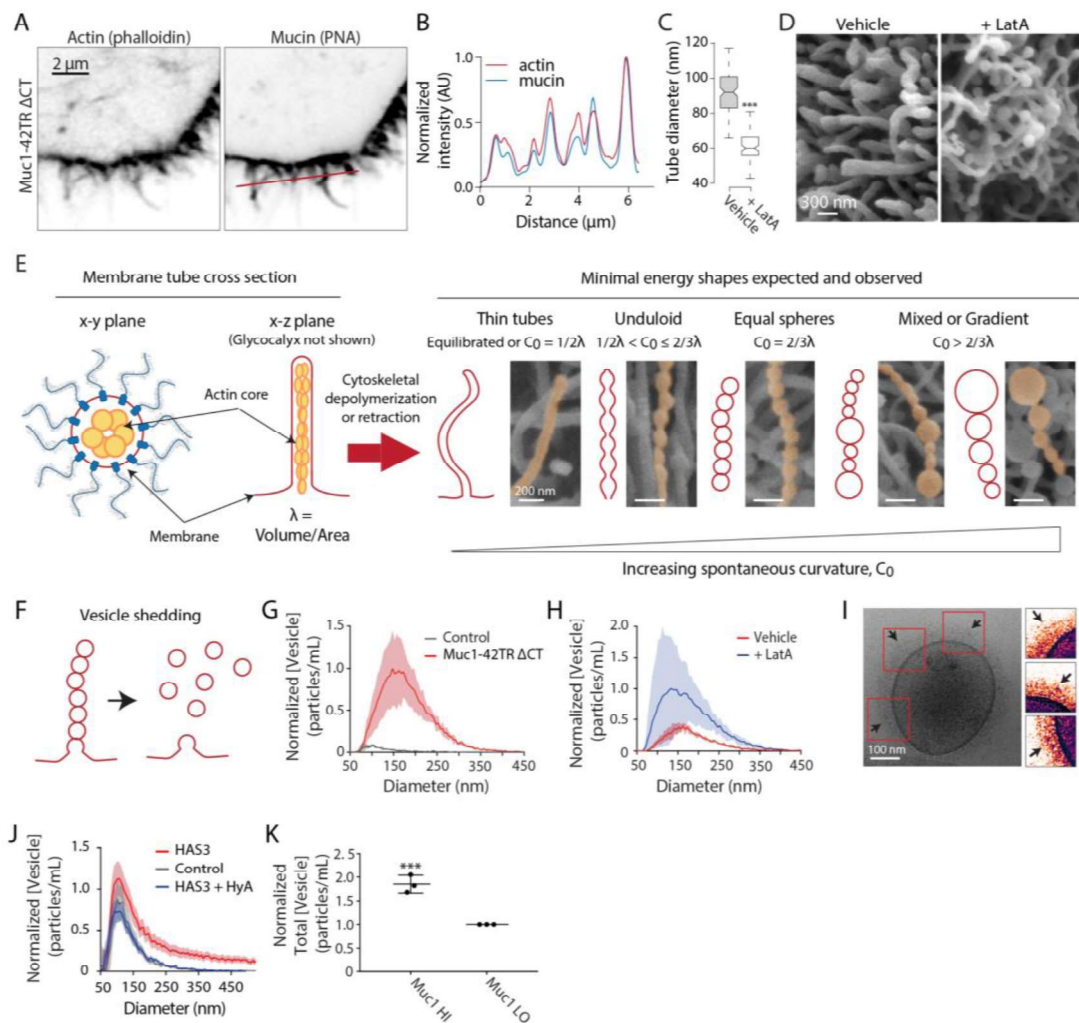


Figure 5.6 – Glycoalyx-mediated membrane instabilities and microvesicle biogenesis. See also Figure 5.S5. **A**, Representative confocal microscopy images of epithelial cells expressing Muc1-42TR ΔCT and stained with PNA (peanut agglutinin) for mucins and phalloidin for actin, $n = 3$. **B**, Fluorescent intensity line trace from (A) (PNA image, red line). Values are normalized for their respective maximum intensities for phalloidin and PNA stains. **C**, Average diameter of tubules in Muc1-42TR ΔCT expressing cells following treatment with DMSO (Vehicle) or with 10 μM Latrunculin-A (+ LatA) to disrupt actin assembly. **D**, Representative SEM images of tubules in vehicle treated or LatA treated cells expressing Muc1-42TR ΔCT. **E**, (left) Cartoon schematic of a proposed model in which the actin core resists the spontaneous membrane curvature driven by the glycocalyx brush. Upon actin depolymerization, membrane tubules are destabilized and predicted to relax into (right) various

pearled structures and/or thin tubes that represent minimal energy surfaces. Schematic drawings of these predictions are shown alongside representative pseudo-colored SEM images of cells expressing Muc1-42TR Δ CT. **F**, Cartoon schematic of proposed mechanism where pearling and vesiculated membrane instabilities (left) are disrupted and lead to microvesicle shedding (right). **G**, Histogram showing the average concentration and size distribution of extracellular vesicles for wild-type (Control) and Muc1-42TR Δ CT expressing cells. Shaded area shows the 95% confidence interval for all histograms. **H**, Histogram showing the average concentration and size distribution of extracellular vesicles for Muc1-42TR Δ CT cells treated with DMSO (Vehicle) or Latrunculin A (+ LatA), $n = 5, 5, 4, 7$, respectively. **I**, Representative cryogenic transmission electron microscopy (cryo-TEM) image of a vesicle collected from cells expressing Muc1-42TR Δ CT. Red boxes indicate pseudo-colored regions of interest shown on the right. **J**, Representative histogram showing average concentration and size distribution of extracellular vesicles for wild-type (Control), hyaluronic acid synthase 3 (HAS3) expressing human mammary epithelial cells, and HAS3-expressing cells treated with hyaluronidase (HyA). Particle concentration is normalized to the max peak for each graph, $n = 4, 5, 3$, respectively. **K**, Average concentration of extracellular vesicles from HeLa cells sorted for high or low Muc1 surface levels. Results represent the sum of all vesicles, independent of size, $n = 3$. *** $p < 0.001$ (*post hoc* two-tailed student's *t* test).

5.3.6 Membrane instabilities and extracellular vesicle generation

We next considered whether other functional membrane shapes could be generated through actions of the glycocalyx. We noted that a progressive increase in spontaneous curvature has been known to trigger membrane instabilities and morphological changes in membrane vesicles (Campelo and Hernández-Machado, 2007; Tsafirir et al., 2001). Therefore, we reasoned that membrane instabilities could arise if the F-actin cores that physiologically resist the spontaneous curvatures of mucins were disrupted. Indeed, our model suggested that ~ 400 mucins per μm^2 or more would be sufficient to drive membrane instabilities in tubules. Accordingly, we observed that LatA

treatment triggered formation of pearled and undulating structures that are characteristic of membrane instabilities following reduced actin core rigidity (Bar-Ziv et al., 1999) (Fig. 5.6D).

Deuling, Helfrich, and others theoretically considered instabilities in membrane tubules with volume to area ratio, λ , and found that for certain spontaneous curvatures, c_0 , the membrane bending energy vanished through the adoption of one of three “Delaunay” shapes: a cylinder for $c_0 = 1/2\lambda$ (Shape 1), a smoothly varying set of unduloids for $1/2\lambda < c_0 < 2/3\lambda$ (Shape 2), and a set of equal-sized “pearls” for $c_0 = 2/3\lambda$ (Shape 3) (Campelo and Hernández-Machado, 2007; Tsafirir et al., 2001). For spontaneous curvatures that exceeded $2/3\lambda$, the lowest energy shapes that satisfied the constraints of volume and surface area were found to include a set of small pearls of the preferred curvature with one or more big pearls necessary to hold excess volume (Shape 4) and a set of pearls with a gradient in size (Shape 5) (Campelo and Hernández-Machado, 2007; Tsafirir et al., 2001). We evaluated whether the minimal energy surfaces, Shapes 1-5, would be formed on cells expressing moderate to high levels of mucin without exogenous treatments, and found commonplace examples of each expected minimal energy shape (Fig. 5.6E). The observation of these shapes provided a compelling argument that membrane instabilities can be driven by specific compositions of the glycocalyx.

Previous theoretical and experimental studies indicated that the thin membrane necks connecting the pearled membrane structures on our cells would be expected to undergo spontaneous fissure due to the high elastic stress accumulated in the elastic stress accumulated in the constricted necks (Kozlovsky and Kozlov, 2003; Morlot et al., 2012; Snead et al., 2017). Therefore, we hypothesized that microvesicles would be released as a consequence of the

mucin-induced membrane instabilities (Fig. 5.6F). We found that the conditioned media from Muc1-42TR-expressing cells contained massive concentrations of particles ranging in size from approximately 100 nm to 400 nm (Fig. 5.6G). Particle generation was further enhanced by LatA treatments that disrupted the supporting F-actin cores of surface projections. As expected, we found that the disruption of the F-actin cores allowed the membrane tubules to equilibrate into pearled forms or tubules of smaller radii (Fig. 5.6H and 5.S5F). Cryo-transmission electron microscopy (cryo-TEM) confirmed that the secreted particles were membrane vesicles. Notably, the vesicles were grafted with a distinct glycocalyx ultrastructure on their surfaces (Fig. 5.6I). The removal of the glycocalyx, such as by HyA treatment to remove HA from the cell surface of HAS3-expressing cells, significantly reduced vesicle production (Fig. 5.6J).

High numbers of microvesicle generation have been reported in many cancer-cell types (Menck et al., 2017; Muralidharan-Chari et al., 2010). We tested whether high mucin expression, which is common in tumor cells, might at least partially explain why these cells have a propensity to generate microvesicles. We sorted HeLa tumor cells into sub-populations with low and high levels of endogenous Muc1 on the cell surface. Tumor cells sorted for high endogenous Muc1 expression produced significantly more vesicles than cells with low endogenous Muc1 levels (Fig. 5.6K).

Together, our results suggested a possible three-step sequence for microvesicle generation: (1) cytoskeletal filaments help extend and stabilize long and thin protrusions from the plasma membrane in a glycocalyx-dependent manner; (2) following disassembly of the cytoskeletal core, spontaneous curvature imposed by the glycocalyx induces membrane

instabilities of the tubules; and (3) membrane pearls spontaneously fissure to release vesicles (Fig. 5.6E, F).

5.4 DISCUSSION

Overall, the theories and experiments presented here implicate an entropic mechanism through which the glycocalyx can strongly influence the favorability of diverse plasma membrane shapes and protrusions. The morphological changes regulated by the glycocalyx could, in principle, have broad consequences on membrane processes, ranging from absorption and secretion to cellular communication, signaling, and motility (Lange, 2011; Paluch and Raz, 2013; Sauvanet et al., 2015; Schmick and Bastiaens, 2014). The flexibility of mucin biopolymers is modulated by glycosylation (Coltart et al., 2002). Given that glycosylation often changes dramatically with cell fate transitions (Buck et al., 1971; Freeze, 2013; Satomaa et al., 2009), and that the pool of monomers for construction of glycans and glycosaminoglycans is tightly coupled to specific metabolic programs (Dennis et al., 2009; Koistinen et al., 2015; Ying et al., 2012), our work raises the intriguing possibility that the glycocalyx may serve as a conduit linking physical morphology to specific cell states.

Contemporary frameworks for understanding membrane shape regulation largely lack a physical description of the glycocalyx. However, long-chain biopolymers in the glycocalyx are almost universally found anchored to the surfaces of curved membrane features and cell-surface organelles (Bennett Jr. et al., 2001; Button et al., 2012; Fowke et al., 2017; Hatstrup and Gendler, 2008; Kesavan et al., 2009; Kesimer et al., 2013; Makabe, S. et al., 2006; van den Pol and Kim, 1993; Zhang et al., 1992). Our work suggests that the principles and

theories of polymer physics can be adopted to understand, at least to a first approximation, the physical regulation of membrane shape generation by the glycocalyx. Undoubtedly, a model of end-anchored polymer mushrooms and polymer brushes is a simple physical representation of the glycocalyx. The actual glycocalyx architecture may also include additional hierarchies of crosslinking, entanglement, and molecular inhomogeneity (Tammi et al., 2002). However, the inverse relationship between the force requirements for membrane extension, as estimated using a relatively simple model of the glycocalyx, and the experimentally observed frequencies of these extensions argue that at least some of the physical behaviors of the glycocalyx can be captured using well established polymer models (Gennes, 1979; Zhulina and Borisov, 1996).

Our model and analyses assume constant membrane tension, leading to the prediction that the lengths of tubular projections are invariant of force. In reality, cells have a finite reservoir of membrane (Raucher and Sheetz, 1999). Increasing membrane tension following depletion of reservoirs would ultimately limit the length of tubular forms projected from the membrane (Cuvelier et al., 2005; Raucher and Sheetz, 1999). Transport limitations of cytoskeletal monomers also likely place an important constraint limiting the overall length of long and thin membrane projections (Mogilner and Rubinstein, 2005). In our experiments, we see only a weak dependence of tubule length on mucin density, as might be expected if mechanisms other than mucin pressure on the membrane ultimately contribute to tubule length (Fig. 5.5B). How the glycocalyx and intracellular shape-generating processes coordinate in space and time to control membrane protrusions must still be fully resolved. In particular, the Rho family of GTPases are master regulators of cytoskeletal

dynamics and cell-surface morphology (Hall, 1998). Our theories and experimental results suggest that by modulating the barrier to membrane bending, the glycocalyx primes the membrane for expansion into specific types of spherical or tubular forms that are subject to regulation by Rho GTPases. This integrated view suggests that perturbation of normal cell-surface morphology could be achieved through deregulation of intracellular shape generating processes, glycocalyx polymer assembly, or both. For instance, deregulation of Rho GTPase signaling, cytoskeletal dynamics, and glycocalyx assembly are all common hallmarks of cancer cells (Paszek et al., 2014; Pinho and Reis, 2015; Porter et al., 2016; Yamaguchi and Condeelis, 2007) and may each contribute to the unique cell-surface dynamics that contribute to the lethality of metastatic cancer cells.

Bending of surfaces by anchored polymers is a general physical phenomenon (Busch et al., 2015; Evans and Rawicz, 1997; Hansen et al., 2003; Hiergeist and Lipowsky, 1996; Kenworthy et al., 1995; Lipowsky, 1995; Stachowiak et al., 2012). As such, membrane shape regulation by the glycocalyx could be a universal feature in the biogenesis of curved membrane organelles and signaling structures. For instance, cilia, axons, cytonemes, microvilli, and microvesicles could all conceivably be regulated by physical forces related to the glycocalyx. Thus, our work argues for a more holistic model of membrane shape regulation that includes consideration of forces on both the intracellular and extracellular faces of the plasma membrane.

5.5 ACKNOWLEDGEMENTS

We thank the Woods Hole Cell Physiology Course and its participants for assistance with preliminary investigations. We acknowledge J. Lakins and

V. Weaver for empty lentiviral and transposon plasmids, as well as helpful discussions. We thank Bridgette Peal for assistance in harvesting synovial tissues. We also thank A. Stroock, L. Archer, J. Lammerding, and D. Koch for helpful discussions. **Funding:** This investigation was supported by the National Institute of General Medical Sciences Ruth L. Kirschstein National Research Service Award 2T32GM008267 (C.R.S., M.J.C.), Knight Family Foundation Graduate Research Fellowship in Nanoscience and Technology (C.R.S.), Samuel C. Fleming Family Graduate Fellowship (C.R.S.), National Science Foundation Graduate Research Fellowship (M.J.C., L.M.R., and K.P.), Ford Foundation Pre-doctoral Fellowship (L.M.R.), Stanford Graduate Fellowship (K.P.), Stanford ChEM-H Chemistry/Biology Interface Predoctoral Training Program (K.P.), National Institute of General Medical Sciences R37GM058867 (C.R.B.), National Institute of General Medical Sciences Grant No. R35GM118067 (W.E.M.), National Institute of Health New Innovator DP2 GM229133 (M.J.P.), and National Cancer Institute U54 CA210184 (M.J.P.). This work made use of the Cornell Center for Materials Research Shared Facilities which are supported through the NSF MRSEC program (DMR-1719875). This work also made use of the Cornell Nanoscale Science and Technology Facility which are supported through the NSF Grant (ECCS-1542081). This work also made use of the Cornell University Biotechnology Resource Center (BRC) Imaging Facility for confocal microscopy and FACS, which is supported through NIH S10OD018516.

5.5.1 Complete author list

Carolyn R. Shurer[†], Joe C. Kuo[†], LaDeidra M. Roberts[†], Jay G. Gandhi, Marshall J. Colville, Thais A. Enoki, Hao Pan, Jin Su, Jade M. Noble, Michael J. Hollander, John P. O'Donnell, Rose Yin, Kayvon Pedram, Leonhard Möckl, Lena F.

Kourkoutis, William E. Moerner, Carolyn R. Bertozzi, Gerald W. Feigenson, Heidi L. Reesink, and Matthew J. Paszek

[†]These authors contributed equally to this work.

5.5.2 Author contributions

All authors contributed to the design of the studies and the preparation of the manuscript. C.R.S., L.M.R., H.P, J.S., and M.J.P. prepared the cDNA and guide RNA vectors. C.R.S., J.C.K., L.M.R., and M.J.C. conducted fluorescence and scanning electron microscopy. C.R.S. conducted flow cytometry analysis and cell sorting. L.M.R., R.Y., and M.J.H. conducted microvesicle experiments. T.A.E. conducted GUV experiments. J.M.N. conducted cryogenic electron microscopy. K.P. and L.M designed the mucin digestion experiments. K.P. prepared samples for mucin digestion and L.M. conducted the localization microscopy and analysis. C.R.S. produced recombinant Muc1 and J.P.O performed the SEC-MALS analysis. J.G.G., and M.J.P. constructed the theoretical model. J.S. and H.L.R. prepared the primary equine synoviocytes, and H.L.R. harvested fresh equine synovial tissue.

5.5.3 Competing interests

A patent application relating to the use of StcE mucinase has been filed by Stanford University (docket number STAN-1510PRV). C.R.B. is a co-founder and Scientific Advisory Board member of Palleon Pharmaceuticals, Enable Bioscience, Redwood Biosciences, and InterVenn Biosciences and a member of the Board of Directors of Eli Lilly & Company.

5.6 KEY RESOURCE TABLE

REAGENT or RESOURCE	SOURCE	IDENTIFIER
Antibodies		
FITC Mouse Anti-Human MUC1 (CD227)	BD Biosciences	Cat#559774, RRID:AB_397318
Purified Mouse Anti-Human MUC1 (CD227)	BD Biosciences	Cat#555925, RRID:AB_396226
Human Podocalyxin Mab (Clone 222328) antibody	R and D Systems	Cat# MAB1658, RRID:AB_2165984
Actin (C-11) antibody	Santa Cruz Biotechnology	Cat# sc-1615, RRID:AB_630835
GFP (4B10) Mouse mAb antibody	Cell Signaling Technology	Cat# 2955, RRID:AB_1196614
6xHis antibody	BD Biosciences	Cat# 552565, RRID:AB_394432
Goat Anti-Mouse IgG-HRP Polyclonal antibody	Santa Cruz Biotechnology	Cat# sc-2005, RRID:AB_631736
Mouse Anti-Goat IgG-HRP antibody	Santa Cruz Biotechnology	Cat# sc-2354, RRID:AB_628490
Bacterial and Virus Strains		
Stbl3 E. coli	ThermoFisher Scientific	Cat#C7373
XL1-Blue E. coli	Agilent / Stratagene	Cat#200236
Chemicals, Peptides, and Recombinant Proteins		
Hyaluronic Acid Binding Protein (HABP), Bovine Nasal Cartilage, Biotinylated	Millipore Sigma	Cat#385911
Hyaluronic Acid Binding Protein (HABP), Bovine Nasal Cartilage	Millipore Sigma	Cat#385910
Latrunculin A (LatA)	Cayman Chemical	Cat#10010630
1,2-dioleoyl- <i>sn</i> -glycero-3-phosphocholine (DOPC)	Avanti Polar Lipids, Inc.	Cat#850375P

1,2-dioleoyl-sn-glycero-3-[(N-(5-amino-1-carboxypentyl)iminodiacetic acid)succinyl] (nickel salt)	Avanti Polar Lipids	Cat#790404P
β -BODIPY FL C5-HPC (BODIPY PC)	Thermo Fisher Scientific	Cat#D3803
Recombinant Human Podocalyxin Protein, CF	R and D Systems	Cat#1658-PD
GFP Binding Protein (Nanobody)	Chromotek	Cat#gt-250
Alexa Fluor 647 NHS Ester (Succinimidyl Ester)	ThermoFisher Scientific	Cat#A37573
Alexa Fluor 568 NHS Ester (Succinimidyl Ester)	ThermoFisher Scientific	Cat#A20003
Alexa Fluor 488 NHS Ester (Succinimidyl Ester)	ThermoFisher Scientific	Cat#A20000
16% Paraformaldehyde (formaldehyde) aqueous solution	Fisher Scientific	Cat#50-980-487
10% Glutaraldehyde aqueous solution	Fisher Scientific	Cat#50-262-13
4% Osmic acid in aqueous solution	VWR	Cat#100504-822
FreeStyle 293 Expression Medium	ThermoFisher Scientific	Cat#12338018
DMEM/F12	ThermoFisher Scientific	Cat#11320033
Horse serum, New Zealand origin	ThermoFisher Scientific	Cat#16050122
Recombinant Murine EGF	Peptotech	Cat#315-09
Insulin solution from bovine pancreas	Millipore Sigma	Cat#I0516
Hydrocortisone	Millipore Sigma	Cat#H0888
Cholera Toxin from <i>Vibrio cholerae</i>	Millipore Sigma	Cat#C8052
Penicillin-Streptomycin	ThermoFisher Scientific	Cat#15140122
DMEM, high glucose	ThermoFisher Scientific	Cat#11965118
Fetal Bovine Serum, qualified, USDA-approved regions	ThermoFisher Scientific	Cat#10437028

RPMI 1640 Medium	ThermoFisher Scientific	Cat#11875093
FreeStyle MAX Reagent	ThermoFisher Scientific	Cat#16447100
G418, Geneticin	ThermoFisher Scientific	Cat#10131035
Puromycin	Millipore Sigma	Cat#P8833
Hygromycin B	Millipore Sigma	Cat#10843555001
Blasticidin	InvivoGen	Cat#ant-bl-1
Doxycycline Hyclate	Santa Cruz Biotechnology	Cat#sc-204734
Doxycycline Hyclate	Applichem	Cat#A2951,0025
Clarity Western ECL Substrate	Bio-Rad	Cat#1705061
Normal Goat Serum	Vector Laboratories	Cat#S-1000
StcE Mucinase	(Malaker et al., 2018)	N/A
Peanut agglutinin (PNA) antibody, biotinylated	Vector Laboratories	Cat# B-1075
CF-568 Dye PNA Lectin (Arachis hypogaea)	Biotium	Cat#29061
CF-640R Dye PNA Lectin (Arachis hypogaea)	Biotium	Cat#29063
CF-633 Dye Wheat Germ Agglutinin (WGA)	Biotium	Cat#29024
Biotinylated Vicia Villosa Lectin (VVL, VVA)	Vector Laboratories	Cat#B-1235
ExtrAvidin-Peroxidase antibody	Sigma-Aldrich	Cat#e2886
Streptavidin-HRP	R and D Systems	Cat#DY998
NeutrAvidin Protein, DyLight 650	Thermo Fisher Scientific	Cat#84607
Ac ₄ GalNAz	Thermo Fisher Scientific	Cat#88905
Alexa Fluor 647 Alkyne, Triethylammonium Salt	Thermo Fisher Scientific	Cat#A10278
BTAA	Click Chemistry Tools	Cat#1236

AlexaFluor-647-hydroxylamine	Thermo Fisher Scientific	Cat#A30632
Apo-Transferrin human	Millipore Sigma	Cat#T2036
GFP booster Atto 647N (GFP nanobody)	Chromotek	Cat#gba647n-100
HisPur Ni-NTA Resin	Thermo Fisher Scientific	Cat#88221
SYPRO Ruby Protein Gel Stain	Thermo Fisher Scientific	Cat#S12000
Alexa Fluor 568 Phalloidin	Thermo Fisher Scientific	Cat#A12380
N-azidoacetylmannosamine-tetraacylated (Ac4ManNAz)	Click Chemistry Tools	Cat#1084-5
AFDye 647 DBCO	Click Chemistry Tools	Cat#1302-1
Acryloyl-X, SE, 6-((acryloyl)amino)hexanoic Acid, Succinimidyl Ester	Invitrogen	Cat#A20770
sodium acrylate	Millipore Sigma	Cat#45-408220
40% acrylamide solution	Biorad	Cat#1610140
2% bis-acrylamide solution	Biorad	Cat#1610142
Ammonium persulfate	Millipore Sigma	Cat#A3678
Tetramethylethylenediamine	Millipore Sigma	Cat#T9281
low glucose (1.0 g/L) DMEM media	Hyclone	Cat#SH30021.01
HEPES	Corning	Cat#25-060-Cl
Fetal bovine serum (for primary cells)	VWR	Cat#97068-085
Penicillin/streptomycin (for primary cells)	Corning	Cat#30-002-Cl
Collagenase	Worthington Biochemical	Cat#LS004177
DNase I	Roche	Cat#10104159001
Ham's F12 media	Corning	Cat#10-080-CV
Hyaluronidase	Millipore Sigma	Cat#389561
ECL substrate (for HA blot)	Amresco	Cat#1B1581-kit-100ml
Cysteamine	Millipore Sigma	Cat#30070
Catalase from bovine liver	Millipore Sigma	Cat#C100

Glucose oxidase	Millipore Sigma	Cat#G2133-50KU
Glucose	BD Difco	Cat#215530
Tris-HCl	Thermo Fisher Scientific	Cat#15567-027
Critical Commercial Assays		
Hyaluronan DuoSet ELISA	R and D Systems	Cat#DY3614
Cell Line Nucleofector Kit V	Lonza	Cat#VVCA-1003
CloneJET PCR Cloning Kit	ThermoFisher Scientific	Cat#K1231
Experimental Models: Cell Lines		
MCF10A	ATCC	Cat#CRL-10317, RRID:CVCL_0598
HEK293T	ATCC	Cat#CRL-3216, RRID:CVCL_0063
T-47D	ATCC	Cat#HTB-133, RRID:CVCL_0553
ZR-75-1	ATCC	Cat#CRL-1500, RRID:CVCL_0588
HeLa	ATCC	Cat#CCL-2, RRID:CVCL_0030
FreeStyle 293-F	ThermoFisher Scientific	Cat#R79007
Primary Equine Synoviocyte	This Paper	N/A
MCF10A rtTA NeoR	(Paszek et al., 2012)	N/A
Freestyle 293-F rtTA NeoR	This Paper	N/A
Primary Equine Synoviocyte rtTA NeoR	This Paper	N/A
MCF10A rtTA NeoR Muc1-42TR Δ CT	(Shurer et al., 2018)	N/A
MCF10A rtTA NeoR Muc1-42TR TM21	(Shurer et al., 2018)	N/A

MCF10A rtTA NeoR Podxl ΔCT	(Shurer et al., 2018)	N/A
MCF10A rtTA NeoR Rational GFP ΔCT	This Paper	N/A
MCF10A rtTA NeoR Muc1 0TR GFP ΔCT	This Paper	N/A
MCF10A rtTA NeoR Muc1 10TR GFP ΔCT	This Paper	N/A
MCF10A rtTA NeoR Muc1 42TR GFP ΔCT	This Paper	N/A
MCF10A rtTA NeoR Notch1 GFP ΔCT	This Paper	N/A
MCF10A rtTA NeoR HAS3	This Paper	N/A
Primary Synovioocyte rtTA NeoR HAS3	This Paper	N/A
MCF10A rtTA NeoR SUMO Muc1-42TR GFP ΔCT	This Paper	N/A
FreeStyle 293-F rtTA NeoR S6 Muc1-42TR 10xHIS	This Paper	N/A
Oligonucleotides		
HAS3 FWD primer: 5'-GGCACCTCGAGGATGCCGGTGCAGCTGACGACA-3'	This Paper	N/A
HAS3 REV primer: 5'-GGCAGAATTCTTACACCTCAGCAAAGCCAAGCT - 3'	This Paper	N/A
moxGFP FWD primer: 5'-GGCAGCTCAGCTATGGTGTCCAAGGGCGAGGAGCTGT-3'	This Paper	N/A
moxGFP REV primer: 5'-GGCAGCTGAGCCCTTATACAGCTCGTCCATGCCGTGAGT-3'	This Paper	N/A
Muc1 tandem repeat deletion FWD primer: 5'-TGGAGGAGCCTCAGGCATACTTATTG-3'	This Paper	N/A

Muc1 tandem repeat deletion REV primer: 5'- CCACCGCCGACCGAGGTGACAT CCTG-3'	This Paper	N/A
S6-tag site-directed mutagenesis FWD primer: 5'- GTTGCGACTGCTTAACGGACAG ATCTCGATGGTGAGC-3'	This Paper	N/A
S6-tag site-directed mutagenesis REV primer: 5'- AGCCAGCTCAGGGAATCCCCAG CATTCTTCTCAGTAGAG-3'	This Paper	N/A
10xHis-tag oligo 1: 5'- TCAGGCCACCACCACCATCACC ATCATCACCACCATTAGGG-3'	This Paper	N/A
10xHis-tag oligo 2: 3'- CCGGTGGTGGTGGTAGTGGTAG TAGTGGTGGTAATCCCTTAA-5'	This Paper	N/A
Human COSMC guide RNA: 5'- GAGTCTTTGGGCTGCAGTAA-3'	(Stolfa et al., 2016)	N/A
Human SLC35A1 guide RNA: 5'- TTCTGTGATACACACGGCTG-3'	This Paper	N/A
Notch1 FWD primer: 5'- GGCAAGATCTCTAGAGGCTTGA GATGCTCCCAGCCA -3'	This Paper	N/A
Notch1 REV primer: 5'- GGCACCTGAGGCGTGGCACAGT AGCCCGTTGAATTTG -3'	This Paper	N/A
Recombinant DNA		
pLV rtTA-NeoR plasmid	(Paszek et al., 2014)	N/A
Hyperactive Transposase plasmid	(Shurer et al., 2018)	N/A
pPB tetOn PuroR plasmid	(Shurer et al., 2018)	N/A
Muc1-42TR ΔCT pPB tetOn PuroR plasmid	(Shurer et al., 2018)	N/A

Muc1-42TR TM21 pPB tetOn PuroR plasmid	(Shurer et al., 2018)	N/A
Podxl ΔCT pPB tetOn PuroR plasmid	(Shurer et al., 2018)	N/A
Muc1 GFP ΔCT pPB tetOn PuroR	(Shurer et al., 2018)	N/A
Rational GFP ΔCT (9-80) pPB tetOn PuroR plasmid	This Paper	N/A
Muc1 0TR GFP ΔCT pPB tetOn PuroR plasmid	This Paper	N/A
Muc1 10TR GFP ΔCT pPB tetOn PuroR plasmid	This Paper	N/A
Muc1 42TR GFP ΔCT pPB tetOn PuroR plasmid	This Paper	N/A
Notch1 GFP ΔCT pPB tetOn PuroR plasmid	This Paper	N/A
pLV tetOn HygroR HAS3 plasmid	This Paper	N/A
SUMO Muc1-42TR GFP ΔCT pPB tetOn PuroR plasmid	This Paper	N/A
pLV HygroR tetOn plasmid	(Paszek et al., 2012)	N/A
Human Hyaluronan Synthase 3/HAS3 (NP_005320) plasmid	R and D Systems	Cat#RDC0920
moxGFP plasmid	(Costantini et al., 2015)	Cat#68070, Addgene #68070
S6 Muc1-42TR 10xHis pPB tetOn PuroR plasmid	This Paper	N/A
6xHis SUMO pcDNA3.1, custom gene synthesis plasmid	General Biosystems	N/A
Muc1 42TR GFP ΔCT pcDNA3.1, custom gene synthesis plasmid	General Biosystems	N/A
lentiCRISPR v2 Blast plasmid	Mohan Babu	Cat#83480, Addgene #83480
lentiCRISPR v2 GFP plasmid	(Walter et al., 2017)	Cat#82416, Addgene #82416
COSMC lentiCRISPR v2 Blast plasmid	This Paper	N/A

SLC35A1 lentiCRISPR v2 GFP plasmid	This Paper	N/A
pCS2 Notch1 Full Length-6MT plasmid	(Schroeter et al., 1998)	Cat#41728, Addgene #41728
Software and Algorithms		
Nanoparticle Tracking Analysis software	Malvern Panalytical	https://www.malvernpanalytical.com/en/products/technology/nanoparticle-tracking-analysis
Prism 8.0	GraphPad	https://www.graphpad.com/scientific-software/prism/
BoxPlotR	Online	http://shiny.chemgrid.org/boxplotr/
FlowJo v10	FlowJo, LLC	https://www.flowjo.com/solutions/flowjo/downloads
BD FACSDiva Software 8.0.1	BD Biosciences	
CFlow Plus Analysis v1.0.227.4	BD Biosciences	http://www.bdbiosciences.com/us/instruments/research/cell-analyzers/bd-accuri/m/1294932/features/software
Image Lab v5.2.1	Bio-Rad	http://www.bio-rad.com/en-us/product/image-lab-software?ID=KRE6P5E8Z
Fiji	NIH	https://fiji.sc/

Matlab 2015b	MathWorks	https://www.mathworks.com/help/matlab/release-notes-R2015b.html
Adobe Photoshop CC	Adobe	https://www.adobe.com/products/photoshop.html
Adobe Illustrator CC	Adobe	https://www.adobe.com/products/illustrator.html

Table 5.1 – Key Resource Table. Shows key reagents and resources used for experiments.

5.7 STAR METHODS

5.7.1 Contact for reagent and resource sharing

Further information and requests for resources and reagents should be directed to and will be fulfilled by the Lead Contact, Matthew Paszek (mjp31@cornell.edu). All plasmids used in this work will be made available to the community through the Addgene repository or directly from the Lead Contact.

5.7.2 Experimental model and subject details

Cell lines

Parental Cell Lines

MCF10A cells were cultured in DMEM/F12 media supplemented with 5% horse serum, 20 ng/mL EGF, 10 µg/ml insulin, 500 ng/mL hydrocortisone, 100 ng/mL cholera toxin and penicillin/streptomycin. HEK293T and HeLa cells were cultured in DMEM high glucose media supplemented with 10% fetal bovine serum and penicillin/streptomycin. T47D cells were cultured in RPMI

media supplemented with 10% fetal bovine serum, 10 µg/ml insulin, and penicillin/streptomycin. FreeStyle 293-F cells were maintained in Freestyle 293 Expression Medium in spinner flasks at 37°C, 8% CO₂, 120 RPM, and 80% RH according to manufacturer's protocol.

Generated Cell Lines

Stable MCF10A, primary equine synoviocyte, and 293-F cells expressing the rtTA-M2 tetracycline transactivator were prepared by lentiviral transduction using the pLV rtTA-NeoR plasmid as previously described (Paszek et al., 2012). Cells were further modified with tetracycline-responsive promoter plasmids. Stable cells expressing hyaluronan synthase 3 (HAS3) were prepared by lentiviral transduction using the pLV HygroR tetOn HAS3 plasmid. For preparation of mucin expressing cell lines and Notch1 expressing cell line (EGF-repeats GFP ΔCT), plasmids with ITR-flanked expression cassettes (i.e. pPB tetOn PuroR plasmids) were co-transfected with the PiggyBac hyperactive transposase using Nucleofection Kit V (Lonza) or FreeStyle Max Reagent (Thermo Fisher) according to manufacturer's protocols. For CRISPR knock-outs, cell lines expressing Muc1-42TR ΔCT were further modified by lentiviral transduction using either SLC35A1 lentiCRISPR v2 GFP or COSMC lentiCRISPR v2 Blast plasmids. Selection of stable cell lines was performed with 750 µg/mL G418, 1 µg/mL puromycin, 200 µg/mL hygromycin, or 15 µg/ml Blasticidin.

Primary synoviocyte isolation and culture

Primary equine synoviocytes were obtained from the shoulder, stifle, carpal, tarsal and fetlock joints of a male thoroughbred yearling horse (*Equus caballus*). To isolate the fibroblast-like type B synovial cells (synoviocytes), synovial membrane tissues were digested with 0.15% collagenase (Worthington

Biochemical, Lakewood, NJ) supplemented with 0.015% DNase I (Roche, Indianapolis, IN) for 3 h at 37 °C in Ham's F12 media, followed by filtration and centrifugation at 250x g for 10 minutes as previously described (Saxer et al., 2001). Equine synoviocytes were cultured in low glucose (1.0 g/L) DMEM media supplemented with 40 mM HEPES, 4 mM L-Glutamine, 110 mg/L sodium pyruvate, 10% fetal bovine serum and penicillin/streptomycin. Subculture of the synoviocytes was performed every 3–4 days. All adherent cells were maintained at 37°C, 5% CO₂, and 90% RH.

Equine synovial tissue resection

Synovial tissues were harvested from the middle carpal joint of two adult thoroughbred horses. The freshly resected tissues were either incubated for 30 min in Ham's F12 media with or without 1 U/mL Hyaluronidase (Sigma) and fixed or immediately fixed for 24 h with 4% paraformaldehyde and 1% glutaraldehyde in PBS. Tissues were then either processed for SEM or reduced with 0.1 mg/mL NaBH₄ for 20 min on ice and further processed for confocal imaging.

5.7.3 Method details

Cloning and constructs

cDNAs for cytoplasmic-tail-deleted human Muc1 with 42 tandem repeats (Muc1-42TR Δ CT), Muc1-42TR polymer domain fusion with the TM21 synthetic membrane domain (Muc1-42TR TM21), cytoplasmic-tail-deleted human Podocalyxin (S/T-Rich Δ CT) were generated and cloned into the tetracycline-inducible PiggyBac expression vector (pPB tetOn PuroR) or mammalian expression vector pcDNA3.1 as previously described (Paszek et al., 2014; Shurer et al., 2018). To make lentiviral vector pLV HygroR tetOn HAS3, the cDNA for human HAS3 (accession NP_005320) was obtained from R&D

Systems and amplified via PCR with the forward primer, 5'-GGCACCTCGAGGATGCCGGTGCAGCTGACGACA-3', and reverse primer, 5'-GGCAGAATTCTTACACCTCAGCAAAAGCCAAGCT - 3'. The PCR product was cloned into pJET1.2 (ThermoFisher) according to manufacturer's protocol, and subcloned into the *AbsI* and *EcoRI* sites of pLV HygroR tetOn (Paszek et al., 2012). For generation of Muc1 GFP Δ CT pPB tetOn PuroR with varying number of tandem repeats, the cDNA for moxGFP (Addgene #68070; heretofore mOxGFP is referred to as GFP) was amplified with primers: 5'-GGCAGCTCAGCTATGGTGTCCAAGGGCGAGGAGCTGT-3' (forward) and 5'-GGCAGCTGAGCCCTTATACAGCTCGTCCATGCCGTGAGT-3' (reverse). The PCR product was cloned into pJET1.2 and subcloned non-directionally into the *BlpI* site of Muc1-42TR Δ CT pPB tetOn PuroR. For constructs with 10 and 42 native tandem repeats (PDTRPAPGSTAPPAHGVTS_A), synthetic cDNAs for the desired repeat units were generated through custom gene synthesis (General Biosystems) and cloned in place of the tandem repeats in Muc1 GFP Δ CT pPB tetOn PuroR using the *BamHI* and *Bsu36I* restriction sites. Muc1 tandem repeats were deleted through Q5 site directed mutagenesis with 5'-TGGAGGAGCCTCAGGCATACTTTATTG-3' (forward) and 5'-CCACCGCCGACCGAGGTGACATCCTG-3' (reverse) primers to generate Muc1 0TR GFP Δ CT pPB tetOn PuroR. To add a SumoStar tag to the Muc1-42TR GFP Δ CT N-terminus, a cDNA encoding the IgG kappa leader sequence, SumoStar tag, and Muc1 N-terminus was generated through custom gene synthesis (General Biosystems) and inserted in place of the Muc1 N-terminus in Muc1 GFP Δ CT pPB tetOn PuroR using the *BamHI* and *BsrGI* restriction sites. For construction of both COSMC and SLC35A1 vectors, we used the pLentiCRISPRv2 system. For generation of the Notch1 GFP Δ CT pPB tetOn

PuroR plasmid (EGF-repeats GFP Δ CT), the cDNA for Notch1 (Addgene #41728) was amplified with primers: 5'-GGCAAGATCTCTAGAGGCTTGAGATGCTCCCAGCCA -3' (forward) and 5'-GGCACCTGAGGCGTGGCACAGTAGCCCGTTGAATTTG -3' (reverse). The PCR product was cloned into the BglIII and Bsu36I sites of the Muc1 42TR Δ CT pPB tetOn PuroR plasmid. The target sequence for human COSMC (5'-GAGTCTTTGGGCTGCAGTAA-3') was cloned into the pLentiCRISPRv2 Blast backbone (Addgene #83480). The target sequence for human SLC35A1 (5'-TTCTGTGATACACACGGCTG-3') was cloned into the pLentiCRISPRv2 GFP backbone (Addgene #82416), both after BsmBI digestion.

For recombinant production of the mucin polymer domain, 42 tandem repeats from Muc1 were fused to an N-terminal S6 tag (GDSLWLLRLLN) and C-terminal 10x-histidine purification tag to make Muc1-42TR 10X His. To insert the S6 tag, Q5 site directed mutagenesis was performed using 5'-GTTGCGACTGCTTAACGGACAGATCTCGATGGTGAGC-3' (forward) and 5'-AGCCAGCTCAGGGAATCCCCAGCATTCTTCTCAGTAGAG-3' (reverse) on a pcDNA3.1 plasmid containing the Muc1 N-terminus from Muc1-42TR Δ CT pPB tetOn PuroR between BamHI and BglIII sites. The S6 tag was subsequently cut at these sites and replaced in the Muc1-42TR Δ CT N-terminus in Muc1-42TR Δ CT pPB tetOn PuroR. The 10x-histidine tag was added by annealing the oligos, 5'-TCAGGCCACCACCACCATCACCATCATCACCACCATTAGGG-3' and 3'-CCGGTGGTGGTGGTAGTGGTAGTGGTGGTAATCCCTTAA-5', and inserting in place of the Muc1-42TR Δ CT C-terminus in Muc1-42TR Δ CT pPB tetOn PuroR using the Bsu36I and EcoRI restriction sites.

Immuno- and lectin blot analysis

Cells were plated at 20,000 cells/cm² and induced with 0.2 μ g/mL

doxycycline (Santa Cruz) for 24 h before lysis with Tris-Triton lysis buffer (Abcam). Lysates were separated on Nupage 4-12% Bis-Tris or 3-8% Tris-Acetate gels (Thermo Fisher) and transferred to PVDF membranes. Primary antibodies were diluted 1:1000 and lectins were diluted to 1 µg/mL in 3% BSA TBST and incubated 4 h at room temperature or overnight at 4°C. Secondary antibodies or ExtrAvidin were diluted 1:2000 in 3% BSA TBST and incubated for 2 h at room temperature. Blots were developed in Clarity ECL (BioRad) substrate, imaged on a ChemiDoc (BioRad) documentation system, and quantified in ImageJ Fiji (Schindelin et al., 2012).

Flow cytometric analysis

Cells were plated at 20,000 cells/cm² and grown for 24 h. Cells were then induced with 0.2 µg/mL doxycycline (Santa Cruz) for 24 h. For sialic acid labeling by ManNAz, separate cultures were plated in parallel with cells treated for 24 h with both 0.2 µg/mL doxycycline (Santa Cruz) and 25 µM Ac4ManNAz (Click Chemistry Tools). Ac4ManNAz treated cells were labeled with 50 µM AF647 DBCO in 1% FBS PBS for 20 min at room temperature. Adherent cells were non-enzymatically detached by incubating with 1 mM EGTA in PBS at 37°C for 20 min and added to the population of floating cells, if present. Affinity reagents: anti-Muc1, GFP nanobody, 650 Neutravidin were diluted 1:200 in 0.5% BSA PBS; 647 PNA and biotin VVA were diluted to 1 µg/mL in 0.5% BSA PBS and incubated with cells at 4°C for 30 min for each stain. A BD Accuri C6 flow cytometer was used for analysis.

Confocal microscopy for cells and tissues

Cells were plated at 5,000 cells/cm² and subsequently induced with 0.2 µg/mL of doxycycline (Santa Cruz) for 24 h before being fixed with 4% paraformaldehyde. Antibodies and HABP were diluted 1:200 in 5% normal goat

serum (Vector Laboratories) PBS and incubated overnight at 4°C. For fluorescent HABP, HABP (Millipore Sigma) was labeled with Alexa Fluor 568 NHS Ester (Thermo Fisher Scientific) per the manufacturer's protocol. Lectins were diluted to 1 µg/mL in 5% normal goat serum PBS and incubated for 2 h at room temperature. For hyaluronic acid staining of cells and tissues, HABP was diluted to 0.125 µg/ml in 0.5% normal goat serum in PBS and incubated on samples for 24 h. Cell samples were imaged on a Zeiss LSM inverted 880 confocal microscope using a 40x water immersion objective (NA 1.1). In addition to HABP, NaBH₄-treated tissues were stained with 1 µg/mL Hoechst for 10 min and imaged on a Zeiss 880 upright confocal microscope with a 40x water dipping lens. Unstained tissue collagen was visualized with second harmonic generation using non-descan detectors.

Scanning electron microscopy

All samples were fixed for 24 h with 4% paraformaldehyde and 1% glutaraldehyde in PBS, post-fixed for 45 min with 1% osmium tetroxide in dH₂O, washed and subsequently dehydrated stepwise in ethanol of 25%, 50%, 70%, 95%, 100%, 100% before drying in a critical point dryer (CPD 030, Bal-Tec). Samples were coated with gold-palladium in a Desk V sputter system (Denton Vacuum) and imaged on a field emission scanning electron microscope (Mira3 FE-SEM, Tescan or FE-SEM LEO 1550, Carl Zeiss Inc.). For actin depolymerization studies, cells were treated for 60 min with 10 µM LatA before fixation, where indicated.

Mucin digestion and super-resolution imaging

Sample prep and azido sugars incorporation

MCF10A Muc1-42TR ΔCT cells were cultured in phenol red free 1:1 DMEM:F12 supplemented as described previously. For imaging, cells were

seeded at a density of 10,000 cells/well on Lab-Tek II Chambered Coverglass (Thermo Fisher Scientific) coated with 0.01% poly-Lysine (Sigma). Media was supplemented with Ac₄GalNAz (Thermo Fisher Scientific) 2 h post-seeding at a concentration of 50 μM. For induction of Muc1-42TR ΔCT expression, doxycycline (Applichem) was added to Lab-Tek wells 16 h post-seeding at 200 ng/mL. Enzymatic de-mucination was performed 24 h post-doxycycline induction with 50 nM StcE in complete media for 2 h at 37 °C immediately before labeling and imaging (Malaker et al., 2018; Möckl et al., 2018).

Cu-click Labeling of GalNAc

Cells were moved to 4°C and washed three times with cold DPBS with Ca²⁺ and Mg²⁺. Immediately after washing, Cu-click conjugation with AlexaFluor-647-alkyne (Thermo Fisher Scientific) was performed. The cells were incubated with 50 μM CuSO₄ (Sigma), 250 μM BTAA (Click Chemistry Tools), 1 mM aminoguanidine (Sigma), 2.5 mM sodium ascorbate (Sigma), and 25 μM AlexaFluor-647-alkyne (Thermo Fisher Scientific) in DPBS for 5 min at 4°C as reported previously (Hong et al., 2010). Cells were washed five times with cold DPBS and fixed with 4% paraformaldehyde (Thermo Fisher Scientific) and 0.2% glutaraldehyde (Sigma) in DPBS for 30 min at room temperature.

Periodate-mediated labeling of sialic acids

Sialic acids were labeled as described previously (Zeng et al., 2009). Cells were moved to 4°C, then washed three times with cold DPBS with Ca²⁺ and Mg²⁺ followed by a 5-minute incubation with 1 mM sodium periodate (Sigma) in DPBS. The periodate was quenched by 1 mM glycerol in cold DPBS, and washed three times with cold DPBS. Samples were stained with 25 μM AlexaFluor-647-hydroxylamine (Thermo Fisher Scientific) in the presence of 10 mM aniline in sterile filtered DPBS + 5% FBS pH 6.7 for 30 min at 4°C in the

dark with gentle agitation. Cells were washed five times with cold DPBS, and fixed with 4% paraformaldehyde (Thermo Fisher Scientific) and 0.2% glutaraldehyde (Sigma) in DPBS for 30 min at room temperature.

Optical Setup

The core of the setup was an inverted microscope (IX71, Olympus, Tokyo, Japan). The laser used for illumination (120 mW 647 nm, CW, Coherent, Santa Clara, CA) was spectrally filtered (ff01-631/36-25 excitation filter, Semrock, Rochester, NY) and circularly polarized (LPVISB050-MP2 polarizers, Thorlabs, Newton, NJ, WPQ05M-633 quarter-wave plate, Thorlabs). The beam was expanded and collimated using Keplerian telescopes. Shutters were used to toggle the lasers (VS14S2T1 with VMM-D3 three-channel driver, Vincent Associates Uniblitz, Rochester, NY). The laser was introduced into the back port of the microscope via a Köhler lens. The sample was mounted onto an XYZ stage (PInano XYZ Piezo Stage and High Precision XY Microscope Stage, Physik Instrument, Karlsruhe, Germany). Emitted light was detected by a high NA detection objective (UPLSAPO100XO, x100, NA 1.4, Olympus) and spectrally filtered (Di01-R405/488/561/635 dichroic, Semrock, ZET647NF notch filter, Chroma, Bellows Falls, VT, ET700/75m).

Image Acquisition and Analysis for SR Microscopy

For single-molecule localization microscopy, a reducing, oxygen scavenging buffer (Halpern et al., 2015) consisting of 20 mM cysteamine, 2 μ L/mL catalase, 560 μ g/mL glucose oxidase (all Sigma-Aldrich), 10% (w/v) glucose (BD Difco, Franklin Lakes, NJ), and 100 mM Tris-HCl (Life Technologies) was added. Image acquisition was started after a short delay needed to convert the majority of the fluorophores into a dark state at a laser intensity of 5 kW/cm². The exposure time was 50 ms and the calibrated EM gain

was 186. SR images were reconstructed from approx. 40000 frames using the ImageJ plugin Thunderstorm (Ovesný et al., 2014). The frames were filtered with a B-spline filter of order 3 and scale 2.0. Single-molecule signals were detected with 8-neighborhood connectivity and a threshold of three times the standard deviation of the first wavelet level. Detected local maxima were fitted with a 2D-Gaussian using least squares. Post-processing involved drift correction by cross-correlation, followed by filtering (settings: sigma of the fitted Gaussian < 200 nm; uncertainty of localization < 20 nm). Images were reconstructed as 2D histograms with bin size = 32 nm.

Giant unilamellar vesicles

Giant Unilamellar Vesicles (GUVs) were prepared by electroformation as described previously (Angelova and Dimitrov, 1986). Briefly, lipids and dye dissolved in chloroform were spread on glass slides coated with ITO (Indium-Tin-Oxide). The slides were placed under vacuum for 2 h to remove all traces of organic solvents. The lipid films were hydrated and swelled in 120 mM sucrose at 55°C. GUVs were electroformed by the application of an oscillating potential of 1.4 V (peak-to-peak) and 12 Hz for 3 h (Busch et al., 2015). GUVs compositions were prepared with DOPC and increasing molar fractions of DOGS-Ni-NTA lipid (5, 10, 15, and 20 mol%). Bodipy-PC was used to label the lipids at a dye/lipid ratio of 1/2500. Recombinant His-tagged Podocalyxin was conjugated with Alexa Fluor 568 NHS Ester (Thermo Fisher Scientific), and the degree of labelling quantified according to the manufacturer's protocol. GUVs were diluted in 20 mM HEPES, 50 mM NaCl, pH = 7.4 (120 mOsm) and then mixed with labeled Podocalyxin (~2 μ M) for at least 20 minutes before imaging (GUVs/proteins = 1/1 by volume). GUVs were imaged on a Nikon C2plus confocal microscope using a 60x water immersion objective (NA 1.2). Lipids

(Bodipy-PC) and protein (Alexa Fluor 568) were imaged through excitation at wavelength $\lambda = 488$ and 561 nm, respectively.

Endocytosis assay

Human apo-Transferrin (Sigma) was diluted to 1 mg/mL in PBS and labeled with Alexa Fluor 488 NHS Ester (Thermo Fisher Scientific) per manufacturer's protocol. Cells were prepared by plating and inducing wild-type (Control) and Muc1-42TR Δ CT-expressing MCF10A cells with 0.2 μ g/mL of doxycycline (Santa Cruz) for 18 h. The 488-labeled transferrin was diluted 1:1000 into fresh cell culture media with doxycycline (Santa Cruz) and incubated at 37°C, 5% CO₂ with cells for 30 min or 60 min. Cells were then detached with 0.05% trypsin EDTA (Thermo Fisher Scientific). Cells were washed with ice cold 0.5% BSA in PBS. Fluorescent signal was measured using a BD Accuri C6 flow cytometer. Confocal images cells were also acquired using a Zeiss LSM i880.

Analysis of HA synthesis

Control and lentiviral transduced MCF10A and primary equine synoviocytes were plated and induced with 0.2 μ g/mL doxycycline (Santa Cruz) for 24 h. Total levels of HA secreted into the cell culture media were measured via the DuoSet Hyaluronan ELISA kit following manufacturer's protocol. Briefly, a 96-well microplate was coated with recombinant human Aggrecan. HA in cell culture media was captured by the coated Aggrecan and detected with Biotin-HABP/HRP-Streptavidin. HA concentration was measured using *S. pyogenes* HA standard (R&D Systems).

Analysis of HA molecular size

HA molecular mass was assayed by electrophoresis and blot analysis essentially as described (Yuan et al., 2013), using agarose instead of

polyacrylamide for gel electrophoresis. Briefly, cell culture media containing HA was loaded in a 0.6% agarose gel in TBE buffer. Following electrophoresis, samples were transferred to HyBond N+ membrane (GE Healthcare). HA was probed with biotin-HABP (0.125 µg/ml in 0.1% BSA-PBS, 1 h) and subsequently detected with HRP-Streptavidin (0.025 µg/ml in 0.1% BSA-PBS, 1 h). Blots were developed in ECL substrate (Amresco), imaged on a ChemiDoc (BioRad) documentation system, and quantified in ImageJ Fiji (Schindelin et al., 2012).

Cancer cell line sorting

MCF10A wild-type (Control) or Muc1-42TR Δ CT-expressing cells and cancer cell lines (T47D, ZR-75-1, HeLa) were plated at 10,000 cell/cm² overnight. MCF10A cells were induced with 0.2 µg/mL doxycycline (Santa Cruz) for 24 h. Cell lines were nonenzymatically detached using 1 mM EDTA in PBS. Detached cells were washed with 0.5% BSA PBS. For each cell line, FITC-conjugated anti-Muc1 antibody was diluted 1:500 per million cells and incubated with cells on ice for 30 min. Cells were washed with 0.5% BSA PBS three time before sorting. Cells were sorted with a BD FACS Aria II onto poly-l-lysine treated 8 mm coverslips at 2,000 to 5,000 cells/cm² for SEM, allowed to adhere for 4 h at 37°C, and fixed for SEM imaging.

Analysis of mucin radius of gyration

The Muc1 polymer domain with 42 tandem repeats (S6 Muc1-42TR 10xHis) was produced recombinantly in suspension adapted Freestyle 293-F cells. Stable Freestyle 293-F cell lines were prepared with the Muc1-42TR 10xHis pPB tetOn PuroR as described above. Production of Muc1 biopolymer was induced with 1 µg/mL doxycycline (Santa Cruz) in 30 mL of suspension culture in Freestyle 293-F media. Induced media was collected after 24 h and purified on HisPur Ni-NTA resin (Thermo Fisher) according to standard protocols.

Briefly, 1 mL bed volume of Ni-NTA resin was rinsed with equilibration buffer (20 mM sodium phosphate, 0.5 M NaCl, pH = 7.4). Equilibrated resin was incubated overnight at 4°C with 10 mL harvested Freestyle 293-F media diluted in 30 mL of equilibration buffer. Beads were washed in equilibration buffer with 5 mM imidazole and eluted in equilibration buffer with 500 mM imidazole. Eluted protein was dialyzed against PBS and analyzed by SDS-PAGE. Gels were stained with SYPRO Ruby Protein Gel Stain (Thermo Fisher) according to manufacturer's instructions to confirm protein size and purity. Gels were blotted and probed with Muc1 and His antibodies to confirm mucin identity and PNA lectin to confirm mucin O-glycosylation. Purified recombinant Muc1 was dialyzed against PBS to remove imidazole.

The radius of gyration of the recombinant Muc1 polymer domain was measured with size-exclusion chromatography-coupled to multiangle light scattering (SEC-MALS). Purified protein (40 μ L of Muc1 with a concentration of 5 μ g/ μ L) was subjected to SEC using a Superdex 200 Increase 10/300 column (GE Healthcare) equilibrated in MALS buffer (20 mM sodium phosphate, 0.5 M NaCl, pH 7.4). The SEC was coupled to a static 18-angle light scattering detector (DAWN HELEOS-II) and a refractive index detector (Optilab T-rEX, Wyatt Technology). Data were collected every second at a flow rate of 0.7 mL/min. Data analysis was carried out using ASTRA VI, yielding the molar mass, mass distribution (polydispersity), and radius of gyration of the sample (32.0 nm \pm 0.4%). For normalization of the light scattering detectors and data quality control, monomeric BSA (Sigma) was used.

Variation of mucin size and surface densities

Mucin lengths

MCF10As expressing Muc1 GFP with 0, 10, or 42 tandem repeats were

sorted for similar levels of GFP on a BD FACs Aria II using the Muc1 antibody first for the 42 tandem repeat population then the GFP nanobody Atto 647N (Chromotek) for the 0, 10, and 42 tandem repeat populations. Stable populations were created from these sorted lines. Cells were plated onto 8 mm coverslips at 10,000 cells/cm² for 16-18 h, then induced with 0.2 µg/mL of doxycycline (Santa Cruz) for 24 h and fixed for SEM analysis.

Mucin cell surface density

Using the GFP nanobody with an approximate size of 2 nm (15 kDa) and picomolar affinity for GFP (GFP Binding Protein, Chromotek) and labeled with NHS-Alexa Fluor 647 according to manufacturer's protocol, 647-nanobody, MCF10A cells expressing Muc1-42TR GFP ΔCT were labeled in 5 µg/ml 647-nanobody for 20 min on ice to label only cell surface mucins. Cells were sorted with a BD FACS Aria II onto poly-l-lysine treated 8 mm coverslips at 5,000 to 10,000 cells/cm² for SEM, allowed to adhere for 4 h at 37°C, and fixed for SEM imaging. Alternatively, cells were sorted with a BD FACS Aria II into 1.7 mL Eppendorf tubes, resuspended in 100 µL 0.5% BSA PBS, and lysed with 100 µL 2x RIPA lysis buffer for estimation of mucin surface densities via SDS-PAGE. Lysed samples were run simultaneously with 647-nanobody standards of known molecular concentration. 647-nanobody fluorescence in lysed samples and standards were imaged on a Typhoon 9400 imaging system (GE Healthcare). Total fluorescence in each sample or standard was quantified in ImageJ Fiji (Schindelin et al., 2012). A standard curve was constructed by relating fluorescence from nanobody standards to their known concentration. The number of labeled mucins in each lysate were estimated based on the standard curve. The mucin surface density was estimated by dividing the total number of mucins by the known number of cells in each sample and their

average surface area of 5,000 μm^2 based on an average radius of 20 μm and spherically shaped wild-type cells in suspension. A standard curve was constructed based on the number of mucins per area and the known mean fluorescence signal from the FACS collected population. This standard curve was then applied to calculate the number of mucins per area of populations collected subsequently.

Expansion microscopy

Expansion microscopy (ExM) was performed as described previously (Tillberg et al., 2016) and involved steps of anchoring fluorescent dyes and proteins, gelation, digestion and expansion to achieve dye retention and separation. Briefly, fixed and stained cells were anchored with 0.1 mg/ml Acryloyl-X, SE (6-((acryloyl)amino)hexanoic acid, succinimidyl ester (ThermoFisher) in PBS for 16 h at RT, washed twice and further incubated 1 h at 37°C in a monomer solution (1 × PBS, 2 M NaCl, 8.625% (w/w) sodium acrylate, 2.5% (w/w) acrylamide, 0.15% (w/w) N,N'-methylenebisacrylamide) mixed with ammonium persulfate 0.2% (w/w) initiator and tetramethylethylenediamine 0.2% (w/w) accelerator for gelation. For digestion, gelled samples were gently transferred into 6 well glass bottom plates (Cellvis) and treated with Proteinase K (New England Biolabs) at 8 units/mL in digestion buffer (50 mM Tris (pH 8), 1 mM EDTA, 0.5% Triton X-100, 1 M NaCl) for 16 h at room temperature. For expansion, digested gels were washed in large excess volume of ddH₂O for 1 h. This was repeated 4 – 6 times until the expansion plateaued. Samples were imaged on a Zeiss LSM inverted 880 confocal microscope using a 40x water immersion objective (NA 1.1) in Airyscan mode to optimize resolution.

Isolation of extracellular vesicles

Cells were plated at 10,000 cells/cm² in appropriate dishes. Following induction with 1 µg/ml doxycycline (Santa Cruz) for 18 h, cells were rinsed with PBS twice then serum-starved for an additional 6 h with 1 µg/mL doxycycline (Santa Cruz). For actin depolymerization studies, cells were treated for 60 min with 10 µM LatA in serum free media prior to isolation. For HAS3 digestion studies, cells were treated with hyaluronidase for 60 min in serum-containing media before 6 h subsequent treatment in serum-starved media. Conditioned media from serum-starved cells was clarified by pelleting cellular debris through two consecutive centrifugations at 600x g for 5 min.

Plunge-freezing vitrification

From clarified media, 3-5 µL of sample was pipetted onto holey carbon-coated 200 mesh copper grids (Quantifoil Micro Tools, Jena, Germany) with hole sizes of ~2 µm. The grids were blotted from the reverse side and immediately plunged into a liquid ethane/propane mixture cooled to liquid nitrogen temperature using a custom-built vitrification device (MPI, Martinsried, Germany). The plunge-frozen grids were stored in sealed cryoboxes in liquid nitrogen until used.

Cryogenic transmission electron microscopy

Cryogenic transmission electron microscopy (cryo-TEM) was performed on a Titan Themis (Thermo Fisher Scientific, Waltham, MA) operated at 300 kV in energy-filtered mode, equipped with a field-emission gun, and 3838x3710 pixel Gatan K2 Summit direct detector camera (Gatan, Pleasanton, CA) operating in Counted, dose-fractionated modes. Images were collected at a defocus of between -1 µm and -3 µm. Images were binned by 2, resulting in pixel sizes of 0.72 -1.1 nm.

5.7.4 Quantification and statistical analysis

Scanning electron microscopy quantification

Cellular tube density, diameter, and length were analyzed in ImageJ Fiji (Schindelin et al., 2012). For quantification of tube density per area, a $\sim 2 \mu\text{m} \times 2 \mu\text{m}$ region of interest was drawn and the encompassed tubes counted manually using the cell counter plug-in. Tube diameter was measured by drawing a strain line through the tube cross section at its mid-point. Tube length was measured for tubes extending approximately parallel to the image plane, as identified by visual inspection, using the ImageJ line segment tool.

Giant unilamellar vesicles quantification

Dye fluorescent intensity was measured by taking 5 different line scans across the GUV in ImageJ Fiji (Schindelin et al., 2012). The intensity profile of each line was analyzed using Mathematica 10.3, where the integral of the intensity peak was calculated and averaged for 5 different lines per GUV.

Nanoparticle tracking analysis

Extracellular vesicles in the clarified media were analyzed using a Malvern NS300 NanoSight. Imaging was performed for 60 s with five captures per sample. Particle analysis was performed using Malvern Nanoparticle Tracking Analysis software.

Expansion microscopy quantification

Line profiles across membrane tubules in expansion images were used to measure the separation of GFP nanobody fluorescence from SUMO fluorescence. Brush height was determined by the difference of the the full width at half maxima (FWHM) between GFP nanobody fluorescence and SUMO fluorescence.

Statistics

Statistics were calculated in Graphpad Prism. One-way ANOVA and

post-hoc two-tailed student's *t* test were used where appropriate as indicated by figure legends. For boxplots - center lines show the medians; box limits indicate the 25th and 75th percentiles as determined by BoxplotR software; whiskers extend 1.5 times the interquartile range from the 25th and 75th percentiles, and notches, where shown, indicate the 95% confidence interval. See individual figure legends for number of replicates and statistical testing details. ns - not significant; */+ $p < 0.05$; **/++ $p < 0.01$; ***/+++ $p < 0.001$.

5.8 SUPPORTING FIGURES

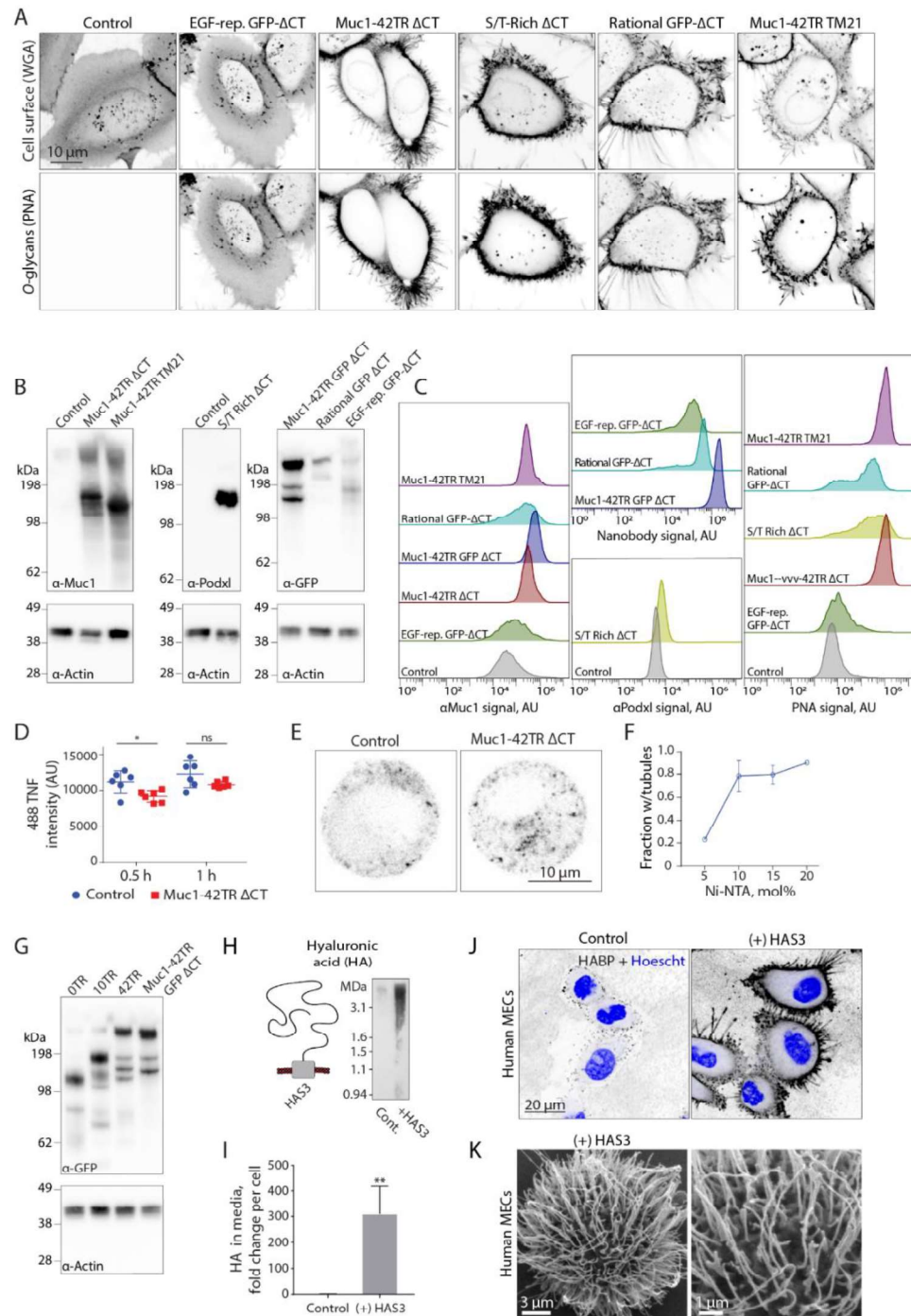


Figure 5.S1 – Related to Figure 5.1; Validation of genetically encoded mucins. **A**, Representative confocal microscopy images showing membrane tubularization induced by various engineered glycoproteins compared to wild-

type (Control) cells. The cell surface is visualized with lectin WGA (wheat germ agglutinin). Mucin staining with lectin PNA (peanut agglutinin) confirms glycoprotein *O*-glycosylation and surface localization on MCF10A cells. Images are individually adjusted for contrast, n = 2. **B**, Representative Western blots showing the relative size of various transmembrane biopolymers compared to each other biopolymer and the endogenous Mucl in wild-type (Control) cells, n = 3. **C**, Representative flow cytometry histograms showing the cell surface level of various transmembrane biopolymers, > 2,000 cells per population, n = 3. **D**, Quantification of endocytosis of Alexa Fluor 488 labeled transferrin (488 TNF) after 0.5 or 1 h of treatment. Quantification performed with flow cytometry, median signal reported with background subtraction, > 10,000 cells per population, n = 6, error bars are S.D. **E**, Representative confocal microscopy images of endocytosed 488 TNF after 0.5 h of treatment. **F**, Quantification of the fraction of GUVs with Podocalyxin tethered to the surface with visible membrane tubularization, n = 25. **G**, Western blot showing polymer sizes expressed in epithelial cells, analyzed with an antibody against the green fluorescent protein (GFP) tag, n = 5. **H**, (left) Cartoon of hyaluronic acid (HA) extruded by the transmembrane protein hyaluronic acid synthase 3 (HAS3). (right) Blot of HA in lysates of wild-type (Cont.) and hyaluronic acid synthase 3 (HAS3) expressing human mammary epithelial cells (MECs, MCF10A). Note that the expressed HA is a giant linear polymer in the MDa range. **I**, ELISA quantification of HA secreted by MECs into their media, normalized to the number of cells in the sample and the HA secretion of Control cells, n = 3. **J**, Representative confocal microscopy images of human MECs, either wild-type (Control) or stably expressing HAS3. Cells are stained with Hoescht (nucleus) and Alexa Fluor 568 hyaluronic acid binding protein (HABP). **K**, Representative SEM images showing highly elongated membrane tubules in HAS3-expressing human MECs (left) and a zoomed in region on the same cell (right). ns – not significant, * p < 0.05, ** p < 0.01, *** p < 0.001 (*post-hoc* student's two-tailed *t* test).

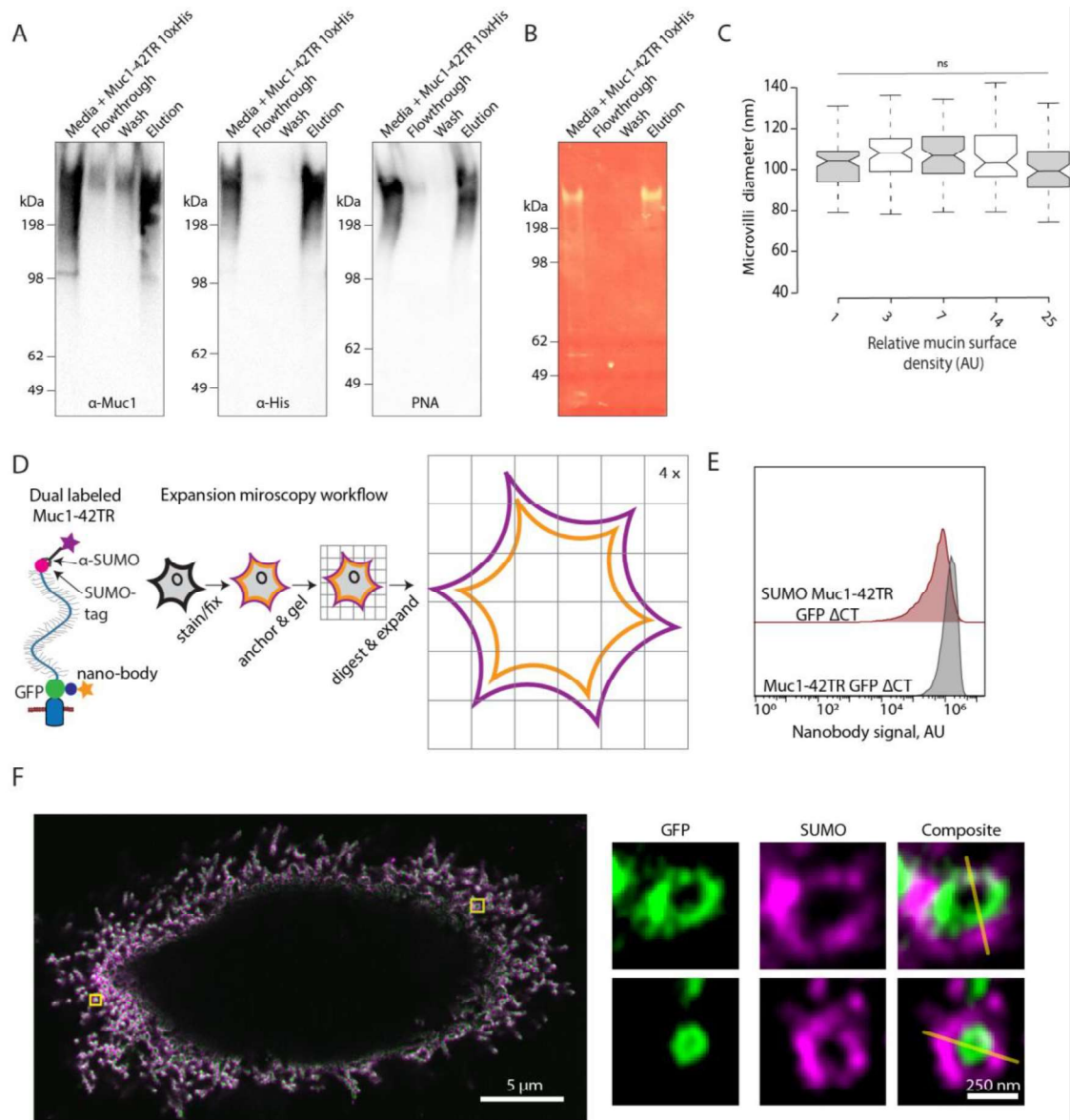


Figure 5.S2 – Related to Figure 5.4; Supporting information for physical characterization of individual mucins and mucin ensembles. A, Western blot validation of recombinant Muc1-42TR production (Media + Muc1-42TR 10xHis), Ni-NTA resin binding of the protein (Flow-through), wash off non-specific proteins (Wash), and purified recombinant Muc1-42TR polymer (Elution). Samples are probed with anti-Muc1 and anti-His antibodies as well as PNA (peanut agglutinin) to bind *O*-linked glycans. **B,** SYPRO Ruby protein gel stain for samples described above. **C,** Quantification of epithelial microvilli diameter for the indicated relative mucin surface densities. Box notches indicate 95% confidence intervals. **D,** (left) Mucin construct (Muc1-42TR) with SUMO

and GFP tags flanking the polymer domain for visualization of polymer extension with expansion microscopy (ExM). (right) ExM sample workflow. First, samples are stained and fixed. Then the proteins are chemically linked (anchored) to monomers which polymerize to form a gel. Proteins are then digested, and the gel is expanded to four times the original size. **E**, Representative flow cytometry histogram showing the geometric mean of GFP nanobody binding for the indicated biopolymers. The two polymers are expressed on the cell surface at comparable levels, > 14,000 cells per population, n = 3. **F**, (left) Representative ExM image with two regions of interest on the cross-section of microvilli indicated by yellow boxes. (right) Zoomed in regions of interest. Yellow line composite image represents a line trace which may be used to calculate the full-width half max value for the GFP nanobody and SUMO antibody signals to calculate the cell surface brush height. ns – not significant.

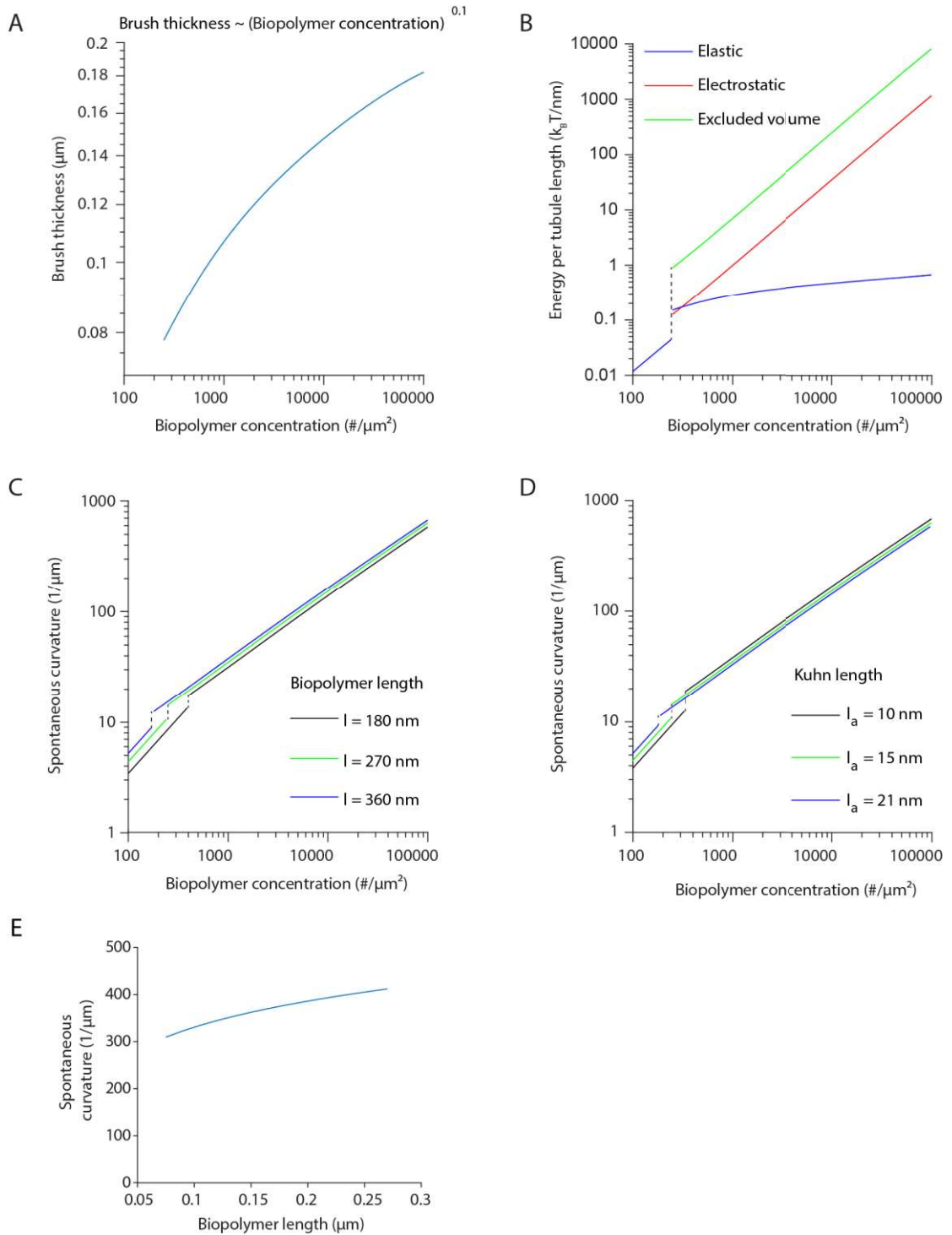


Figure 5.S3 – Related to Figure 5.4; Additional polymer brush theory predictions for curvature generation by intermolecular interactions in the glycocalyx. A, Graph for the predicted brush thickness as a function of biopolymer surface density in the brush regime. Brush thickness scales

approximately as a power law with biopolymer concentration. **B**, Plot showing energetic contributions as functions of the biopolymer density. In the mushroom regime, polymers have only elastic energy, while in an extended brush, excluded volume and electrostatic interactions contribute to biopolymer free energy. **C**, Plot depicting variation of spontaneous curvature generated with biopolymer density and molecular length. **D**, Graph displaying trend of spontaneous curvature as a function of biopolymer density and Kuhn length. Kuhn length, equal to twice the persistence length, is directly proportional to polymer bending stiffness, and is referred to as the length of a monomeric segment in the manuscript. Plots in (A-D) are in log-log format. Plots in (A) and (B) use biopolymer length, $l = 270$ nm, and monomeric segment length, $l_a = 15$ nm. Plot (C) employs polymer monomer segment size of 15 nm, and (D) uses biopolymer length of 270 nm. **E**, Predicted dependence of spontaneous curvature on biopolymer length at high density. This graph uses polymers of $l_a = 15$ nm packed at a density of $50000 \text{ \#}/\mu\text{m}^2$.

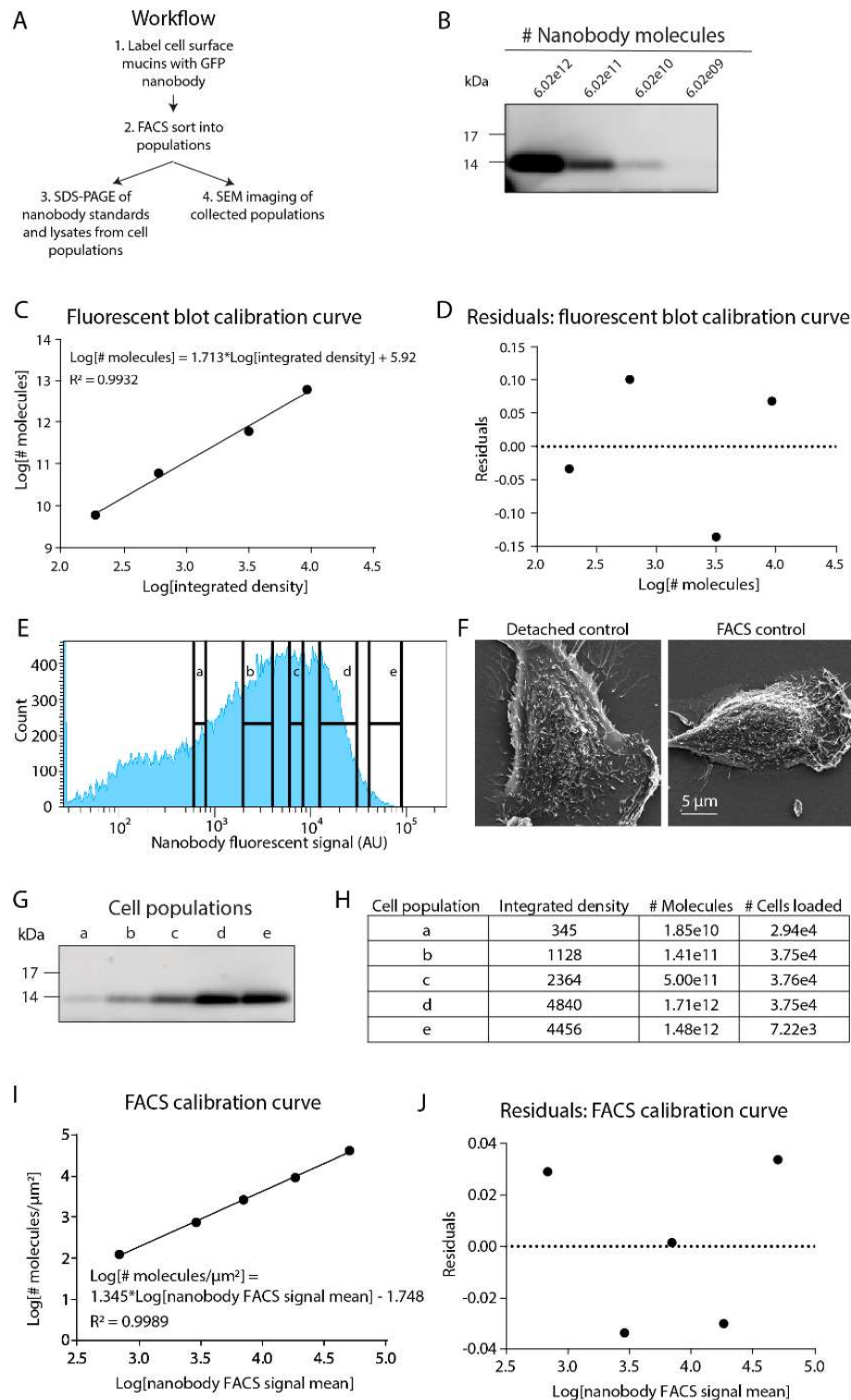


Figure 5.S4 – Related to Figure 5.5; Fluorescence-activated sorting and quantification of Muc1 surface densities. A, Extended workflow for

quantitative experiments at different Muc1 surface densities. **B**, SDS-Page calibration of Alexa Fluor 647 labeled nanobody. **C**, Calibration curve between the log value for integrated density of fluorescence signal from nanobody dilution series (shown in (B)) versus the log value of the number of molecules loaded. A linear regression fit and R^2 value are shown. **D**, Residuals for the linear regression fit shown in (C). **E**, Fluorescence-activated cell sorting (FACS) histogram showing the nanobody fluorescence signal and the populations 'a' through 'e' collected for these experiments. **F**, Representative scanning electron microscopy (SEM) images of wild type cells which were non-enzymatically detached from the substrate then re-adhered (detached control) for SEM imaging and cells which were non-enzymatically detached from the substrate, collected through the FACS, then re-adhered (FACS control). These images demonstrate that the method of FACS collection did not influence the membrane shapes observed with Muc1-42TR Δ CT expression (shown in Fig. 5.2F). **G**, SDS-Page analysis of fluorescent nanobody signal in each cell population, a-e, after collection and lysis of the cells. **H**, Table describing the integrated density signal from the fluorescence image shown in (G), the calculated number of molecules based on the calibration curve in (C), and the number of cells loaded in the protein gel, (G), based on the number of cells collected with FACS for each population, (E). **I**, Calibration curve between the log of the nanobody mean signal from the FACS versus the number of molecules calculated for each population. The number of molecules per sample was normalized by the number of cells loaded and the approximate area per cell. Linear regression fit and R^2 values shown. **J**, Residuals for linear regression fit shown in (I).

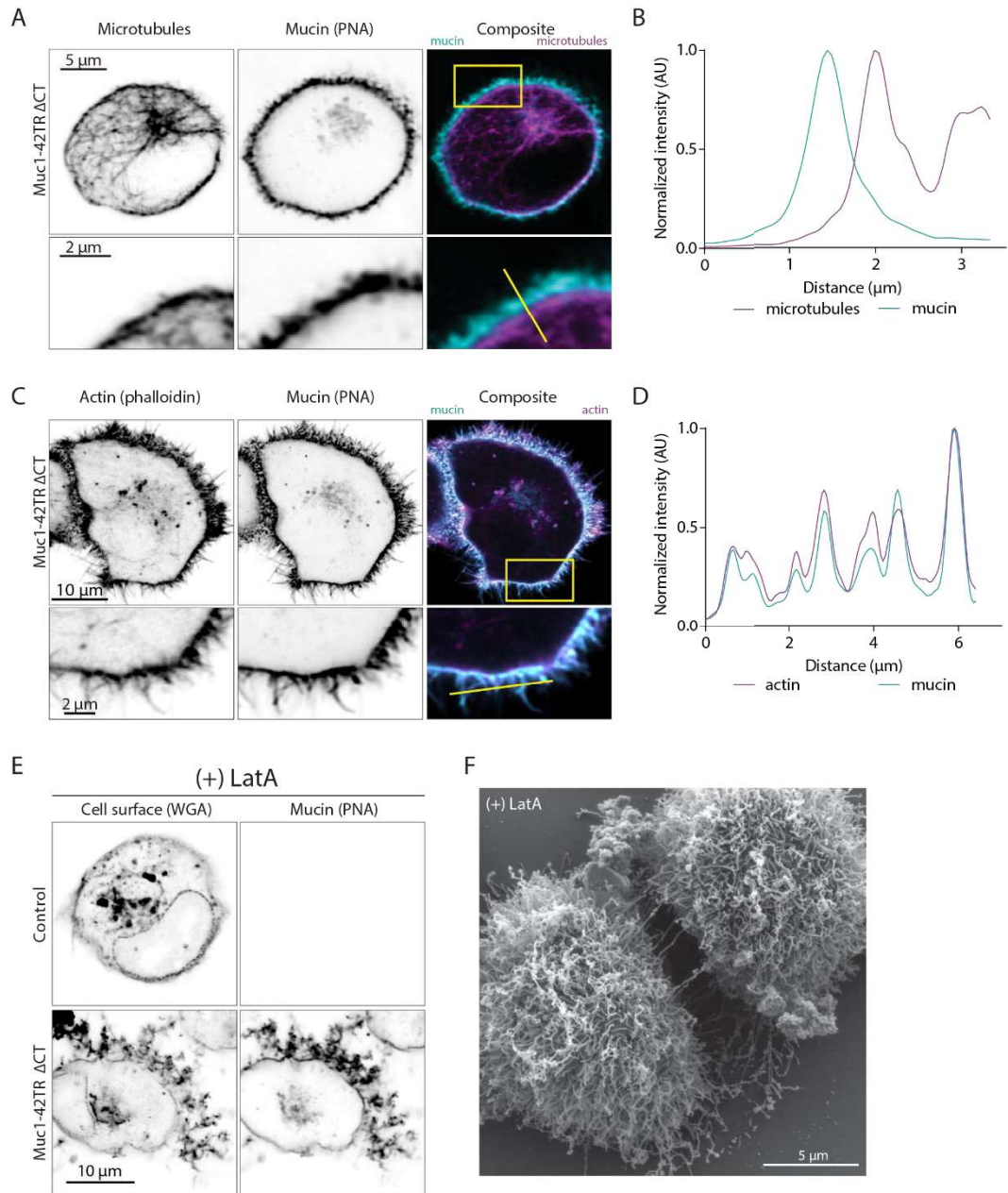


Figure 5.S5 – Related to Figure 5.6; Tubular membrane shapes contain filamentous actin cores and resemble microvilli. A, Representative confocal microscopy images of epithelial cells expressing Muc1-42TR Δ CT showing indirect microtubule staining with anti-microtubule and Alexa Fluor 568-labeled secondary antibodies. Mucins are labeled with Alexa Fluor 647 PNA (peanut agglutinin). The bottom row shows the region of interest from the composite image (yellow box), $n = 3$. **B,** Fluorescent intensity line trace from (A) (bottom row, yellow line). Values are normalized for their respective maximum

intensities. **C**, Representative confocal microscopy images of epithelial cells expressing Muc1-42TR Δ CT showing actin staining with Alexa Fluor 568 phalloidin. Mucins are labeled with Alexa Fluor 647 PNA. The bottom row shows the region of interest from the composite image (yellow box), $n = 3$. This data repeats and elaborates on (Fig. 5.5A, B). **D**, Fluorescent intensity line trace from (C) (bottom row, yellow line). Values are normalized for their respective maximum intensities. **E**, Representative confocal microscopy images of the midplane of wild type (Control) or Muc1-42TR Δ CT cells which have been treated with 10 μ M Latrunculin-A (LatA) for 1 h, $n = 3$. **F**, Representative SEM image of LatA treated Muc1-42TR Δ CT cells.

5.9 SUPPLEMENTAL NOTE: THEORETICAL CONSIDERATIONS

5.9.1 Glycocalyx polymer brush model

We propose a simple model to explain how biopolymers in the glycocalyx can generate entropic driving forces for membrane curvature. The model considers long chain polymers anchored on one end to the plasma membrane. Common examples of long-chain polymers in the glycocalyx include mucins and hyaluronic acid (HA), which we model specifically here. The modeling framework could be similarly applied to other types of glycocalyx polymers, including polysialic acid and other glycosaminoglycans. Hyaluronic acid is a semi-flexible linear polysaccharide comprised of repeating units of glucuronic acid and N-acetylglucosamine. Mucins have a more complex bottlebrush structure comprised of a central polypeptide backbone and densely clustered glycan side chains along the backbone. Although their structure is complex, bottlebrush polymers can be modelled as effective linear polymers with a monomer size on the order of the side chains (Paturej et al., 2016). Therefore, we consider all glycocalyx polymers in our model to be linear or effectively linear.

Biopolymers in the glycocalyx are anchored to the cell surface in several

ways, including through transmembrane anchors, covalent conjugation to integral membrane proteins, and non-covalently to specific transmembrane receptors. Cell surface mucins are anchored directly near their carboxy terminus by a single transmembrane domain. Hyaluronic acid is anchored to the cell surface through specific transmembrane receptors on the cell surface. While it is possible for hyaluronic acid to be anchored at multiple points along the polymer backbone, for simplicity, we consider all glycocalyx polymers to have a single membrane anchor at one end.

The cell surface is also decorated with many types of integral and peripheral membrane proteins. These molecules could also contribute to an entropic pressure on the cell membrane, similar to a 2D gas pressure. To isolate the effects of glycocalyx polymers on the membrane, we neglect possible contributions from other cell surface proteins, as well as intracellular forces. However, the model could be extended to include these additional contributions to the system energy.

Biopolymers have excluded volumes accounting for steric interactions between monomers on the same polymer as well as between monomers on adjacent molecules (de Gennes, 1980). Large negative charges on acidic sugars, such as glucuronic acid and sialic acid, give rise to intramolecular and intermolecular electrostatic interactions (Israels et al., 1994). Finally, the polymers and the brush have entropic contributions due to the elastic energy, which captures the stretch of the molecules (de Gennes, 1980). Embedded in a deformable lipid membrane, the energy of this polymer glycocalyx and that of the membrane can minimize to yield the equilibrium configuration (Lipowsky, 1995; Stachowiak et al., 2012). Hence, in our model below, we perform an energy minimization of the glycocalyx and the underlying membrane to describe the

surface curvature.

Depending on surface density, polymers tethered to a surface exhibit two particular regimes of physical behavior – mushroom and brush. The Flory radius measures the approximate size of an entire polymer, and is given by $R_F \approx l_a N_a^\nu = l^\nu l_a^{1-\nu}$, where N_a is the number of monomers in the polymer, l_a is the size of each monomer or effective monomer, l is the fully extended length of the polymer chain, and ν is called the Flory exponent. $\nu \cong 0.6$ for hydrophilic biopolymers in good solvents like water. At low densities, such that intermolecular spacing is larger than the polymer Flory radius, i.e. $C_G < 1/(R_F)^2$, where C_G is biopolymer concentration, biopolymers take up preferable conformations independent of neighbor interactions. In this regime, the flexible molecules can coil up to exhibit mushroom-like structures. On the other hand, at high surface concentrations, when the intermolecular spacing is smaller than the Flory radius, intermolecular interactions can dominate and stretch the biopolymers out into a brush-like structure. The polymer layer extension or thickness, the stored energy, and the generated membrane curvatures exhibit different scaling laws in these regimes, as described below.

In the mushroom regime, the attachment of a biopolymer to a flat, impenetrable surface reduces the number of accessible molecular conformations, cutting down the polymer shapes that penetrate the surface. Curving the impenetrable grafting surface can marginally increase the permissible configurations, and increase the entropy of the polymer. Thus, flexible biopolymers tethered to a deformable membrane can generate curvatures, as described by Lipowsky (Lipowsky, 1995). However, the additional entropy due to membrane curvature is small and consequently, curvatures generated by polymer mushrooms are also small, relative to

deformations elicited by intermolecular interactions in polymer brushes. In this mushroom regime, the free energy due to the entropic contribution of each mushroom polymer tethered to a curved membrane is:

$$F_{mushroom} = -TS_{mushroom} \sim -k_B T \frac{2\pi R_{mushroom}}{R}, \quad (1)$$

where the reference configuration is the polymer tethered to a flat surface, $S_{mushroom}$ is the corresponding entropic contribution, $R_{mushroom}$ is the Flory radius of the mushroom-shaped biopolymer, and R is the radius of curvature of the underlying membrane. In the mushroom regime, we consider the formation of spherical membrane structures. The bending energy of the curved membrane is:

$$F_{membrane} = \frac{\kappa}{2C_G R^2}, \quad (2)$$

where κ is the bending stiffness of the membrane bilayer, C_G is the surface density of the biopolymers, and $1/C_G$ is the area available for each polymer. Minimizing the total energy, $F_{total} = F_{mushroom} + F_{membrane}$ with respect to the radius of curvature, R , as $\partial F_{total}/\partial R = 0$, we obtain the following scaling law for R :

$$R \sim \frac{\kappa}{k_B T} \frac{1}{2\pi C_G l_a N_a^{v'}}, \quad (3)$$

where l_a is the size of monomeric segments and N_a is the number of such monomers in a polymer molecule.

At high surface densities, such that neighboring polymer molecules interact with each other, grafted polymers exhibit a brush-like structure (de Gennes, 1980). In this regime, we consider the formation of tubular structures from the membrane and predict the tubule curvatures generated by intermolecular crowding effects on the cell surface. An energy minimization approach elucidates the equilibrium curvature and brush extension as follows. For a tubule with radius R , the energy of the glycocalyx per length of the tubule contains elastic, excluded volume, and electrostatic components (Borisov and Zhulina, 2002; Bracha et al., 2013; Zhulina et al., 2006):

$$F_{brush} = F_{elastic} + F_{excluded\ volume} + F_{electrostatic}, \quad (4)$$

$$F_{brush} = k_B T \int_R^{R+H} \left[\frac{3}{2l_a^2 c_p s} + \left(w + \frac{\alpha_b^2}{2\Phi_{ion}} \right) c_p^2 s \right] dr, \quad (5)$$

where R is the radius of the tubule, H is the thickness of the glycocalyx brush, l_a is the size of monomeric segments that form the biopolymers, c_p is the monomer concentration, and s is the area per polymer. At the tubule surface, the area per polymer, $s(r = R)$ is related to the biopolymer surface density, C_G , as $s(r = R) = 1/C_G$. w is the excluded volume of monomer segments, α_b is the degree of ionization of a monomer, Φ_{ion} is the ion concentration in bulk solution, and r is a radial coordinate.

Zhulina et al. (Zhulina et al., 2006) provide expressions for c_p . Given the monomer length and diameter are similar (Paturej et al., 2016), we consider the monomeric segments to be cylinders with an aspect ratio close to 1. The energy per length of the underlying membrane bent into the tubular structure is

(Helfrich, 2014):

$$F_{membrane} = \frac{\pi\kappa}{R}, \quad (6)$$

where κ is the membrane bending modulus. Thus, the total energy per tubule length is:

$$F_{total} = F_{brush} + F_{membrane} \quad (7)$$

$$= k_B T \int_R^{R+H} \left[\frac{3}{2l_a^2 c_p s} + \left(w + \frac{\alpha_b^2}{2\Phi_{ion}} \right) c_p^2 s \right] dr + \frac{\pi\kappa}{R},$$

Minimizing the total energy with respect to the tubule radius ($dF_{total}/dR = 0$) reveals the dependence of the spontaneous curvature on the properties of the glycocalyx and the cell membrane, including the surface density of biopolymers.

We consider the implications of this theory for native Muc1, as an example mucin. We course-grain the bottlebrush biopolymer into N_a effective monomers of size $l_{a,eff}$ (Paturej et al., 2016). In this work, we measure the radius of gyration, R_G , of Muc1 to be 32 nm. We estimate the overall stretched length, l , to be 270 nm based on electron micrographs of Muc1 purified from human HEP-2 epithelial cells (Bramwell et al., 1986). The radius of gyration is related to the Flory radius by $R_G \approx \frac{1}{\sqrt{6}} R_F = \frac{1}{\sqrt{6}} l^\nu l_{a,eff}^{1-\nu}$. Using estimates of $R_G = 32$ nm, $l = 270$ nm, and $\nu = 0.6$, we estimate the mucin to be described by $N_a = 18$ effective monomeric segments each having a size of $l_{a,eff} = 15$ nm. We note that this effective monomer size is in good agreement with expectations based on estimates of the mucin side chain size to be 5-10 nm (Kesimer et al., 2013;

McMaster et al., 1999). We assume that sialic acids on mucins contribute to a charge density of approximately $5 e^-$ per 20 amino acid tandem repeat. Our assumption is based on most mucin *O*-glycosylation sites being occupied with sialylated glycans (Bäckström et al., 2003; Müller et al., 1999).

The scaling law for the mucin mushroom regime predicts small spontaneous curvatures for low biopolymer densities (Fig. 5.3C). The predicted spontaneous curvatures are comparable to the curvatures of the bleb-like protrusions observed in cells expressing low surface densities of mucins, as shown in Fig. 5.4B, 180 mucins/ μm^2 . For higher densities, where the biopolymers form a brush, the corresponding model above predicts the generation of curvatures similar or greater to those observed in the tubules on the cells of Fig. 5.4B, 52000 mucins/ μm^2 . The curvature of such tubules is predicted to increase exponentially with biopolymer density. Notably, the continuous transition between mushroom and brush regimes predicted about a biopolymer density of 250 #/ μm^2 accompanies a change in cell surface morphology from bleb-like to tubulated (Fig. 5.4B, D, E).

Similarly, HA molecules closely resemble linear polymer chains. For instance, a 1 MDa HA molecule has a length of 2.5 μm when stretched out, and can be modeled as a chain of 250 monomeric units approximately 10 nm long (Cleland Robert L., 2004; Hayashi et al., 1995). Polymer theory predicts such a polymer to have a large Flory radius of about 1 μm , which is more than an order of magnitude larger than that of Muc1. Thus, HA is expected to have a much larger effective volume and physical presence on the cell surface than Muc1. The consequently stronger intramolecular and intermolecular interactions in HA should render it significantly more effective at bending the membrane than Muc1. Furthermore, considerably lower surface density of HA is expected to

generate the same membrane curvature as a surface densely crowded with Muc1.

We also conducted numerical calculations for the specific example of HA. Adopting the approach of Bracha et al. on DNA, also a linear polyelectrolyte, we coarse grain hyaluronic acid into N_a cylindrical segments of length l_a and diameter d to allow application of polymer brush theory scaling laws (Bracha et al., 2013). The Kuhn length, l_a , of the biopolymers is twice the persistence length and the length scale at which the molecule is straight. Hyaluronic acid is semi-rigid owing to the local stiffness that arises from intrinsically large size of the sugar ring monomers and the hindered rotations about the glycosidic linkages (Day and Sheehan, 2001). Measurements of the persistence length range from 5 to 9 nm. The diameter of the hyaluronic acid chain is about 0.6 nm (Cowman et al., 2005). In this work, we measure the molecular weight of hyaluronic acid produced by the hyaluronic acid synthase 3 (HAS3) to be approximately 3 MDa. This large size corresponds to a fully stretch length of approximately 10 μm , assuming a disaccharide size of 1 nm.

5.9.2 Force requirements for cell surface blebs and tubes

To predict the relative frequencies of blebs and tubes on the cell surface, we perform energetic calculations for the cell membrane. The crowding pressure of the glycopolymers effectively increases the natural curvature of the cell membrane. Hence, we lump together the crowding effects of the glycocalyx into a spontaneous membrane curvature, c_0 .

Intracellular forces pushing the cell membrane out, e.g. actin polymerization, can generate cylindrical tubes (Weichsel and Geissler, 2016). Here we consider a tube of length L and radius R_{tube} generated due to a force

f . On the other hand, a hydrostatic pressure difference p between inside and outside the cell can form spherical blebs of radius R_{bleb} (Charras and Paluch, 2008). The energy of the membrane in these configurations includes the bending energy, surface tension, and contributions from the pressure p or the force f (Derényi et al., 2002; Helfrich, 2014; Seifert et al., 1991):

$$F = \int_A \frac{\kappa}{2} (c_1 + c_2 - c_0)^2 dA + \sigma A - pV - fL, \quad (8)$$

where κ is the bending stiffness of the membrane, c_1 and c_2 are the principal curvatures, c_0 is the spontaneous curvature of the membrane – generated due to the crowding pressure of the biopolymers, A is the area of the membrane, and σ is the surface tension of the membrane. For tubes, $p = 0$, $f \neq 0$, and L is the length of the tube, whereas for blebs, $f = 0$, $p \neq 0$, and V is the bleb volume.

A cylindrical tube of radius R_{tube} has $c_1 = 0$ and $c_2 = 1/R_{tube}$, which simplify the energy:

$$F_{tube} = \left[\frac{\kappa}{2} \left(\frac{1}{R_{tube}} - c_0 \right)^2 + \sigma \right] 2\pi R_{tube} L - fL, \quad (9)$$

The case of a spherical bleb with a very thin neck provides an upper limit on the energy of a bleb. For a bleb with radius R_{bleb} , $c_1 = c_2 = 1/R_{bleb}$, and

$$F_{bleb} = \left[\frac{\kappa}{2} \left(\frac{2}{R_{bleb}} - c_0 \right)^2 + \sigma \right] 4\pi R_{bleb}^2 - \frac{4\pi R_{bleb}^3}{3} p, \quad (10)$$

At equilibrium, these energies are minimized with respect to the radii of the blebs and tubes (Derényi et al., 2002). The tube energy is also minimized with respect to the tube length L at steady state (Derényi et al., 2002). That is,

$$\frac{\partial F_{tube}}{\partial R_{tube}} = 0, \quad \frac{\partial F_{tube}}{\partial L} = 0, \quad (11)$$

$$\frac{\partial F_{bleb}}{\partial R_{bleb}} = 0, \quad (12)$$

at equilibrium. The equilibrium equations (Eq. 11) for the tube imply:

$$R_{tube} = \frac{1}{\sqrt{c_0^2 + 2\sigma/\kappa}}, \quad (13)$$

And

$$f = 2\pi\kappa \left(\sqrt{c_0^2 + 2\sigma/\kappa} - c_0 \right), \quad (14)$$

These equilibrium calculations predict the tube radius is completely governed by the mechanical properties of the lipid bilayer and the spontaneous curvature. These calculations do not account for the structural support of actin filaments widening the tubes.

Bleb energy minimization (Eq. 12) yields the pressure requirement for a bleb of a given size:

$$p = \frac{2\sigma}{R_{bleb}} - \frac{c_0\kappa}{R_{bleb}} \left(\frac{2}{R_{bleb}} - c_0 \right). \quad (15)$$

Eq.13-15 relate the force or pressure required to maintain a tube or bleb with the spontaneous curvature generated by the biopolymers. Fig. 5.3C details the dependence of the spontaneous curvature on biopolymer concentration. We thus graph the force and pressure requirements against the biopolymer concentration (Fig. 5.3D). Comparisons with typically observed forces from actin polymerization and hydrostatic pressures explain the relative densities of tubes and blebs as a function of biopolymer density.

CHAPTER 6
THE CANCER GLYCOCALYX DYNAMICALLY TUNES CELLULAR
MIGRATION

6.1 ABSTRACT

Muc1 is a large, heavily *O*-glycosylated membrane protein that is overexpressed in the majority of cancers and constitutes the major structural element of the cancer cell glycocalyx. While the biophysical properties of the glycocalyx directly regulate cell-extracellular matrix adhesion, cell-cell interactions, and receptor spatial organization, how these properties change dynamically during acquisition of a metastatic phenotype is largely unknown. First, we evaluate how a mucinous glycocalyx impacts cellular migratory mode. Cellular mucins were highly rigid and mechanically disrupted integrin adhesion, resulting in complete dissociation of cells from the substrate. The cells exhibit striking and rapid 3D motility compared to wild-type cells without Muc1. To dissect the relationship among glycan biosynthesis, mucin rigidity, and the bulk properties of the cancer-specific glycocalyx, we use Darwinian evolution to isolate sub-populations of Muc1-expressing breast epithelial cells that present with distinct mucin glycophenotypes. Remarkably, alterations in glycosylation were associated with profound differences in glycocalyx structure, even in isogenic cell lines. We isolated a stable population of cells that expresses high levels of Muc1, but these mucins were apparently flexible and had no observable effect on cell adhesion. Based on lectin profiling, we identified specific patterns of Muc1 *O*-glycosylation associated with the two extremes in glycocalyx structures, rigid or flexible. Of notable significance, we discovered that metabolic reprogramming by the hypoxia could induce a glycophenotype consistent with mechanically rigid

mucins. Future studies will identify the specific glycosylation machinery associated with the different glycophenotypes, with the hope of identifying new avenues of therapeutic intervention based on normalizing the mechano-phenotype of the cancer cell glycocalyx.

6.2 INTRODUCTION

6.2.1 Cells exhibit distinct migratory modes based on extracellular matrix interactions

Cancer cells must migrate in order to metastasize from the primary tumor site – first locally invading the tissue surrounding the tumor, then entering the bloodstream, circulating, exiting the bloodstream, and finally colonizing a distant site (Nguyen et al., 2009). Cells can migrate using a variety of distinct modes – either as individual cells (using mesenchymal-like, adhesion-dependent mechanisms or amoeboid-like, adhesion-independent mechanisms) or collectively (as coordinated groups with strong cell-cell junctions, often with a “leader” cell and stream of “follower” cells) – with the ability to switch between those modes depending on various chemical and physical determinants (Friedl and Wolf, 2010; Liu et al., 2015).

Cellular migration mode is determined by many factors related to both features of the extracellular matrix (ECM) and features of the cell. Cellular determinants of migratory mode include strength of cell-cell junctions, strength of cell-ECM adhesion, and cell protrusion and traction generated by pulling the ECM (Friedl and Wolf, 2010). Cells with strong focal adhesions that turn-over slowly will exhibit mesenchymal migration (Friedl and Wolf, 2010; Liu et al., 2015). Amoeboid migration generally refers to migration without mature focal-adhesion formation, weak interactions with the ECM, and either a blebbing or

pseudopodal mechanism of leading-edge protrusion (Friedl and Wolf, 2003, 2010; Liu et al., 2015; Yoshida and Soldati, 2006). Without focal adhesion interactions, these cells instead migrate by frictional coupling between the cell-surface and the ECM. Metastatic cells may benefit from amoeboid migration because cells migrating in an amoeboid migratory mode can more easily fit through gaps in the ECM and migrate at a higher velocity than cells in a mesenchymal migratory mode (Liu et al., 2015). Though these determinants – adhesion strength, cell protrusion, and cell contractility – are clear indicators of cellular migration mode, not all molecular determinants to migration mode are known. Interactions which change the strength of focal adhesion or cell-cell adhesion may also cause cells to switch between migratory modes.

6.2.2 The glycocalyx physically separates cells from their extracellular matrix

Physically separating the cell from the ECM, the cellular glycocalyx – the sugary coating on the surface of eukaryotic cells – is uniquely positioned to dynamically regulate cell-ECM and cell-cell interactions. Glycosylation – the process of covalent attachment of polysaccharides to proteins at Asn (N-linked) or Ser/Thr (O-linked) residues – is the most abundant post-translational modification of proteins, with half of all proteins predicted to be glycosylated therefore glycans represent significant cellular biomass (Apweiler et al., 1999; Ju et al., 2013; Varki et al., 2009a). Mucins – a family of heavily O-glycosylated, membrane bound proteins – are a major structural element of the glycocalyx (Hatrup and Gendler, 2008; Kufe, 2009). Mucins normally line the apical surface of the secretory epithelium in the body; however, upon neoplastic transformation, there is a loss of cell polarity which results in mucins coating the entire cell surface, a feature linked to poor prognosis in metastatic disease

(Hattrup and Gendler, 2008; Hayes et al., 1991; McGuckin et al., 1995; Rahn et al., 2001). Muc1 expression level correlates with cancer aggressiveness, poor therapeutic response, and poor survival in many different types of cancer; and Muc1 is found on the surface of more than 60% of circulating tumor cells indicating its role in metastasis (Guddo et al., 1998; Hinoda et al., 2003; Hollingsworth and Swanson, 2004; Horm and Schroeder, 2013; Joshi et al., 2009). More than half of the molecular weight of mucins comes from the sugar structures on the protein which frequently carry a negative charge due to sialylation of *O*-glycans giving mucins anti-adhesive properties (Hattrup and Gendler, 2008; Horm and Schroeder, 2013; Kufe, 2009; Varki et al., 2009a). The glycocalyx can be seen as a large, negatively charged biopolymer network which sterically repels intercellular interactions, specifically preventing adhesion molecules like integrins and cadherins from performing their functions therefore enabling detachment from the primary tumor and initiation of metastasis.

6.2.3 Cellular adhesion is regulated by the cellular glycocalyx

Previous research has begun to explore the role of the glycocalyx in mediating cell-ECM interactions and cellular adhesion. Theoretical work studying the effect of glycocalyx thickness and stiffness on cell-surface integrins has indicated that the mechanical forces generated between the glycocalyx and ECM can alter the spatial and temporal dynamics of integrin interaction with the ECM through a purely biophysical mechanism, without added signaling or cytoskeletal-binding information (Paszek et al., 2009). Experimental work has validated these findings. Paszek et. al. have recently shown decreased adhesion rates and increased adhesion area for cells with increased glycocalyx

thicknesses (Paszek et al., 2014). This indicates that the glycocalyx can influence cellular adhesion dynamics. Others have shown that high levels of Muc1-expression can completely block integrin-mediated adhesion (Shurer et al., 2018; Wesseling et al., 1995) as well as blocking cadherin interactions (Wesseling et al., 1996). However, these experiments were performed without added information about cellular glycosylation status.

O-glycosylation of mucins impacts their structural properties. Light-scattering experiments have shown the O-glycosylation of mucin extends the random coil structure of the protein and increases the stiffness of the chain (Shogren et al., 1989). NMR studies have shown increased glycosylation confers decreased conformational freedom of mucins (Gerken et al., 1989). Transmembrane mucins are generally considered to be “rod-like”, extending straight out from the cell-surface. The mechanical properties of purified mucins depend on the glycosylation state of the protein. However, there is lack of studies exploring the effect of these mechanical properties on sterically inhibiting cellular adhesion.

The cancer cell glycocalyx has a distinct composition which differs from the glycocalyx found on healthy cells (Varki et al., 2009b). An especially thick or rigid glycocalyx – dictated by glycoprotein expression and extent of glycosylation – may directly impact the force balance between cells and the ECM and potentially result in complete disassociation of focal adhesion – a required step for initiation of amoeboid migration. It is currently unknown what specific cellular features are required to produce a thick glycocalyx which can sterically inhibit integrin adhesion and if production of excess glycocalyx – either increased in density or another property such as charge – can promote an efficient amoeboid form of migration by reducing cellular adhesion.

6.2.4 Cancer-specific metabolic changes reshape the glycocalyx

Neoplastic transformation is associated with significant changes to the metabolic phenotype of cells. An increase in aerobic glycolysis of cells is now seen as a hallmark of cancer (DeBerardinis and Chandel, 2016; Ying et al., 2012). Cancer cells use increased glycolytic flux to generate the necessary biomass such as proteins, nucleic acids, and sugars, for rapid cell proliferation (Lunt and Vander Heiden, 2011). Hypoxia-inducible factor 1-alpha (HIF-1 α) is a master regulator of the metabolic switch from oxidative phosphorylation to glycolysis (Dibble and Manning, 2013). Hypoxia has also been shown to be an adverse prognostic marker with decreased disease-free survival rates among patients (Vaupel and Mayer, 2007). Changes to cellular metabolism such as increased flux through glycolysis brought on by changes in the cell microenvironment such as hypoxia may be linked cancer progression and aggressiveness.

Changes to cell-surface glycosylation are also frequently observed in cancer cells. Cell-surface *O*-glycans have been observed to be truncated and reduced in complexity in cancer cells (Pinho and Reis, 2015), typically thought to be due to a decrease or change in the expression of glycosyltransferases (Berois et al., 2013; Gomes et al., 2009). For example, there is an increase in expression of the cancer-specific *O*-glycan STn (Neu5Ac α 2-6GalNAc α) on cancer cells (Fu et al., 2016; Munkley, 2016).

HIF-1 α may specifically mediate changes to the glycocalyx to drive cancer progression and metastasis by changing cellular metabolism and glycotransferase expression levels. HIF-1 α has been shown to promote changes to glycosyltransferase expression, sugar transporter expression, and the synthesis of nucleotide sugars via the hexosamine biosynthesis pathway

(Dall'Olio et al., 2012; Koike et al., 2004; Shirato et al., 2011). The secretion of some mucins has been linked directly to hypoxia (Zhou et al., 2012). Muc1-expression has both been shown to attenuate HIF-1 α activity by promoting HIF-1 α degradation (Yin et al., 2007), and, conversely, Muc1 has been shown to stabilize HIF-1 α (Chaika et al., 2012). This indicates a complex and context specific interplay between Muc1 and HIF-1 α in cells.

Muc1 interferes with cellular adhesion in a manner dependent on steric interactions at the cell surface. Previous studies have shown that the conformation of the protein backbone of mucin predominately determined by the initial sugar residue attached by protein glycosylation (Coltart et al., 2002). This indicates that the glycosylation status of Muc1 may be critical to determining its anti-adhesive properties. Hypoxia modulates the glycosylation status of Muc1 and its expression level which may impact the adhesive phenotype and therefore the migratory phenotype of cells. Further, a migratory mode switch from the highly adherent collective migration mode to poorly adherent amoeboid migration mode has been reported for cells under hypoxia (Lehmann et al., 2017). More research is needed to determine the role of Muc1, the glycocalyx, and hypoxia-mediated glycosylation changes to the migration and metastasis of cancer cells.

6.3 RESULTS AND DISCUSSION

6.3.1 Muc1 expression sterically blocks cell/cell and cell/extra-cellular matrix adhesions

In order to study cellular migration and metastasis, we used the highly metastatic mouse breast cancer line 4T1. To study the impact of a bulky, mucinous glycocalyx on this highly motile cell line, we updated and used the

previously characterized genetically-encoded toolbox developed by Shurer, Paszek, and colleagues (Shurer et al., 2018, 2019a, 2019b). Two Muc1 Δ CT (truncated cytoplasmic tail) cDNAs were used – one with an internal ribosome entry site (IRES) followed by GFP and the other a Muc1 Δ CT GFP fusion (Fig. 6.1A). The encoded gene responded as predicted to treatment with different concentrations of the inducing drug, doxycycline, measured by both binding of a Muc1 ectodomain specific antibody and the IRES GFP signal (Fig. 6.1B). The protein expression kinetics of the cDNA also matched previous reports (Gossen et al., 1995; Shurer et al., 2018, 2019a), with expression of the cDNA saturating between 24 and 48 h (Fig. 6.1C). The 4T1 cell line showed non-specific binding of the human specific anti-Muc1 antibody tested, as predicted (Fig. 6.1D, left). The cell line also showed a very low level of ‘leaky’ expression of the Muc1 gene and of the IRES GFP when cells were not induced with the doxycycline (Fig. 6.1D, Muc1+Ab, 0 μ g/mL compared to 1 μ g/mL). The Muc1-specific antibody binding and IRES GFP signal were strongly correlated, indicating that the IRES GFP can be used as a readout for the Muc1-expression level (Fig. 6.1E).

Having validated the new 4T1 cell line model, we tested whether previous observations of Muc1 expression blocking integrin and cadherin interactions was reproducible (Shurer et al., 2018, 2019a; Wesseling et al., 1995, 1996). Indeed, cells expressing Muc1 Δ CT IRES GFP fully detached from their substrate – approximately 50% of cells were detached, and detached cells were viable (Fig. 6.2A). The 4T1 Muc1 Δ CT IRES GFP cells also maintained their surface levels of E-cadherin, despite existing in suspension as single cells (Fig. 6.2). Taken together, these results indicate that previous findings reported by Shurer and colleagues should hold for the new 4T1 Muc1-expressing cell lines, and that Muc1-expression sterically blocks or interferes with integrin-mediated

focal adhesion to 2D substrates and E-cadherin interactions.

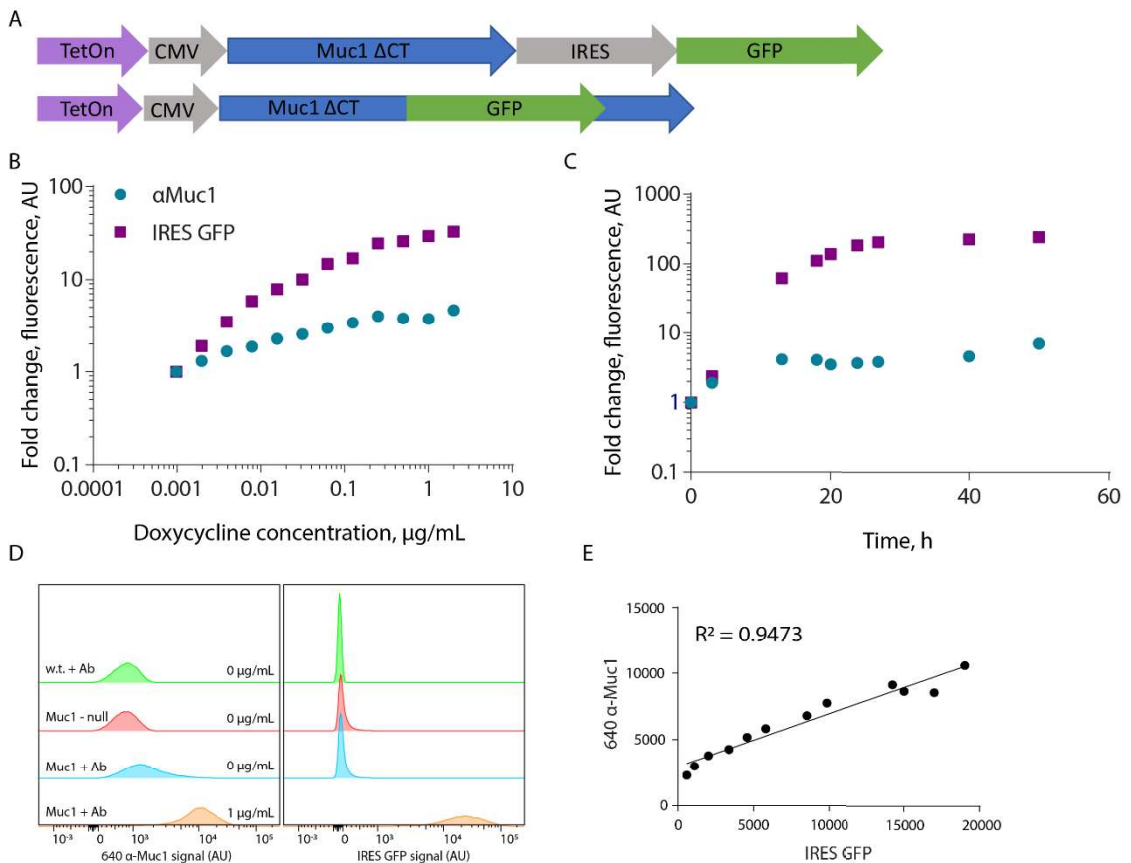


Figure 6.1 – Characterization of 4T1 Muc1 Δ CT cell line. **A**, Schematic of two genetically-encoded Muc1 cDNAs used in these studies; TetOn – reverse tetracycline inducible promoter, CMV – cytomegalovirus promoter, Muc1 Δ CT – human Muc1 gene with a deleted cytoplasmic tail, IRES – internal ribosome entry site, GFP – green fluorescent protein (top: copGFP, bottom: mOxGFP). **B**, Fold change in expression level of Muc1 Δ CT IRES GFP was titrated using various concentrations of doxycycline, measured by flow cytometry after 48 h of doxycycline treatment with either an anti-Muc1 antibody (α Muc1) or the genetically encoded IRES GFP signal (see A, top), $n = 2$, $> 30,000$ cells per sample. **C**, Fold change in expression level of Muc1 Δ CT IRES GFP over time with treatment of 1 μ g/mL doxycycline, measured by flow cytometry. **D**, Representative flow cytometry histograms for wild-type (w.t.) or Muc1 Δ CT IRES GFP-expressing (Muc1) 4T1 cells unlabeled (null) or labeled with an anti-Muc1 antibody (+ Ab) and treated for 48 h with 0 or 1 μ g/mL doxycycline. **E**, Values from A show the strong linear correlation between anti-Muc1 antibody

binding and the IRES GFP signal.

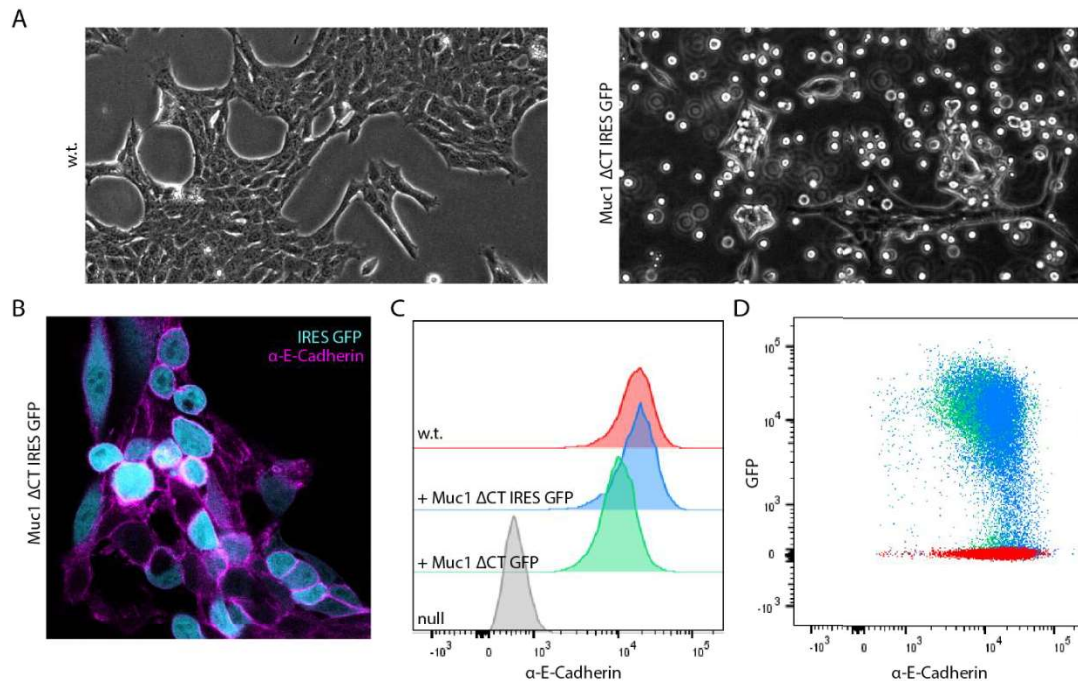


Figure 6.2 – Muc1 Δ CT expression blocks integrin and cadherin interactions. **A**, Representative phase contrast images for w.t. or Muc1 Δ CT IRES GFP-expressing 4T1 cells. **B**, Representative confocal image of 4T1 Muc1 Δ CT IRES GFP cells labeled with an anti-E-Cadherin antibody. **C**, Representative flow cytometry histograms showing similar cell-surface levels of anti-E-Cadherin antibody binding for w.t., Muc1 Δ CT IRES GFP, and Muc1 Δ CT GFP 4T1 cells. Unlabeled (null) 4T1 w.t. cells are also shown. **D**, Representative cross-plot for GFP signal and anti-E-Cadherin signal, $n = 2$, $> 9,000$ cells per sample.

6.3.2 Muc1-expression increases frequency of single cell migration

Having established that Muc1-expressing cells detach from cell-cell and cell-ECM adhesions, we tested if this reduced level of adhesion could impact the migration of these cells away from tumor spheroids in 3D collagen gels. 4T1 wild-type (w.t.) cells have previously been shown to migrate in a collective fashion as large strands of cells with tight cell-cell junctions when observed as tumor spheroids implanted in 3D collagen gels (Lehmann et al., 2017).

Compared to w.t. cells, cells expressing Muc1 Δ CT IRES GFP were observed to migrate less often as collective strands in 3D collagen gels (Fig. 6.3A). 4T1 Muc1 Δ CT IRES GFP-expressing spheroids covered a smaller 2D area in the gel compared to w.t. cells, most likely due to the large surface area of the collective strands observed in w.t. cell migration (Fig. 6.3B). Quantification showed that the number of single cells migrating away from the tumor spheroids significantly higher, approximately double, in Muc1 Δ CT IRES GFP-expressing cells compared to w.t.

Next, we sought to determine if the migration observed *in vitro* in 3D collagen gels recapitulated the migration of Muc1-expressing cells *in vivo*. To this end, we surgically implanted an imaging window over the 4th mammary fat pad of 6-8-week-old female mice (Fig. 6.4A). Tumor spheroids implanted into the mammary fat pad can be observed by intravital microscopy for several days through this implanted window (Fig. 6.4B). Preliminary results showed that Muc1 Δ CT IRES GFP-expressing 4T1 cells migrated often as single cells in the mammary fat pad (Fig. 6.4B).

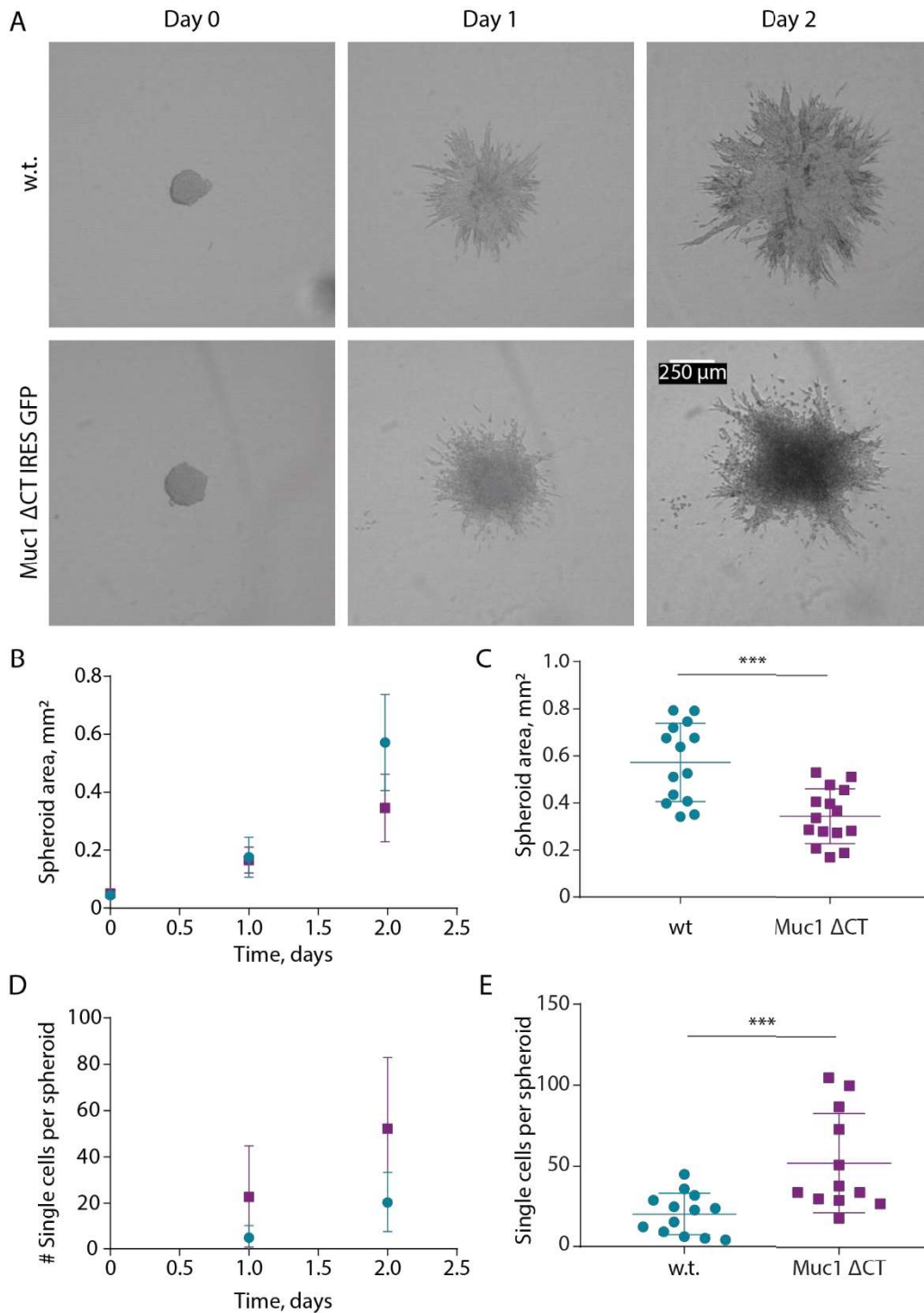


Figure 6.3 – Muc1 ΔCT cells migrate as single-cells in 3D. **A**, Representative phase contrast microscopy images of 4T1 w.t. or Muc1 ΔCT IRES GFP-expressing spheroids migrating in a 2.5 mg/mL sandwich collagen gel. **B**, Quantification of spheroid area from **A**, n = 3, 14 spheroids. **C**, Plot showing the distribution of data from **B** at Day 2, each point represents one spheroid. **D**,

Quantification of the number of single cells observed in phase contrast images from A, n = 2, 12 spheroids. E, Plot showing the distribution of data from D at Day 2, each point represents one spheroid analyzed. Mean and S.D. are shown for B, D; lines indicate mean and S.D. for C, E; *** p < 0.005.

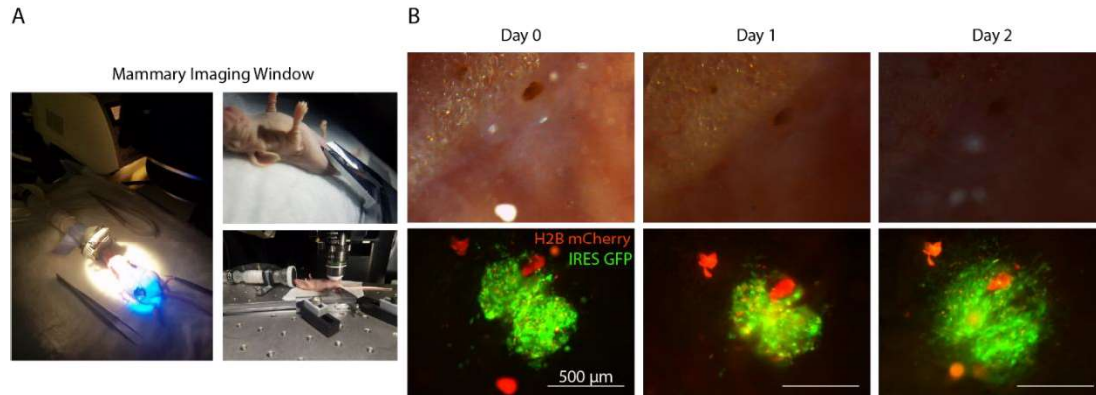


Figure 6.4 – Tracking cell migration *in vivo* using a mammary imaging window. **A**, The mammary imaging window is surgically implanted into the abdomen of athymic nude mice over the fourth mammary fat pat. Individual spheroids are surgically implanted into the fat pad. Cells can then be imaged through the window over time. **B**, Representative stereomicroscopy images of a 4T1 H2B mCherry Muc1 ΔCT IRES GFP spheroid implanted into the fat pad of a mouse, imaged over two days. The top row shows the brightfield image of the fat pad. The bottom row shows the fluorescence image of the implanted spheroid.

6.3.3 Muc1-expression causes fast, unjammed migration of cells

We wanted to better characterize the migratory mode of the Muc1-expressing cells *in vitro*. In order to better characterize the migratory mode of Muc1-expressing cells, we used confocal microscopy to observe the migration at a higher resolution (Fig. 6.5). Cells frequently adopted a pseudopodal ameboid-like morphology with a round cell body and a single long, leading-edge protrusion (Fig. 6.5B). Cells were also able to readily escape the core of the tumor spheroid due to its loose packing resulting from decreased cell-cell adhesion. For example, a cell was observed to rapidly escape the core of the

spheroid, traveling multiple cell-body lengths in 28 mins, passing many other cells without engaging in apparent interactions (Fig. 6.5C).

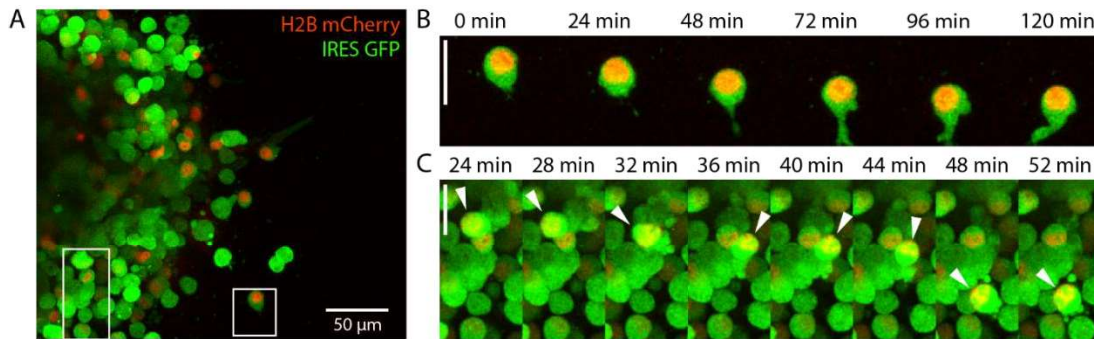


Figure 6.5 – Muc1 Δ CT cells exhibit a distinct 3D migration phenotype. **A**, Maximum intensity projection taken from a confocal z-stack movie of 4T1 H2B mCherry Muc1 Δ CT IRES GFP-expressing cells migrating in a 3D sandwich collagen gel after 48 h. **B**, Expanded region of interest from A (white box, right side), showing the migration of a single cell over time. **C**, Expanded region of interest from A (white box, left side), showing the migration of a single cell from the core to the edge of the spheroids over time.

6.3.4 Evolution by selective pressure changes the glycocalyx

The ability of Muc1 to block cell-cell and cell-ECM interactions is expected to be critical for Muc1-mediated migration mode. To test the importance of Muc1-mediated adhesion blocking, we set out to generate a cell line with a similar level of Muc1 expression but without the impact on cellular adhesion associated with Muc1 expression. Because of the complexity of the processes which control glycosylation, we used a top-down strategy to separating distinct adhesive phenotypes of Muc1-expressing cells. We hoped to both identify the key players in altering the biophysical properties of the glycocalyx and the important glycan motifs which contribute to these properties. Using the selective pressure of cellular adhesion, we evolved, over time, an isogenic cell line of Muc1-expressing 4T1 cells (Fig. 6.6A). By selecting

cells with continuous doxycycline treatment, we pushed the cells towards a more adhesive phenotype. Over time, we observed a constant level of GFP signal from Muc1 Δ CT GFP-expressing cells with constant cell-surface levels of Muc1 Δ CT GFP (Fig. 6.6B). However, a significant shift in binding of peanut agglutinin was observed (Fig. 6.6B). This demonstrates that the anti-adhesive properties of Muc1 were modulated by its glycan profile.

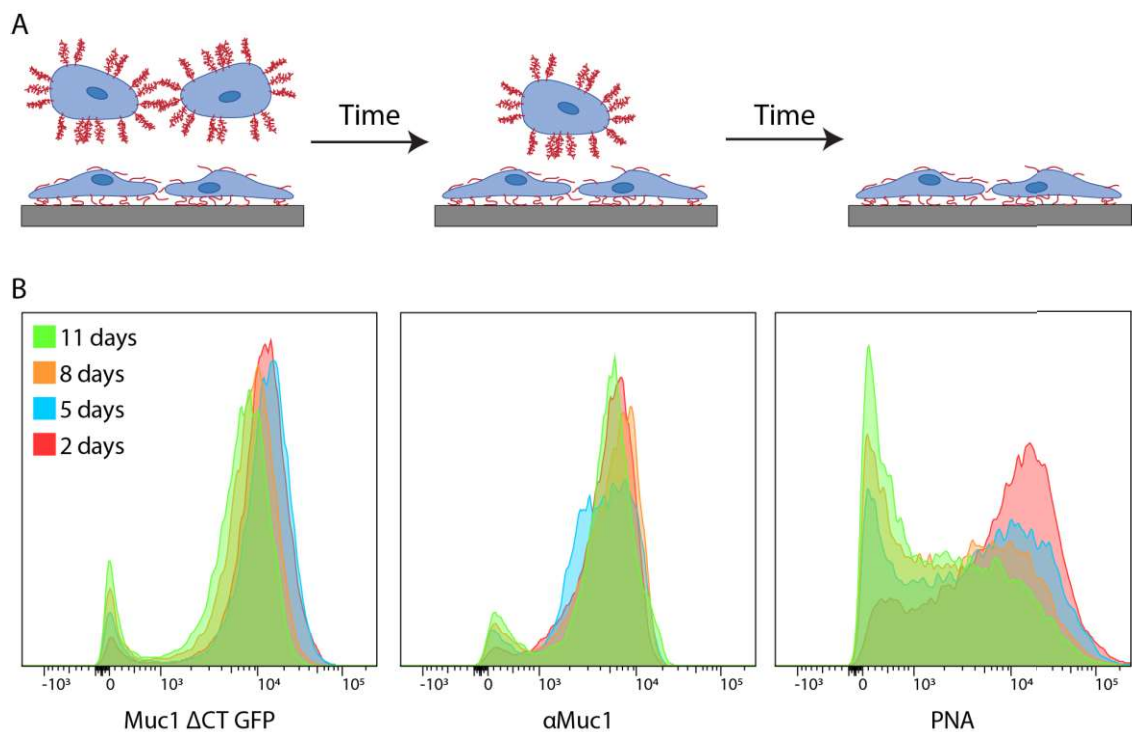


Figure 6.6 – Evolution by selective pressure of an isogenic Muc1 Δ CT-expressing cell population which is highly adhesive. A, Schematic representation of Darwinian evolution by selective pressure on cellular adhesion. Over time, fewer and fewer Muc1 Δ CT-expressing cells detach from their 2D substrate. B, Representative flow cytometry histograms showing the signal from the GFP, an anti-Muc1 antibody, and peanut agglutinin (PNA) for isogenic 4T1 Muc1 Δ CT GFP-expressing cells which have been treated with doxycycline for 2, 5, 8, or 11 days, >10,000 cells per sample.

6.3.5 Hypoxia changes the glycocalyx

In order to determine if hypoxia-mediated glycosylation changes played a role in hypoxia-mediated migratory mode switching, we first evaluated the impact of hypoxia on the glycocalyx. Using w.t. 4T1 cells, we treated cells with DMOG, a chemical stabilizer of HIF-1 α , and evaluated the impact of this treatment on the cell-surface glycocalyx. 4T1 cells have previously been shown to express cell-surface Podocalyxin (Podxl) (Snyder et al., 2015). Knock-down of Podxl in 4T1 has also previously been shown to change the *in vitro* migration cells in 3D gels (Graves et al., 2016). We observed that treating cells with DMOG to stabilize HIF-1 α caused an approximately 2-fold increase in cell-surface Podxl expression level (Fig. 6.7A). Changes in the presentation of glycans were also observed by lectin binding on the surface of w.t. 4T1 cells treated with DMOG (Fig. 6.7B). When exposed to a hypoxic environment (2% O₂), similar changes in lectin binding to those observed by DMOG treatment were again observed (Fig. 6.7C). Taken together, this data indicates that hypoxia does indeed change the presentation of glycans on the cell-surface.

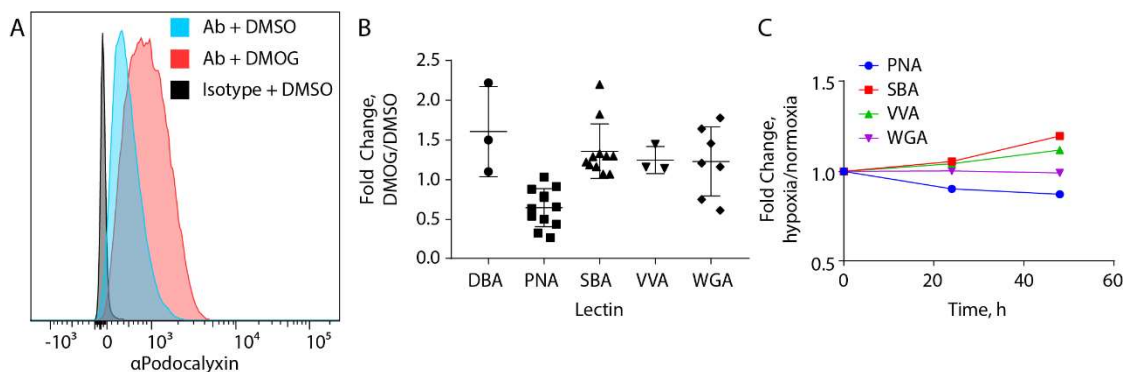


Figure 6.7 – Hypoxia induces changes to the glycocalyx. **A**, Representative flow cytometry histogram of w.t. 4T1 cells treated with DMSO or 1 mM DMOG for 48 h and labeled with an anti-Podocalyxin or Isotype control antibody, > 35,000 cells per sample. **B**, Fold change in lectin binding upon DMOG treatment, measured by geometric mean or median of flow cytometry histogram, each

point represents a replicate, > 10,000 cells per sample, mean and S.D. are shown. C, Fold change in lectin binding upon treatment with 2% O₂ for the indicated amount of time, measured by median of flow cytometry histogram, mean for three technical replicates shown.

6.4 CONCLUSION AND FUTURE WORK

We have shown that Muc1-expression interferes with cellular adhesion (Fig. 6.2). This interference causes a migratory mode switch from collectively invading cells to single, amoeboid-like cells migrating from tumor spheroids in 3D collagen gels (Fig. 6.3 and 6.5). Future work will seek to establish the relevance of these *in vitro* observation *in vivo* by intravital microscopy experiments, such as those preliminary experiments discussed here (Fig. 6.4). Further and more thorough characterization of *in vitro* migration can also be performed to better understand the phenotype of migrating Muc1-expressing cells.

Muc1-expression alone does not interfere with cellular adhesion; rather certain glycan motifs are required (Fig. 6.6). Future work will evaluate if the 3D migration of highly adhesive Muc1-expressing cells reverts to the migratory modes observed in w.t. cells or another migratory mode associated with highly adhesive cells. We can then evaluate at a higher level of detail the specific glycosylation changes brought on by the evolutionary selection on adhesion performed in these studies. Identification of specific glycan motifs which are essential to Muc1-mediated migration may open new therapeutic avenues aimed at the mechanical properties of the cellular glycocalyx.

Hypoxia treatment has been shown to impact the expression of the endogenous mucin-like glycoprotein Podxl and on the presentation of some glycan motifs, as indicated by lectin binding experiments (Fig. 6.7). Because

previous reports have shown both that Podxl knock-out (Graves et al., 2016; Snyder et al., 2015) and hypoxia treatment impact 3D migration from tumor spheroids (Lehmann et al., 2017), future researchers could knock-out expression of the endogenous Podxl and evaluate migration under hypoxia versus normoxia. These experiments may identify a direct link between hypoxia-mediated migratory mode switching and the glycocalyx. Further, the impact of hypoxia treatment on Muc1-expressing cells could be evaluated in order to understand the role of hypoxia on Muc1-mediated migration mode, which may be more physiologically relevant to human carcinomas.

6.5 METHODS

6.5.1 Antibodies and reagents

The following antibodies were used: Human CD227 (Muc1; 555925, BD Biosciences) (Muc1), Mouse Podocalyxin (MAB1556, R&D Systems), E-Cadherin (3195S, Cell Signaling), Alexa Fluor 633 goat anti-rabbit (A-21070, Thermo Fisher Scientific), Alexa Fluor 633 goat anti-rat (A-21094, Thermo Fisher Scientific), and FITC-Rat IgG2b kappa Isotype Control (11-4031-82, Thermo Fisher Scientific). Lectins used were: CF568 Arachis hypogaea Lectin PNA (29061, Biotium), CF640R Arachis hypogaea Lectin PNA (29063, Biotium), CF633 Wheat Germ Agglutinin (WGA; 29024, Biotium), Biotinylated Soybean Agglutinin (SBA, B-1015, Vector Laboratories), Fluorescein labeled Soybean Agglutinin (SBA, FL-1011, Vector Laboratories), Fluorescein labeled Vicia Villosa Lectin (VVA, FL-1231, Vector Laboratories), and Fluorescein labeled Dolichos Bioflorus Agglutinin (DBA, FL-1021-2, Vector Laboratories). Biotinylated lectins were detected using NeutrAvidin Protein, DyLight 650 (84607, Thermo Fisher Scientific). To induce transactivator cell lines,

doxycycline was used (sc-204734, Santa Cruz). For collagen gels, Corning Collagen I, High Concentration, Rat Tail (CB354249, Fisher Scientific). For hypoxia studies, hypoxia inducible factor alpha (HIF-1 α) stabilizer dimethyloxallyl glycine (DMOG, 71210, Cayman Chemical) was used. To form spheroids, 1.2% w/v methyl cellulose (M6385, Millipore Sigma) in DMEM was used.

6.5.2 Constructs

The Muc1 Δ CT pPB rtTA NeoR IRES GFP plasmid was prepared by excision of the Muc1 Δ CT gene using BamHI and EcoRI restriction enzymes from the Muc1 Δ CT pPB TetOn PuroR plasmid (Shurer et al., 2018). The Muc1 Δ CT gene was inserted by cutting the pPB rtTA NeoR IRES GFP plasmid (Shurer et al., 2019b) similarly and ligating the two pieces. Similarly, the Muc1 Δ CT GFP pPB rtTA NeoR plasmid was generated by excision of the Muc1 Δ CT GFP gene from the Muc1 Δ CT GFP pPB TetOn PuroR plasmid (Shurer et al., 2018) and insertion into the similarly cut pPB rtTA NeoR plasmid (Shurer et al., 2019b). H2B mCherry pLenti construct was provided by Peter Friedl (M.D. Anderson Cancer Center).

6.5.3 Cell lines and culture

4T1 and 4T1 H2B mCherry cells were provided by Peter Friedl (M.D. Anderson Cancer Center). 4T1 cells were culture in RPMI medium (R8758, Millipore Sigma) supplemented with 10% FBS (F0926, Millipore Sigma), penicillin/streptomycin, and 1 mM sodium pyruvate (11360070, Thermo Fisher Scientific). Cells were maintained at 37°C, 5% CO₂, and 90% RH. 4T1 Muc1 Δ CT IRES GFP and 4T1 Muc1 Δ CT GFP cells were prepared by co-transfection of the Muc1 Δ CT pPB rtTA NeoR IRES GFP or the Muc1 Δ CT GFP pPB rtTA NeoR plasmid, respectively, and the Hyperactive Transposase plasmid as

previously described (Shurer et al., 2019a) into the 4T1 or 4T1 H2B mCherry cell line using Lipofectamine 2000 Transfection Reagent (11668027, Thermo Fisher Scientific) per manufacturer's protocol. Cell lines were sorted for high Muc1 expression after inducing with 1 $\mu\text{g}/\text{mL}$ doxycycline for 48 h by fluorescence-activated cell sorting (FACS) using a Beckman Coulter MoFlo Astrios.

6.5.4 Flow cytometry

Cells were plated at 20,000 cells/cm² and grown for overnight. Cells were then induced with 1 $\mu\text{g}/\text{mL}$ doxycycline for 24 hours. Adherent cells were nonenzymatically detached by incubating with 1 mM EGTA in PBS at 37°C for 20 min and added to the population of floating cells, if present. Antibodies were diluted 1:200 and lectins were diluted to 1 $\mu\text{g}/\text{mL}$ in 0.5% BSA PBS and incubated with cells at 4°C for 30 min. A BD FACS Canto II was used to collect data. For doxycycline-titration flow cytometry, Muc1 ΔCT IRES GFP-expressing 4T1 cells were plated and induced similarly with varying concentrations of doxycycline (0.001 – 2000 ng/mL). Cells were nonenzymatically detached as described above and labeled as above. For doxycycline time-course, cells were plated at 20,000 cells/cm² and grown overnight. Samples were then induced by adding media containing 1 $\mu\text{g}/\text{mL}$ of doxycycline at various timepoints (0 – 50 h before analysis). Cells were nonenzymatically detached and labeled as described above. Geometric mean of signal is reported.

6.5.5 Sandwich collagen gel migration assay

Prepare spheroids per hanging drop protocol previously described (Lehmann et al., 2017). Briefly, detach cells with 0.05% trypsin EDTA. Neutralize trypsin with complete medium. Pellet cells at 200 rcf for 5 min. Resuspend cells to 1e6 cells/mL. Add 200,000 cells to 3.7 mL of complete

medium. Add 1 mL of methyl cellulose solution to the cells and medium. Additives may be included in this suspension, as described. Distribute 25 μL droplets of the solution onto the inside surface of the lid of a 150 mm petri dish. Carefully invert the petri dish so that the droplets are ‘hanging’. Place dish into incubator overnight. When forming spheroids for *in vivo* experiments, cells were induced by adding 1 $\mu\text{g}/\text{mL}$ doxycycline and treated with 1:100 dilution of collagen to facilitate tight spheroid aggregation.

Verify spheroid formation using a phase contrast or bright field microscope. Collect droplets containing well-formed spheroids into 1 mL of PBS (with Ca^{2+} and Mg^{2+}). Allow spheroids to settle. Wash spheroids by removing the supernatant and resuspending in fresh 1 mL PBS (with Ca^{2+} and Mg^{2+}). Repeat wash.

Prepare collagen gel. Combine the following reagents to the final concentration, in the following order, to a 1.7 mL Eppendorf tube, on ice:

Reagent	Stock Concentration	Final Concentration	Representative Volumes (for 100 μL of collagen solution)
Sterile H_2O	--	--	10.64 μL
PBS	10x	1x	10 μL
Complete Medium	1x	0.5x	50 μL
NaOH^1	0.5 N	0.5 N	1.3 μL
Rat Tail Collagen	8.91 mg/mL^2	2.5 mg/mL	28.06 μL

¹ Acidified rat tail collagen pH balances NaOH to maintain a constant $[\text{OH}^-]$. Use 0.046 times the collagen volume.

² Verify collagen concentration which varies batch to batch.

Table 6.1 – Collagen gel preparation calculations. Table showing the necessary reagents and protocol to prepare collagen gel for 3D gel experiments.

Always prepare only enough collagen solution to immediately use. Do not use collagen gel solution which has been mixed for longer than 10 minutes. Place a silicone divider into the bottom of a 12-well plate, pressing down to ensure a seal to the bottom of the plate. Dispense 25 μL of prepared collagen solution into the silicone divider. Allow collagen to gel in the incubator for 10 min. Using a 10 μL pipette, draw up a single spheroid and place it onto the gel. Repeat to place the desired number of spheroids into the gel, 2-3 per well. Add a 25 μL droplet of collagen solution onto the spheroids. Allow the collagen to gel in the incubator for 30 min. Carefully remove the silicone divider from the collagen gel. Add medium or medium containing drug to the well. Image the spheroids using phase contrast or brightfield microscopy. Incubate the spheroids for the desired amount of time, acquiring images at regular intervals. Fiji was used for image processing (Schindelin et al., 2012).

6.5.6 Confocal microscopy

For confocal microscopy of cells on 2D substrates, cells were plated at 5,000 cells/cm² and grown for 24 hours and subsequently induced with 1 $\mu\text{g}/\text{mL}$ of doxycycline for 24 hours before being fixed with 4% paraformaldehyde. Samples were blocked with 5% normal goat serum PBS for 1 hour at room temperature. Antibodies were diluted 1:200 in 5% normal goat serum PBS and incubated overnight at 4°C. Lectins were diluted to 1 $\mu\text{g}/\text{mL}$ in 5% normal goat serum PBS and incubated for 2 h at room temperature. Samples were imaged on an upright Leica TCS SPE confocal microscope using a 63x oil immersion objective. Fiji was used for image processing (Schindelin et al., 2012).

For confocal microscopy of cells in 3D gels, prepare spheroids and sandwich collagen gels as described above in Ibidi imaging dish (81158) using 70 μL of collagen for the bottom layer. Incubate cells for 48 h. Image samples on

an inverted Leica SP8 confocal using 40x water objective, acquiring an image every 4 min for 2 h.

6.5.7 Mammary imaging window

Athymic nu/nu female mice (6-8 weeks) were obtained from Experimental Radiation Oncology. Animal procedures were conducted at M.D. Anderson and approved by the MD Anderson Institutional Animal Care and Use Committee.

For implantation of the mammary imaging window, previously established protocols were used (Ilina et al., 2018). Briefly, mice were anesthetized with 1-2% isoflurane in oxygen. The fourth mammary fat pad was exposed by incision under a Leica MZ10 F microscope with an Achromatic 0.5x lens. Individual spheroids prepared via the hanging drop method described above were inserted into the mammary fat pad using a 30 G needle. A 10 mm metal window was inserted into the incision and affixed to the skin by tightening of purse-string like sutures in the skin. The window was closed with a cover glass and custom 3D printed plastic ring. Mice received carprofen by subcutaneous injection pre- and post-operation. Mice were treated with 200 μ L of 1 μ g/mL doxycycline by oral gavage 24 h prior to operation and every 48 h subsequently. Implanted spheroids were imaged through the window using a Leica M205 FA with a Planapo 2.0x, M-series objective.

6.6 ACKNOWLEDGEMENTS

We thank Peter Friedl for providing cell lines and insights into this project. We thank Michael Weiger for providing microscopy support. We thank Ryan Nini for supporting animal surgeries. This investigation was supported by the National Institute of General Medical Sciences Ruth L.

Kirschstein National Research Service Award 2T32GM008267 (C.R.S.), Samuel C. Fleming Family Graduate Fellowship (C.R.S), and National Cancer Institute U54 CA210184 (M.J.P). This work was supported by NIH/NCI award number P30 CA016672 and the Genitourinary Cancers Program of the CCSG shared resources, at MD Anderson Cancer Center.

CHAPTER 7

CONCLUSION AND PERSPECTIVE

New tools developed in this work enable the broad pursuit and application of research into the cellular glycocalyx. By developing a new toolkit for glycocalyx editing, we were able to study effect of inflating the cellular glycocalyx and the recreation of the cancer glycocalyx on normal cell lines (Chapter 2) (Shurer et al., 2018). Using insights gleaned from the development of the toolbox, we produced some of the first recombinant human mucins which have potential future therapeutic uses (Chapter 3) (Shurer et al., 2019b). We applied our observations of cells with a thick, mucinous glycocalyx, such as having including enhanced survival in suspension and decreased adhesion, to develop a new technology for decreasing problematic aggregation of cells in suspension bioreactors (Chapter 4) (Shurer et al., 2019a). Using our unique perspective of the glycocalyx as a polymer network, we created a new model for membrane bending driven entropically by glycocalyx biopolymers (Chapter 5). Finally, given the observed anti-adhesive impact of mucin expression and the established role of adhesive forces in cellular migration, we studied the impact of the mucinous glycocalyx on three-dimensional cellular migration (Chapter 6). Of note is the use of a cytoplasmic tail-deleted Muc1 throughout these studies. This indicates that the observations made here are primarily biophysical in nature and only require the polymeric, glycosylated ectodomain of Muc1.

There are essentially boundless future opportunities for research applying similar approaches to those discussed here. Using the tools for creating a dense, mucinous glycocalyx, future studies could look at how receptor signaling and organization are impacted by crowding in the

glycocalyx. A thick glycocalyx on cancer cells may play a role in immune cell binding and infiltration immunotherapies. Using codon-scrambling strategies described here to empower synthetic biology approaches to the highly repetitive mucin cDNA, a new generation of mucin biopolymer tools could be developed which have specific mutations effecting glycosylation. Such a toolkit could reveal new patterns and significance in O-linked glycosylation. Insights into membrane shape generation could be applied to study different physiological structures. Perhaps other shapes or structures besides plasma membrane structures could be formed, in part, by contributions from the glycocalyx as a polymer layer.

Despite the overwhelming body of data showing that Muc1 is frequently over-expressed on the surface of cancer cells in patient samples and circulating tumor cells (Gendler, 2001; Hatstrup and Gendler, 2008; Kufe, 2009), the majority of ongoing cancer research does not take the glycocalyx or Muc1 into consideration. One potential reason for this could be the limited tools available (Hang and Bertozzi, 2005). Another potential explanation is, similar to the evolution by selective pressure described in Chapter 6, routinely cultured cell lines may not recapitulate the true *in vivo* cancer glycocalyx. While many important and significant advancements have been made using cultured cell lines, scientists are coming to see cultured cells as a fundamentally flawed system with many caveats to consider, including genetic and phenotypic instability of cultured cell lines (Freedman et al., 2015; Geraghty et al., 2014; Hidalgo et al., 2014). Additionally, scientists are shifting towards using three-dimensional rather than two-dimensional approaches to perform research, as three-dimensional systems more realistically capture the biomechanical and biochemical environments found *in vivo* (Duval et al., 2017). Given the

instability of Muc1 in the genome (Gemayel et al., 2010; López Castel et al., 2010; Oren et al., 2016; Shurer et al., 2019b) and the propensity of Muc1-expressing cells to have reduced adhesion (Shurer et al., 2018; Wesseling et al., 1995, 1996), it is possible that these two features combine to deplete Muc1 on the surface of cancer cell lines grown in two-dimensional culture. Therefore, ongoing researchers are not ignoring the glycocalyx, but rather working with a model system that does not capture a glycocalyx representative of that found in *in vivo*. Continued progress in the field of cell biology and cancer research which utilizes new model systems such as patient derived xenografts (Hidalgo et al., 2014) may more accurately capture the role of the glycocalyx.

We hope our work contributes to a new paradigm in thinking about the function of the glycocalyx as an important biomaterial coating on the surface of mammalian cells. New insights into the role of the glycocalyx may reveal new therapeutic avenues for the treatment of human disease including cancer, arthritis, and more. Further, appreciation of the glycocalyx from a physics perspective may reveal new roles for this biomaterial in determining cellular phenotypes.

APPENDIX A

SOLID SURFACE STRESSES DIRECT CELLULAR BEHAVIORS THROUGH INTEGRIN-BASED MECHANOTRANSDUCTION^{1,2}

A.1 ABSTRACT

The deformation of solids depends on both the bulk elasticity and surface stress of the material. Biomaterials that mimic natural extracellular matrices are frequently designed to have high compliance, a condition in which surface stresses can become dominant. We report that cells sense solid surface stresses through integrins and canonical mechanotransduction pathways. For soft materials with high surface energies, we find that surface stresses can override directives from the elastic modulus in controlling cell response. Strikingly, even when the elastic modulus of the material is vanishingly small, surface stress can support cell spreading, the assembly of stable focal adhesions, force-dependent integrin signaling, YAP/TAZ-based mechanotransduction, cell survival, and cell proliferation. Our findings emphasize the importance of solid surface stress as a design parameter for soft biomaterial scaffolds.

A.2 INTRODUCTION

Physical directives from the extracellular matrix (ECM) instruct complex cellular and multicellular behaviors, including proliferation (Paszek et al., 2005; Yeung et al., 2005), differentiation (Engler et al., 2006), migration (Lo et al., 2000; Pelham and Wang, 1997), and tissue assembly (Paszek et al., 2005). A major

¹A version of this manuscript is currently under review at *Science Advances*. Z. Cheng, et al., The Surface Stress of Biomedical Silicones is a Stimulant of Cellular Response. *Sciences Advances* (in review).

²C.R.S. prepared the cell lines, planned and conducted the focal adhesion and YAP/TAZ imaging experiments and gene expression experiments. See sections A.6.1 and A.6.2 for a complete author list and specific author contributions.

challenge in designing synthetic ECMs is encoding the physical information necessary to elicit specific biological programs. The modulus (Paszek et al., 2005; Yeung et al., 2005), porosity (Trappmann et al., 2012), rate of stress relaxation (Chaudhuri et al., 2015, 2016), ligand tethering (Wen et al., 2014), and degradation kinetics (Khetan et al., 2013) of the ECM all are known to influence cell behavior. Of these parameters, the modulus has received considerable attention due to its direct and well-established role in regulating cell fate and morphogenesis (Discher et al., 2005; Engler et al., 2004; Paszek et al., 2005). Cells physically probe the modulus of the ECM using integrin-based adhesion complexes (Geiger et al., 2009). On more rigid substrates, integrin receptors assemble into larger multi-molecular complexes that trigger activation of regulatory signaling cascades (Paszek et al., 2005; Wang et al., 2001; Yeung et al., 2005). In terms of biomaterials design, tuning integrin-based mechanotransduction is critical for programming desired cellular responses.

While the ECM modulus typically serves as a primary physical cue from the microenvironment, cell behaviors that defy expectations based on ECM rigidity alone have been observed. For example, cells seemingly misinterpret silicone substrates as being rigid, even when the material is highly compliant (Trappmann et al., 2012; Wen et al., 2014). While some reports argue that this anomalous behavior is attributed to how adhesive proteins are tethered to the silicone substrate (Trappmann et al., 2012), others affirm that ECM stiffness regulates cellular behaviors independently of protein tethering (Wen et al., 2014). Our limited understanding of why cells “missense” rigidity cues from certain synthetic ECMs continues to remain a significant challenge in the rational design of cell-adhesive scaffolds and biomaterials.

The surface of all materials has an energy penalty per unit surface area

called the surface energy. In a liquid, this energy penalty gives rise to a uniform surface stress called the surface tension, which is the only means for a liquid to resist deformation. For example, insects such as fishing spiders would not be able to walk on water if not for surface tension. In solids, surface energy also gives rise to surface stresses, and these surface stresses along with bulk elasticity resist deformation. In isotropic solids that have uniform mechanical properties, the surface stress is an isotropic tensor determined by a single parameter, γ . Like liquids, this parameter is often referred to as the surface tension of the solid. Recent studies have illustrated that solid surface tension can have a dominant role in the mechanical behavior of soft materials (Hui et al., 2015; Style et al., 2013, 2017; Xu et al., 2014) when the size of a deforming object is comparable or smaller than the elasto-capillary length, γ/E , where E is the Young's modulus that quantifies the bulk elasticity of the solid.

For soft gels, elasto-capillary lengths on the micrometer scale have been observed (Style et al., 2013), suggesting that solid surface tension could resist the micron-sized deformations induced by cells and their contractile machinery acting on soft biomaterials. Here we investigate the influence of solid surface stresses on substrate rigidity sensing through integrins and cellular adhesion complexes, and we evaluate how surface stresses direct downstream cellular programs, including cell spreading, gene expression, and survival.

A.3 RESULTS AND DISCUSSION

A.3.1 Rigidity sensing on materials of high and low surface energy

To investigate how cellular rigidity sensing varies depending on the surface energy of the ECM substrate, we studied cell behavior on polyacrylamide (PA) and silicone substrates. These materials have been used

extensively as synthetic ECM to study rigidity sensing due to their biocompatibility and tunable mechanical properties that cover a wide range of biological tissue stiffnesses. These materials are also useful to investigate the effects of surface energy on cell behavior. PA is hydrophilic and would be expected to have a low surface energy in liquid growth medium, whereas silicone is considerably more hydrophobic and would be expected to have a higher surface energy.

For our investigations we prepared a series of PA gels of varying stiffness by adjusting the ratio of bis-acrylamide crosslinker to acrylamide monomers (Fig. A.S1a) (Denisin and Pruitt, 2016; Pelham and Wang, 1997). Silicone gels of varying stiffness were prepared by changing the proportion of base silicone (part A) to curing reagent (part B; Fig. A.S1b) (Brown et al., 2005). The PA and silicone gels were functionalized with the ECM protein, fibronectin, at approximately equal surface densities (Fig. A.S2). Of note, we did not oxidize our silicone substrates with treatments such as gas plasma or UV/ozone, since these procedures are known to form a rigid silica layer on the gel surface (Li et al., 2014). To evaluate the surface energies of our functionalized substrates, we measured the contact angles formed with a liquid water droplet. As expected for a hydrogel, PA had a low surface energy with water (contact angle = $49.6 \pm 28.5^\circ$ mean \pm s.d.). The functionalized silicone substrates had a considerably higher surface energy in water, as indicated by a significantly reduced wettability (contact angle = $101.4 \pm 4.2^\circ$ mean \pm s.d.; Fig. A.1a and A.S3).

To test how cells perceive the rigidity of materials with differing surface energies, we plated MCF10A epithelial cells on PA and silicone gels with elastic moduli ranging from 0.1 kPa to 22 kPa. Rigidity sensing pathways were previously shown to regulate cell morphology and spread cell area (Dupont et

al., 2011). Consistent with previous reports (Engler et al., 2004; Pelham and Wang, 1997; Ulrich et al., 2009; Yeung et al., 2005), we observed that cells on compliant PA gels were rounded and had a small spread area, whereas cells on stiff ECM were well spread and polygonal in shape (Fig. A.1b, c). The cell spread area on PA substrates scaled linearly with the log of the elastic modulus (Slope = 396; $R^2 = 0.9893$; Fig. A.1d). On silicone substrates, cells were relatively well spread and had a polygonal shape on all substrate compliances tested (Fig. A.1b, c). We observed no significant differences in cell spread area for hydrophobic silicone biomaterials with elastic moduli ranging from 0.1 – 1 kPa (Fig. A.1d). For silicone biomaterials with moduli greater than approximately 2 kPa, we observed a modest dependence of cell area on bulk elasticity (slope = 294; Fig. A.1d). These results clearly indicate that rigidity-sensing pathways in cells do not exclusively perceive the elastic modulus of ECM substrates and may be biased by the substrate surface energy.

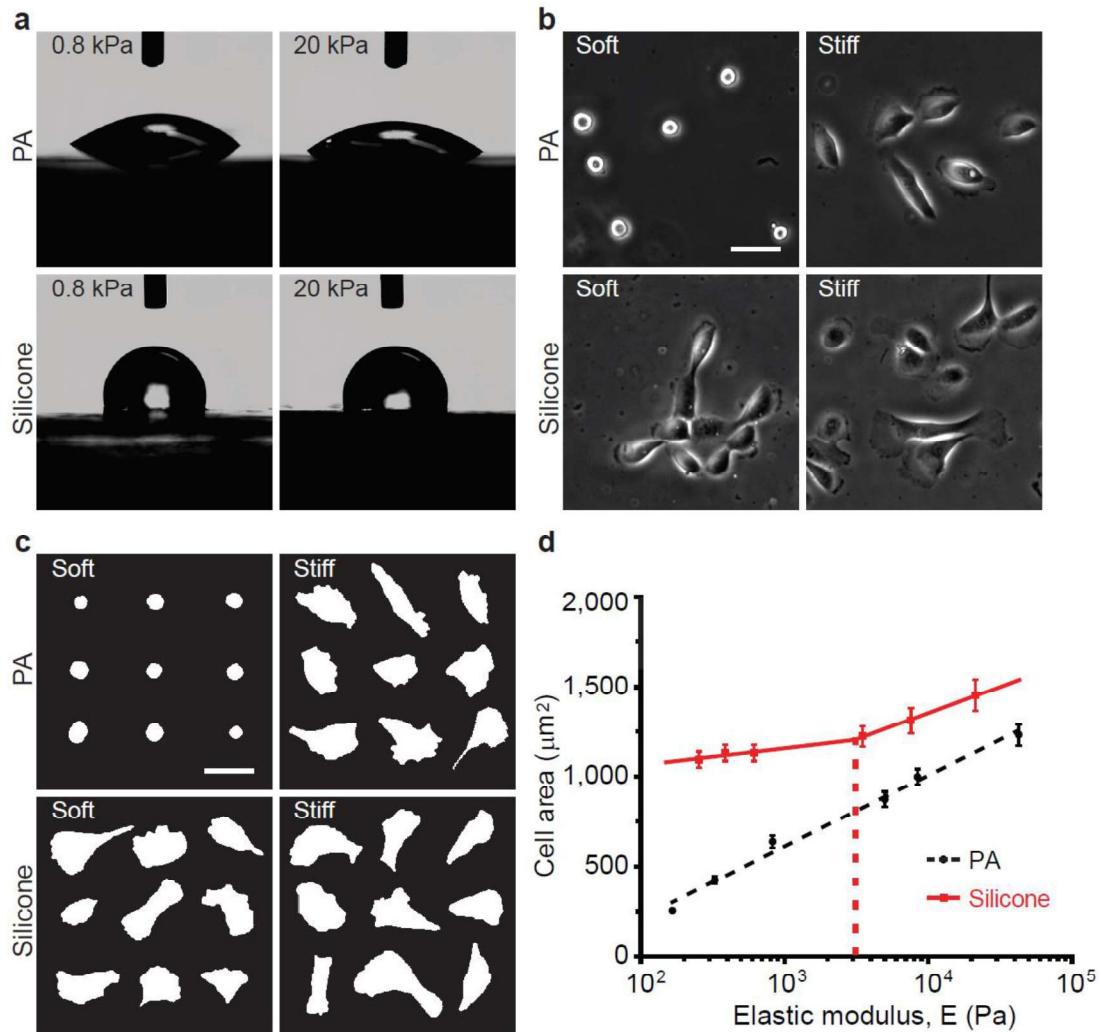


Figure A.1 – Relationships among cell morphology, substrate elastic modulus, and ECM substrate surface energy. **a**, Contact angle measurements on fibronectin-conjugated polyacrylamide (PA) and silicone substrates of the indicated elastic modulus. **b**, Phase contrast images of MCF10A mammary epithelial cells (MECs) on PA and silicone substrates of the indicated stiffness; PA gel soft: 0.12 kPa, stiff: 20 kPa; silicone gel soft: 0.1 kPa, stiff: 21 kPa; Scale bar, 50 μm. **c**, Cell masks showing representative morphologies of cells on soft and stiff substrates; Scale bar, 50 μm. **d**, Quantification of cell spread area of MECs on PA and silicone gels of the indicated stiffness ($n \geq 55$ cells per condition). Error bars show standard error of the mean.

A.3.2 Substrate surface tension can dominate in cellular rigidity sensing of soft materials

We next investigated how surface energy alters the cellular perception of bulk ECM stiffness. In liquid-liquid systems, it is well known that hydrophobic droplets are immiscible in water due to the high surface tension that develops at the interface of the liquids. In solid-liquid systems, analogous surface stresses are expected for hydrophobic materials, like silicone, that have high surface energies in aqueous solutions. Thus, we asked whether solid surface stresses could dominate in the mechanical response of compliant biomaterials to small deforming bodies, like cells.

To test for the existence of surface stresses in our biomaterials, we used confocal fluorescence microscopy to measure the indentation of small, spherical steel balls into our gels. The gels were functionalized with fluorescently labeled fibronectin, which served as a marker of the gel surface. We coated the surface of the steel balls with a thin non-adhesive polymer coating to minimize adhesion and frictional contact with the substrate surface (Fig. A.S4). Indentation depth was measured on substrates whose bulk elasticity ranged from 0.1 kPa to 4 kPa (Young's Modulus), as independently confirmed by dynamic mechanical thermal analysis. We observed that the surface indentation of soft silicone gels was much smaller than that of PA gels of comparable bulk elasticity (Fig. A.2a). We next compared these deformations to Hertz contact theory, which originally was developed to describe the indentation of isotropic elastic solids (Hertz, 1882). PA substrates agreed well with Hertz's prediction that indentation depth scales with $E^{-2/3}$ (Fig. A.2b, c) (Hertz, 1882), indicating that the PA hydrogels behave as isotropic solids with negligible surface stresses. In contrast, indentation of silicone biomaterials did not follow Hertz scaling law, suggesting that a force in addition to elasticity resists deformation of these materials (Fig. A.2b, c).

To test more specifically whether surface tension resists the deformation of hydrophobic biomaterials, like our silicone substrates, we measured their surface hardness. Hardness provides a relationship between indentation force, F , and deformation, d , and is defined as $F/(a \cdot d)$, where a is the contact radius of the indenter with the substrate. The observed hardness for PA gels again matches Hertz contact theory for isotropic elastic solids. In contrast, the observed hardness of the silicone substrates was significantly greater than Hertz's prediction (Fig. A.2d). We next asked if this increased apparent hardness could be explained by solid surface stresses. Surfactants are known to reduce the surface energy at liquid-liquid and liquid-solid interfaces (Rosen and Kunjappu, 2012). With the addition of the surfactant, Triton X-100, the observed hardness of the silicone biomaterials approached expectations for an isotropic elastic solid (Fig. A.2d and A.S5), strongly suggesting that solid surface tension is non-negligible in more hydrophobic biomaterials, such as those fabricated of silicone.

We next compared our experimental measurements to theoretical predictions based on a modified theory of Hertz contact which accounts for the effect of surface stresses (Hui et al., 2015; Long and Wang, 2013). This theory predicts that deviation of hardness from classical Hertz theory depends on a single dimensionless quantity, the elasto-capillary number, $a \cdot E/\gamma$. Thus, if surface stresses account for the increase in apparent hardness of silicone biomaterials, the hardness for different indenter radii should converge on a single curve when plotted against the elasto-capillary number. Figure A.2e shows that this is indeed the case. By fitting the experimental data to the model, we found that our silicone biomaterials have a surface tension of 0.04 N/m and Triton X-100 reduced this surface tension to 0.007 N/m (Fig. A.2e and A.S5). As

mentioned earlier, solid surface stresses will dominate bulk elasticity when the elasto-capillary length, γ/E , is larger than the deforming body. For a typical cell size of 20 μm in diameter, surface stresses should become significant in the deformation of our silicone biomaterials when the substrate elastic modulus is less than 2 kPa. This simple scaling argument agrees exceptionally well with the experimentally observed transition in cell spreading behavior from a flat response to an upward trend with increasing substrate moduli starting at approximately 3 kPa (Fig. A.1d).

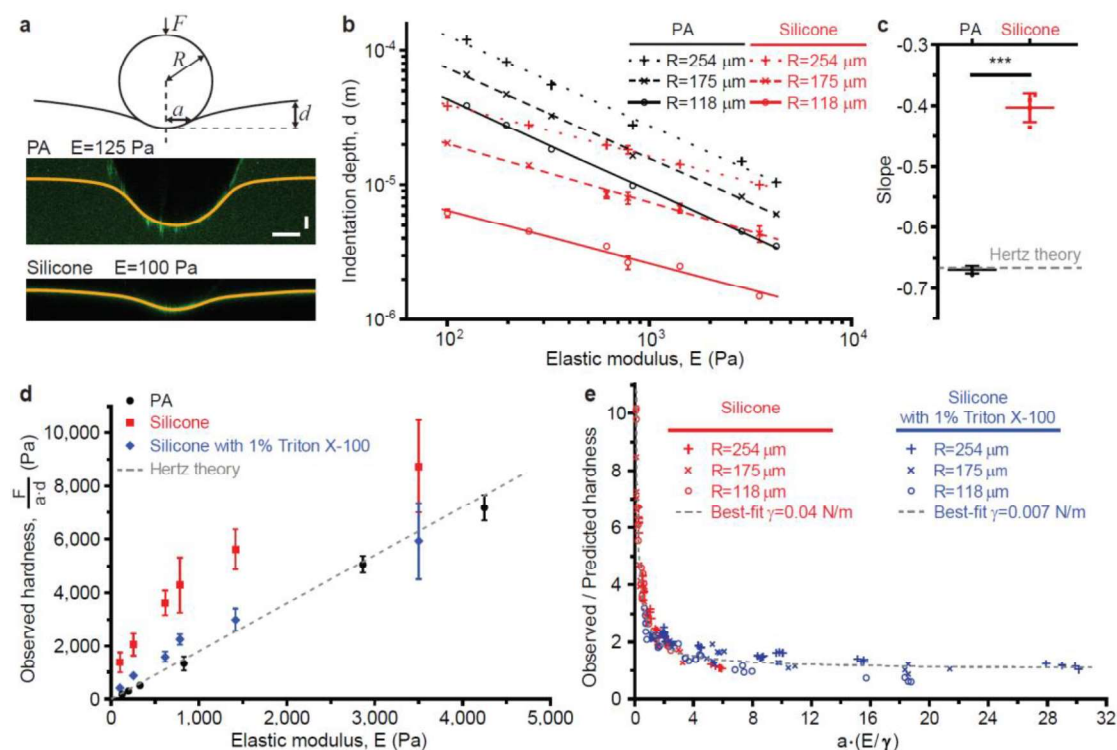


Figure A.2 – Surface stresses in compliant ECM substrates. **a**, Top: Schematic depicting the indentation of a rigid indenter (steel ball) into an elastic substrate. Middle and bottom: confocal fluorescent images showing the surface profiles of PA gels ($E=125$ Pa) and silicone gels ($E=100$ Pa) submerged in buffer and indented by steel balls with radii of 254 μm ; horizontal scale bar, 100 μm ; vertical scale bar, 30 μm . **b**, Indentation depth, d , of the steel ball versus substrate elastic modulus, E , for PA and silicone gels of the indicated stiffness. Steel balls used were 254 μm , 175 μm , 118 μm in radii, as indicated; $n \geq 5$. **c**,

Slopes of the log-log scale plots shown in panel **b**; Hertz contact theory predicts a slope of $-2/3$; *** $p < 0.001$ (t test); $n = 4$. **d**, Observed substrate hardness, $F/(a \cdot d)$, versus elastic modulus; F is the indentation force and a is the measured contact radius of the indenter; dashed line shows the prediction by Hertz contact theory; $n \geq 12$. **e**, Ratio of observed and predicted hardness, $(a^* \cdot d^*)/(a \cdot d)$, versus the elasto-capillary number, $a \cdot (E/\gamma)$, for silicone gels submerged in buffer or buffer with surfactant; a^* and d^* are the Hertz predicted contact radius and indentation depth, respectively; experimental data converge on a theoretical model of contact for an elastic substrate having surface tension; best-fit surface tensions are 0.04 N/m and 0.007 N/m for measurements in buffer and buffer with surfactant, respectively. All error bars show standard error of the mean.

A.3.3 Integrins sense substrate surface tension

We next considered whether cells could sense solid surface tension through canonical integrin-based rigidity sensing mechanisms. It is well known that sufficient mechanical resistance from the ECM substrate is required for the force-dependent maturation of integrin adhesion structures from small, dot-like nascent adhesions and focal complexes to larger focal adhesions (Geiger et al., 2009). To investigate whether solid surface tension can support adhesion maturation, cells were grown on PA and silicone biomaterials of varying stiffness. Per expectation, cells on rigid PA and silicone biomaterials assemble clear actin arcs and longitudinal stress fibers (Fig. A.3a) and display an abundance of large focal adhesions (Fig. A.3b). No discernable stress fibers or focal adhesions were observed on soft biomaterials with negligible surface tension (i.e. PA gels; Fig. A.3a, b). However, on our silicone biomaterials that have relatively high surface tension, the quantity of stress fibers and focal adhesions were comparable to those in cells on rigid substrates, suggesting that mechanical cues provided by solid surface stresses can override directives from the bulk elasticity of the ECM substrate (Fig. A.3a, b). Notably, the dynamic life

cycle of adhesion initiation, growth, and turnover on compliant materials with larger surface tension was comparable to cycles observed on rigid substrates (Fig. A.3c). On rigid substrates and compliant silicone biomaterials, focal adhesions matured on a time-scale of approximately 10 minutes, and then typically disassembled over the next 15 minutes (Fig. A.3c; See red arrowheads).

We next tested whether adhesions formed on soft materials with high surface tension could generate intracellular signals. Phosphorylation of focal adhesion kinase (FAK) at tyrosine 397 is a canonical relay in integrin-based mechanotransduction (Shi and Boettiger, 2003). Using immunofluorescence to image FAK^{pY397}, we observed robust FAK activation on compliant substrates with large surface stresses (Fig. A.3d). FAK was not activated on compliant substrates with negligible surface stresses (Fig. A.3d). Together, these results suggest that solid surface stresses are sufficient to trigger activation of integrin mechano-signaling.

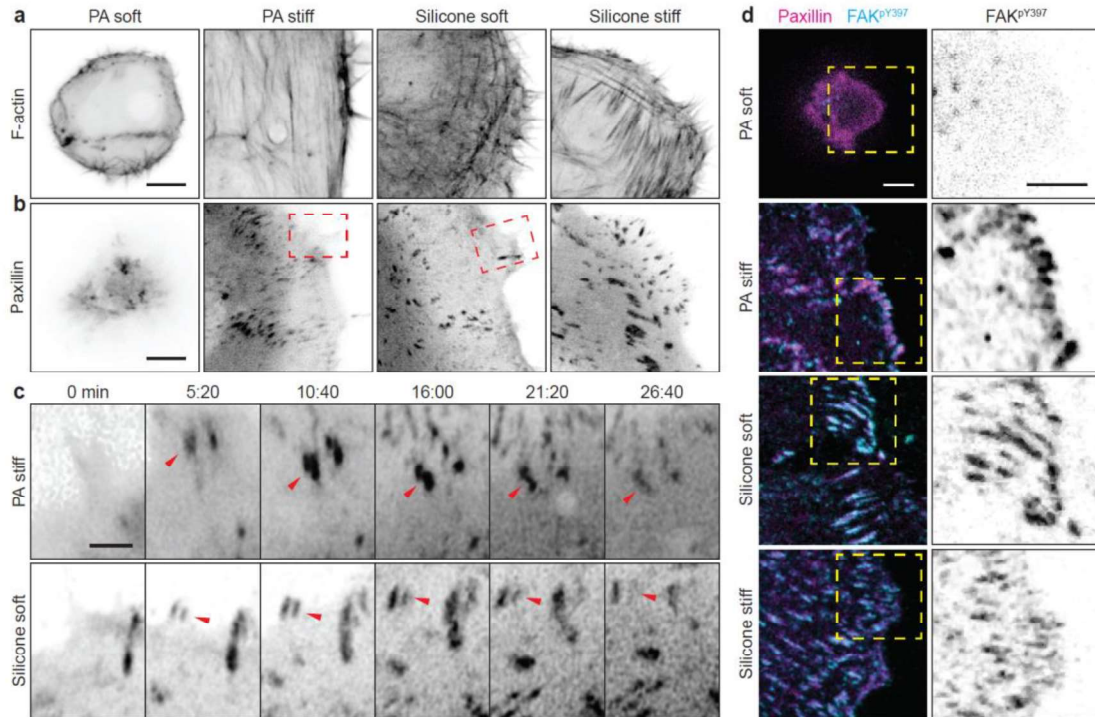


Figure A.3 – Substrate surface tension activates stress fiber formation, focal adhesion assembly and signaling. **a**, Representative images of filamentous actin in MECs expressing F-tractin-EGFP and grown on the indicated substrates; Scale bar, 5 μ m. **b**, Representative images of adhesions in MECs expressing Paxillin-mCherry and grown on the indicated substrates; Scale bar, 5 μ m. **c**, Representative time-lapse sequences of focal adhesion dynamics in Paxillin-mCherry expressing MECs on stiff PA (top) and soft silicone (bottom) substrates in the regions indicated in **b**; red arrowheads show representative life cycles of adhesion complexes; Scale bar, 2 μ m. **d**, Representative immunofluorescence images of activated focal adhesion kinase (pY397) in MECs on the indicated gels. PA gel soft: 0.12 kPa, stiff: 20 kPa; silicone gel soft: 0.1 kPa, stiff: 21 kPa; Scale bars, 5 μ m. All experiments performed in triplicate.

A.3.4 Substrate surface tension drives nuclear localization of YAP

We next tested whether solid surface stresses could induce transcriptional activation through integrin-based rigidity sensing pathways. The gene regulatory factor Yes-associated protein (YAP) is known to direct cell fate transitions in response to mechanical stimuli (Dupont et al., 2011). When

rigidity sensing pathways are activated, YAP shuttles from the cytoplasm to the nucleus where it complexes with the transcriptional coactivator, TAZ, to turn on gene expression (Halder et al., 2012). In agreement with previous studies (Kim and Gumbiner, 2015), we found that blocking rigidity signaling through pharmacological inhibition of activated FAK stunted YAP translocation to the nucleus (Fig. A.4a). We next tested whether induction of rigidity signaling by solid surface stresses could trigger flux of YAP into the nucleus. Similar to the potency of bulk elasticity, solid surface tension was capable of robust and statistically significant induction of YAP relocation to the nucleus (Fig. A.4b, c). YAP was mostly cytosolic in cells on soft PA gels that had negligible surface stresses, but localized prominently in the nuclei of cells on rigid substrates and compliant substrates with high surface tension (Fig. A.4b, c). We also observed that surface tension could induce YAP/TAZ mediated gene expression. Expression levels of YAP-dependent connective tissue growth factor (CTGF) and Ankyrin Repeat Domain 1 (ANKRD1) were each significantly induced through cellular interaction with biomaterials of high surface tension, even in cases when the bulk elasticity alone was insufficient to trigger gene activation (Fig. A.4d). Together, these results indicate that solid surface stresses can regulate gene expression through induction of rigidity sensing pathways.

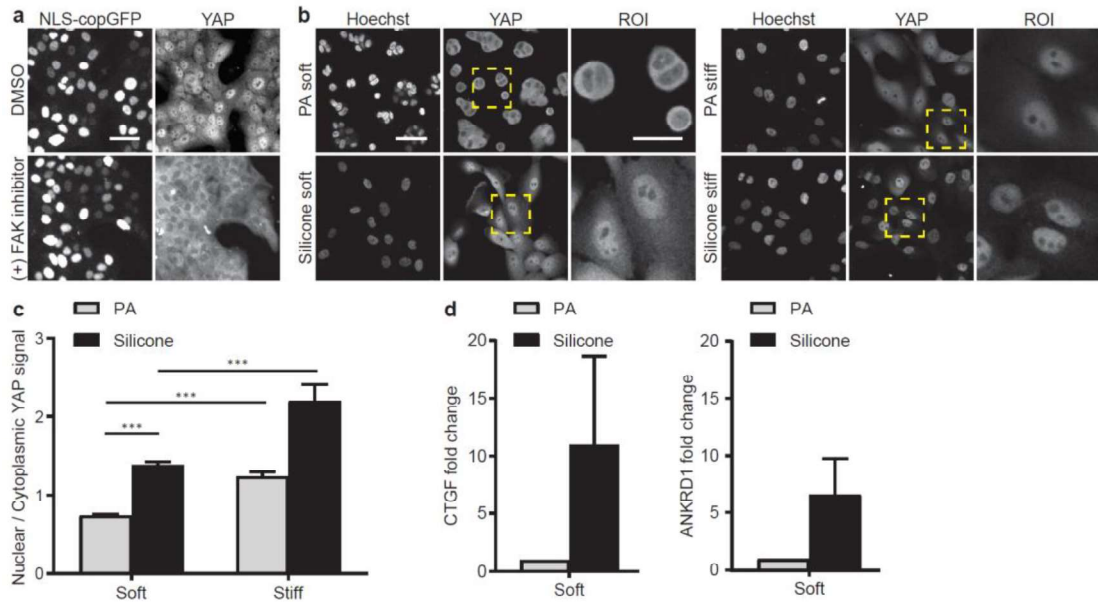


Figure A.4 – Substrate surface tension directs YAP/TAZ-mediated gene expression. **a**, Representative images of YAP localization on glass substrates; cells are serum starved overnight, treated with DMSO control or 5 μ M PF-573228 (FAK inhibitor) for two hours, then stimulated with EGF for 20 minutes; $n = 1$. **b**, Representative images of nuclei and YAP localization in MECs grown on the indicated gels; experiments conducted in triplicate. **c**, Ratio of nuclear YAP signal to cytoplasmic YAP signal. *** $p < 0.001$ (t test); 50-58 cells were analyzed for each condition; $n = 3$. **d**, Relative fold change in CTGF and ANKRD1 gene expression on soft PA and silicone gels; $n = 3$. PA gel soft: 0.12 kPa, stiff: 20 kPa; silicone gel soft: 0.1 kPa, stiff: 21 kPa; scale bars are 50 μ m and 25 μ m in the ROI; error bars show standard error of the mean.

A.3.5 Substrate surface tension promotes cell proliferation and viability

We next asked whether ECM surface stresses could inform cellular decisions for proliferation and survival, two biological programs that are directly linked to rigidity sensing pathways (Geiger et al., 2009). We found that proliferation was significantly upregulated on compliant substrates with higher surface tension (Fig. A.5a). Strikingly, the proliferation rates of cells on compliant matrices of high surface tension were indistinguishable from the rates we observed for cells plated on rigid glass, hydrogel, and elastomeric

substrates (Fig. A.5a). We also evaluated cell survival and observed that cells on highly compliant hydrogels with negligible surface tension had poor viability. However, cells on highly compliant elastomers with significant surface tension were robust and had viabilities comparable to cells on rigid substrates (Fig. A.5b). Indeed, we observed that approximately 20% of cells were dead 24 hours after being cultured on soft PA gels, but less than 5% of cells were found dead on glass, stiff PA gels, and soft and stiff silicone gels over the same duration (Fig. A.5b).

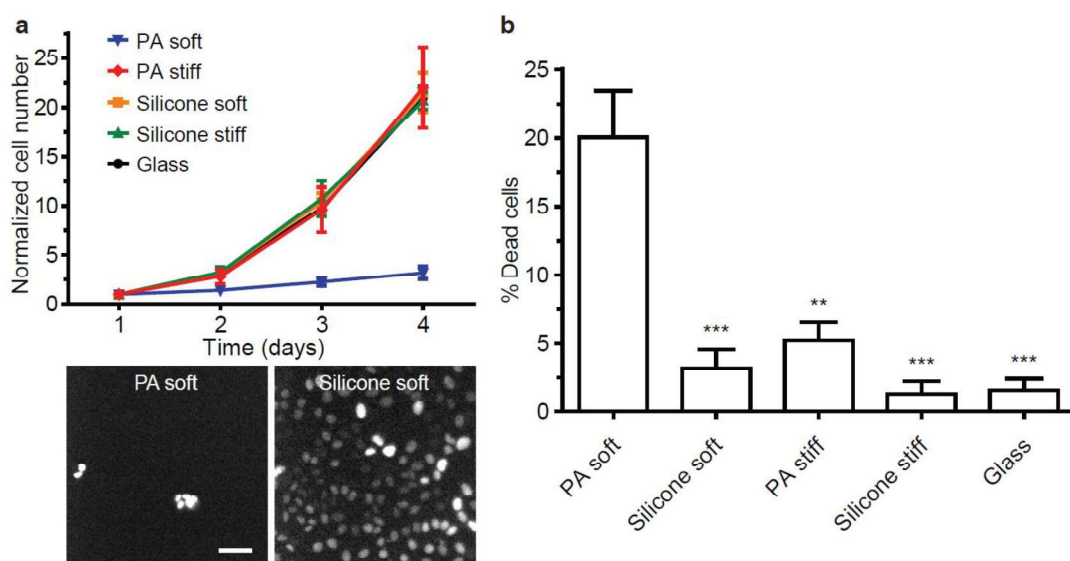


Figure A.5 – Substrate surface tension promotes cell proliferation and survival. **a**, Top: Quantification of MECs growing on glass, soft and stiff silicone gels, soft and stiff PA gels from day 1 to day 4 after seeding; data normalized to day one. Bottom: Fluorescent images of MECs expressing nuclear located GFP on compliant PA and silicone substrates four days after seeding. Scale bar, 50 μm . **b**, Percentage of dead cells among total cells growing on PA and silicone gels 24 hours after seeding. ** $p < 0.005$; *** $p < 0.001$ (t test); 170-290 cells were analyzed for each condition. For all experiments, PA gel soft: 0.12 kPa, stiff: 20 kPa; silicone gel soft: 0.1 kPa, stiff: 21 kPa; error bars show standard error of the mean.

A.4 CONCLUSIONS

Taken together, our results indicate that surface stresses of the ECM substrate can regulate gene expression and complex biological programs, including morphological changes, proliferation, and survival. The effect of substrate surface tension is mediated through integrin-based rigidity sensing, resulting in articulated focal adhesion patterns, well-organized stress fibers, and upregulated mechano-signaling. Given that surface tension can dominate the deformation of highly compliant materials and override directives related to bulk elasticity, our results argue that surface stresses should be strongly considered in the design of biomaterial scaffolds for tissue engineering.

Substrate stiffness (Engler et al., 2004; Paszek et al., 2005), stress relaxation (Chaudhuri et al., 2015, 2016), creep compliance (Cameron et al., 2011, 2014), porosity (Trappmann et al., 2012), and ligand tethering (Engler et al., 2004; Wen et al., 2014) are all significant parameters in the mechano-regulation of cells. The current work adds surface stress to known list of ECM parameters that physically direct cell behavior. Consideration of surface stresses provides a mechanism for cell-matrix responses that have previously defied expectations based on consideration of bulk elasticity alone (Trappmann et al., 2012; Wen et al., 2014). Most notably, we provide a mechanism for why cells sense and respond to the bulk elasticity of some materials, like polyacrylamide, but largely ignore the bulk elasticity of other materials, including silicone elastomers.

The effects of solid surface stresses on cell behavior can become significant when the elasto-capillary length, γ/E , of the material is greater than the cell body (Style et al., 2017). Elastomers, such as polydimethylsiloxane (PDMS), are becoming increasingly popular as a biomaterial scaffolds in basic

research and engineering due to their biocompatibility (Lee et al., 2004), ease of molding with micron-scale features (Whitesides et al., 2001), tunable optical properties (Gutierrez et al., 2011), and controllable bulk elasticity (Gutierrez et al., 2011). However, hydrophobic substrates can have moderate to high surface stresses in aqueous environments, which could mask cellular perception of the material's bulk elasticity. Surface modification to reduce surface energy and improve wettability would be one avenue to tune the surface stresses of biomaterials. For example, treatments with gas plasma or UV/ozone are often used to render PDMS more hydrophilic (Efimenko et al., 2002). Unfortunately, these approaches are known to create a rigid surface layer on silicone and other materials, and this layer could also mask the underlying elasticity of the material (Li et al., 2014). In our experiments, we avoid plasma and UV treatments for this reason. Surfactants are often an excellent choice for surface modification (Rosen and Kunjappu, 2012), but their ability to solubilize the plasma membrane is a concern in biomaterials applications (Nazari et al., 2012). Given that biomaterial surface energy and deformability are coupled, our results call for exploration and development of robust and biocompatible methods of chemical surface modification for tuning the surface tension of compliant biomaterials.

Our results also suggest important guidelines for the mechanical characterization of biomaterials. Nanoindentation with Atomic Force Microscopy (AFM), for example, is one of the most popular techniques for mechanical analysis of biomaterials (Dimitriadis et al., 2002). Extraction of mechanical parameters is typically achieved through data fitting to a Hertz deformation model that assumes negligible surface stresses (Dimitriadis et al., 2002). However, if the size of the AFM or nanoindenter tip is significantly

smaller than the elasto-capillary length, γ/E , surface stresses could dominate over bulk elasticity in the deformation of the material (Style et al., 2013; Wen et al., 2014). For nano- to micro- scale analysis of biomaterials with elasto-capillary lengths, solid surface stresses should be considered with one of several appropriate models that have now been developed (Style et al., 2013, 2017).

In conclusion, our findings indicate that the surface chemistry and deformability of biomaterials are inextricably connected. Tuning surface chemistry should be a viable strategy for controlling the nano- to micro-scale deformability of compliant biomaterials. Thus, surface chemistry and solid surface stresses are important criteria for the design of compliant biomaterials that are intended to physically orchestrate complex cellular and tissue-level behaviors.

A.5 METHODS

A.5.1 Gel fabrication

To make polyacrylamide hydrogels, glass bottom dishes were activated by 2% 3-aminopropyltriethoxysilane followed by 0.5% glutaraldehyde to facilitate polyacrylamide gel attachment to the glass. Meanwhile, coverslips were treated with Sigmacote to ensure detachment of polyacrylamide gels. Polyacrylamide solutions with acrylamide at final concentrations of 3% or 7.5% and bis-acrylamide at final concentrations ranging from 0.035% to 0.35% were mixed, N,N,N',N'-tetramethylethylenediamine (TEMED) was added to a final concentration of 0.01% in solution. The PA solution was degassed for 30 min and ammonium persulfate was added to a final concentration of 0.01% to initiate the polymerization. PA solution was sandwiched between the activated glass bottom dish and Sigmacote-treated coverslip and left to polymerize for

20-30 min. The coverslip was then removed and the polymerized PA gel was submerged in distilled water. To prepare silicone gels, parts A and B of QGel 310 (Quantum Silicones) were mixed in various ratios ranging from 1:0.60 to 1:8.9 in a Thinky planetary mixer and then degassed for 15 min. The mixtures were cured at room temperature for 1 hour and baked at 60°C for 21 hours.

A.5.2 Gel functionalization

PA gels were functionalized with fibronectin using the crosslinker Acryloyl-X, SE, 6-((acryloyl)amino)hexanoic Acid, Succinimidyl Ester (N6, ThermoFisher). The PA gel functionalization was adapted from a previous protocol (Lakins et al., 2012). Briefly, desired amount of 0.2% bis-acrylamide, 3% Irgacure 2959, 0.5 M HEPES pH 6.0, 0.3% N6 were mixed and applied onto gels, gels were overlaid with Sigmacote-treated coverslips, then placed under a UV source to activate photo-initiator for 10 min. The top coverslips were removed and the gels were gently washed with 50mM HEPES buffer for 5 min on ice for three times. The gel substrates were then incubated in 20 µg/ml fibronectin in 50mM HEPES buffer overnight at 4°C. The PA gels were washed with PBS. For silicone gel functionalization, the cured silicone gels were incubated in 10 µg/ml fibronectin in PBS overnight at 4°C to allow fibronectin adsorption onto the gels, and then washed with PBS.

A.5.3 Mechanical characterization

The elastic moduli of PA and silicone gels were measured by Dynamic Mechanical Thermal Analysis (DMTA) on a Q800 (TA Instruments). PA gels were cast into Teflon molds of 10mm in diameter and 3.5mm in depth between two Sigmacote-treated cover glasses. Silicone gels were cast into agarose molds of 10mm in diameter and ~3.8mm in depth and cured as above. Mechanical tests were conducted by compressing the gel samples between two compression

clamps along the axes of cylindrical samples with forces slowly ramping up. Vegetable oil was used between gel samples and compression clamps to prevent adhesion. Elastic moduli were calculated from the slope of the stress-strain curves from 7.5% to 12.5% strain.

A.5.4 Contact angle measurements

Measurements of water contact angle were conducted on VCA Optima Contact Angle (AST Products). 1.5 μL of water droplets were applied onto fibronectin-coated PA and silicone substrates.

A.5.5 Steel ball indentation measurements

PA and silicone gels were cast in glass bottom dishes at a thickness of approximately 500 μm and conjugated with Atto488-labelled fibronectin. Steel balls of 254 μm , 175 μm , 118 μm in radii were coated with hydrophilic coatings (Coatings2Go) according to manufacturer protocol to minimize ball-substrate adhesion. Gel surface profiles were visualized by taking z stack images of Atto488 fibronectin on the indented gel-buffer interfaces using Zeiss LSM880 Confocal Inverted Microscope with a 10x, NA 0.45 objective.

A.5.6 Cell lines and culture

MCF10A cells (ATCC) were cultured in DMEM/F12 media supplemented with 5% horse serum, 20 ng/ml EGF, 10 $\mu\text{g}/\text{ml}$ insulin, 500 ng/ml hydrocortisone and 100 ng/ml cholera toxin. MCF10A NLS-copGFP and MCF10A Paxillin-mCherry stable lines were prepared by lenti-viral transformation using NLS copGFP pCDH and Paxillin-mCherry pLV hygro tetOn plasmids, respectively. MCF10A F-tractin-EGFP stable lines were prepared using a transposon-based method with an F-tractin-EGFP plasmid. The backbone pPB puro tetOn was modified by swapping eukaryotic antibiotic resistance marker from puromycin to zeocin. Then the F-tractin-EGFP plasmid

was prepared by inserting F-tractin-EGFP from F-tractin-EGFP C1 into pPB tetOn using BamHI and EcoRI restriction sites.

A.5.7 Antibodies and reagents

The following antibodies were used: monoclonal FAK (13009S, Cell Signaling); FAK^{pY397} (8556S, Cell Signaling); YAP (sc-101199, Santa Cruz). FAK inhibitor was PF-573228 (14924, Cayman Chemical).

A.5.8 Cell morphology and spreading assays

MCF10A cells were plated on the PA and silicone gels at a density of 2600 cells/cm² and imaged 24 hours later with phase contrast microscopy on an Olympus IX81 microscope with a 20x objective. Cell area was manually measured and analyzed with ImageJ.

A.5.9 Immunofluorescence imaging

Cells were seeded at 5000 cells/cm² and fixed directly using 4% paraformaldehyde at room temperature after 24 hours. For inhibitor treatments, 5000 cells/cm² were plated for 24 hours, serum starved for 16 hours, treated with inhibitors for 2 hours, and stimulated with 20 ng/mL EGF before fixation in 4% paraformaldehyde at room temperature. All samples were incubated with primary antibody followed by Alexa-conjugated secondary antibodies. Nuclei were stained with Hoechst or through expression of NLS-copGFP. Imaging was performed on a Zeiss LSM i880. Nuclear to cytoplasmic YAP signal was measured manually with ImageJ.

A.5.10 Cell proliferation and viability assays

Cell proliferation was measured over a period of 4 days after seeding cells with at an initial density of 2600 cells/cm². MCF10A NLS copGFP proliferation was continuously monitored custom epi-fluorescence microscope housed in a standard tissue-culture incubator (37°C, 90% humidity, 5% CO₂; 10x

objective; 1 hour acquisition intervals). Cell numbers were quantified manually every 24 hours using ImageJ. To measure cell viability, cells were seeded at a density of 1300 cells/cm² on fibronectin functionalized PA and silicone gels in a 12-well-plate and assayed after 24 hours with a LIVE/DEAD Viability/Cytotoxicity Kit (ThermoFisher). Fluorescent images were acquired using GFP and TXRED channels in Olympus IX81 with a 10x objective and quantified manually in ImageJ.

A.5.11 Gene expression analysis

Cells were grown on gels for 24 hours before harvesting with TRIzol (Invitrogen) for total RNA extraction. Power SYBR RNA-to-CT 1 Step Kit (ThermoFisher 4391178) was used for reactions. The qPCR reactions were run with the ViiA 7 Real-Time PCR System and analyzed with QuantStudio Real-Time PCR Software. CTGF and ANKRD1 gene expression were calculated with the comparative Ct method relative to GAPDH. ANKRD1 forward primer: AGTAGAGGAACTGGTCACTGG; ANKRD1 reverse primer: TGGGCTAGAAGTGTCTTCAGAT; CTGF forward primer: AGGAGTGGGTGTGTGACGA; CTGF reverse primer: CCAGGCAGTTGGCTCTAATC; GAPDH forward primer: CTGGGCTACACTGAGCACC; GAPDH reverse primer: AAGTGGTCGTTGAGGGCAATG.

Statistics. Statistical significance was determined by student's *t* test, as appropriate.

A.6 ACKNOWLEDGEMENTS

We thank J. Lammerding for NLS copGFP pCDH plasmid; V. Weaver and J. Lakins for Paxillin-mCherry pLV hygro tetOn and pPB puro tetOn

plasmids; and C. Waterman for the F-tractin-EGFP C1 plasmid. We thank M. Colville for assistance with cloning and imaging. This investigation was supported by the National Institutes of Health under Ruth L. Kirschstein National Research Service Award (2T32GM008267) from the National Institute of General Medical Sciences (C.R.S), the Knight Family Foundation Graduate Research Fellowship in Nanoscience and Technology (C.R.S), Samuel C. Fleming Family Graduate Fellowship (C.R.S), National Cancer Institute R33-CA193043 (M.J.P), and U.S. Department of Energy DEFG02-07ER46463 (C.-Y.H). Confocal imaging was supported through the Cornell University Biotechnology Resource Center (BRC) Imaging Facility (Grant NIH S10OD018516). This work made use of the Cornell NanoScale Facility, a member of the National Nanotechnology Coordinated Infrastructure (NNCI), which is supported by the National Science Foundation (Grant ECCS-1542081). This work also made use of the Cornell Center for Materials Research Shared Facilities, which are supported through the NSF MRSEC program (DMR-1120296).

A.6.1 Complete author list

Zhu Cheng[†], Carolyn R. Shurer[†], Vivek K. Gupta, Grace Chuang, Chung-Yuen Hui, Matthew J. Paszek

[†]These authors contributed equally to this work.

A.6.2 Author contributions

Z.C., C.R.S., and M.J.P conceived and designed the experimental plan. Z.C. and V.K.G. conducted the mechanical testing. C.R.S. and M.J.P prepared the cell lines. C.R.S. and Z.C. planned and conducted the focal adhesion and YAP/TAZ imaging experiments. C.R.S. and G.C. planned and conducted the gene expression experiments. Z.C. executed the proliferation and viabilities

studies. Z.C., C.R.S, C.-Y.H, and M.J.P wrote the manuscript. All authors discussed the results and contributed to the final preparation of the manuscript.

A.6.3 Competing financial interests

The authors declare no competing financial interests.

A.7 SUPPLEMENTAL FIGURES

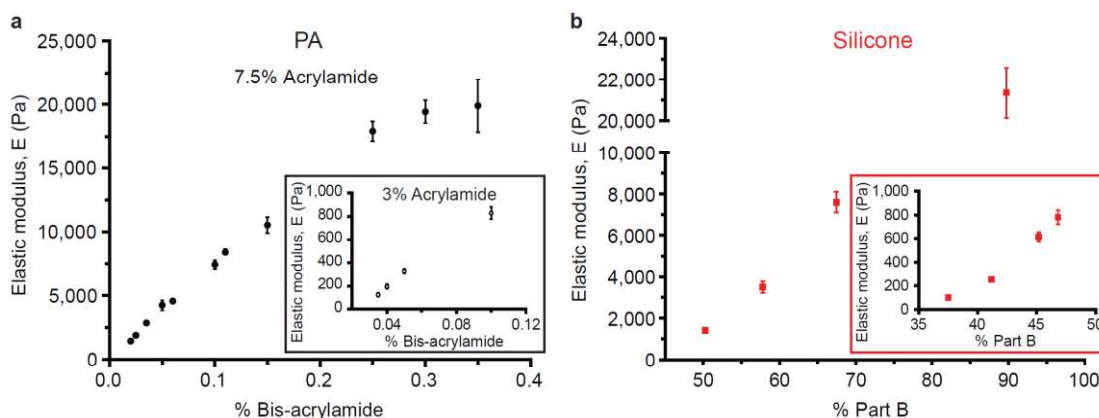


Figure A.S1 – Mechanical characterization of PA and silicone substrates. a, Elastic moduli of polyacrylamide (PA) gels with various acrylamide to bis-acrylamide ratios measured by Dynamic Mechanical Thermal Analysis (DMTA). 7-9 independent samples were tested for each point. **b,** Elastic moduli of silicone substrates with varying proportions of base silicone to curing reagent measured by DMTA. 7-9 independent samples were tested for each point. Error bars show standard deviation of the mean.

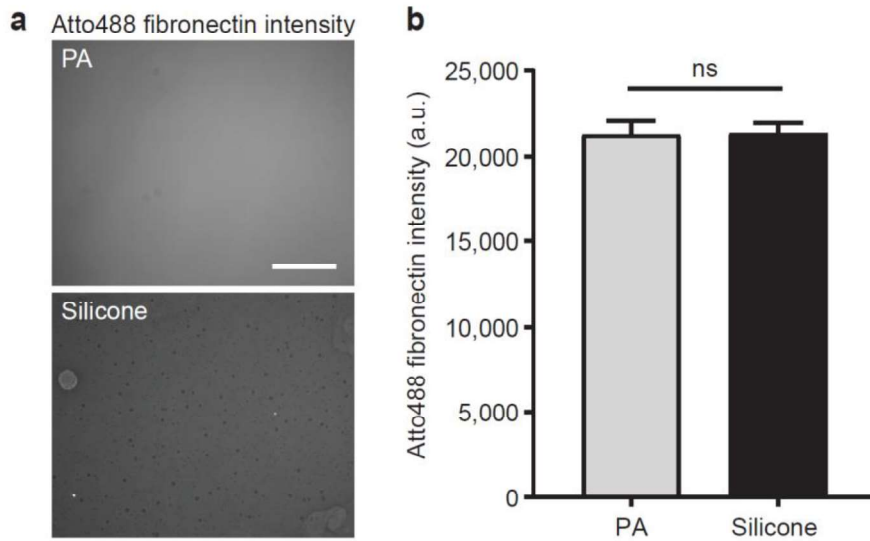


Figure A.S2 – Fibronectin coating on PA and silicone substrates. a, Representative fluorescent images of Atto488-conjugated fibronectin on PA and silicone substrates; Scale bar: 100 μ m. **b,** Average Atto488 intensity recorded on the substrate surface; $n \geq 9$ for each condition; error bars show standard deviation of the mean.

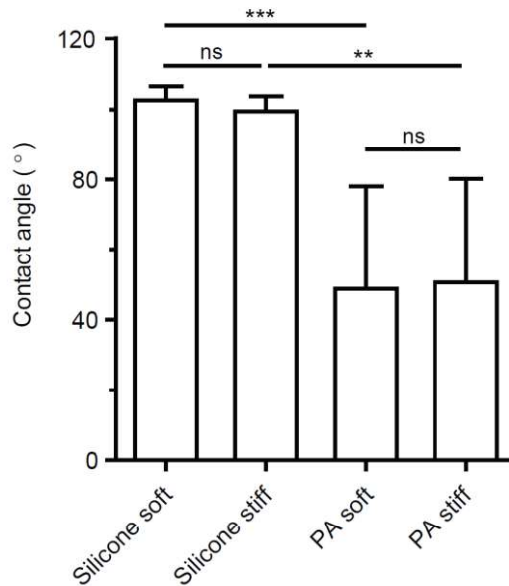


Figure A.S3 – Contact angles of water droplets on PA and silicone substrates. Quantified contact angles of water droplets on fibronectin-functionalized PA and silicone materials. ** $p < 0.005$; *** $p < 0.001$; ns, not significant (t test); More than 5 independent samples were analyzed for each condition. Error bars show standard deviation of the mean.

REFERENCES

Agrawal, B., Krantz, M.J., Parker, J., and Longenecker, B.M. (1998). Expression of MUC1 Mucin on Activated Human T Cells: Implications for a Role of MUC1 in Normal Immune Regulation. *Cancer Research* 58, 4079–4081.

Alexander, S. (1977). Adsorption of chain molecules with a polar head a scaling description. *Journal de Physique* 38, 983–987.

Amaral, R.L.F. do, Bomfim, A. de S., Abreu-Neto, M.S. de, Picanço-Castro, V., Russo, E.M. de S., Covas, D.T., and Swiech, K. (2016). Approaches for recombinant human factor IX production in serum-free suspension cultures. *Biotechnol Lett* 38, 385–394.

Angelova, M.I., and Dimitrov, D.S. (1986). Liposome electroformation. *Faraday Discussions of the Chemical Society* 81, 303–311.

Antonyak, M.A., Li, B., Boroughs, L.K., Johnson, J.L., Druso, J.E., Bryant, K.L., Holowka, D.A., and Cerione, R.A. (2011). Cancer cell-derived microvesicles induce transformation by transferring tissue transglutaminase and fibronectin to recipient cells. *Proceedings of the National Academy of Sciences* 108, 4852–4857.

Apweiler, R., Hermjakob, H., and Sharon, N. (1999). On the frequency of protein glycosylation, as deduced from analysis of the SWISS-PROT database1. *Biochimica et Biophysica Acta (BBA) - General Subjects* 1473, 4–8.

Backliwal, G., Hildinger, M., Kuettel, I., Delegrange, F., Hacker, D.L., and Wurm, F.M. (2008). Valproic acid: a viable alternative to sodium butyrate for enhancing protein expression in mammalian cell cultures. *Biotechnol Bioeng* 101, 182–189.

Backstrom, M., Link, T., Olson, F.J., Karlsson, H., Graham, R., Picco, G., Burchell, J., Taylor-Papadimitriou, J., Noll, T., and Hansson, G.C. (2003). Recombinant MUC1 mucin with a breast cancer-like O-glycosylation produced in large amounts in Chinese-hamster ovary cells. *Biochem J* 376, 677–686.

Bäckström, M., Link, T., Olson, F.J., Karlsson, H., Graham, R., Picco, G., Burchell, J., Taylor-Papadimitriou, J., Noll, T., and Hansson, G.C. (2003). Recombinant MUC1 mucin with a breast cancer-like O-glycosylation

produced in large amounts in Chinese-hamster ovary cells. *Biochem. J.* 376, 677–686.

Bahabri, S.A., Suwairi, W.M., Laxer, R.M., Polinkovsky, A., Dalaan, A.A., and Warman, M.L. (1998). The camptodactyly-arthropathy-coxa vara-pericarditis syndrome: Clinical features and genetic mapping to human chromosome 1. *Arthritis & Rheumatism* 41, 730–735.

Bar-Ziv, R., Tlusty, T., Moses, E., Safran, S.A., and Bershadsky, A. (1999). Pearling in cells: A clue to understanding cell shape. *Proc Natl Acad Sci U S A* 96, 10140–10145.

Becker, A., Thakur, B.K., Weiss, J.M., Kim, H.S., Peinado, H., and Lyden, D. (2016). Extracellular Vesicles in Cancer: Cell-to-Cell Mediators of Metastasis. *Cancer Cell* 30, 836–848.

Bennett, E.P., Mandel, U., Clausen, H., Gerken, T.A., Fritz, T.A., and Tabak, L.A. (2012). Control of mucin-type O-glycosylation: A classification of the polypeptide GalNAc-transferase gene family. *Glycobiology* 22, 736–756.

Bennett Jr., R., Jarvela, T., Engelhardt, P., Kostamovaara, L., Sparks, P., Carpen, O., Turunen, O., and Vaheri, A. (2001). Mucin MUC1 is seen in cell surface protrusions together with ezrin in immunoelectron tomography and is concentrated at tips of filopodial protrusions in MCF-7 breast carcinoma cells. *J Histochem Cytochem* 49, 67-77.

Benson, G. (1999). Tandem repeats finder: a program to analyze DNA sequences. *Nucleic Acids Research* 27, 573–580.

Bergert, M., Erzberger, A., Desai, R.A., Aspalter, I.M., Oates, A.C., Charras, G., Salbreux, G., and Paluch, E.K. (2015). Force transmission during adhesion-independent migration. *Nature Cell Biology* 17, 524–529.

Berois, N., Gattolliat, C.-H., Barrios, E., Capandeguy, L., Douc-Rasy, S., Valteau-Couanet, D., Bénard, J., and Osinaga, E. (2013). GALNT9 gene expression is a prognostic marker in neuroblastoma patients. *Clin. Chem.* 59, 225–233.

Bischoff, M., Gradilla, A.-C., Seijo, I., Andrés, G., Rodríguez-Navas, C., González-Méndez, L., and Guerrero, I. (2013). Cytosomes are required for the

- establishment of a normal Hedgehog morphogen gradient in *Drosophila* epithelia. *Nature Cell Biology* 15, 1269–1281.
- Borisov, O.V., and Zhulina, E.B. (2002). Effect of Salt on Self-Assembly in Charged Block Copolymer Micelles. *Macromolecules* 35, 4472–4480.
- Bosques, C.J., Collins, B.E., Meador, J.W., Sarvaiya, H., Murphy, J.L., DelloRusso, G., Bulik, D.A., Hsu, I.H., Washburn, N., Sipsy, S.F., et al. (2010). Chinese hamster ovary cells can produce galactose- α -1,3-galactose antigens on proteins. *Nature Biotechnology* 28, 1153–1156.
- Boussif, O., Lezoualc'h, F., Zanta, M.A., Mergny, M.D., Scherman, D., Demeneix, B., and Behr, J.P. (1995). A versatile vector for gene and oligonucleotide transfer into cells in culture and in vivo: polyethylenimine. *Proc Natl Acad Sci U S A* 92, 7297–7301.
- Bracha, D., Karzbrun, E., Shemer, G., Pincus, P.A., and Bar-Ziv, R.H. (2013). Entropy-driven collective interactions in DNA brushes on a biochip. *PNAS* 110, 4534–4538.
- Bramwell, M.E., Wiseman, G., and Shotton, D.M. (1986). Electron-microscopic studies of the CA antigen, epitectin. *J. Cell. Sci.* 86, 249–261.
- Brooks, S.A. (2004). Appropriate glycosylation of recombinant proteins for human use. *Molecular Biotechnology* 28, 241–255.
- Brown, X.Q., Ookawa, K., and Wong, J.Y. (2005). Evaluation of polydimethylsiloxane scaffolds with physiologically-relevant elastic moduli: interplay of substrate mechanics and surface chemistry effects on vascular smooth muscle cell response. *Biomaterials* 26, 3123–3129.
- Buck, C.A., Glick, M.C., and Warren, L. (1971). Glycopeptides from the surface of control and virus-transformed cells. *Science* 172, 169–171.
- Busch, D.J., Houser, J.R., Hayden, C.C., Sherman, M.B., Lafer, E.M., and Stachowiak, J.C. (2015). Intrinsically disordered proteins drive membrane curvature. *Nature Communications* 6, 7875.
- Butler, M., and Spearman, M. (2014). The choice of mammalian cell host and possibilities for glycosylation engineering. *Current Opinion in Biotechnology* 30, 107–112.

Button, B., Cai, L.-H., Ehre, C., Kesimer, M., Hill, D.B., Sheehan, J.K., Boucher, R.C., and Rubinstein, M. (2012). A periciliary brush promotes the lung health by separating the mucus layer from airway epithelia. *Science (New York, N.Y.)* 337, 937–941.

Cameron, A.R., Frith, J.E., and Cooper-White, J.J. (2011). The influence of substrate creep on mesenchymal stem cell behaviour and phenotype. *Biomaterials* 32, 5979–5993.

Cameron, A.R., Frith, J.E., Gomez, G.A., Yap, A.S., and Cooper-White, J.J. (2014). The effect of time-dependent deformation of viscoelastic hydrogels on myogenic induction and Rac1 activity in mesenchymal stem cells. *Biomaterials* 35, 1857–1868.

Campeau, E., Ruhl, V.E., Rodier, F., Smith, C.L., Rahmberg, B.L., Fuss, J.O., Campisi, J., Yaswen, P., Cooper, P.K., and Kaufman, P.D. (2009). A Versatile Viral System for Expression and Depletion of Proteins in Mammalian Cells. *PLOS ONE* 4, e6529.

Campelo, F., and Hernández-Machado, A. (2007). Model for Curvature-Driven Pearling Instability in Membranes. *Physical Review Letters* 99, 088101.

Carraway, K.L., Ramsauer, V.P., Haq, B., and Carothers Carraway, C.A. (2003). Cell signaling through membrane mucins. *Bioessays* 25, 66–71.

Carter, P.J. (2011). Introduction to current and future protein therapeutics: A protein engineering perspective. *Experimental Cell Research* 317, 1261–1269.

Casademunt, E., Martinelle, K., Jernberg, M., Winge, S., Tiemeyer, M., Biesert, L., Knaub, S., Walter, O., and Schröder, C. (2012). The first recombinant human coagulation factor VIII of human origin: human cell line and manufacturing characteristics. *Eur J Haematol* 89, 165–176.

Chaika, N.V., Gebregiworgis, T., Lewallen, M.E., Purohit, V., Radhakrishnan, P., Liu, X., Zhang, B., Mehla, K., Brown, R.B., Caffrey, T., et al. (2012). MUC1 mucin stabilizes and activates hypoxia-inducible factor 1 alpha to regulate metabolism in pancreatic cancer. *Proc Natl Acad Sci U S A* 109, 13787–13792.

Charras, G., and Paluch, E. (2008). Blebs lead the way: how to migrate without lamellipodia. *Nature Reviews Molecular Cell Biology* 9, 730–736.

Charras, G.T., Yarrow, J.C., Horton, M.A., Mahadevan, L., and Mitchison, T.J. (2005). Non-equilibration of hydrostatic pressure in blebbing cells. *Nature* 435, 365–369.

Charras, G.T., Coughlin, M., Mitchison, T.J., and Mahadevan, L. (2008). Life and Times of a Cellular Bleb. *Biophysical Journal* 94, 1836–1853.

Chatham, J.C., Nöt, L.G., Fülöp, N., and Marchase, R.B. (2008). HEXOSAMINE BIOSYNTHESIS AND PROTEIN O-GLYCOSYLATION: THE FIRST LINE OF DEFENSE AGAINST STRESS, ISCHEMIA, AND TRAUMA. *Shock* 29, 431.

Chatterjee, S.K., Bhattacharya, M., and Barlow, J.J. (1979). Glycosyltransferase and Glycosidase Activities in Ovarian Cancer Patients. *Cancer Res* 39, 1943–1951.

Chaudhuri, O., Gu, L., Darnell, M., Klumpers, D., Bencherif, S.A., Weaver, J.C., Huebsch, N., and Mooney, D.J. (2015). Substrate stress relaxation regulates cell spreading. *Nat Commun* 6, 6365.

Chaudhuri, O., Gu, L., Klumpers, D., Darnell, M., Bencherif, S.A., Weaver, J.C., Huebsch, N., Lee, H., Lippens, E., Duda, G.N., et al. (2016). Hydrogels with tunable stress relaxation regulate stem cell fate and activity. *Nat Mater* 15, 326–334.

Chen, W.L., Cordero, R., Tran, H., and Ober, C.K. (2017). 50th Anniversary Perspective: Polymer Brushes: Novel Surfaces for Future Materials. *Macromolecules* 50, 4089–4113.

Cheng, J.-P., Yan, Y., Wang, X.-Y., Lu, Y.-L., Yuan, Y.-H., Jia, J., and Ren, J. (2011). MUC1-positive circulating tumor cells and MUC1 protein predict chemotherapeutic efficacy in the treatment of metastatic breast cancer. *Chin J Cancer* 30, 54–61.

Cleland Robert L. (2004). Viscometry and sedimentation equilibrium of partially hydrolyzed hyaluronate: Comparison with theoretical models of wormlike chains. *Biopolymers* 23, 647–666.

Cloosen, S., Thio, M., Vanclée, A., Leeuwen, V., M, E.B., Senden-Gijsbers, B.L.M.G., Oving, E.B.H., Germeraad, W.T. V., and Bos, G.M.J. (2004). Mucin-1 is expressed on dendritic cells, both in vitro and in vivo. *International Immunology* 16, 1561–1571.

- Coltart, D.M., Royyuru, A.K., Williams, L.J., Glunz, P.W., Sames, D., Kuduk, S.D., Schwarz, J.B., Chen, X.-T., Danishefsky, S.J., and Live, D.H. (2002). Principles of Mucin Architecture: Structural Studies on Synthetic Glycopeptides Bearing Clustered Mono-, Di-, Tri-, and Hexasaccharide Glycodomains. *J. Am. Chem. Soc.* *124*, 9833–9844.
- Costantini, L.M., Baloban, M., Markwardt, M.L., Rizzo, M., Guo, F., Verkhusha, V.V., and Snapp, E.L. (2015). A palette of fluorescent proteins optimized for diverse cellular environments. *Nat Commun* *6*, 7670.
- Cowman, M.K., Spagnoli, C., Kudasheva, D., Li, M., Dyal, A., Kanai, S., and Balazs, E.A. (2005). Extended, relaxed, and condensed conformations of hyaluronan observed by atomic force microscopy. *Biophys. J.* *88*, 590–602.
- Croci, D.O., Cerliani, J.P., Dalotto-Moreno, T., Méndez-Huergo, S.P., Mascanfroni, I.D., Dergan-Dylon, S., Toscano, M.A., Caramelo, J.J., García-Vallejo, J.J., Ouyang, J., et al. (2014). Glycosylation-Dependent Lectin-Receptor Interactions Preserve Angiogenesis in Anti-VEGF Refractory Tumors. *Cell* *156*, 744–758.
- Cruz-Chu, E.R., Malafeev, A., Pajarskas, T., Pivkin, I.V., and Koumoutsakos, P. (2014). Structure and Response to Flow of the Glycocalyx Layer. *Biophysical Journal* *106*, 232–243.
- Cuvelier, D., Chiaruttini, N., Bassereau, P., and Nassoy, P. (2005). Pulling long tubes from firmly adhered vesicles. *Europhys. Lett.* *71*, 1015–1021.
- Dall’Olio, F., Malagolini, N., Trinchera, M., and Chiricolo, M. (2012). Mechanisms of cancer-associated glycosylation changes. *Front Biosci (Landmark Ed)* *17*, 670–699.
- D’Aloia, M.M., Zizzari, I.G., Sacchetti, B., Pierelli, L., and Alimandi, M. (2018). CAR-T cells: The long and winding road to solid tumors review-article. *Cell Death and Disease* *9*, 282.
- Day, A.J., and Sheehan, J.K. (2001). Hyaluronan: polysaccharide chaos to protein organisation. *Curr. Opin. Struct. Biol.* *11*, 617–622.
- Daye, D., and Wellen, K.E. (2012). Metabolic reprogramming in cancer: Unraveling the role of glutamine in tumorigenesis. *Seminars in Cell & Developmental Biology* *23*, 362–369.

- DeBerardinis, R.J., and Chandel, N.S. (2016). Fundamentals of cancer metabolism. *Sci Adv* 2.
- Dee, K.U., Shuler, M.L., and Wood, H.A. (1997). Inducing single-cell suspension of BTI-TN5B1-4 insect cells: I. The use of sulfated polyanions to prevent cell aggregation and enhance recombinant protein production. *Biotechnology and Bioengineering* 54, 191–205.
- Denisin, A.K., and Pruitt, B.L. (2016). Tuning the Range of Polyacrylamide Gel Stiffness for Mechanobiology Applications. *ACS Appl. Mater. Interfaces*.
- Dennis, J.W., Nabi, I.R., and Demetriou, M. (2009). Metabolism, Cell Surface Organization, and Disease. *Cell* 139, 1229–1241.
- Derényi, I., Jülicher, F., and Prost, J. (2002). Formation and Interaction of Membrane Tubes. *Phys. Rev. Lett.* 88, 238101.
- Derouazi, M., Girard, P., Van Tilborgh, F., Iglesias, K., Muller, N., Bertschinger, M., and Wurm, F.M. (2004). Serum-free large-scale transient transfection of CHO cells. *Biotechnol. Bioeng.* 87, 537–545.
- Dhanisha, S.S., Guruvayoorappan, C., Drishya, S., and Abeesh, P. (2018). Mucins: Structural diversity, biosynthesis, its role in pathogenesis and as possible therapeutic targets. *Critical Reviews in Oncology/Hematology* 122, 98–122.
- Dibble, C.C., and Manning, B.D. (2013). Signal integration by mTORC1 coordinates nutrient input with biosynthetic output. *Nat Cell Biol* 15, 555–564.
- Dimitriadis, E.K., Horkay, F., Maresca, J., Kachar, B., and Chadwick, R.S. (2002). Determination of Elastic Moduli of Thin Layers of Soft Material Using the Atomic Force Microscope. *Biophysical Journal* 82, 2798–2810.
- Discher, D.E., Janmey, P., and Wang, Y. (2005). Tissue Cells Feel and Respond to the Stiffness of Their Substrate. *Science* 310, 1139–1143.
- Dumont, J., Euwart, D., Mei, B., Estes, S., and Kshirsagar, R. (2016). Human cell lines for biopharmaceutical manufacturing: history, status, and future perspectives. *Critical Reviews in Biotechnology* 36, 1110–1122.

Dupont, S., Morsut, L., Aragona, M., Enzo, E., Giulitti, S., Cordenonsi, M., Zanconato, F., Le Digabel, J., Forcato, M., Bicciato, S., et al. (2011). Role of YAP/TAZ in mechanotransduction. *Nature* 474, 179–183.

Durocher, Y., Perret, S., and Kamen, A. (2002). High-level and high-throughput recombinant protein production by transient transfection of suspension-growing human 293-EBNA1 cells. *Nucleic Acids Res* 30, e9.

Duval, K., Grover, H., Han, L.-H., Mou, Y., Pegoraro, A.F., Fredberg, J., and Chen, Z. (2017). Modeling Physiological Events in 2D vs. 3D Cell Culture. *Physiology (Bethesda)* 32, 266–277.

Edelstein, A.D., Tsuchida, M.A., Amodaj, N., Pinkard, H., Vale, R.D., and Stuurman, N. (2014). Advanced methods of microscope control using μ Manager software. *Journal of Biological Methods* 1, 10.

Efimenko, K., Wallace, W.E., and Genzer, J. (2002). Surface Modification of Sylgard-184 Poly(dimethyl siloxane) Networks by Ultraviolet and Ultraviolet/Ozone Treatment. *Journal of Colloid and Interface Science* 254, 306–315.

Elsaid, K.A., Fleming, B.C., Oksendahl, H.L., Machan, J.T., Fadale, P.D., Hulstyn, M.J., Shalvoy, R., and Jay, G.D. (2008). Decreased lubricin concentrations and markers of joint inflammation in the synovial fluid of patients with anterior cruciate ligament injury. *Arthritis & Rheumatism* 58, 1707–1715.

Engelmann, K., Kinlough, C.L., Müller, S., Razawi, H., Baldus, S.E., Hughey, R.P., and Hanisch, F.-G. (2005). Transmembrane and secreted MUC1 probes show trafficking-dependent changes in O-glycan core profiles. *Glycobiology* 15, 1111–1124.

Engler, A., Bacakova, L., Newman, C., Hategan, A., Griffin, M., and Discher, D. (2004). Substrate Compliance versus Ligand Density in Cell on Gel Responses. *Biophysical Journal* 86, 617–628.

Engler, A.J., Sen, S., Sweeney, H.L., and Discher, D.E. (2006). Matrix Elasticity Directs Stem Cell Lineage Specification. *Cell* 126, 677–689.

- Estrella, R.P., Whitelock, J.M., Packer, N.H., and Karlsson, N.G. (2010). The glycosylation of human synovial lubricin: implications for its role in inflammation. *Biochemical Journal* 429, 359–367.
- Evanko, S.P., Tammi, M.I., Tammi, R.H., and Wight, T.N. (2007). Hyaluronan-Dependent Pericellular Matrix. *Advanced Drug Delivery Reviews* 59, 1351–1365.
- Evans, E., and Rawicz, W. (1997). Elasticity of “Fuzzy” Biomembranes. *Phys. Rev. Lett.* 79, 2379–2382.
- Flannery, C.R., Zollner, R., Corcoran, C., Jones, A.R., Root, A., Rivera-Bermudez, M.A., Blanchet, T., Gleghorn, J.P., Bonassar, L.J., Bendele, A.M., et al. (2009). Prevention of cartilage degeneration in a rat model of osteoarthritis by intraarticular treatment with recombinant lubricin. *Arthritis Rheum* 60, 840–847.
- Footer, M.J., Kerssemakers, J.W.J., Theriot, J.A., and Dogterom, M. (2007). Direct measurement of force generation by actin filament polymerization using an optical trap. *Proceedings of the National Academy of Sciences* 104, 2181–2186.
- Fowke, T.M., Karunasinghe, R.N., Bai, J.-Z., Jordan, S., Gunn, A.J., and Dean, J.M. (2017). Hyaluronan synthesis by developing cortical neurons *in vitro*. *Scientific Reports* 7, 44135.
- Freedman, L.P., Gibson, M.C., Ethier, S.P., Soule, H.R., Neve, R.M., and Reid, Y.A. (2015). Reproducibility: changing the policies and culture of cell line authentication. *Nature Methods* 12, 493–497.
- Freeze, H.H. (2013). Understanding Human Glycosylation Disorders: Biochemistry Leads the Charge. *J. Biol. Chem.* 288, 6936–6945.
- Friedl, P., and Wolf, K. (2003). Tumour-cell invasion and migration: diversity and escape mechanisms. *Nat Rev Cancer* 3, 362–374.
- Friedl, P., and Wolf, K. (2010). Plasticity of cell migration: a multiscale tuning model. *J Cell Biol* 188, 11–19.

- Fu, C., Zhao, H., Wang, Y., Cai, H., Xiao, Y., Zeng, Y., and Chen, H. (2016). Tumor-associated antigens: Tn antigen, sTn antigen, and T antigen. *HLA* 88, 275–286.
- Gangoda, L., Boukouris, S., Liem, M., Kalra, H., and Mathivanan, S. (2015). Extracellular vesicles including exosomes are mediators of signal transduction: are they protective or pathogenic? *Proteomics* 15, 260–271.
- Geiger, B., Spatz, J.P., and Bershadsky, A.D. (2009). Environmental sensing through focal adhesions. *Nat Rev Mol Cell Biol* 10, 21–33.
- Gemayel, R., Vinces, M.D., Legendre, M., and Verstrepen, K.J. (2010). Variable tandem repeats accelerate evolution of coding and regulatory sequences. *Annu. Rev. Genet.* 44, 445–477.
- Gendler, S.J. (2001). MUC1, The Renaissance Molecule. *J Mammary Gland Biol Neoplasia* 6, 339–353.
- Gendler, S.J., and Spicer, A.P. (1995). Epithelial Mucin Genes. *Annual Review of Physiology* 57, 607–634.
- Genies, P.-G. (1979). *Scaling Concepts in Polymer Physics* (Ithaca, NY: Cornell University Press).
- de Gennes, P. (1980). Conformations of polymers attached to an interface. *Macromolecules* 13, 1069–1075.
- Geraghty, R.J., Capes-Davis, A., Davis, J.M., Downward, J., Freshney, R.I., Knezevic, I., Lovell-Badge, R., Masters, J.R.W., Meredith, J., Stacey, G.N., et al. (2014). Guidelines for the use of cell lines in biomedical research. *British Journal of Cancer* 111, 1021–1046.
- Gerken, T.A., Butenhof, K.J., and Shogren, R. (1989). Effects of glycosylation on the conformation and dynamics of O-linked glycoproteins: carbon-13 NMR studies of ovine submaxillary mucin. *Biochemistry* 28, 5536–5543.
- Ghaderi, D., Zhang, M., Hurtado-Ziola, N., and Varki, A. (2012). Production platforms for biotherapeutic glycoproteins. Occurrence, impact, and challenges of non-human sialylation. *Biotechnol Genet Eng Rev* 28, 147–175.

- Gipson, I.K., Spurr-Michaud, S., Tisdale, A., and Menon, B.B. (2014). Comparison of the Transmembrane Mucins MUC1 and MUC16 in Epithelial Barrier Function. *PLOS ONE* 9, e100393.
- Gleghorn, J.P., and Bonassar, L.J. (2008). Lubrication mode analysis of articular cartilage using Stribeck surfaces. *J Biomech* 41, 1910–1918.
- Godula, K., Umbel, M.L., Rabuka, D., Botyanszki, Z., Bertozzi, C.R., and Parthasarathy, R. (2009a). Control of the Molecular Orientation of Membrane-Anchored Biomimetic Glycopolymers. *J. Am. Chem. Soc.* 131, 10263–10268.
- Godula, K., Rabuka, D., Nam, K.T., and Bertozzi, C.R. (2009b). Synthesis and Microcontact Printing of Dual End-Functionalized Mucin-like Glycopolymers for Microarray Applications. *Angewandte Chemie International Edition* 48, 4973–4976.
- Gomes, J., Marcos, N.T., Berois, N., Osinaga, E., Magalhães, A., Pinto-de-Sousa, J., Almeida, R., Gärtner, F., and Reis, C.A. (2009). Expression of UDP-N-acetyl-D-galactosamine: polypeptide N-acetylgalactosaminyltransferase-6 in gastric mucosa, intestinal metaplasia, and gastric carcinoma. *J. Histochem. Cytochem.* 57, 79–86.
- Gossen, M., Bender, G., Muller, G., al, et, and Freundlieb, S. (1995). Transcriptional activation by tetracyclines in mammalian cells. *Science* 268, 1766.
- Le Graverand-Gastineau, M.P. (2010). Disease modifying osteoarthritis drugs: facing development challenges and choosing molecular targets. *Curr Drug Targets* 11, 528–535.
- Graves, M.L., Cipollone, J.A., Austin, P., Bell, E.M., Nielsen, J.S., Gilks, C.B., McNagny, K.M., and Roskelley, C.D. (2016). The cell surface mucin podocalyxin regulates collective breast tumor budding. *Breast Cancer Research* 18, 11.
- Guddo, F., Giatromanolaki, A., Koukourakis, M.I., Reina, C., Vignola, A.M., Chlouverakis, G., Hilkens, J., Gatter, K.C., Harris, A.L., and Bonsignore, G. (1998). MUC1 (episialin) expression in non-small cell lung cancer is independent of EGFR and c-erbB-2 expression and correlates with poor survival in node positive patients. *J Clin Pathol* 51, 667–671.

Guillaumond, F., Leca, J., Olivares, O., Lavaut, M.-N., Vidal, N., Berthezène, P., Dusetti, N.J., Loncle, C., Calvo, E., Turrini, O., et al. (2013). Strengthened glycolysis under hypoxia supports tumor symbiosis and hexosamine biosynthesis in pancreatic adenocarcinoma. *PNAS* *110*, 3919–3924.

Gupton, S.L., and Gertler, F.B. (2007). Filopodia: the fingers that do the walking. *Science's STKE: Signal Transduction Knowledge Environment* *2007*, re5.

Gutierrez, E., Tkachenko, E., Besser, A., Sundd, P., Ley, K., Danuser, G., Ginsberg, M.H., and Groisman, A. (2011). High Refractive Index Silicone Gels for Simultaneous Total Internal Reflection Fluorescence and Traction Force Microscopy of Adherent Cells. *PLOS ONE* *6*, e23807.

Hakomori, S. (2001). Tumor-associated carbohydrate antigens defining tumor malignancy: basis for development of anti-cancer vaccines. *Adv. Exp. Med. Biol.* *491*, 369–402.

Halder, G., Dupont, S., and Piccolo, S. (2012). Transduction of mechanical and cytoskeletal cues by YAP and TAZ. *Nat Rev Mol Cell Biol* *13*, 591–600.

Hall, A. (1998). Rho GTPases and the actin cytoskeleton. *Science (New York, N.Y.)* *279*, 509–514.

Halpern, A.R., Howard, M.D., and Vaughan, J.C. (2015). Point by Point: An Introductory Guide to Sample Preparation for Single-Molecule, Super-Resolution Fluorescence Microscopy. *Curr Protoc Chem Biol* *7*, 103–120.

Haltiwanger, R.S., and Lowe, J.B. (2004). Role of glycosylation in development. *Annu. Rev. Biochem.* *73*, 491–537.

Han, Y., Liu, X.-M., Liu, H., Li, S.-C., Wu, B.-C., Ye, L.-L., Wang, Q.-W., and Chen, Z.-L. (2006). Cultivation of Recombinant Chinese hamster ovary cells grown as suspended aggregates in stirred vessels. *Journal of Bioscience and Bioengineering* *102*, 430–435.

Hang, H.C., and Bertozzi, C.R. (2005). The chemistry and biology of mucin-type O-linked glycosylation. *Bioorganic & Medicinal Chemistry* *13*, 5021–5034.

Hansen, P.L., Cohen, J.A., Podgornik, R., and Parsegian, V.A. (2003). Osmotic properties of poly(ethylene glycols): quantitative features of brush and bulk scaling laws. *Biophys. J.* 84, 350–355.

Hattrup, C.L., and Gendler, S.J. (2008). Structure and function of the cell surface (tethered) mucins. *Annual Review of Physiology* 70, 431–457.

Häuselmann, I., and Borsig, L. (2014). Altered tumor-cell glycosylation promotes metastasis. *Front Oncol* 4, 28.

Hayashi, K., Tsutsumi, K., Nakajima, F., Norisuye, T., and Teramoto, A. (1995). Chain-stiffness and excluded-volume effects in solutions of sodium hyaluronate at high ionic strength. *Macromolecules* 28, 3824–3830.

Hayes, D.F., Mesa-Tejada, R., Papsidero, L.D., Croghan, G.A., Korzun, A.H., Norton, L., Wood, W., Strauchen, J.A., Grimes, M., and Weiss, R.B. (1991). Prediction of prognosis in primary breast cancer by detection of a high molecular weight mucin-like antigen using monoclonal antibodies DF3, F36/22, and CU18: a Cancer and Leukemia Group B study. *J. Clin. Oncol.* 9, 1113–1123.

Helfrich, W. (2014). Elastic Properties of Lipid Bilayers: Theory and Possible Experiments. *Zeitschrift Für Naturforschung C* 28, 693–703.

Hertz, H. (1882). Ueber die Berührung fester elastischer Körper. *Journal für die reine und angewandte Mathematik* 92, 156–171.

Hidalgo, M., Amant, F., Biankin, A.V., Budinská, E., Byrne, A.T., Caldas, C., Clarke, R.B., Jong, S. de, Jonkers, J., Mælandsmo, G.M., et al. (2014). Patient-Derived Xenograft Models: An Emerging Platform for Translational Cancer Research. *Cancer Discov* 4, 998–1013.

Hiergeist, C., and Lipowsky, R. (1996). Elastic Properties of Polymer-Decorated Membranes. *Journal de Physique II* 6, 1465–1481.

Hinoda, Y., Ikematsu, Y., Horinouchi, M., Sato, S., Yamamoto, K., Nakano, T., Fukui, M., Suehiro, Y., Hamanaka, Y., Nishikawa, Y., et al. (2003). Increased expression of MUC1 in advanced pancreatic cancer. *J. Gastroenterol.* 38, 1162–1166.

Hollingsworth, M.A., and Swanson, B.J. (2004). Mucins in cancer: protection and control of the cell surface. *Nat Rev Cancer* 4, 45–60.

Hong, V., Steinmetz, N.F., Manchester, M., and Finn, M.G. (2010). Labeling Live Cells by Copper-Catalyzed Alkyne–Azide Click Chemistry. *Bioconjugate Chem.* 21, 1912–1916.

Hooper, L.V., and Gordon, J.I. (2001). Glycans as legislators of host-microbial interactions: spanning the spectrum from symbiosis to pathogenicity. *Glycobiology* 11, 1R-10R.

Horm, T.M., and Schroeder, J.A. (2013). MUC1 and metastatic cancer. *Cell Adhesion & Migration* 7, 187–198.

Hu, W., Berdugo, C., and Chalmers, J.J. (2011). The potential of hydrodynamic damage to animal cells of industrial relevance: current understanding. *Cytotechnology* 63, 445–460.

Huang, M.L., Cohen, M., Fisher, C.J., Schooley, R.T., Gagneux, P., and Godula, K. (2015). Determination of receptor specificities for whole influenza viruses using multivalent glycan arrays. *Chem. Commun.* 51, 5326–5329.

Hudak, J.E., and Bertozzi, C.R. (2014). Glycotherapy: New Advances Inspire a Reemergence of Glycans in Medicine. *Chemistry & Biology* 21, 16–37.

Hudak, J.E., Canham, S.M., and Bertozzi, C.R. (2014). Glycocalyx engineering reveals a Siglec-based mechanism for NK cell immunoevasion. *Nat Chem Biol* 10, 69–75.

Hughes, R.A., Miklos, A.E., and Ellington, A.D. (2011). Gene synthesis: methods and applications. *Meth. Enzymol.* 498, 277–309.

Hui, C.-Y., Liu, T., Salez, T., Raphael, E., and Jagota, A. (2015). Indentation of a rigid sphere into an elastic substrate with surface tension and adhesion. *Proc. R. Soc. A* 471, 20140727.

Ilina, O., Campanello, L., Gritsenko, P.G., Vullings, M., Wang, C., Bult, P., Losert, W., and Friedl, P. (2018). Intravital microscopy of collective invasion plasticity in breast cancer. *Disease Models & Mechanisms* 11, dmm034330.

- Israels, R., Leermakers, F.A.M., Fler, G.J., and Zhulina, E.B. (1994). Charged Polymeric Brushes: Structure and Scaling Relations. *Macromolecules* 27, 3249–3261.
- Janik, M.E., Lityńska, A., and Vereecken, P. (2010). Cell migration—The role of integrin glycosylation. *Biochimica et Biophysica Acta (BBA) - General Subjects* 1800, 545–555.
- Jay, G.D., and Waller, K.A. (2014). The biology of Lubricin: Near frictionless joint motion. *Matrix Biology* 39, 17–24.
- Jones, A.R.C., Gleghorn, J.P., Hughes, C.E., Fitz, L.J., Zollner, R., Wainwright, S.D., Caterson, B., Morris, E.A., Bonassar, L.J., and Flannery, C.R. (2007). Binding and localization of recombinant lubricin to articular cartilage surfaces. *Journal of Orthopaedic Research* 25, 283–292.
- Jordan, M., and Wurm, F. (2004). Transfection of adherent and suspended cells by calcium phosphate. *Methods* 33, 136–143.
- Joshi, M.D., Ahmad, R., Yin, L., Raina, D., Rajabi, H., Bublely, G., Kharbanda, S., and Kufe, D. (2009). MUC1 oncoprotein is a druggable target in human prostate cancer cells. *Mol. Cancer Ther.* 8, 3056–3065.
- Ju, T., Wang, Y., Aryal, R.P., Lehoux, S.D., Ding, X., Kudelka, M.R., Cutler, C., Zeng, J., Wang, J., Sun, X., et al. (2013). Tn and sialyl-Tn antigens, aberrant O-glycomics as human disease markers. *Prot. Clin. Appl.* 7, 618–631.
- Jung, Y., Riven, I., Feigelson, S.W., Kartvelishvily, E., Tohya, K., Miyasaka, M., Alon, R., and Haran, G. (2016). Three-dimensional localization of T-cell receptors in relation to microvilli using a combination of superresolution microscopies. *Proceedings of the National Academy of Sciences* 113, E5916–E5924.
- Kaszuba, K., Grzybek, M., Orłowski, A., Danne, R., Róg, T., Simons, K., Coskun, Ü., and Vattulainen, I. (2015). N-Glycosylation as determinant of epidermal growth factor receptor conformation in membranes. *PNAS* 112, 4334–4339.
- Kenworthy, A.K., Hristova, K., Needham, D., and McIntosh, T.J. (1995). Range and magnitude of the steric pressure between bilayers containing

phospholipids with covalently attached poly(ethylene glycol). *Biophys J* 68, 1921–1936.

Kesavan, G., Sand, F.W., Greiner, T.U., Johansson, J.K., Kobberup, S., Wu, X., Brakebusch, C., and Semb, H. (2009). Cdc42-Mediated Tubulogenesis Controls Cell Specification. *Cell* 139, 791–801.

Kesimer, M., Ehre, C., Burns, K.A., Davis, C.W., Sheehan, J.K., and Pickles, R.J. (2013). Molecular organization of the mucins and glycocalyx underlying mucus transport over mucosal surfaces of the airways. *Mucosal Immunol* 6, 379–392.

Khetan, S., Guvendiren, M., Legant, W.R., Cohen, D.M., Chen, C.S., and Burdick, J.A. (2013). Degradation-mediated cellular traction directs stem cell fate in covalently crosslinked three-dimensional hydrogels. *Nat Mater* 12, 458–465.

Kim, N.-G., and Gumbiner, B.M. (2015). Adhesion to fibronectin regulates Hippo signaling via the FAK–Src–PI3K pathway. *J Cell Biol* 210, 503–515.

Kim, Y.J., and Varki, A. Perspectives on the significance of altered glycosylation of glycoproteins in cancer. *Glycoconj J* 14, 569–576.

Kim, S.A., Tai, C.-Y., Mok, L.-P., Mosser, E.A., and Schuman, E.M. (2011). Calcium-dependent dynamics of cadherin interactions at cell–cell junctions. *PNAS* 108, 9857–9862.

Klinken, B.J.V., Dekker, J., Buller, H.A., and Einerhand, A.W. (1995). Mucin gene structure and expression: protection vs. adhesion. *American Journal of Physiology - Gastrointestinal and Liver Physiology* 269, G613–G627.

Koike, T., Kimura, N., Miyazaki, K., Yabuta, T., Kumamoto, K., Takenoshita, S., Chen, J., Kobayashi, M., Hosokawa, M., Taniguchi, A., et al. (2004). Hypoxia induces adhesion molecules on cancer cells: A missing link between Warburg effect and induction of selectin-ligand carbohydrates. *Proc. Natl. Acad. Sci. U.S.A.* 101, 8132–8137.

Koistinen, V., Kärnä, R., Koistinen, A., Arjonen, A., Tammi, M., and Rilla, K. (2015). Cell protrusions induced by hyaluronan synthase 3 (HAS3) resemble mesothelial microvilli and share cytoskeletal features of filopodia. *Experimental Cell Research* 337, 179–191.

Kolata, G.B. (1975). Microvilli: A Major Difference Between Normal and Cancer Cells? *Science* 188, 819–820.

Kornberg, T.B., and Roy, S. (2014). Cytonemes as specialized signaling filopodia. *Development* 141, 729–736.

Kosinska, M.K., Ludwig, T.E., Liebisch, G., Zhang, R., Siebert, H.-C., Wilhelm, J., Kaesser, U., Dettmeyer, R.B., Klein, H., Ishaque, B., et al. (2015). Articular Joint Lubricants during Osteoarthritis and Rheumatoid Arthritis Display Altered Levels and Molecular Species. *PLOS ONE* 10, e0125192.

Kosuri, S., and Church, G.M. (2014). Large-scale de novo DNA synthesis: technologies and applications. *Nature Methods* 11, 499.

Kovall, R.A., Gebelein, B., Sprinzak, D., and Kopan, R. (2017). The Canonical Notch Signaling Pathway: Structural and Biochemical Insights into Shape, Sugar, and Force. *Dev. Cell* 41, 228–241.

Kozlovsky, Y., and Kozlov, M.M. (2003). Membrane Fission: Model for Intermediate Structures. *Biophys J* 85, 85–96.

Kramer, R.H., and Nicolson, G.L. (1979). Interactions of tumor cells with vascular endothelial cell monolayers: a model for metastatic invasion. *Proceedings of the National Academy of Sciences of the United States of America* 76, 5704–5708.

Kramer, J.R., Onoa, B., Bustamante, C., and Bertozzi, C.R. (2015). Chemically tunable mucin chimeras assembled on living cells. *PNAS* 112, 12574–12579.

Kudo, T., Ikehara, Y., Togayachi, A., Morozumi, K., Watanabe, M., Nakamura, M., Nishihara, S., and Narimatsu, H. (1998). Up-regulation of a set of glycosyltransferase genes in human colorectal cancer. *Lab Invest* 78, 797–811.

Kufe, D.W. (2009). Mucins in cancer: function, prognosis and therapy. *Nature Reviews Cancer* 9, nrc2761.

Kufe, D., Inghirami, G., Abe, M., Hayes, D., Justi-Wheeler, H., and Schlom, J. (1984). Differential reactivity of a novel monoclonal antibody (DF3) with human malignant versus benign breast tumors. *Hybridoma* 3, 223–232.

- Kuo, J.C.-H., Gandhi, J.G., Zia, R.N., and Paszek, M.J. (2018). Physical biology of the cancer cell glycocalyx. *Nature Physics* 14, 658–669.
- Lajoie, P., Partridge, E.A., Guay, G., Goetz, J.G., Pawling, J., Lagana, A., Joshi, B., Dennis, J.W., and Nabi, I.R. (2007). Plasma membrane domain organization regulates EGFR signaling in tumor cells. *J Cell Biol* 179, 341–356.
- Lakins, J.N., Chin, A.R., and Weaver, V.M. (2012). Exploring the link between human embryonic stem cell organization and fate using tension-calibrated extracellular matrix functionalized polyacrylamide gels. *Methods Mol. Biol.* 916, 317–350.
- LaMont, J.T., and Isselbacher, K.J. (1975). Alterations in Glycosyltransferase Activity in Human Colon Cancer. *J Natl Cancer Inst* 54, 53–56.
- Lange, K. (2011). Fundamental role of microvilli in the main functions of differentiated cells: Outline of an universal regulating and signaling system at the cell periphery. *Journal of Cellular Physiology* 226, 896–927.
- Lau, K.S., Partridge, E.A., Grigorian, A., Silvescu, C.I., Reinhold, V.N., Demetriou, M., and Dennis, J.W. (2007). Complex N-Glycan Number and Degree of Branching Cooperate to Regulate Cell Proliferation and Differentiation. *Cell* 129, 123–134.
- Leader, B., Baca, Q.J., and Golan, D.E. (2008). Protein therapeutics: a summary and pharmacological classification. *Nat Rev Drug Discov* 7, 21–39.
- Lee, G.M., Johnstone, B., Jacobson, K., and Caterson, B. (1993). The dynamic structure of the pericellular matrix on living cells. *The Journal of Cell Biology* 123, 1899–1907.
- Lee, J.N., Jiang, X., Ryan, D., and Whitesides, G.M. (2004). Compatibility of Mammalian Cells on Surfaces of Poly(dimethylsiloxane). *Langmuir* 20, 11684–11691.
- Lehmann, S., Boekhorst, V. te, Odenthal, J., Bianchi, R., Helvert, S. van, Ikenberg, K., Ilina, O., Stoma, S., Xandry, J., Jiang, L., et al. (2017). Hypoxia Induces a HIF-1-Dependent Transition from Collective-to-Amoeboid Dissemination in Epithelial Cancer Cells. *Current Biology* 27, 392–400.

- Levitin, F., Stern, O., Weiss, M., Gil-Henn, C., Ziv, R., Prokocimer, Z., Smorodinsky, N.I., Rubinstein, D.B., and Wreschner, D.H. (2005). The MUC1 SEA module is a self-cleaving domain. *J. Biol. Chem.* 280, 33374–33386.
- Li, J., Han, D., and Zhao, Y.-P. (2014). Kinetic behaviour of the cells touching substrate: the interfacial stiffness guides cell spreading. *Scientific Reports* 4.
- Li, L., Qin, J., Feng, Q., Tang, H., Liu, R., Xu, L., and Chen, Z. (2011). Heparin Promotes Suspension Adaptation Process of CHO–TS28 Cells by Eliminating Cell Aggregation. *Mol Biotechnol* 47, 9–17.
- Li, X., Burnight, E.R., Cooney, A.L., Malani, N., Brady, T., Sander, J.D., Staber, J., Wheelan, S.J., Joung, J.K., McCray, P.B., et al. (2013). piggyBac transposase tools for genome engineering. *PNAS* 110, E2279–E2287.
- Lipowsky, R. (1995). Bending of Membranes by Anchored Polymers. *EPL (Europhysics Letters)* 30, 197.
- Litvinov, S.V., and Hilkens, J. (1993). The epithelial sialomucin, episialin, is sialylated during recycling. *J. Biol. Chem.* 268, 21364–21371.
- Liu, M., and Goudar, C.T. (2013). Gene expression profiling for mechanistic understanding of cellular aggregation in mammalian cell perfusion cultures. *Biotechnol. Bioeng.* 110, 483–490.
- Liu, T.-L., Upadhyayula, S., Milkie, D.E., Singh, V., Wang, K., Swinburne, I.A., Mosaliganti, K.R., Collins, Z.M., Hiscock, T.W., Shea, J., et al. (2018). Observing the cell in its native state: Imaging subcellular dynamics in multicellular organisms. *Science* 360, eaaq1392.
- Liu, Y.-J., Le Berre, M., Lautenschlaeger, F., Maiuri, P., Callan-Jones, A., Heuzé, M., Takaki, T., Voituriez, R., and Piel, M. (2015). Confinement and Low Adhesion Induce Fast Amoeboid Migration of Slow Mesenchymal Cells. *Cell* 160, 659–672.
- Lo, C.-M., Wang, H.-B., Dembo, M., and Wang, Y. (2000). Cell Movement Is Guided by the Rigidity of the Substrate. *Biophysical Journal* 79, 144–152.
- Long, J.M., and Wang, G.F. (2013). Effects of surface tension on axisymmetric Hertzian contact problem. *Mechanics of Materials* 56, 65–70.

López Castel, A., Cleary, J.D., and Pearson, C.E. (2010). Repeat instability as the basis for human diseases and as a potential target for therapy. *Nature Reviews Molecular Cell Biology* 11, 165.

de los Milagros Bassani Molinas, M., Beer, C., Hesse, F., Wirth, M., and Wagner, R. (2014). Optimizing the transient transfection process of HEK-293 suspension cells for protein production by nucleotide ratio monitoring. *Cytotechnology* 66, 493–514.

Lou, E., Fujisawa, S., Barlas, A., Romin, Y., Manova-Todorova, K., Moore, M.A.S., and Subramanian, S. (2012). Tunneling Nanotubes. *Commun Integr Biol* 5, 399–403.

Lunt, S.Y., and Vander Heiden, M.G. (2011). Aerobic Glycolysis: Meeting the Metabolic Requirements of Cell Proliferation. *Annual Review of Cell and Developmental Biology* 27, 441–464.

Ma, S., Tang, N., and Tian, J. (2012). DNA synthesis, assembly and applications in synthetic biology. *Curr Opin Chem Biol* 16, 260–267.

Makabe, S., Naguro, T., and Stallone, T. (2006). Oocyte–follicle cell interactions during ovarian follicle development, as seen by high resolution scanning and transmission electron microscopy in humans. *Microscopy Research and Technique* 69, 436–449.

Malaker, S.A., Pedram, K., Ferracane, M.J., Woods, E.C., Kramer, J., Dorigo, O., and Bertozzi, C. (2018). A Mucin-Specific Protease Enables Molecular and Functional Analysis of Human Cancer-Associated Mucins.

Mantelli, F., and Argüeso, P. (2008). Functions of ocular surface mucins in health and disease. *Current Opinion in Allergy and Clinical Immunology* 8, 477–483.

Marcelino, J., Carpten, J.D., Suwairi, W.M., Gutierrez, O.M., Schwartz, S., Robbins, C., Sood, R., Makalowska, I., Baxevanis, A., Johnstone, B., et al. (1999). CACP, encoding a secreted proteoglycan, is mutated in camptodactyly-arthropathy-coxa vara-pericarditis syndrome. *Nature Genetics* 23, 319.

Marshall, W.F. (2012). Gangod. *Bioessays* 34, 721–724.

Marth, J.D., and Grewal, P.K. (2008). Mammalian glycosylation in immunity. *Nat Rev Immunol* 8, 874–887.

Mauris, J., and Argüeso, P. (2012). Mucins and Galectin-3 in Ocular Surface Health and Disease. In *Galectins and Disease Implications for Targeted Therapeutics*, (American Chemical Society), pp. 409–414.

McConnell, R.E., Higginbotham, J.N., Shifrin, D.A., Tabb, D.L., Coffey, R.J., and Tyska, M.J. (2009). The enterocyte microvillus is a vesicle-generating organelle. *Journal of Cell Biology* 185, 1285–1298.

McGuckin, M.A., Walsh, M.D., Hohn, B.G., Ward, B.G., and Wright, R.G. (1995). Prognostic significance of mucl epithelial mucin expression in breast cancer. *Human Pathology* 26, 432–439.

McMaster, T.J., Berry, M., Corfield, A.P., and Miles, M.J. (1999). Atomic force microscopy of the submolecular architecture of hydrated ocular mucins. *Biophys. J.* 77, 533–541.

Meissner, P., Pick, H., Kulangara, A., Chatellard, P., Friedrich, K., and Wurm, F.M. (2001). Transient gene expression: recombinant protein production with suspension-adapted HEK293-EBNA cells. *Biotechnol. Bioeng.* 75, 197–203.

Menck, K., Bleckmann, A., Wachter, A., Hennies, B., Ries, L., Schulz, M., Balkenhol, M., Pukrop, T., Schatlo, B., Rost, U., et al. (2017). Characterisation of tumour-derived microvesicles in cancer patients' blood and correlation with clinical outcome. *J Extracell Vesicles* 6, 1340745.

Mercanti, V., Marchetti, A., Lelong, E., Perez, F., Orci, L., and Cosson, P. (2010). Transmembrane domains control exclusion of membrane proteins from clathrin-coated pits. *J Cell Sci* 123, 3329–3335.

Metallo, C.M., and Heiden, M.G.V. (2010). Metabolism strikes back: metabolic flux regulates cell signaling. *Genes Dev.* 24, 2717–2722.

Milner, S.T. (1991). Polymer brushes. *Science* 251, 905–914.

Möckl, L., Pedram, K., Roy, A.R., Krishnan, V., Gustavsson, A.-K., Dorigo, O., Bertozzi, C., and Moerner, W.E. (2018). Quantitative Super-Resolution Microscopy of the Mammalian Glycocalyx.

- Mogilner, A., and Rubinstein, B. (2005). The Physics of Filopodial Protrusion. *Biophys J* 89, 782–795.
- Morlot, S., Galli, V., Klein, M., Chiaruttini, N., Manzi, J., Humbert, F., Dinis, L., Lenz, M., Cappello, G., and Roux, A. (2012). Membrane shape at the edge of the dynamin helix sets location and duration of the fission reaction. *Cell* 151, 619–629.
- Müller, S., Alving, K., Peter-Katalinic, J., Zachara, N., Gooley, A.A., and Hanisch, F.G. (1999). High density O-glycosylation on tandem repeat peptide from secretory MUC1 of T47D breast cancer cells. *J. Biol. Chem.* 274, 18165–18172.
- Munkley, J. (2016). The Role of Sialyl-Tn in Cancer. *Int J Mol Sci* 17.
- Muralidharan-Chari, V., Clancy, J.W., Sedgwick, A., and D’Souza-Schorey, C. (2010). Microvesicles: mediators of extracellular communication during cancer progression. *J Cell Sci* 123, 1603–1611.
- Nairn, A.V., York, W.S., Harris, K., Hall, E.M., Pierce, J.M., and Moremen, K.W. (2008). Regulation of Glycan Structures in Animal Tissues TRANSCRIPT PROFILING OF GLYCAN-RELATED GENES. *J. Biol. Chem.* 283, 17298–17313.
- Nath, S., and Mukherjee, P. (2014). Muc1: a multifaceted oncoprotein with a key role in cancer progression. *Trends in Molecular Medicine* 20, 332–342.
- Nazari, M., Kurdi, M., and Heerklotz, H. (2012). Classifying Surfactants with Respect to Their Effect on Lipid Membrane Order. *Biophysical Journal* 102, 498–506.
- Nguyen, D.X., Bos, P.D., and Massagué, J. (2009). Metastasis: from dissemination to organ-specific colonization. *Nat Rev Cancer* 9, 274–284.
- Nielsen, J.S., and McNagny, K.M. (2009). The Role of Podocalyxin in Health and Disease. *JASN* 20, 1669–1676.
- Ohtsubo, K., and Marth, J.D. (2006). Glycosylation in Cellular Mechanisms of Health and Disease. *Cell* 126, 855–867.
- Oren, M., Barela Hudgell, M.A., D’Allura, B., Agronin, J., Gross, A., Podini, D., and Smith, L.C. (2016). Short tandem repeats, segmental duplications, gene

deletion, and genomic instability in a rapidly diversified immune gene family. *BMC Genomics* 17, 900.

Ovesný, M., Křížek, P., Borkovec, J., Svindrych, Z., and Hagen, G.M. (2014). ThunderSTORM: a comprehensive ImageJ plug-in for PALM and STORM data analysis and super-resolution imaging. *Bioinformatics* 30, 2389–2390.

Paluch, E.K., and Raz, E. (2013). The role and regulation of blebs in cell migration. *Current Opinion in Cell Biology* 25, 582–590.

Park, J.H., Lim, M.S., Woo, J.R., Kim, J.W., and Lee, G.M. (2016). The molecular weight and concentration of dextran sulfate affect cell growth and antibody production in CHO cell cultures. *Biotechnology Progress* 32, 1113–1122.

Parry, S., Silverman, H.S., McDermott, K., Willis, A., Hollingsworth, M.A., and Harris, A. (2001). Identification of MUC1 Proteolytic Cleavage Sites in Vivo. *Biochemical and Biophysical Research Communications* 283, 715–720.

Paszek, M.J., Zahir, N., Johnson, K.R., Lakins, J.N., Rozenberg, G.I., Gefen, A., Reinhart-King, C.A., Margulies, S.S., Dembo, M., Boettiger, D., et al. (2005). Tensional homeostasis and the malignant phenotype. *Cancer Cell* 8, 241–254.

Paszek, M.J., Boettiger, D., Weaver, V.M., and Hammer, D.A. (2009). Integrin Clustering Is Driven by Mechanical Resistance from the Glycocalyx and the Substrate. *PLOS Comput Biol* 5, e1000604.

Paszek, M.J., DuFort, C.C., Rubashkin, M.G., Davidson, M.W., Thorn, K.S., Liphardt, J.T., and Weaver, V.M. (2012). Scanning angle interference microscopy reveals cell dynamics at the nanoscale. *Nat Meth* 9, 825–827.

Paszek, M.J., DuFort, C.C., Rossier, O., Bainer, R., Mouw, J.K., Godula, K., Hudak, J.E., Lakins, J.N., Wijekoon, A.C., Cassereau, L., et al. (2014). The cancer glycocalyx mechanically primes integrin-mediated growth and survival. *Nature* 511, 319–325.

Paturej, J., Sheiko, S.S., Panyukov, S., and Rubinstein, M. (2016). Molecular structure of bottlebrush polymers in melts. *Science Advances* 2, e1601478.

Pearson, C.E., Edamura, K.N., and Cleary, J.D. (2005). Repeat instability: mechanisms of dynamic mutations. *Nature Reviews Genetics* 6, 729.

Pelaseyed, T., Bergström, J.H., Gustafsson, J.K., Ermund, A., Birchenough, G.M.H., Schütte, A., Post, S. van der, Svensson, F., Rodríguez-Piñero, A.M., Nyström, E.E.L., et al. (2014). The mucus and mucins of the goblet cells and enterocytes provide the first defense line of the gastrointestinal tract and interact with the immune system. *Immunological Reviews* 260, 8–20.

Pelham, R.J., and Wang, Y. (1997). Cell locomotion and focal adhesions are regulated by substrate flexibility. *PNAS* 94, 13661–13665.

Peshwa, M.V., Kyung, Y.-S., McClure, D.B., and Hu, W.-S. (1993). Cultivation of mammalian cells as aggregates in bioreactors: Effect of calcium concentration of spatial distribution of viability. *Biotechnol. Bioeng.* 41, 179–187.

Peskin, C.S., Odell, G.M., and Oster, G.F. (1993). Cellular motions and thermal fluctuations: the Brownian ratchet. *Biophysical Journal* 65, 316–324.

Pilon, C., Levast, B., Meurens, F., Le Vern, Y., Kerboeuf, D., Salmon, H., Velge-Roussel, F., Lebranchu, Y., and Baron, C. (2009). CD40 engagement strongly induces CD25 expression on porcine dendritic cells and polarizes the T cell immune response toward Th1. *Molecular Immunology* 46, 437–447.

Pinho, S.S., and Reis, C.A. (2015). Glycosylation in cancer: mechanisms and clinical implications. *Nat Rev Cancer* 15, 540–555.

van den Pol, A.N., and Kim, W.T. (1993). NILE/L1 and NCAM-polysialic acid expression on growing axons of isolated neurons. *The Journal of Comparative Neurology* 332, 237–257.

Polefka, T.G., Garrick, R.A., Redwood, W.R., Swislocki, N.I., and Chinard, F.P. (1984). Solute-excluded volumes near the Novikoff cell surface. *American Journal of Physiology-Cell Physiology* 247, C350–C356.

Porter, A.P., Papaioannou, A., and Malliri, A. (2016). Deregulation of Rho GTPases in cancer. *Small GTPases* 7, 123–138.

Radhakrishnan, P., Dabelsteen, S., Madsen, F.B., Francavilla, C., Kopp, K.L., Steentoft, C., Vakhrushev, S.Y., Olsen, J.V., Hansen, L., Bennett, E.P., et al. (2014). Immature truncated O-glycophenotype of cancer directly induces oncogenic features. *PNAS* 111, E4066–E4075.

- Rahn, J.J., Dabbagh, L., Pasdar, M., and Hugh, J.C. (2001). The importance of MUC1 cellular localization in patients with breast carcinoma. *Cancer* 91, 1973–1982.
- Raina, D., Kharbanda, S., and Kufe, D. (2004). The MUC1 oncoprotein activates the anti-apoptotic phosphoinositide 3-kinase/Akt and Bcl-xL pathways in rat 3Y1 fibroblasts. *J. Biol. Chem.* 279, 20607–20612.
- Raucher, D., and Sheetz, M.P. (1999). Characteristics of a membrane reservoir buffering membrane tension. *Biophys. J.* 77, 1992–2002.
- Reesink, H.L., Bonnevie, E.D., Liu, S., Shurer, C.R., Hollander, M.J., Bonassar, L.J., and Nixon, A.J. (2016). Galectin-3 Binds to Lubricin and Reinforces the Lubricating Boundary Layer of Articular Cartilage. *Scientific Reports* 6, 25463.
- Reitsma, S., Slaaf, D.W., Vink, H., van Zandvoort, M.A.M.J., and oude Egbrink, M.G.A. (2007). The endothelial glycocalyx: composition, functions, and visualization. *Pflugers Arch - Eur J Physiol* 454, 345–359.
- Rhee, D.K., Marcelino, J., Baker, M., Gong, Y., Smits, P., Lefebvre, V., Jay, G.D., Stewart, M., Wang, H., Warman, M.L., et al. (2005). The secreted glycoprotein lubricin protects cartilage surfaces and inhibits synovial cell overgrowth. *J Clin Invest* 115, 622–631.
- Riemersma, M., Sandrock, J., Boltje, T.J., Büll, C., Heise, T., Ashikov, A., Adema, G.J., van Bokhoven, H., and Lefeber, D.J. (2015). Disease mutations in CMP-sialic acid transporter SLC35A1 result in abnormal α -dystroglycan O-mannosylation, independent from sialic acid. *Human Molecular Genetics*.
- Rodrigues, M.E., Costa, A.R., Henriques, M., Cunnah, P., Melton, D.W., Azeredo, J., and Oliveira, R. (2013). Advances and Drawbacks of the Adaptation to Serum-Free Culture of CHO-K1 Cells for Monoclonal Antibody Production. *Appl Biochem Biotechnol* 169, 1279–1291.
- Rosen, M.J., and Kunjappu, J.T. (2012). *Surfactants and Interfacial Phenomena* (John Wiley & Sons).
- Sansom, M.L., Morrison, S., Masala, N., Sullivan, B.D., Sullivan, D.A., Sheardown, H., and Schmidt, T.A. (2014). Characterization of full-length recombinant human Proteoglycan 4 as an ocular surface boundary lubricant. *Experimental Eye Research* 127, 14–19.

- Sandberg, H., Kannicht, C., Stenlund, P., Dadaian, M., Oswaldsson, U., Cordula, C., and Walter, O. (2012). Functional characteristics of the novel, human-derived recombinant FVIII protein product, human-cl rhFVIII. *Thromb. Res.* *130*, 808–817.
- Sanderson, M.J., and Sleight, M.A. (1981). Ciliary activity of cultured rabbit tracheal epithelium: beat pattern and metachrony. *Journal of Cell Science* *47*, 331–347.
- Satoomaa, T., Heiskanen, A., Mikkola, M., Olsson, C., Blomqvist, M., Tiittanen, M., Jaatinen, T., Aitio, O., Olonen, A., Helin, J., et al. (2009). The N-glycome of human embryonic stem cells. *BMC Cell Biol.* *10*, 42.
- Sauvanet, C., Wayt, J., Pelaseyed, T., and Bretscher, A. (2015). Structure, Regulation, and Functional Diversity of Microvilli on the Apical Domain of Epithelial Cells. *Annual Review of Cell and Developmental Biology* *31*, 593–621.
- Saxer, R.A., Bent, S.J., Brower-Toland, B.D., Mi, Z., Robbins, P.D., Evans, C.H., and Nixon, A.J. (2001). Gene mediated insulin-like growth factor-I delivery to the synovium. *Journal of Orthopaedic Research: Official Publication of the Orthopaedic Research Society* *19*, 759–767.
- Schachter, H. (1986). Biosynthetic controls that determine the branching and microheterogeneity of protein-bound oligosaccharides. *Biochem. Cell Biol.* *64*, 163–181.
- Schindelin, J., Arganda-Carreras, I., Frise, E., Kaynig, V., Longair, M., Pietzsch, T., Preibisch, S., Rueden, C., Saalfeld, S., Schmid, B., et al. (2012). Fiji: an open-source platform for biological-image analysis. *Nat. Methods* *9*, 676–682.
- Schmick, M., and Bastiaens, P.I.H. (2014). The Interdependence of Membrane Shape and Cellular Signal Processing. *Cell* *156*, 1132–1138.
- Schmidt, T.A., Sullivan, D.A., Knop, E., and et al. (2013). Transcription, translation, and function of lubricin, a boundary lubricant, at the ocular surface. *JAMA Ophthalmology* *131*, 766–776.
- Schroeter, E.H., Kisslinger, J.A., and Kopan, R. (1998). Notch-1 signalling requires ligand-induced proteolytic release of intracellular domain. *Nature* *393*, 382–386.

- Seifert, U., Berndl, K., and Lipowsky, R. (1991). Shape transformations of vesicles: Phase diagram for spontaneous- curvature and bilayer-coupling models. *Phys. Rev. A* 44, 1182–1202.
- Shi, Q., and Boettiger, D. (2003). A Novel Mode for Integrin-mediated Signaling: Tethering Is Required for Phosphorylation of FAK Y397. *Mol Biol Cell* 14, 4306–4315.
- Shirato, K., Nakajima, K., Korekane, H., Takamatsu, S., Gao, C., Angata, T., Ohtsubo, K., and Taniguchi, N. (2011). Hypoxic regulation of glycosylation via the N-acetylglucosamine cycle. *J Clin Biochem Nutr* 48, 20–25.
- Shogren, R., Gerken, T.A., and Jentoft, N. (1989). Role of glycosylation on the conformation and chain dimensions of O-linked glycoproteins: light-scattering studies of ovine submaxillary mucin. *Biochemistry* 28, 5525–5536.
- Shukla, A.A., and Thömmes, J. (2010). Recent advances in large-scale production of monoclonal antibodies and related proteins. *Trends in Biotechnology* 28, 253–261.
- Shurer, C.R., Colville, M.J., Gupta, V.K., Head, S.E., Kai, F., Lakins, J.N., and Paszek, M.J. (2018). Genetically Encoded Toolbox for Glycocalyx Engineering: Tunable Control of Cell Adhesion, Survival, and Cancer Cell Behaviors. *ACS Biomaterials Science & Engineering* 4, 388–399.
- Shurer, C.R., Head, S.E., Goudge, M.C., and Paszek, M.J. (2019a). Mucin-Coating Technologies for Protection and Reduced Aggregation of Cellular Production Systems. *Biotechnology and Bioengineering*.
- Shurer, C.R., Wang, Y., Feeney, E., Head, S.E., Zhang, V.X., Su, J., Cheng, Z., Stark, M.A., Bonassar, L.J., Reesink, H.L., et al. (2019b). Stable recombinant production of codon-scrambled lubricin and mucin in human cells. *Biotechnol. Bioeng.*
- Sjaastad, M.D., and Nelson, W.J. (1997). Integrin-mediated calcium signaling and regulation of cell adhesion by intracellular calcium. *Bioessays* 19, 47–55.
- Snead, W.T., Hayden, C.C., Gadok, A.K., Zhao, C., Lafer, E.M., Rangamani, P., and Stachowiak, J.C. (2017). Membrane fission by protein crowding. *Proc Natl Acad Sci U S A* 114, E3258–E3267.

Snyder, K.A., Hughes, M.R., Hedberg, B., Brandon, J., Hernaez, D.C., Bergqvist, P., Cruz, F., Po, K., Graves, M.L., Turvey, M.E., et al. (2015). Podocalyxin enhances breast tumor growth and metastasis and is a target for monoclonal antibody therapy. *Breast Cancer Research* 17, 46.

Soler, M., Desplat-Jego, S., Vacher, B., Ponsonnet, L., Fraterno, M., Bongrand, P., Martin, J.M., and Foa, C. (1998). Adhesion-related glycocalyx study: quantitative approach with imaging-spectrum in the energy filtering transmission electron microscope (EFTEM). *FEBS Lett.* 429, 89–94.

Sonawane, N.D., Szoka Jr., F.C., and Verkman, A.S. (2003). Chloride accumulation and swelling in endosomes enhances DNA transfer by polyamine-DNA polyplexes. *J Biol Chem* 278, 44826–44831.

Stachowiak, J.C., Schmid, E.M., Ryan, C.J., Ann, H.S., Sasaki, D.Y., Sherman, M.B., Geissler, P.L., Fletcher, D.A., and Hayden, C.C. (2012). Membrane bending by protein-protein crowding. *Nat. Cell Biol.* 14, 944–949.

Stolfa, G., Mondal, N., Zhu, Y., Yu, X., Buffone, A., and Neelamegham, S. (2016). Using CRISPR-Cas9 to quantify the contributions of O-glycans, N-glycans and Glycosphingolipids to human leukocyte-endothelium adhesion. *Scientific Reports* 6, 30392.

Style, R.W., Hyland, C., Boltyanskiy, R., Wettlaufer, J.S., and Dufresne, E.R. (2013). Surface tension and contact with soft elastic solids. *Nat Commun* 4, 2728.

Style, R.W., Jagota, A., Hui, C.-Y., and Dufresne, E.R. (2017). Elastocapillarity: Surface Tension and the Mechanics of Soft Solids. *Annual Review of Condensed Matter Physics* 8, null.

Swiech, K., Kamen, A., Ansorge, S., Durocher, Y., Picanço-Castro, V., Russo-Carbolante, E.M., Neto, M.S., and Covas, D.T. (2011). Transient transfection of serum-free suspension HEK 293 cell culture for efficient production of human rFVIII. *BMC Biotechnol* 11, 114.

Tammi, M.I., Day, A.J., and Turley, E.A. (2002). Hyaluronan and Homeostasis: A Balancing Act. *Journal of Biological Chemistry* 277, 4581–4584.

Tang, N.C., and Chilkoti, A. (2016). Combinatorial codon scrambling enables scalable gene synthesis and amplification of repetitive proteins. *Nature Materials* 15, 419–424.

Thi, M.M., Tarbell, J.M., Weinbaum, S., and Spray, D.C. (2004). The role of the glycocalyx in reorganization of the actin cytoskeleton under fluid shear stress: A “bumper-car” model. *PNAS* 101, 16483–16488.

Thornton, D.J., Rousseau, K., and McGuckin, M.A. (2008). Structure and Function of the Polymeric Mucins in Airways Mucus. *Annual Review of Physiology* 70, 459–486.

Tillberg, P.W., Chen, F., Piatkevich, K.D., Zhao, Y., Yu, C.-C. (Jay), English, B.P., Gao, L., Martorell, A., Suk, H.-J., Yoshida, F., et al. (2016). Protein-retention expansion microscopy of cells and tissues labeled using standard fluorescent proteins and antibodies. *Nat Biotech* 34, 987–992.

Tolbert, W.R., Hitt, M.M., and Feder, J. (1980). Cell aggregate suspension culture for large-scale production of biomolecules. *In Vitro* 16, 486–490.

Trappmann, B., Gautrot, J.E., Connelly, J.T., Strange, D.G.T., Li, Y., Oyen, M.L., Cohen Stuart, M.A., Boehm, H., Li, B., Vogel, V., et al. (2012). Extracellular-matrix tethering regulates stem-cell fate. *Nat Mater* 11, 642–649.

Tricarico, C., Clancy, J., and D’Souza-Schorey, C. (2017). Biology and biogenesis of shed microvesicles. *Small GTPases* 8, 220–232.

Tsafir, I., Sagi, D., Arzi, T., Guedeau-Boudeville, M.-A., Frette, V., Kandel, D., and Stavans, J. (2001). Pearling Instabilities of Membrane Tubes with Anchored Polymers. *Physical Review Letters* 86, 1138–1141.

Tsao, Y.S., Condon, R., Schaefer, E., Lio, P., and Liu, Z. (2001). Development and improvement of a serum-free suspension process for the production of recombinant adenoviral vectors using HEK293 cells. *Cytotechnology* 37, 189–198.

Turley, E.A., Wood, D.K., and McCarthy, J.B. (2016). Carcinoma Cell Hyaluronan as a “Portable” Cancerized Prometastatic Microenvironment. *Cancer Research* 76, 2507–2512.

Ulrich, T.A., Pardo, E.M. de J., and Kumar, S. (2009). The Mechanical Rigidity of the Extracellular Matrix Regulates the Structure, Motility, and Proliferation of Glioma Cells. *Cancer Res* 69, 4167–4174.

Varki, A. (1998). Factors controlling the glycosylation potential of the Golgi apparatus. *Trends in Cell Biology* 8, 34–40.

Varki, A., and Sharon, N. (2009). Historical Background and Overview. In *Essentials of Glycobiology*, A. Varki, R.D. Cummings, J.D. Esko, H.H. Freeze, P. Stanley, C.R. Bertozzi, G.W. Hart, and M.E. Etzler, eds. (Cold Spring Harbor (NY): Cold Spring Harbor Laboratory Press), p.

Varki, A., Cummings, R.D., Esko, J.D., Freeze, H.H., Stanley, P., Bertozzi, C.R., Hart, G.W., and Etzler, M.E. (2009a). *Essentials of Glycobiology* (Cold Spring Harbor Laboratory Press).

Varki, A., Kannagi, R., and Toole, B.P. (2009b). Glycosylation Changes in Cancer. In *Essentials of Glycobiology*, A. Varki, R.D. Cummings, J.D. Esko, H.H. Freeze, P. Stanley, C.R. Bertozzi, G.W. Hart, and M.E. Etzler, eds. (Cold Spring Harbor (NY): Cold Spring Harbor Laboratory Press), p.

Vaupel, P., and Mayer, A. (2007). Hypoxia in cancer: significance and impact on clinical outcome. *Cancer Metastasis Rev* 26, 225–239.

Vermeer, P.D., Einwalter, L.A., Moninger, T.O., Rokhlina, T., Kern, J.A., Zabner, J., and Welsh, M.J. (2003). Segregation of receptor and ligand regulates activation of epithelial growth factor receptor. *Nature* 422, 322–326.

Vink, T., Oudshoorn-Dickmann, M., Roza, M., Reitsma, J.-J., and de Jong, R.N. (2014). A simple, robust and highly efficient transient expression system for producing antibodies. *Methods* 65, 5–10.

Walter, D.M., Venancio, O.S., Buza, E.L., Tobias, J.W., Deshpande, C., Gudiel, A.A., Kim-Kiselak, C., Cicchini, M., Yates, T.J., and Feldser, D.M. (2017). Systematic In Vivo Inactivation of Chromatin-Regulating Enzymes Identifies Setd2 as a Potent Tumor Suppressor in Lung Adenocarcinoma. *Cancer Res.* 77, 1719–1729.

Wang, H.-B., Dembo, M., Hanks, S.K., and Wang, Y. (2001). Focal adhesion kinase is involved in mechanosensing during fibroblast migration. *PNAS* 98, 11295–11300.

Wang, Y., Ju, T., Ding, X., Xia, B., Wang, W., Xia, L., He, M., and Cummings, R.D. (2010). Cosmc is an essential chaperone for correct protein O-glycosylation. *Proceedings of the National Academy of Sciences of the United States of America*.

Weichsel, J., and Geissler, P.L. (2016). The More the Tubular: Dynamic Bundling of Actin Filaments for Membrane Tube Formation. *PLOS Computational Biology* 12, e1004982.

Weissshuhn, P.C., Sheppard, D., Taylor, P., Whiteman, P., Lea, S.M., Handford, P.A., and Redfield, C. (2016). Non-Linear and Flexible Regions of the Human Notch1 Extracellular Domain Revealed by High-Resolution Structural Studies. *Structure* 24, 555–566.

Wellen, K.E., Lu, C., Mancuso, A., Lemons, J.M.S., Ryczko, M., Dennis, J.W., Rabinowitz, J.D., Collier, H.A., and Thompson, C.B. (2010). The hexosamine biosynthetic pathway couples growth factor-induced glutamine uptake to glucose metabolism. *Genes Dev.* 24, 2784–2799.

Wen, J.H., Vincent, L.G., Fuhrmann, A., Choi, Y.S., Hribar, K.C., Taylor-Weiner, H., Chen, S., and Engler, A.J. (2014). Interplay of matrix stiffness and protein tethering in stem cell differentiation. *Nat Mater* 13, 979–987.

Wesseling, J., van der Valk, S.W., Vos, H.L., Sonnenberg, A., and Hilkens, J. (1995). Episialin (MUC1) overexpression inhibits integrin-mediated cell adhesion to extracellular matrix components. *J. Cell Biol.* 129, 255–265.

Wesseling, J., van der Valk, S.W., and Hilkens, J. (1996). A mechanism for inhibition of E-cadherin-mediated cell-cell adhesion by the membrane-associated mucin episialin/MUC1. *Mol. Biol. Cell* 7, 565–577.

Whitesides, G.M., Ostuni, E., Takayama, S., Jiang, X., and Ingber, D.E. (2001). Soft Lithography in Biology and Biochemistry. *Annual Review of Biomedical Engineering* 3, 335–373.

Wilson, M.H., Coates, C.J., and George Jr, A.L. (2007). PiggyBac Transposon-mediated Gene Transfer in Human Cells. *Molecular Therapy* 15, 139–145.

Woodard, L.E., and Wilson, M.H. (2015). piggyBac-ing models and new therapeutic strategies. *Trends Biotechnol.* 33, 525–533.

- Woods, E.C., Yee, N.A., Shen, J., and Bertozzi, C.R. (2015). Glycocalyx Engineering with a Recycling Glycopolymer that Increases Cell Survival In Vivo. *Angew. Chem. Int. Ed. Engl.* 54, 15782–15788.
- Wurm, F.M. (2004). Production of recombinant protein therapeutics in cultivated mammalian cells. *Nature Biotechnology* 22, 1393–1398.
- Wurm, F., and Bernard, A. (1999). Large-scale transient expression in mammalian cells for recombinant protein production. *Current Opinion in Biotechnology* 10, 156–159.
- Xiao, H., Woods, E.C., Vukojcic, P., and Bertozzi, C.R. (2016). Precision glycocalyx editing as a strategy for cancer immunotherapy. *PNAS* 113, 10304–10309.
- Xu, X., Jagota, A., and Hui, C.-Y. (2014). Effects of surface tension on the adhesive contact of a rigid sphere to a compliant substrate. *Soft Matter* 10, 4625–4632.
- Yamaguchi, H., and Condeelis, J. (2007). Regulation of the actin cytoskeleton in cancer cell migration and invasion. *Biochimica et Biophysica Acta (BBA) - Molecular Cell Research* 1773, 642–652.
- Yamamoto, S., Matsuda, H., Takahashi, T., Xing, X.-H., Tanji, Y., and Unno, H. (2000). Aggregate formation of rCHO cells and its maintenance in repeated batch culture in the absence of cell adhesion materials. *Journal of Bioscience and Bioengineering* 89, 534–538.
- Yeung, T., Georges, P.C., Flanagan, L.A., Marg, B., Ortiz, M., Funaki, M., Zahir, N., Ming, W., Weaver, V., and Janmey, P.A. (2005). Effects of substrate stiffness on cell morphology, cytoskeletal structure, and adhesion. *Cell Motil. Cytoskeleton* 60, 24–34.
- Yin, L., Kharbanda, S., and Kufe, D. (2007). Mucin 1 Oncoprotein Blocks Hypoxia-inducible Factor 1 α Activation in a Survival Response to Hypoxia. *J. Biol. Chem.* 282, 257–266.
- Ying, H., Kimmelman, A.C., Lyssiotis, C.A., Hua, S., Chu, G.C., Fletcher-Sananikone, E., Locasale, J.W., Son, J., Zhang, H., Coloff, J.L., et al. (2012). Oncogenic Kras Maintains Pancreatic Tumors through Regulation of Anabolic Glucose Metabolism. *Cell* 149, 656–670.

- Yoshida, K., and Soldati, T. (2006). Dissection of amoeboid movement into two mechanically distinct modes. *Journal of Cell Science* 119, 3833–3844.
- Yuan, H., Tank, M., Alsofyani, A., Shah, N., Talati, N., LoBello, J.C., Kim, J.R., Oonuki, Y., de la Motte, C.A., and Cowman, M.K. (2013). Molecular mass dependence of hyaluronan detection by sandwich ELISA-like assay and membrane blotting using biotinylated hyaluronan binding protein. *Glycobiology* 23, 1270–1280.
- Yusa, K., Zhou, L., Li, M.A., Bradley, A., and Craig, N.L. (2011). A hyperactive piggyBac transposase for mammalian applications. *Proceedings of the National Academy of Sciences* 108, 1531–1536.
- Zanghi, J.A., Renner, W.A., Bailey, J.E., and Fussenegger, M. (2000). The Growth Factor Inhibitor Suramin Reduces Apoptosis and Cell Aggregation in Protein-Free CHO Cell Batch Cultures. *Biotechnol Progress* 16, 319–325.
- Zeng, Y., Ramya, T.N.C., Dirksen, A., Dawson, P.E., and Paulson, J.C. (2009). High efficiency labeling of glycoproteins on living cells. *Nat Methods* 6, 207–209.
- Zhang, H., Miller, R.H., and Rutishauser, U. (1992). Polysialic acid is required for optimal growth of axons on a neuronal substrate. *The Journal of Neuroscience: The Official Journal of the Society for Neuroscience* 12, 3107–3114.
- Zhou, X., Tu, J., Li, Q., Kolosov, V.P., and Perelman, J.M. (2012). Hypoxia induces mucin expression and secretion in human bronchial epithelial cells. *Transl Res* 160, 419–427.
- Zhu, J. (2012). Mammalian cell protein expression for biopharmaceutical production. *Biotechnology Advances* 30, 1158–1170.
- Zhulina, E.B., and Borisov, O. V. (1996). Polyelectrolytes Grafted to Curved Surfaces. *Macromolecules* 29, 2618–2626.
- Zhulina, E.B., Birshtein, T.M., and Borisov, O.V. (2006). Curved polymer and polyelectrolyte brushes beyond the Daoud-Cotton model. *Eur. Phys. J. E* 20, 243–256.